CAL-2572

National Aeronautics and Space Administration

FINAL TECHNICAL REPORT FOR NAS 5-32063

Submitted to:

National Aeronautics and Space Administration
Goddard Space Flight Center
Greenbelt Road
Greenbelt, MD 20771

Submitted by:

The Trustees of Columbia University
in the City of New York
351 Engineering Terrace
New York, New York 10027

Prepared by:

Columbia Astrophysics Laboratory
Departments of Astronomy and Physics
Columbia University
538 West 120^{th} Street
New York, New York 10027

Principal Investigator:

David J. Helfand

Title of Research:

"A Complete Public Archive for the *Einstein* Imaging Proportional Counter"

Period of Covered by Report:

24 September 1992 – 23 September 1996

October 1996

Final Technical Report for NASA NAS5-32063:

"A Complete Public Archive for the *Einstein* IPC"

David J. Helfand

Abstract

Consistent with our proposal to the Astrophysics Data Program in 1992, we have completed the design, construction, documentation, and distribution of a flexible and complete archive of the data collected by the Einstein Imaging Proportional Counter. Along with software and data delivered to the High Energy Astrophysics Science Archive Research Center at Goddard Space Flight Center, we have compiled and, where appropriate, published catalogs of point sources, soft sources, hard sources, extended sources, and transient flares detected in the database along with extensive analyses of the instrument's backgrounds and other anomalies. We include in this document a brief summary of the archive's functionality, a description of the scientific catalogs and other results, a bibliography of publications supported in whole or in part under this contract, and a list of personnel whose pre- and post-doctoral education consisted in part in participation in this project.

I. Project Goals and Achievements

A. The archive software.

The goal of our proposal "A Complete Public Archive for the *Einstein* IPC" was to provide for the community a flexible archive and analysis system. The need for such a system has been apparent for some time, and the progress made at Columbia over the past ten years in understanding and characterizing fully this ground-breaking X-ray astronomy instrument, coupled with the enormous advances in computing power since the original mission, make such a system both desirable and practical. The continued interest and scientific value of the IPC data is apparent from the publication statistics compiled by Dr. F.D. Seward at the Smithsonian Astrophysical Observatory: in 1990 alone, 13 years after the launch (and 9 years after the demise) of the mission, 91 papers using Einstein data appeared in the literature. With the advent of several new X-ray missions in the 1990s (two in progress and four more to come), the value of these archival data will only increase. Placing the powerful Columbia analysis system in the public domain under the aegis of the HEASARC offers permanent access to this important dataset.

This primary goal was accomplished by last fall. After extensive interaction with HEASARC personel, we completed the transfer of the full IPC archive along with a documented set of software which provides for the user a suite of flexible tools with which to derive fluxes and upper limits for any celestial position covered by the 4082 pointings

conducted during the mission. The tools include the flat-fielding algorithm developed at Columbia to correct IPC images for the substantial 1–30 arcminute-scale features in the response of the instrument which seriously compromised some early analysis efforts. A hypercube of flat-fields derived from the full, source-subtracted dataset is invoked when an image is to be analyzed, and a customized flat-field corresponding precisely to the editing criteria used on the image is applied (an option for the user to employ the global flat field using all energy channels and aspect criteria is offered for cases in which the data-editing flags applied to the image produce a corresponding flat field with insufficient statistical precision). Since the user may select from all possible energy ranges, aspect qualities, and viewing geometries in any combination, complete flexibility is achieved.

The source search algorithm used for analyzing a selected, flat-fielded image can perform a source search of a single field or to a user-specified threshold over the entire dataset. A complete description of the algorithm is provided in our paper "The *Einstein* Two-Sigma Catalog" (Moran et al. 1996) which was published in the *Astrophysical Journal* last April. Further details of the many enhancements we have made to the database and analysis system may be found in that paper and/or in last year's annual report.

We have applied this algorithm to the entire dataset and compiled, as we originally proposed, a number of definitive source catalogs which we describe in the next section.

The HEASARC personnel have indicated they are satisfied with the level of documentation of both the data and the analysis software, and it is now in their hands, as specified in the contract, to provide access to the user community.

B. Data products.

Using our IPC analysis system, we have, as proposed, constructed a number of definitive catalogs from the pointed IPC database. These include:

- The two-sigma catalog, containing over 46,000 entries, more than triple the number of real celestial X-ray sources in the original SAO IPC catalog. The utility of this catalog is demonstrated in Moran et al. (1996) where we show how crosscorrelation of this data product with catalogs from other wavelength regimes can yield important new discoveries such sa several high-z quasars up to $z = 4.3$ (no quasars with $z > 2.9$ were found in the Einstein Medium Sensitivity Survey). A reprint of the paper is included in the Appendix where much greater detail on both the algorithms and the science emerging from their application can be found.

- Hard and Soft source catalogs were also produced as a byproduct of the two-sigma catalog creation process, although the latter required the invention of an automated technique for filtering our spurious sources detected in regions of extended emission. The results are presented in two Columbia PhD Dissertations (Moran 1994 and Yancopoulos 1996); the soft search has led to the identification of several candidates for

isolated neutron stars accreting from the ISM on which followup observations are continuing.

- An *Einstein* eXtended Source Survey (EXSS) has just been completed (Oppenheimer et al. 1997). A total of 321 previously unidentified discrete sources ranging in size from 2–10 arcminutes has been catalogued, and optical followup observations indicate that many are indeed unrecognized clusters of galaxies. A preprint describing this work may be found in the Appendix.

- A Burst Catalog was also published this year, describing a complete search of the IPC database for short-timescale (1–30 seconds) flashes in the X-ray sky (Gotthelf et al. 1996). While several dozen such events were detected and they defy all attempts to asssociate them with environmental or instrumental anomalies, we remain skeptical that they are truly astrophysical phenomena. Nonetheless, their relatively small number has allowed us to tighten substantially existing constraints on Galactic halo models for gamma ray bursts.

- Diffuse X-ray emission maps have also been derived from the IPC database and published in the literature. In addition, we recently demonstrated the utility of these data by analyzing the crosscorrelation between faint galaxy counts and the IPC arcminute background fluctuations, detecting the signal on this scale for the first time and discovering a non-zero correlation amplitude out to scales of $\sim 10'$ (Refregier et al. 1997; preprint attached).

Thus, we have acheived all of the goals laid out in our proposal for creating and publishing useful data products from the IPC archive using our flexible analysis system.

II. Bibliography

The work reported in the following papers was supported in whole or in part by the funding received under this NASA contract. Reprints or preprints are included in the Appendix.

"The *Einstein* Observatory Detection of Faint X-ray Flashes," 1996, E.V. Gotthelf, T.T. Hamilton, and D.J. Helfand, ApJ, 466, 779.

"The Absence of X-ray Flashes From Nearby Galaxies and the Gamma-Ray Burst Distance Scale," 1996, T.T. Hamilton, E.V. Gotthelf, and D.J. Helfand, ApJ, 466, 795.

"The *Einstein* Two-Sigma Catalog: Silver Needles in the X-ray Haystack," 1996, E.C. Moran, D.J. Helfand, R.H. Becker, and R.L. White, ApJ, 461, 127.

"Detailed Analysis of the Cross-Correlation Function between the X-ray Background and Foreground Galaxies," 1996, A. Refregier, D.J. Helfand, and R.G. McMahon, ApJ, 477 (Mar 1, 1997, in press).

"A Survey of the *Einstein* IPC Database for Extended X-ray Sources," 1996, B.R. Oppenheimer, D.J. Helfand, and E.J. Gaidos, ApJ (submitted).

"Silver Needles in the Two-Sigma Haystack: Galaxies, Clusters, and the XRB," 1993, in Observational Cosmology, ed. G. Chincarini, A. Iovino, T. Maccacaro, and D. Macagni, ASP Conf. Ser. 51, 470.

"Isolating the Foreground of the X-ray Background," 1996 A. Refregier, D.J. Helfand and R.G. McMahon in *Rontgenstralung from the Universe*, ed. H.U. Zimmermann, J.E. Trumper, and H. Yorke, p337.

"Neutron Stars in Binaries and in Isolation," 1996 S. Yancopoulos PhD. Dissertation, Columbia University, Chapter 4.

"Transient X-ray Phenomena in Astrophysics," E.V. Gotthelf, PhD. Dissertation, Columbia University, Chapter 3.

III. Personnel

During the four years that this contract was in effect, a number of undergraduate students, graduate students, and postdoctoral fellows contributed substantially to the work involved and, in turn, received a significant fraction of their research education under the contract's sponsorship. These are listed here with their status at the time and their current affiliations:

Undergraduates:

Ben. R. Oppenheimer (Columbia College student). Ben graduated in 1994, won an NSF graduate Fellowship, and is now beginning his third year in the Astronomy PhD. program at Cal Tech.

Graduate Students:

Lance Wobus (Physics graduate student): Currently in the Physics PhD. program at the University of Texas.

Edward Moran (Astronomy graduate student): Ed received his PhD. in 1994 and is currently a Postdoctoral Fellow at the Institute for Geophysics and Planetary Physics at Lawrence Livermore National Laboratory.

Eric V. Gotthelf (Physics graduate student): Eric received his PhD. in 1993 and is currently a staff member at the HEASARC at Goddard Space Flight Center.

Sophia Yancopoulos (Physics graduate student): Sophia received her PhD. in 1996 and is currently a visiting assistant professor at Vassar College.

Mallika Talla (Physics graduate student): Mallika is currently pursuing her graduate studies in India.

Post Doctoral Fellows at Columbia:

Thomas T. Hamilton: Tom had postdoctoral positions at Columbia, at SAO, and at Cal Tech. He is now a staff member at the Rand Corporation.

Austin Tomaney: Austin is about to leave his postdoc at Columbia for a similar positon at the University of Washington, Seattle.

Appendices

THE ASTROPHYSICAL JOURNAL, 466:779–794, 1996 August 1

THE *EINSTEIN OBSERVATORY* DETECTION OF FAINT X-RAY FLASHES

E. V. GOTTHELF[1]
Laboratory for High Energy Astrophysics, NASA/Goddard Space Flight Center, Greenbelt, MD 20771; gotthelf@gsfc.nasa.gov
T. T. HAMILTON
Department of Astronomy, California Institute of Technology, Pasadena, CA 91125; tth@astro.caltech.edu
AND
D. J. HELFAND
Department of Astronomy and Columbia Astrophysics Laboratory, Columbia University, 538 West 120th Street, New York, NY 10027; djh@carmen.phys.columbia.edu
Received 1995 March 17; accepted 1996 February 8

ABSTRACT

We report on the result of an extensive search for X-ray counterparts to gamma-ray bursts (GRBs) using data acquired with the imaging proportional counter (IPC) on board the *Einstein Observatory*. We examine background sky fields from all pointed observations for short timescale ($\lesssim 10$ s), transient X-ray phenomena not associated a priori with detectable point sources. A total of 1.5×10^7 s of exposure time was searched on arcminute spatial scales down to a limiting sensitivity of 10^{-11} ergs cm^{-2} s^{-1} in the 0.2–3.5 keV IPC band. Forty-two highly significant X-ray flashes (Poisson probability less than 10^{-7} of being produced by statistical fluctuations) are discovered, of which 18 have spectra consistent with an extragalactic origin and light curves similar to the *Ginga*-detected X-ray counterparts to GRBs. Great care is taken to identify and exclude instrumental and observational artifacts; we develop a set of tests to cull events that may be associated with spacecraft or near-Earth space backgrounds. The flashes are found to be distributed isotropically on the sky and have an approximately Euclidean number-size relation. They are not associated with any known sources, and, in particular, they do not correlate with the nearby galaxy distribution. Whether or not these flashes are astrophysical and/or associated with GRBs, the limits imposed by the search described herein produces important constraints on GRB models. In this paper, we discuss possible origins for these flashes; in a companion paper, we use the results of our search to constrain strongly all halo models for GRBs.

Subject headings: gamma rays: bursts — surveys — X-rays: bursts

1. INTRODUCTION

Observational evidence for X-ray counterparts to classical GRBs in the 0.1–100 keV range has been found by several experiments. X-ray bursts in the 6–150 keV band are located to 1° precision with the WATCH all-sky monitor on board the *Granat Observatory* at a rate of ~ 4 yr^{-1} $(4\pi$ sr$)^{-1}$ (Lund, Brandt, & Castro-Tirado 1991). *Ginga* has detected X-ray bursts associated with GRBs in the 1–10 keV band with similar spatial resolution (Yoshida et al. 1989) and has provided evidence for X-ray precursors to GRBs (Murakami et al. 1991). The XMON instrument on the *P78-1* mission also detected coincident X-ray emission in this band (Laros et al. 1984). As with most GRB observations, these experiments, with their broad sky coverage and high background, offer limited spatial resolution and detection sensitivity, leaving open the origin, and thus the nature, of classical GRBs (see Higdon & Lingenfelter 1990 for a pre–*Gamma Ray Observatory* review). The existence of such X-ray counterparts raises the possibility that they could be used to gain more detailed positional information about the associated bursts, constrain models for the burst number as a function of sensitivity, and, of course, constrain directly models of the underlying physical phenomenon. To this end, the imaging X-ray experiment on board the *Einstein Observatory* is ideally suited to search for GRBs with unprecedented sensitivity and spatial resolution.

The *Einstein* IPC operated for 3 yr, producing images of the X-ray sky with arcminute resolution over a 1 deg^2 field of view (FOV). Considering the operating efficiency of the *Einstein Observatory*, this is equivalent to observing the whole sky for 7 minutes. It is therefore not surprising that *Einstein* was not coincidentally pointed at any cataloged GRB that occurred during its mission. However, by searching all images for serendipitous flashes that occurred in portions of the FOV not occupied by any detectable point source, we can locate all transient events with a fluence greater than 10^{-11} ergs cm^{-2}, 3 orders of magnitude lower than the X-ray counterparts of GRBs at the BATSE detection threshold. About 3% of the *Einstein* database was searched previously, and one potentially astronomical event was found (Helfand & Vrtilek 1983); we also find this event in the current search, although we exclude it from our formal sample because it does not meet the stringent background requirements described below. Apart from this pioneering effort, previous standard analysis of these fields used software that was not designed to detect such flashes.

We present the results of our search below. We have found 42 highly significant X-ray flashes. The sky positions of these candidates are not correlated with sources cataloged in the SIMBAD or NED databases, nor are the events found to be coincident in time with known GRBs or solar flares detected by the gamma-ray spectrometer (GRS) aboard the *Solar Maximum Mission* (*SMM*). Most importantly, they are not preferentially found in the direction of nearby galaxies, allowing us to challenge the viability of all

[1] Universities Space Research Association.

cells with 5 or more counts. To exclude all discrete sources, including the bright target object typically found in the center of the FOV, we searched only those spatial cells with a count rate less than 6×10^{-4} counts s^{-1} arcmin^{-2}. Thus, those cells flagged as meeting our criteria contained a minimum flux enhancement of a factor of ~ 50 over the mean rate for that point in space. As a practical matter, all 2179 files with less than 400 s of good time were excluded, since 5 counts in one spatial cell in these short files would exceed our count rate threshold (1084 of these excluded files contained zero events satisfying our data editing criteria). To avoid missing flashes that straddle two cells, we actually binned the data at twice the needed resolution and constructed each search cell from the sum of the eight adjacent (three-dimensional) subcells (i.e., we searched all possible overlapping cells).

A total of 69 events flagged in this way were then inspected for their spatial extent and compared with a simultaneous background count rate defined by a concentric annulus 7′–15′ in radius and ± 20 s in time of the detection cell (50 s duration).

We rejected all events that represented deviations of less than 3 σ above this local background [i.e., in which $3 > |N_{obs} - N_{exp}|/(N_{exp})^{1/2}$, where N_{obs} is the number of counts recorded in the spatial pixel of interest and N_{exp} is the predicted number from the background annulus]. Subsequent scrutiny revealed that the events excluded by this test were associated with satellite sunrise, sunset, or the approach of the South Atlantic Anomaly. Furthermore, in order to exclude events possibly associated with glitches at the beginning or end of an observation interval, we eliminate those occurring within 20 s of gaps in the data. These cuts left a total of 42 accepted events. Formally, we would expect less than one event of such intensity as a result of Poisson noise.

2.4. *Detection of X-Ray Flashes*

The 42 X-ray flash candidates were analyzed for their spectral and temporal structure. The data constituting an "event" were further characterized in the following manner. The sky position is given by the mean position of all counts falling within 3′ in space and ± 20 s in time of the three-dimensional detection cell. The event time is taken as the (first) 1 s bin containing the maximum number of counts as determined using a 0.1 s sliding box during the 50 s time window. Each event was then classified based on its time structure as slow or rapid, and based on its spectrum as soft or hard. The rapid events are defined as having more than 4 counts occurring within the 1 s maximum bin defined above. Events for which $N(<1.3 \text{ keV}) < N(\geq 1.3 \text{ keV})$ are defined as hard. The sky position, event times, and characteristics of the events passing the initial inspection are presented in Table 1. Of the 42 events, 36 are slow, 6 are rapid, 18 are hard, and 24 are soft. It is found that all but one of the hard events are slow and that, similarly, all but one of the rapid events are soft. The converse in both cases is not true, however: soft events are both slow (79%) and rapid (21%), and slow events are composed of nearly equal parts hard and soft events.

Light curves are shown in Figure 1 for four representative flashes. The fact that the rise times are shorter than the decay times is not an artifact of our search criteria. In Figure 2, a composite light curve for each temporal class is shown. Each flash has been centered on the 1 s bin with the most counts as described above. Most of the accepted events have a "slow" time structure, with 90% of the counts clustered within a window 15 s in duration compared with 90% window boundaries of 1 s for the rapid events. An aggregate point-spread function (PSF) using all accepted events was produced by centering and stacking events on the computed mean sky positions. The result is plotted in Figure 3 along with the summed spectrum. The resulting PSF resembles a point source, and the summed spectrum, although quite soft, appears astrophysical (see below). The events were then grouped by spectral hardness and analyzed in a similar manner.

Figure 4 displays the PSF and spectra for the soft and hard events separately. The soft events contain on average 11 counts per event and produce a PSF with a normalized radial distribution consistent with a Gaussian of FWHM $\simeq 3'$. This is the signature expected for a point source with the observed soft spectrum imaged by the mirror plus the IPC. The hard events average 7 counts and also produce a radial distribution consistent with an astronomical origin.

In Figure 5, the soft events are compared directly with data from the cataclysmic variable U Gem in outburst, put through the same analysis; it is clear that both the PSF and the spectrum are consistent with those of a real astrophysical source. Figure 6 displays the properties of slow and rapid events separately. The characteristics for the slow events are similar to those of the sample as a whole. The six rapid events contain ~ 16 counts per event for a total of 100 counts and produce a very soft spectrum with 75% of the counts below ~ 0.4 keV. Inspection of the counts contained within those 1 s bins that contained more than 4 counts reveal an even softer spectrum. Recent studies of supersoft objects show that such spectra, although rare, are found in nature (Brown et al. 1994; Greiner, Hasinger, & Kahabka 1991).

A sky exposure map was produced for the complete IPC database by summing up the filtered time intervals for each sky pointing. The map is plotted in Galactic coordinates in Figure 7 with the candidate flash locations overlaid. The accepted events are roughly isotropic on the celestial sphere. In particular, as we show in the accompanying paper (Hamilton et al. 1996), they are not found preferentially in the direction of nearby galaxies.

A log N–log S curve for all accepted events was constructed using a mean conversion factor of 2.6×10^{-11} ergs cm^{-2} counts^{-1}. We compensated for the off-axis mirror reflection efficiency using the standard IPC vignetting correction (Harris & Irwin 1984, chap. 5, p. 18). The result is plotted in Figure 8 along with various GRB measurements (Hingdon & Lingenfelter 1990). Although it is quite possible that both the γ-ray and the X-ray event curves suffer from instrumental bias (see Higdon & Lingenfelter 1984 and Mazets & Golenetskii 1987 for a review of this issue as related to the *Konus* data, and Meegan 1994 for a discussion of the BATSE results), a simple straight line between the two curves gives a differential slope of ~ -1.7, similar to the slope detected by BATSE for the number-size relationship of the faintest bursts it detects and considerably flatter than the ~ -2.5 slope for a homogeneous Euclidean distribution.

As discussed above, the flashes exhibit a variety of temporal and spectral characteristics. These effects are not uncorrelated, the softest flashes often having the fastest rise times.

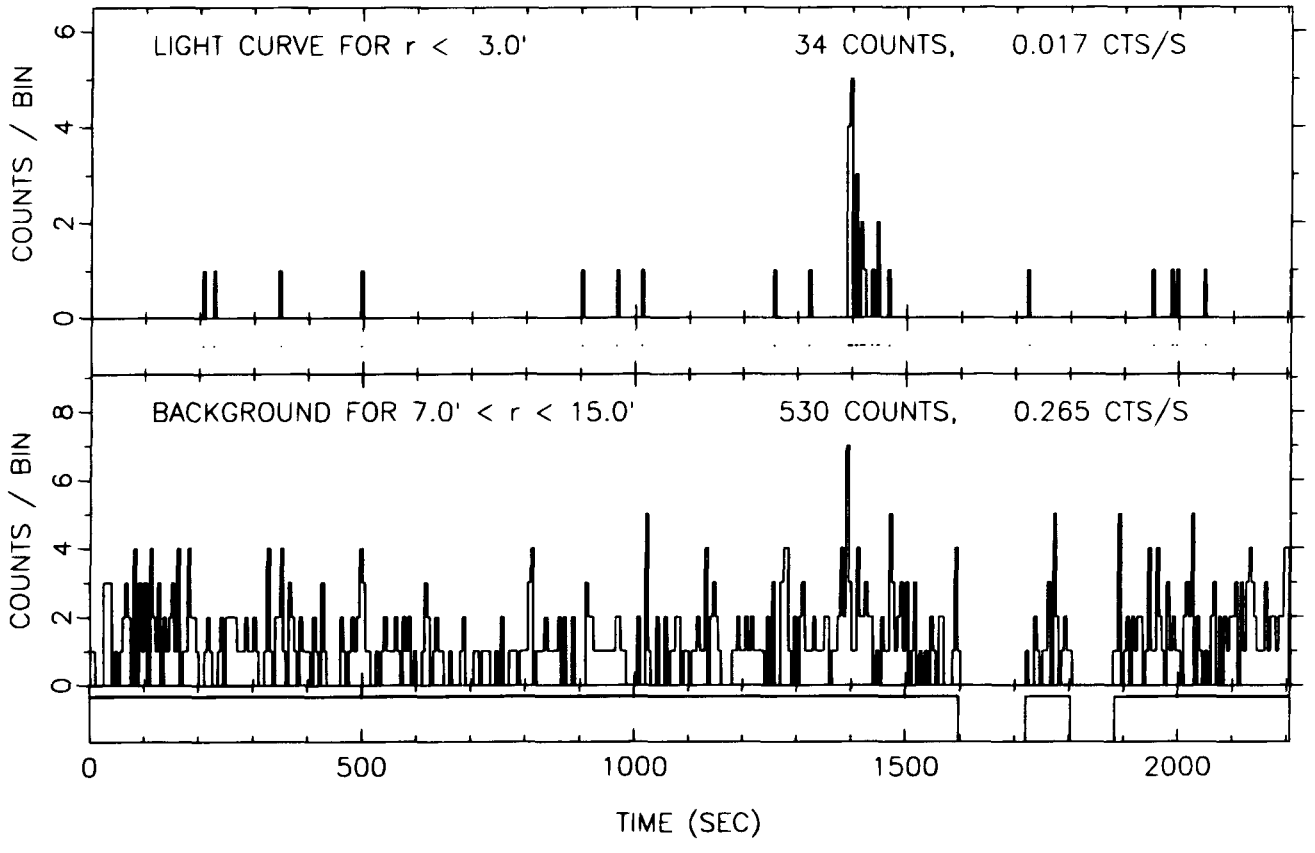

FIG. 1*a*

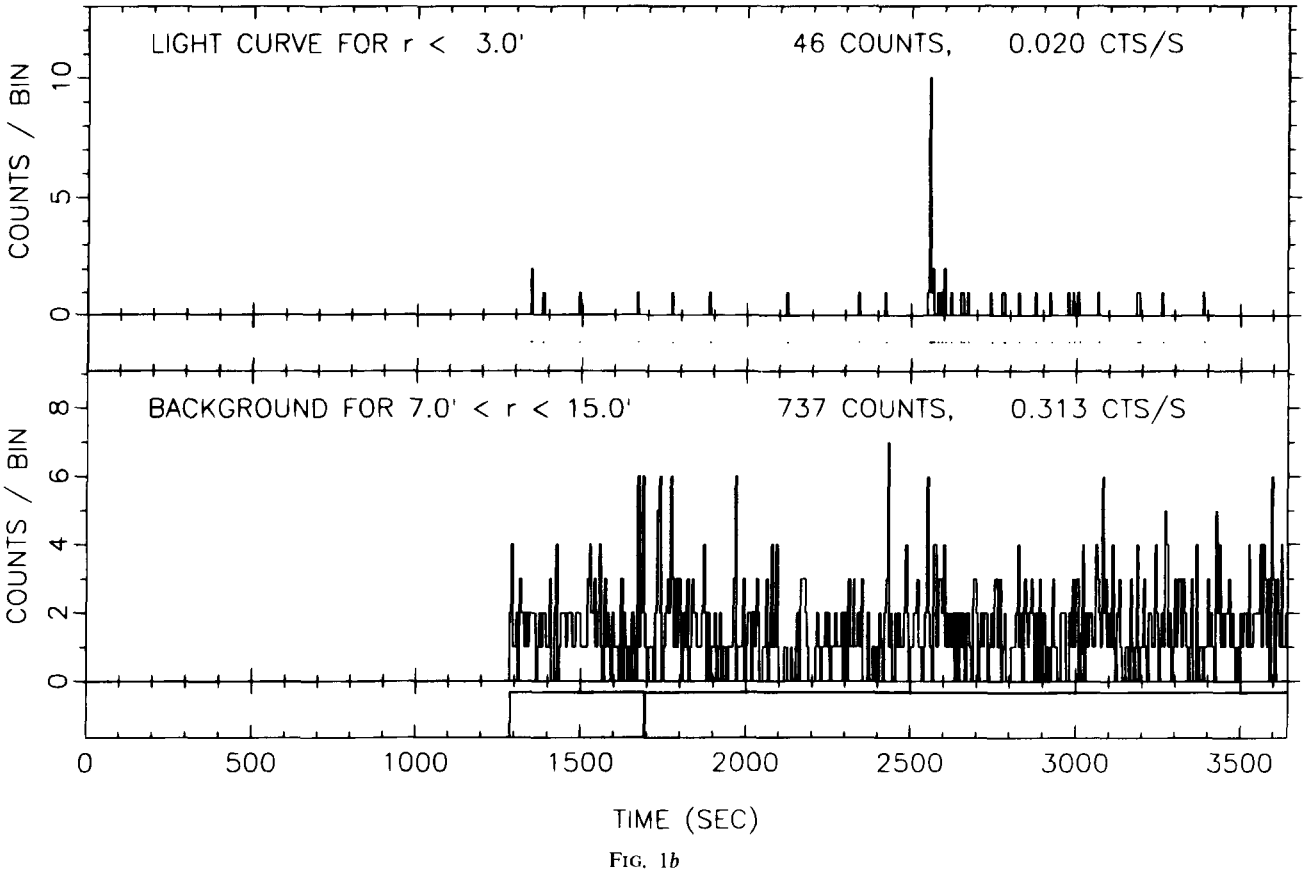

FIG. 1*b*

FIG. 1.—Light curves for four typical flash events. The flashes in (*a*) and (*b*) are categorized as slow, and those in (*c*) and (*d*) as rapid. The central strip in each plot shows the arrival times of the photons as dots. The bottom strip shows the times of housekeeping status changes as vertical lines. This indicates that the flashes are not associated with detectable changes in the state of spacecraft or instrument.

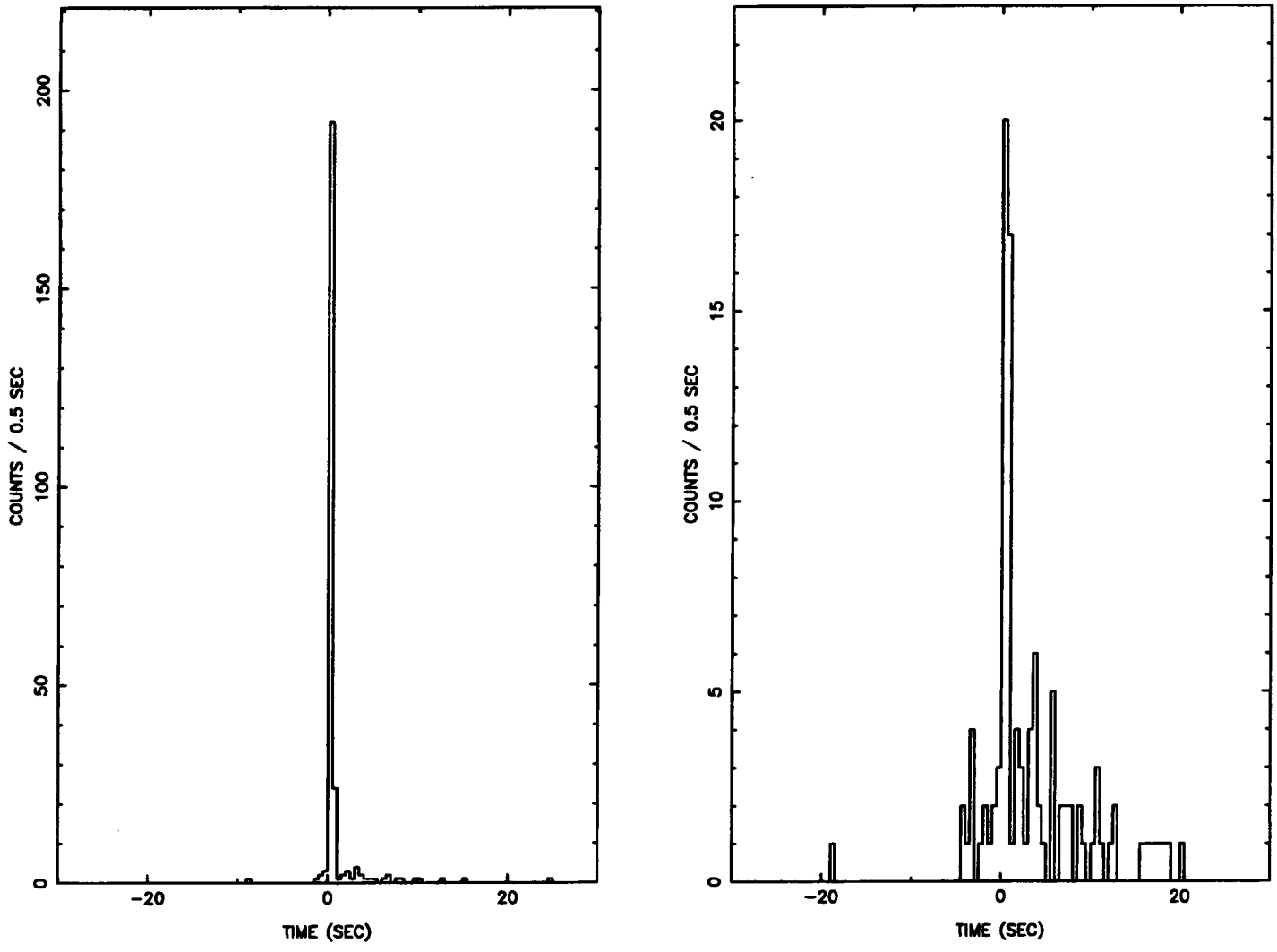

FIG. 2.—Composite light curves for the X-ray flashes are shown for both slow (*right*) and rapid (*left*) events. Both curves show a rise time significantly shorter than the decay time. Since our search method is symmetric with respect to time, this asymmetry is a real effect.

physics Science Archive Research Center (HEASARC) at Goddard Space Flight Center report the total MPC counts in 2.6 s bins. A typical bin in a field with no bright sources, such as those examined in our IPC investigation, contains about 40 counts. We compared the counts in the time bin in which we detect flashes to an expected background equal to the mean of the four preceding and four following bins. Of the 18 hard events, which one might reasonably expect to have MPC counterparts, three had no MPC data, one came at the first bin of an MPC observation, and one corresponded to a mean MPC rate of over 100 counts s^{-1}. Excluding those five events leaves 13 hard events with good MPC data. The mean MPC rate was 45, the extremes 64 and 37. None of the MPC intervals corresponded to a count rate excursion of more than 14, or about 2 σ. In four of the intervals, the count rate at the time of the flash was less than or equal to the expected background. In 10 of the intervals, the count rate was higher. The total count in the thirteen 2.6 s bins corresponding to the flash peaks was 647. This is 2.5 σ above the expected background of 587. This is encouraging but hardly a definitive confirmation of an astronomical origin for the flashes.

The mean fluence per MPC flash is therefore 4.6 photons, although this number is probably an underestimate of the true fluence as a result of the restrictive time bin used here. If the MPC events had the same time signature as the IPC flashes, our procedure would detect about half of the total fluence. The hard IPC flashes themselves have a mean fluence of 7 photons. The ratio between MPC and IPC is consistent with a 1.7 keV thermal plasma or a power law with a photon index of 2. This is reasonably near the observed *Ginga* GRB X-ray spectrum.

3.1. *Discussion*

Our search for X-ray transients found a total of 42 in the *Einstein* database. This result is a robust upper limit on transient X-ray phenomena at the detected flux levels. However, the origin of the signals that we do detect remains a mystery. While we have been unable to provide a definitive explanation, several possibilities are evident. The least interesting is that the flashes are a result of some hitherto unknown phenomenon that takes place entirely within the detector. As discussed above, it may be that many (or even all) of the flashes are the result of a phenomenon analogous to the afterpulses detected in *ROSAT* (Snowden et al. 1994). Of course, it is unlikely that such a phenomenon would manifest itself with a point response function and spectrum that perversely imitate incident cosmic X-rays, but this

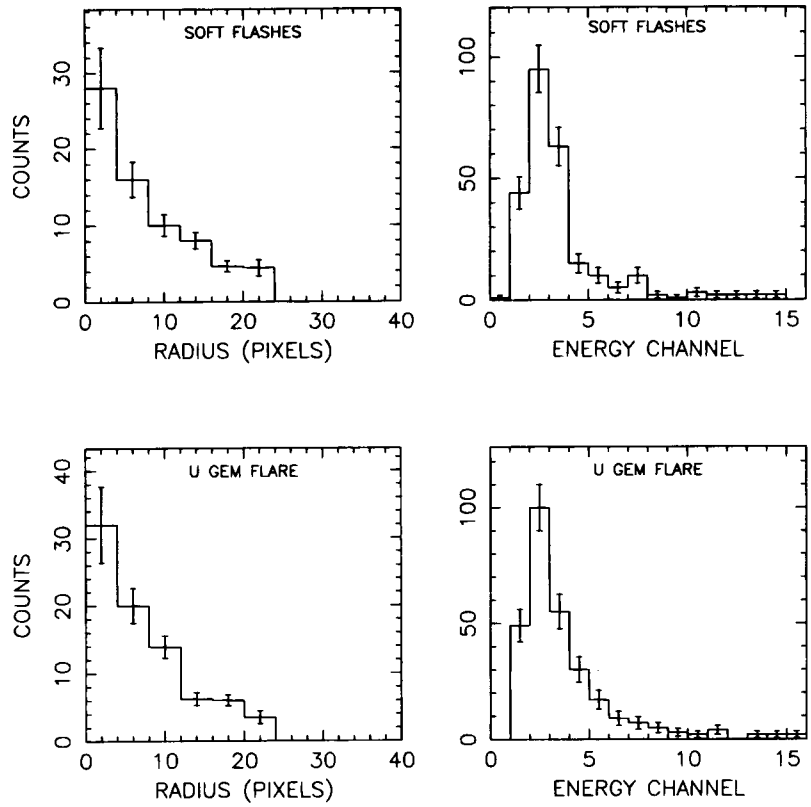

FIG. 5.—Comparison of the composite radial distribution and spectrum of the soft flashes and that of U Gem in outburst analyzed in the same manner. The U Gem outburst was one of the softest celestial sources detected by the IPC. This plot contains 200 s of data from the HUT 1474851 + 4100. The similarity of the spectra demonstrates that, although the soft flashes do have an extremely soft spectrum, it is a spectrum consistent with a celestial origin of the photons.

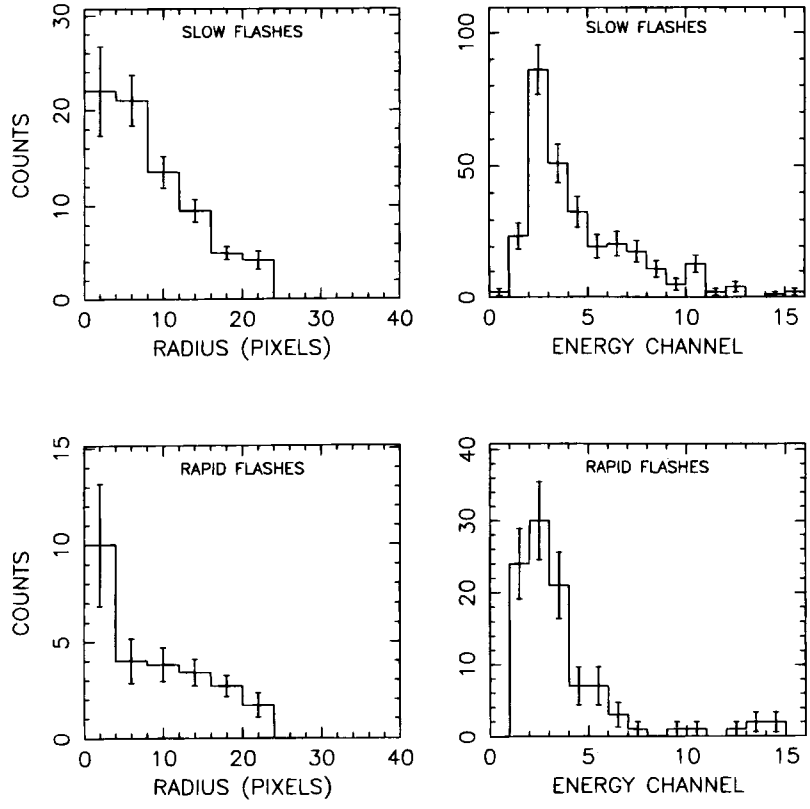

FIG. 6.—Composite radial distributions and spectra sorted by temporal class. In the bottom two panels, only events occurring in the brightest 1 s of the rapid flashes are included.

by the flash log N–log S relation is consistent with either an extragalactic or a local origin for the flashes. While the time structure, space distribution, and apparent luminosity function of the X-ray flashes is reminiscent of GRBs, the fluence of the observed flashes is several orders of magnitude fainter. If the flashes originate at a distance of 1 pc, the required energy is $\sim 10^{28}$ ergs, equivalent to the energy released by the accretion of $\sim 10^{9}$ g of material onto a compact object. If the flashes originate at 1 Gpc, then a typical energy would be $\sim 10^{46}$ ergs.

Although our experiment is sensitive to flashes on a timescale of up to ~ 10 s, the flashes we detect characteristically have a substantially shorter timescale; indeed, the flashes have a timescale shorter than the X-ray counterparts of GRBs detected by *Ginga*, especially if one postulates an origin at cosmological distances that would require substantial time dilation in the faintest (most distant) bursts. They are not obviously shorter than the X-ray timescale of the soft gamma repeaters (SGRs) detected by the *Advanced Satellite for Cosmology and Astrophysics* (*ASCA*), although the X-ray light curve of the *ASCA* SGR is not well constrained because the *ASCA* gas scintillators saturated their telemetry buffer after only five events (Murakami et al. 1994). We note, however, that the flashes we detect cannot be counterparts to cosmological GRBs if the latter are standard candles, since, for a faint BATSE burst redshift of ~ 1–2, there is insufficient volume of universe at greater distances to produce events 30 times fainter with the frequency we observe.

The flashes are also far more numerous than known GRBs: we observe a rate of 2×10^{6} yr^{-1} over the whole sky. This is approximately the frequency with which supernovae occur within 1 Gpc, which prompts the speculation that the X-ray flashes are produced by the breakout of supernova shocks as they reach the optically thin regions of exploding stars. This would require the release of $\sim 10^{-7}$ of the supernova's energy in a prompt ultraviolet/soft X-ray flash. It is clear, however, that not all of the observed flashes originate beyond the Galaxy, since one soft event occurs at a Galactic latitude of 2°.

The isotropic nature of the flashes' distribution is of course consistent with an origin relatively nearby in the Galaxy. It is tempting to propose as progenitors local flare stars and/or RS CVn systems. The soft spectra of the detected flashes indeed suggest a coronally active star population. Given the flare frequency and duration of a typical flare star, there is a reasonable chance to catch a flare event during a typical IPC observation. But, again, the number of flashes is inconsistent with local field star densities. Perhaps the flashes are associated with a Galactic population of old, isolated neutron stars that is otherwise invisible.

Of course, there is no reason to believe that the 42 events we have detected, or even the 18 with harder spectra and slow timescales, have a common origin. They may represent a maddening combination of interesting astronomical events and indistinguishable counter artifacts. In any case, the observed flash rate is a definite upper limit on the occurrence of faint astronomical X-ray transients. The significance of this limit as related to GRBs is explored in Hamilton et al. (1996).

D. J. H. acknowledges support from NASA grant NAS 5-32063. T. T. H. acknowledges support from NASA grant NAGW-4110. Part of this research has made use of data obtained through the HEASARC on-line service, provided by the NASA/Goddard Space Flight Center. This paper is contribution No. 544 of the Columbia Astrophysics Laboratory.

APPENDIX A

TESTS FOR A NONASTROPHYSICAL ORIGIN OF THE IPC FLASHES

In order to determine if the detected flashes truly have an astrophysical origin, we devised a series of tests based on coverage and sensitivity arguments.

One possible nonastrophysical origin for the observed flashes is arcing associated with a particular spot on a counter wire. If this were the cause of our events, the point response function should differ significantly from that observed for real celestial sources. Our search box is much larger than the IPC point response function (18 vs. $\lesssim 7$ arcmin^2), so a statistical noise fluctuation would also look very different. In addition, the spectrum from instrumental artifacts would not show the familiar effects of counter window absorption (mainly carbon at 0.28 keV). As mentioned in § 3, the PSF resembles a point source, and the spectrum appears astrophysical.

The gain and other counter properties varied substantially during the life of the satellite, so we knew that, if occurrence of transients was concentrated in one part of the mission, the cause was probably instrumental. Thus, we plotted the time of occurrence for events during the mission. The result is shown in Figure 9 along with the daily fraction of filtered IPC time coverage (total time intervals passing the standard processing criteria per day). A Kolmogorov-Smirnov (K-S) test yields a probability of 78% that the distribution is random with respect to spacecraft lifetime (Fig. 10). We also calculated the distribution of events with respect to local solar time. The total filtered IPC observing time was binned into hourly intervals and compared with the event distribution. An excess of occurrences on the leading side of the Earth's orbital motion would suggest X-rays from meteoritic material interacting with the Earth's atmosphere. No such effect is seen (Fig. 11).

Nuclear reactors aboard Soviet spy satellites are a potential source of nonastrophysical γ-ray and X-ray transients. Recently, declassified results from the *SMM* GRS experiment have detailed the cause and properties of these events (Rieger et al. 1989; Share et al. 1989; Hones & Higbie 1989; O'Neill et al. 1989). *SMM* and *Einstein* flew concurrently and in similar orbits for about a year from 1980 February 14 onward. During the overlap of the two missions, an average of three anomalous events per month were detected by *SMM*. We compared the monthly event rates given by Rieger et al. (1989; see Fig. 12) with that of our flashes (normalizing by coverage) and do not see a significant correlation. However, this is not a strong test because the data set is too sparse, and the rate is dependent on altitude and orbit. We looked for a periodic recurrence rate relative to the *Einstein* orbit by plotting the time of day of the flash occurrence against day number (see Rieger et al. 1989). Again no obvious trend is evident.

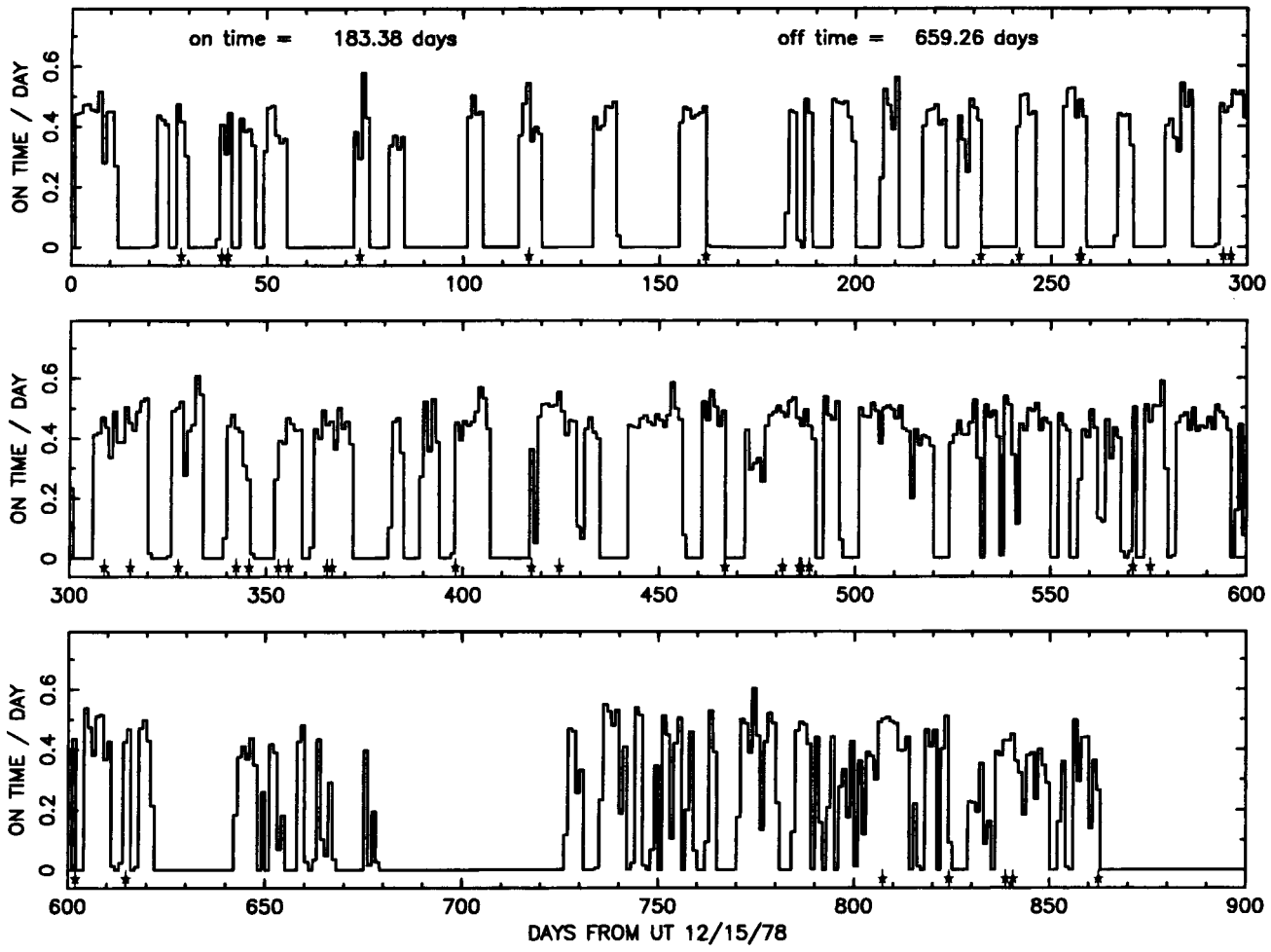

FIG. 9.—Daily IPC time coverage, including only the time intervals passing the standard processing criteria (see Table 2). The times of occurrence of the 42 flashes are indicated along the abscissa.

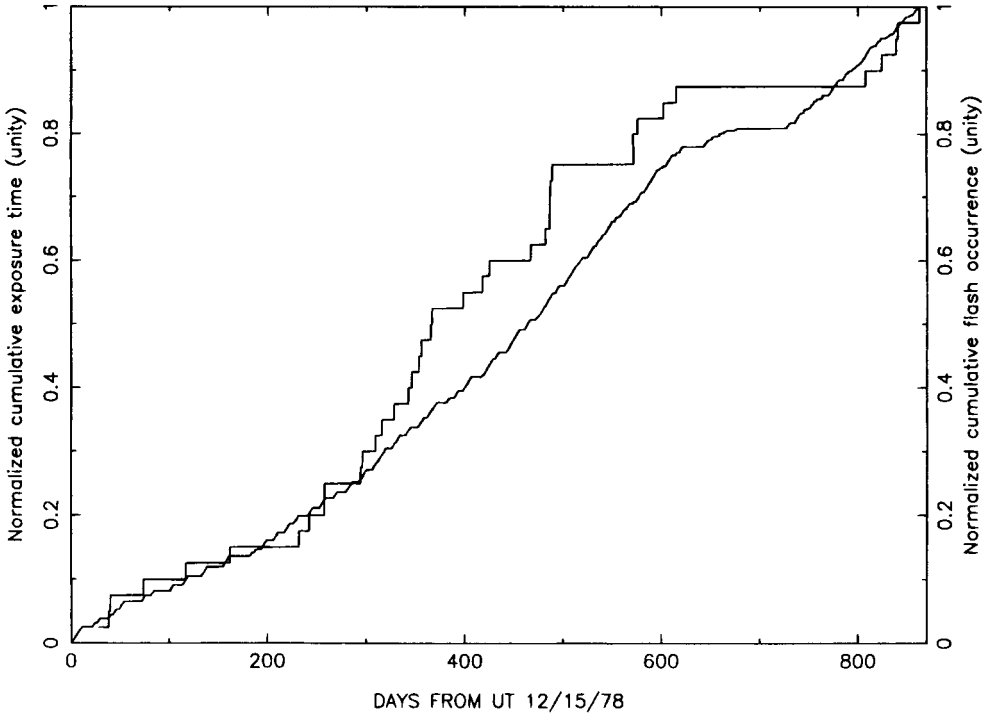

FIG. 10.—Graphical representation of the K-S test for flash occurrence time. We see no evidence that the flashes do not occur randomly with respect to the time in the mission.

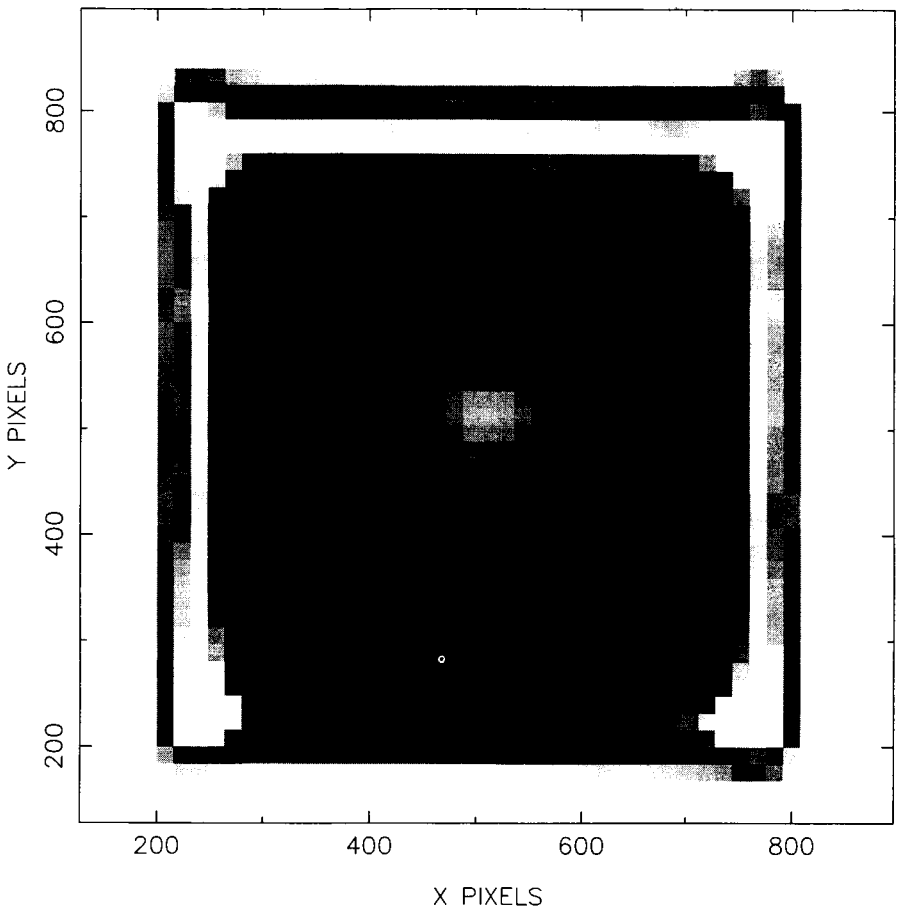

FIG. 13

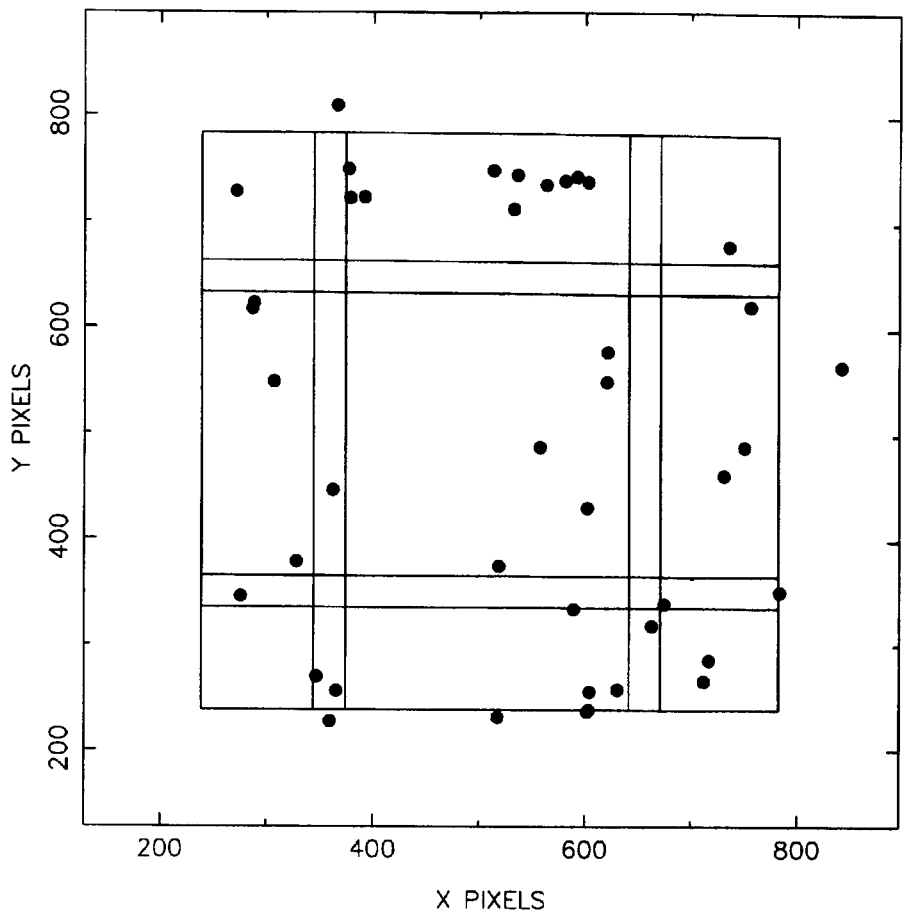

FIG. 14

FIG. 13.—Gray-scale representation of the total amount of time the IPC was sensitive to flashes meeting our search criteria as a function of flash position in detector coordinates. Note that there is a minimum in the exposure time at the center of the detector, where we are unable to search for faint flashes because of the typical placement of strong X-ray sources there. The highest regions of sensitivity correspond to the area just outside the detector window support ribs.

FIG. 14.—Location of flash events over the face of the IPC detector. This plot corresponds to the exposure map in Fig. 5. The lines delineate the location of the detector window support ribs. The outer box encloses the region of the IPC for which a reliable aspect solution was computed. The flashes are disproportionately concentrated toward the edge of the detector and away from the ribs, qualitatively consistent with the exposure map.

THE ASTROPHYSICAL JOURNAL, 466:795–801, 1996 August 1

THE ABSENCE OF X-RAY FLASHES FROM NEARBY GALAXIES AND THE GAMMA-RAY BURST DISTANCE SCALE

T. T. HAMILTON
Department of Astronomy, California Institute of Technology, Pasadena, CA 91125
E. V. GOTTHELF[1]
Laboratory for High Energy Astrophysics, NASA/Goddard Space Flight Center, Greenbelt, MD 20771
AND
D. J. HELFAND
Department of Astronomy and Columbia Astrophysics Laboratory, Columbia University, 538 West 120th Street, New York, NY 10027
Received 1995 March 17; accepted 1996 February 8

ABSTRACT

If typical gamma-ray bursts (GRBs) have X-ray counterparts similar to those detected by *Ginga*, then sensitive-focusing X-ray telescopes will be able to detect GRBs 3 orders of magnitude fainter than the detection limit of the Burst and Transient Source Experiment (BATSE). If a substantial portion of the burst population detected by BATSE originates in a Galactic halo at distances greater than or equal to 150 kpc, existing X-ray telescopes will be able to detect GRBs in external galaxies out to a distance of at least 4.5 Mpc. As reported in Gotthelf, Hamilton, & Helfand, the imaging proportional counter (IPC) on board the *Einstein Observatory* detected 42 transient events with pointlike spatial characteristics and timescales of less than 10 s. These events are distributed isotropically on the sky; in particular, they are not concentrated in the directions of nearby external galaxies. For halo models of the BATSE bursts with radii of 150 kpc or greater, we would expect to see several burst events in observations pointed toward nearby galaxies. We see none. We therefore conclude that if the *Ginga* detections are representative of the population of GRBs sampled by BATSE, GRBs cannot originate in a Galactic halo population with limiting radii between 150 and 400 kpc. Inasmuch as halos with limiting radii outside of this range have been excluded by the BATSE isotropy measurements, our result indicates that all halo models are excluded. This result is independent of whether the flashes we do detect have an astronomical origin.

Subject headings: gamma rays: bursts — surveys — X-rays: bursts

1. INTRODUCTION

Although their existence has been recognized for over two decades, gamma-ray bursts (GRBs) remain enigmatic, their distances and inherent luminosities uncertain by many orders of magnitude. In recent years, our understanding has increased enormously as a consequence of the isotropy and apparent luminosity function measurements carried out by the BATSE instrument on board the *Compton Gamma Ray Observatory* (*CGRO*) (Meegan et al. 1992; Hakkila et al. 1994a, 1994b; see Fishman et al. 1989 for a discussion of the BATSE experiment). The preponderance of evidence suggests that GRBs originate at one of two possible classes of sites, either in an extended Galactic halo or at cosmological redshifts. Many workers have developed models in which the GRBs arise from a halo population at distances of tens to hundreds of kiloparsecs from the Galactic center (e.g., Smith & Lamb 1993; Podsiadlowski, Rees, & Ruderman 1995). In this scenario, the observed inhomogeneity in the number-size relation is understood as the result of the finite extent of the halo. The BATSE results have effectively excluded models with limiting halo radii of less than 150 kpc (Hakkila et al. 1994a). Other workers have proposed that GRBs originate at cosmological distances. The inhomogeneity is then understood as a result of a combination of evolutionary effects and redshift-induced spectral effects (Paczyński 1986; Paczyński & Rhoads 1993 and references therein).

In this paper, we propose and execute a new test of Galactic halo models. We begin with a review of the observed X-ray properties of GRBs and outline our strategy for using existing X-ray–imaging data to constrain models of the GRB source distribution (§ 2). We then define the halo models and construct a catalog of nearby galaxies whose halos were observed by the *Einstein* IPC. Section 4 presents our principal result—the complete absence of bursts from nearby galaxies—and uses this to constrain burst distances. The final section examines the robustness of our conclusions and summarizes our results.

2. X-RAYS FROM GRBs

If our Galaxy is typical, Galactic halo models predict that external galaxies will have sources of GRBs similar to those surrounding the Milky Way, presumably with similar spectral and temporal characteristics. GRBs in these external halos would, of course, be much fainter than those from the halo of our Galaxy. Because absorption effects will be insignificant over the distances to nearby galaxies, however, measurement of the flux of GRBs from the halo of an external galaxy at a known distance would provide an immediate measure of the intrinsic burst luminosity and, hence, the distance of Galactic GRBs. Similarly, an upper limit on the flux of GRBs in nearby galaxies provides, in the context of halo models, a lower limit on the distance of the BATSE-detected bursts.

If we assume that the faintest BATSE bursts originate at a distance of 150 kpc, the smallest limiting distance consistent with the BATSE isotropy tests, it is clear that bursts

[1] Universities Space Research Association.

lower. As a practical matter, given the existence of a limited set of observations in the *Einstein* database, these two effects work against each other. If bursts originate in relatively extended halos, then the number of bursts per unit surface area per unit time will be less for individual galaxies. However, a relatively extended halo implies a relatively high intrinsic burst luminosity. Therefore, they can be seen at greater distances, and more existing *Einstein* fields would be expected to contain bursts.

We have calculated the expected number of bursts for all halo models consistent with the BATSE isotropy result. The adopted lower limit for the limiting burst distance of 150 kpc follows from the upper limit on the GRB quadrupole moment with respect to the plane of the Milky Way, and the upper limit of 400 kpc follows from the upper limit to the dipole with respect to M31 (Hakkila et al. 1994b). We calculate the expected surface density of bursts ρ_s at a distance r from the center of the Galaxy for burst source models in which

$$\rho_s \propto \frac{1}{1 + (r/r_c)^\alpha}, \quad r < r_{\rm lim},$$

$$\rho_s = 0, \quad r > r_{\rm lim},$$

where $\alpha \approx 2$, and the population abruptly cuts off at a radius $r_{\rm lim}$. This formalism is commonly used in the analysis of BATSE data, primarily because it is similar to models of dark matter distributions that are invoked to explain galaxy velocity profiles (Fich & Tremaine 1991; Innanen, Harris, & Webbink 1983). Models in which $\alpha < 2$ can also fit the BATSE data and may be physically more reasonable; as shown in Hakkila et al. (1994a), such models require a larger limiting radius. We adopt the model with the conservative assumption that $\alpha = 2$, not because of any belief in its physical significance, but because the use of such a model facilitates interpretation of our results in the context of other GRB studies, especially those interpreting BATSE data.

The surface density in such models is not significantly dependent on the value of r_c, the softening parameter in the burst site distribution. For all values of r_c substantially less than $r_{\rm lim}$, the expected projected surface density of sources at the center of the halo is $\rho_s = 6.9(D/D_{\rm lim})^2$ per 10^6 s deg^{-2}, where $D_{\rm lim}$ is the maximum distance to which a BATSE burst at $r_{\rm lim}$ could be detected. For a halo limit of 150 kpc implying $D_{\rm lim} = 4.5$ Mpc, we expect one burst every 145,000 s in the *Einstein* field of view. A 150 kpc halo at 4.5 Mpc subtends roughly 10 deg^2, as indeed does any halo of size $r_{\rm lim}$ viewed at the distance corresponding to the limiting sensitivity.

3.2. *Galaxy Catalog*

A complete list of nearby galaxies with distances from 1 to 12 Mpc and with $M_V < -16$ was drawn from the Nearby Galaxies Catalog (Tully 1988). We have excluded all galaxies that are within 30′ of a brighter galaxy at the same distance, in order to ensure that satellite galaxies deep within the halo of a larger galaxy are not counted as independent objects. We have not applied any weighting by mass to the galaxies. In our calculations, we have formally assumed that the typical galaxy we observe has a halo identical to that of the Milky Way. The observation times are skewed somewhat toward more luminous galaxies, which were more likely to be chosen as IPC targets for reasons unrelated to our search. This means that assuming all catalog galaxies to be equal contributors to the burst population is a conservative assumption with regard to the distribution of bursts. If we weighted the galaxies, any plausible scheme would place more weight on the systems that were in fact most observed.

This does not, however, resolve the question of the overall normalization of the total galaxy luminosity in our sample. Gott & Turner (1976) estimate that the local density of galaxy optical luminosity is about 2.75 times the optical luminosity density on large scales. Adopting their numbers, we calculate that our assumptions are equivalent to assuming that the burst/galaxy luminosity ratio for our sample is approximately 1.6 times the value for the Galaxy. Specifically, we assume that the total burst-producing material along the line of sight to our sample galaxies has a ratio to those galaxies' luminosity 1.6 times as great as the ratio of burst-producing material within the model radius of the Milky Way to our Galaxy's luminosity. This is roughly comparable to assuming that burst production traces mass and applying standard comparisons of mass-to-light ratios for galaxies. If a substantial fraction of the intergalactic mass inferred from kinematic studies emits bursts, then the expected bursts will be correspondingly more numerous. Trimble (1987) provides a thorough review of the uncertainties of computing galactic and intergalactic masses in regions with no visible emission. The fact that the mass of material far from the luminous regions of the disk is so uncertain leads us to our simple approach.

We next constructed a database containing all IPC pointings whose centers lay within 5° of any of the 189 galaxies in our catalog, thus including both observations that were deliberately pointed at a nearby galaxy and serendipitous observations in which a galaxy or part of its putative halo is within the field of view. A total of 2.8×10^6 s was accumulated, with most of the time spent in scheduled observations of well-known nearby galaxies; one flash was detected. Since *Einstein* detected 18 potentially astronomical flashes in 1.6×10^7 s, this is not statistically unexpected. This result is not dependent on the arguments used in Paper I to extract the 18 potentially astronomical events from the complete list of 42 candidates; none of the 24 likely counter events fell within the nearby galaxy database. Table 1 lists the galaxy positions, distances, and the total time that *Einstein* spent observing a putative 400 kpc halo about each galaxy's position. The observing times for nearby galaxies are large. However, as explained above, the expected surface density of bursts is low for nearby galaxies, and, as a result, most of the contribution to the expected burst total comes from galaxies near the limiting distance for a particular halo model.

Since larger halo models imply higher luminosities for the BATSE burst sample, we must examine observations of galaxies at larger distances as the assumed $r_{\rm lim}$ increases. A 200 kpc radius halo would produce bursts visible out to 6 Mpc, while a 400 kpc halo is visible to 12 Mpc and so on. Similarly, the surface density of bursts from the halos of galaxies at distances less than that of the limiting sensitivity is reduced by a factor proportional to the square of the ratio of the distance to the limiting distance.

3.3. *Results*

Table 2 lists the predicted number of *Einstein*-detected bursts for six model halos with different limiting radii. No

TABLE 1—*Continued*

R.A. (B1950)	Decl. (B1950)	Distance (Mpc)	Time (s)
Galaxies at 4–12 Mpc			
$13^h01^m36^s$	−05°17′	6.4	40986
13 02 30	−49 12	5.2	24633
13 10 00	44 18	6.0	6201
13 13 30	42 17	7.2	6201
13 16 18	−20 47	6.7	12865
13 22 24	−42 45	4.9	72177
13 27 42	58 40	4.8	39344
13 27 48	47 27	7.7	0
13 34 12	−29 37	4.7	53825
14 01 30	54 36	5.4	62760
14 03 18	53 54	6.0	61442
14 09 18	−65 06	4.2	62192
14 18 12	56 57	7.0	42017
15 27 12	64 55	11.2	12942
17 49 54	70 10	6.1	203860
18 23 30	−67 01	8.9	2575
18 44 06	−65 14	10.9	17959
20 33 48	59 59	5.5	27662
20 47 24	−69 24	6.7	85610
21 25 36	−52 59	10.6	0
21 33 00	−54 47	10.4	0
22 01 30	43 30	10.5	49241
22 18 18	−46 19	11.1	0
23 19 42	40 34	8.6	1850
23 22 18	41 04	9.3	1850
23 27 36	40 43	9.2	1850
23 31 48	−36 22	8.4	4142
23 33 36	−38 12	8.2	2630
Galaxies at 1–4 Mpc			
00 44 36	−21 01	2.1	33505
00 45 06	−25 34	3.0	29926
00 52 30	−37 57	1.2	116295
01 06 42	35 27	2.4	111305
01 32 54	−41 40	3.9	46641
03 17 42	−66 41	3.7	7988
03 42 00	67 56	3.9	8081
04 26 00	64 45	1.6	27389
04 27 06	71 48	3.0	12895
07 23 36	69 18	2.9	100820
09 43 12	68 08	2.1	116847
09 51 30	69 18	1.4	238546
09 59 24	68 59	2.1	134772
10 00 48	−25 55	1.8	12750
10 24 48	68 40	2.7	80551
12 13 06	36 36	3.5	94632
12 14 18	69 45	2.2	113804
12 15 00	38 05	3.1	107833
12 23 24	33 49	3.6	128582
12 25 48	44 22	3.0	85825
13 19 06	−36 22	3.5	63770
13 37 06	−31 24	3.2	55790
17 42 12	−64 37	3.0	25746
23 55 18	−32 51	2.8	37713

X-ray flashes were detected in the halos described by any of these six models.

Column (1) of Table 2 lists the value of $r_{\rm lim}$ in equation (1). Column (2) lists the limiting distance at which bursts can be detected by *Einstein* if the bursts at the BATSE flux limit are at a distance $r_{\rm lim}$. Column (3) lists the total exposure time for all galaxies with $M_V < -16$ whose halos fall within the field of view of an *Einstein* exposure. Column (4) lists the adjusted exposure time. To compute this quantity, the actual exposure time for each halo was reduced by the square of the ratio of the halo's distance to the limiting distance. Note that if galaxies were distributed uniformly in space, column (4) would always equal half of column (3). Columns (5) and (6) give the number of bursts whose detection is expected and the probability that no bursts would be detected if the model applied. Column (7) lists the probability of no bursts being detected if the physical extent of the halo were twice the distance at which BATSE is able to detect bursts (see below).

For $r_{\rm lim} = 600$ kpc, bursts would be observable from the Virgo Cluster. We would easily see them, since *Einstein* observed in the direction of the cluster for 4.243×10^6 s, often with multiple galaxies in the field of view. Indeed, one burst is seen in the direction of the Virgo Cluster (burst No. 3 in Table 1 of Paper I). This is lower than the expected random occurrence rate, and certainly inconsistent with the 23 bursts from Virgo we would see if typical halos had 600 kpc radii. A halo this large would also produce an anisotropy in the direction of M31 observable with BATSE (Hakkila et al. 1994b). Our exclusion of such models is therefore an independent confirmation of the M31 results.

We have also considered the possibility that the BATSE does not sample the entire extent of the Galactic halo. There is, of course, no reason why the halo could not extend well beyond BATSE's sampling distance. Note that BATSE's nondetection of a dipole toward M31 excludes halos larger than 400 kpc *only* if BATSE is able to detect halos that large. That is, BATSE obviously cannot constrain the location of bursts it cannot see. However, our experiment can test for the existence of halos extended well beyond the BATSE limit. Such halos produce many more expected bursts in our galaxy sample and can be readily excluded (see col. [7] of Table 2).

We therefore conclude that the GRBs detected by BATSE are not associated with X-ray bursts coming from a Galactic halo with a limiting radius greater than 250 kpc and less than 400 kpc, or, equivalently, from bursts with luminosities between 7×10^{38} ergs s^{-1} and 2×10^{39} ergs s^{-1} in the 0.16–3.5 keV band. This is the range of halo radii favored by the analysis of Hakkila et al. (1994b). Although our exclusion of halo models with limiting radii as small as 150 kpc is only weakly significant (73%), this result is much stronger if combined with the prior result of Hakkila et al. (1994b). If the GRBs originate in a 150 kpc halo, then three independent probabilities must be considered: (1) this halo radius is at the 90% confidence contour of Hakkila et al. (1994b) result; (2) our result excludes such a halo with 73% confidence; and (3) BATSE must have been fortuitously designed to see most of the way to the halo's edge but not beyond. The a priori probability of these three independent coincidences is approximately 1%. That is, combining our result with that of Hakkila et al. (1994b) excludes all halo models with $\geq$99% confidence. If we believe that X-ray counterparts are a common feature of GRBs, this would argue strongly for a cosmological GRB origin. The regions of parameter space allowed by Hakkila et al. (1994b)'s results and ours are illustrated in Figure 1. As discussed below, this chart uses the conservative and inconsistent assumption that GRBs are standard candles in both the γ-ray and X-ray bands. Deviation from either of these assumptions results in the exclusion of halo models with greater confidence.

4. ROBUSTNESS OF OUR CONCLUSION

We consider the uncertainty in the GRB X-ray/gamma-ray flux ratio to be easily the weakest link in our argument.

galaxy with an appropriate history of supernovae. If this is the case, it is not completely obvious what types of galaxies would have what types of GRB halos. There may be a complex relationship between mass, galaxy type and halo extent or density. Knowing little, we have followed a simple approach. Because we make the implausible assumption that the BATSE detection threshold represents an absolute limit on the burst population—i.e., that there are no bursts in our Galaxy below the BATSE limit—we consider our estimates to be conservative. However, it is obviously possible that our Galaxy is anomalous with respect to its GRB source population.

T. T. H. acknowledges support from NASA grant NAGW-4110 and wishes to thank Fiona Harrison, David Hogg, and Stephen Thorsett for useful discussions. D. J. H. acknowledges support from NASA grant NAS 5-32063 and wishes to express his gratitude to his local wine merchant whose case-discount policy has allowed him to avoid bankruptcy in covering his bets that GRBs were Galactic.

REFERENCES

Band, D., et al. 1993, ApJ, 413, 281
Fich, M., & Tremaine, S., 1991, ARA&A, 29, 409
Fishman, G. J., et al. 1989, in Proc. Gamma-Ray Observatory Science Workshop, ed. W. N. Johnson (Greenbelt: NASA), 2, 39
Gott, J. R., III, & Turner, E. L. 1976, ApJ, 209, 1
Gotthelf, E. V., Hamilton, T. T., & Helfand, D. J. 1996, ApJ, 466, 779 (Paper I)
Hakkila, J., et al. 1994a, in Proc. 1993 Huntsville Gamma-Ray Burst Conference, in press
Hakkila, J., et al. 1994b, ApJ, 422, 659
Innanen, K. A., Harris, W. E., & Webbink, R. F. 1983, AJ, 88, 338
Rothschild, R. E., Kulkarni, S. R., & Lingenfelter, R. E. 1994, Nature, 368, 432
Laros, J. G., Evans, W. D., Fenimore, E. E., Klebesadel, R. W., Shulman, S., & Fritz, G. 1984, ApJ, 286, 681
Lyne, A. G., & Lorimer, D. R. 1994, Nature, 369, 127
Meegan, C. A., Fishman, G. J., Wilson, R. B., Paciesas, W. S., Pendleton, G. N., Horack, J. M., Brock, M. N., & Kouveliotou, C. 1992, Nature, 355, 143
Meegan, C. A., et al. 1994, Status report available from gronews@grossc.gsfc.nasa.gov
Meźaŕos, P., & Rees, M. 1993, ApJ, 418, L59
Murakami, T., Inoue, H., Nishimura, J., van Paradijs, J., & Fenimore, E. E. 1991, Nature, 350, 592
Murakami, T., Tanaka, Y., Kulkarni, S. R., Ogasaka, Y., Sonobe, T., Ogawara, Y., Aoki, T., & Yoshida, A. 1994, Nature, 368, 127
Norris, J. P., Share, G. H., Messina, D. C., Dennis, B. R., Desai, U. D., Cline, T. L., Matz, S. M., & Chupp, E. L. 1986, ApJ, 301, 213
Paczyński, B. 1986, ApJ, 308, L43
Paczyński, B., & Rhoads, J. 1993, ApJ, 418, L5
Podsiadlowski, P., Rees, M., & Ruderman, M. A. 1995, MNRAS, 273, 755 preprint
Smith, I. A., & Lamb, D. Q. 1993, ApJ, 410, L23
Stark, A. A., Gammie, C. F., Wilson, R. W., Bally, J., Linke, R. A., Heiles, C., & Hurwitz, M. 1992, ApJS, 79, 77
Tully, B. 1988, Nearby Galaxies Catalog (Cambridge: Cambridge Univ. Press)
Trimble, V. 1987, ARA&A, 25, 425
Yoshida, A., Murakami, T., Itoh, M., Nishimura, J., & Tsuchiya, T. 1989, PASJ, 41, 509

THE ASTROPHYSICAL JOURNAL, 461:127–145, 1996 April 10

THE *EINSTEIN* TWO-SIGMA CATALOG: SILVER NEEDLES IN THE X-RAY HAYSTACK

EDWARD C. MORAN[1] AND DAVID J. HELFAND
Department of Astronomy, Columbia University, 538 West 120th Street, New York, NY 10027
ROBERT H. BECKER
Physics Department, University of California, Davis, CA 95616; and Institute of Geophysics and Planetary Physics, Lawrence Livermore National Laboratory, Livermore, CA 94550
AND
RICHARD L. WHITE
Space Telescope Science Institute, 3700 San Martin Drive, Baltimore, MD 21218
Received 1995 June 22; accepted 1995 October 12

ABSTRACT

To facilitate the study of [redacted]y sources fainter than those contained in the *Einstein* Medium-Sensitivity Survey (EMSS), we have constructed a new catalog of sources and fluctuations exceeding 2 σ significance in 2520 high-latitude *Einstein* IPCC images. We have employed various tests to validate our source-search algorithm for both high- and low-significance sources, and to identify and remove the small number of spurious sources induced by our detection procedure. Based on the known vignetting and background characteristics of the IPC and the measured X-ray log N–log S relation, we have modeled the number of real sources e[redacted]ed in the catalog in order to evaluate its statistical properties below 4 σ significance. Our modeling suggests that $\sim$13,000 sources in the catalog are real celestial X-ray sources, an increase of $\sim$9100 over the number found in previous analyses of the same IPC images. We find that not only is the reliability of the Two-Sigma Catalog a function of source significance σ, it is a function of off-axis angle on the detector as well. The application of different signal-to-noise thresholds at different off-axis angles thus enables one to tune the reliability of the catalog.

The chief motivation for studying large numbers of faint X-ray sources is to search for possible new components of the cosmic X-ray background. To select out real celestial X-ray sources in the Two-Sigma Catalog, we apply astronomical catalogs at other wavelengths as filters. For example, the cross-correlation of the Two-Sigma Catalog with catalogs from surveys of the radio and infrared sky has yielded large samples of faint X-ray sources that are $\sim$90% reliable. Optical spectroscopy of 77 unidentified faint X-ray sources has turned up several surprises, illustrating the merits of selecting X-ray sources using a variety of methods: high-redshift quasars (one at $z = 4.30$), which are absent in the EMSS, X-ray–luminous ($L_X \approx 10^{43}$ ergs s^{-1}) radio-loud elliptical galaxies with optical spectra devoid of emission lines, and infrared-bright active galactic nuclei whose optical spectra are dominated by starburst galaxy features. Follow-up observations are scheduled to determine whether any of these types of objects represent a previously unrecognized component of the X-ray background.

Subject headings: catalogs — galaxies: active — methods: data analysis — X-rays: galaxies

1. INTRODUCTION

Historically, progress in X-ray astronomy has been regulated by the number of celestial high-energy photons available for study. Advancements in mirror and detector technologies, and the resulting gains in the sensitivity, angular resolution, and spectral resolution of successive generations of X-ray observatories, have led to steady improvements in our understanding of the X-ray sky. For example, the use of focusing optics and position-sensitive detectors on the *Einstein Observatory* resulted in the detection of several thousand discrete X-ray sources, a substantial increase over the number found with all the nonimaging instruments that preceded it. *Einstein* sources were detected with arcminute positional accuracy, making, for the first time, identification of the optical counterparts of X-ray sources an efficient process. As a consequence, the study of *Einstein* sources has largely shaped our current knowledge of discrete X-ray source populations.

The imaging proportional counter (IPC) was the primary instrument used on the *Einstein Observatory*. In the years before the launch of *ROSAT*, the $\sim$4000 deg^2 of IPC images represented a unique resource for X-ray astronomers, providing them with ample incentive to characterize fully the IPC, reexamine important early IPC results, and exploit further the IPC data. Better understanding and calibration of the IPC permitted the construction of the *Einstein* Extended Medium-Sensitivity Survey (EMSS; Gioia et al. 1990; Stocke et al. 1991), which contains nearly 8 times as many sources as the original large-area survey (MSS; Maccacaro et al. 1982; Gioia et al. 1984) and remains the largest complete, unbiased, fully identified sample of X-ray sources ever assembled.

The study of the 1–3.5 keV background (XRB) and discrete source contributions to it has perhaps benefited most from more careful treatments of the IPC data. Several important papers have appeared in the literature in past years, fueling the debate over the origin of the XRB. For instance, the luminosity function for active galactic nuclei (AGNs) in this band, derived from the EMSS by Maccacaro et al. (1991), demonstrated that AGNs (of the types represented in the EMSS) contribute no more than $\sim$40% of

[1] Present address: Institute of Geophysics and Planetary Physics, Lawrence Livermore National Laboratory, Livermore, CA 94550.

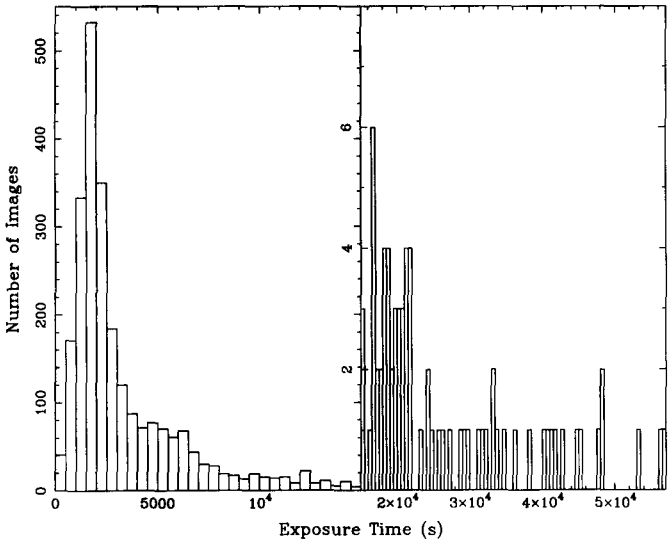

FIG. 1.—Distribution of exposure times for the 2520 IPC images used to construct the Two-Sigma Catalog.

substantive philosophical differences between our new procedure and that described by Hamilton et al. (1991); our modifications have merely optimized the algorithm for the detection of sources fainter than those they considered. This has come at the expense of computing efficiency; however, since the entire photon event database is on line at Columbia, the complete search takes as little as 12 hours.

Our procedure begins with the construction of two maps for each satellite orbit (called a HUT): one for the counts and one for the exposure time (which is initially constant across an image and is equal to the "good" exposure time for the HUT). We use data in the pulse-height–invariant (PI) channels 2–10, which covers the energy range 0.16–3.5 keV, collected when the Sun-angle viewing geometries (VG) were most favorable (i.e., VG = 1–3). We have opted to bin the IPC data in 32″ × 32″ pixels, rather than pixels 4 times as large, as was done by Wu et al. (1991) and Hamilton et al. (1991). This permits the use of a detection cell which better samples the IPC point response function. The IPC flat field (Wu et al. 1991) is applied to the exposure map for each HUT, accounting for energy-dependent vignetting due to the *Einstein* optics and spatial nonuniformities in the IPC response. Next, the count maps for all HUTs in an observation are combined in sky coordinates, as are the exposure maps.

In the next step, we compute the signal-to-noise ratio at each pixel in the image as though a source were centered there. Potential source counts n_S are collected within 1.′25 of this central pixel, and background counts are collected from within a concentric annulus with inner and outer radii of 3′ and 6′. In practice, this means that there are 21 pixels in the source aperture, covering 5.97 arcmin^2, and 304 pixels in the background annulus, covering 86.5 arcmin^2 (if both source and annulus are unshadowed). The number of background counts n_B expected within the source aperture is the number of counts in the background annulus weighted by the relative areas of the source and annulus and the mean flat-field values in the two regions. The signal-to-noise ratio is computed using the formula $\sigma = n_S/(n_S + n_B)^{1/2}$. This procedure is carried out for every pixel in the IPC image.

The search for sources occurs in an iterative fashion, in which the signal-to-noise threshold for detection, σ_{th}, is lowered with each successive iteration. We perform five iterations, with σ_{th} = 10, 6, 4, 3, and 2. In any iteration, the "most significant" pixel, i.e., the one centered on the source with the highest signal-to-noise ratio σ exceeding σ_{th}, is examined first for a source. Provided that the source meets the sampling requirements—at least ~60% of the source pixels and ~30% of the annulus pixels are unshadowed and undeleted—the source is considered detected. After the source parameters are recorded, the pixel values for the source region are blanked in the count and exposure maps. The radius to which data are deleted is proportional to ln σ, an empirically determined value found to be suitable for typical spectrum sources over a wide range of σ (however, see § 3.1 below). The procedure continues to the next most significant source with $\sigma > \sigma_{th}$. If within an iteration the number of undeleted source or annulus pixels for a source decreases as a result of the excision of a brighter nearby source, the detection of this source is deferred to the next iteration. When no more sources with σ above the current threshold are left, the signal-to-noise ratios are recomputed at each of the remaining pixels, excluding the deleted data, and σ_{th} is lowered appropriately for the next search iteration.

The advantages of the use of a flat field and a locally determined background for the detection of faint IPC sources were discussed in detail by Hamilton et al. (1991). We have made several minor modifications to their detection scheme, the most salient of which we summarize here:

1. We search for sources in order of their brightness, not by scanning, as in the sliding-box methods often employed in automatic search procedures. This ensures that the significance of a source is not compromised by the presence of brighter sources in its background annulus and greatly reduces the number of "edge effect" 2 σ sources found near the edges of the IPC and along the window support ribs.
2. We iteratively decrease the signal-to-noise threshold for detection, σ_{th}, in several stages, recomputing σ at each undeleted pixel between iterations. Furthermore, we defer detection of sources "corrupted" by the deletion of a nearby brighter source to a subsequent search iteration. Again, these strategies improve the accuracy of our computed source significances.
3. We have increased the size of the background annulus and have made more stringent requirements for the minimum area used to compute the background level. This also reduces the number of spurious detections at the lower values of σ.

In concert, these modifications have improved the accuracy of our detections and have afforded us consistent, predictable behavior regarding the detection of the faintest sources, as we demonstrate in § 2.2.

A total of 49,537 sources are found in 2520 IPC images, using the above procedure. Some sources in redundant images appear in the catalog more than once. In such cases we keep only the entry with the highest signal-to-noise ratio. After removal of duplicate sources and the spurious "satellite sources" identified in § 3.1, 46,186 sources remain. Of these, 4764 have significances greater than 3.5 σ, compared to 3912 sources with significances greater than 3.5 σ in the same 2520 images in the *Einstein* 2E Catalog, assembled by the Smithsonian Astrophysical Observatory (SAO).

only sources detected in IPC images with single roll angles, since sources in fields with multiple roll angles have more than one set of corresponding detector coordinates. Thus, ~39,000 of the ~46,000 sources in the catalog are represented in Figure 4*a*, and 93% of these are below 4 σ. The excess of sources at the center of the detector due to targets, and the lack of sources where data near the ribs have been deleted, are obvious. Otherwise, it appears that the distribution of sources is roughly uniform. Some faint structure parallel to the charge collection wires remains present in the source distribution. But compare this source distribution to the IPC flat field, displayed in Figure 4*b*, which also shows structure parallel to the charge collection wires. The pattern of sources on the IPC mimics *in detail* the flat field. Darker regions on the flat-field image represent areas where the detector is more sensitive. Thus, we are finding more sources at places where the detector is more sensitive, exactly what should happen if the excess sources are real.

To test this assertion, we divided the Two-Sigma Catalog into two parts, separating sources detected where the flat-field values are above the median value from those detected where the flat-field values are below the median. Sixty-three percent of the sources are detected where the flat field is above the median value. Next, we cross-correlated each subcatalog with the Green Bank 6 cm radio catalog (this procedure is described in § 4.1.1). Seventy-two percent of the X-ray sources that match 6 cm radio sources are from the "above-the-median" subcatalog, and the fraction of matches expected to arise by chance is significantly less for these (9% vs. 12%). This tells us that the excess sources found where the detector is more sensitive are predominantly real sources. This result is an important confirmation of the flat-fielding procedure and a strong endorsement of our detection algorithm. In the next section we determine exactly what fraction of sources in the catalog, as a function of the signal-to-noise ratio, are real celestial X-ray sources.

3. STATISTICAL PROPERTIES OF THE TWO-SIGMA CATALOG

Having established that our methods for constructing the IPC Two-Sigma Catalog are qualitatively well behaved, quantitative analysis is needed to determine the usefulness of the catalog as well as its limitations. In this section we explore a way of finding and removing spurious sources that are artifacts of our source detection scheme. We then model the number of real X-ray sources expected to be present in the catalog, thereby determining the spurious source detection rate as a function of the signal-to-noise ratio and the location on the detector.

3.1. *Removal of "Satellite" Sources*

We are confident that searching for sources in order of significance, rather than scanning for them, makes the most sense when a local background is used and when sources are deleted after detection. However, in the implementation of our detection algorithm we have had to assume that all sources we detect are point sources and that they have approximately the same spectrum, neither of which is strictly true. In certain instances, these assumptions lead to insufficient data being deleted after the detection of a source. For bright, extended sources the reasons are obvious; this is why we were careful to exclude images containing extended sources and diffuse emission. But similar problems can arise for some point sources as well. The point response function (PRF) for the IPC is characterized by two components: (1) a quasi-Gaussian core, the exact shape and width of which are determined by the geometric figure of the optics and the event-centroiding capabilities of the IPC, and (2) non-Gaussian wings, caused by X-rays being scattered to wide angles by mirror microroughness. Both of these components have a strong spectral dependence. For soft X-rays, the core of the PRF is broader than it is for hard X-rays, because soft X-rays deposit less charge on the detector wires, making the determination of event centroids less accurate. Mirror scattering, on the other hand, is much more severe for hard X-rays, and a higher fraction of them are scattered out of the core and into the wings. Thus, especially soft- or hard-spectrum sources (e.g., stars or some AGNs) will tend to have a nonnegligible fraction of counts outside the deletion radius, which has been set for sources with typical spectra. These undeleted counts might then be detected as independent "satellite" sources in a subsequent iteration of our detection procedure.

To test for this effect, we cross-correlated the Two-Sigma Catalog with itself to see whether sources tend to be found close to bright sources above the level expected by chance. For a given "primary" source of significance σ_1, only matches to it with sources having $\sigma < \sigma_1$ in the same image were considered. The accumulated results for the number of matches to primary sources as a function of positional offset are displayed in Figure 5. The primary sources are grouped by σ_1, and the number in each offset bin has been normalized by the solid angle of the annulus represented by the angular range of that bin. The resulting distribution is constant at each offset if the two sets of objects being compared are positionally uncorrelated, making the identification of a correlation straightforward.

Each panel in Figure 5 has qualitatively the same characteristics. The number of matches is zero out to the deletion radius determined by σ_1 and is approximately constant at large position offsets, as expected. However, at offsets just beyond the deletion radius, excesses of sources are observed. These are satellite sources and should be deleted from the catalog. Of course, there are also real celestial X-ray sources at small offsets as well, but the fraction of these determined from the observed source density at a given σ is low (19%–29%). Instead of removing every source within a certain distance of a bright X-ray source, we only remove those below 5 σ, to recover some of the real sources at small offsets. This procedure flags 1729 entries in our catalog, the removal of which leaves 46,186 sources in the final *Einstein* Two-Sigma Catalog. It is interesting that a strong correlation is observed even in the 4–6 σ range for primary sources. We suspect that the satellite sources in these cases are largely due to faint but extended primary sources, rather than point sources with unusually hard or soft spectra, since the magnitude of the number of undeleted counts in the latter case is expected to be small. This could be confirmed by the new search for extended sources in the IPC database being conducted by Oppenheimer, Gaidos, & Helfand (1996).

3.2. *The $N(>\sigma)$–σ Relation*

With the removal of the satellite sources, the Two-Sigma Catalog is now largely free of sources induced by our detection procedure. But before we use the catalog for astronomical purposes, we would like to gauge its reliability. A

and t is the exposure time, we obtain an expression for S in terms of σ:

$$S = \frac{\sigma^2 + \sqrt{\sigma^4 + 4Bt\sigma^2}}{2t} . \quad (2)$$

Substituting this in equation (1), the $N(>\sigma)$ relation is derived:

$$N(>\sigma) = N_0\left(\frac{\sigma^2 + \sqrt{\sigma^4 + 4Bt\sigma^2}}{2t}\right)^{-\alpha} . \quad (3)$$

Ultimately, we wish to compare directly the number of sources expected in a particular σ interval with the actual number present in the Two-Sigma Catalog; therefore, it is not the integrated number of sources above some σ that we are after, but rather the differential source counts $n(\sigma)$, given by

$$N(>\sigma) = \int_\sigma^\infty n(\sigma')d\sigma' . \quad (4)$$

Thus, differentiating equation (3) and applying the appropriate limits, we obtain the expression for the differential source counts:

$$n(\sigma) = -\frac{dN(>\sigma)}{d\sigma}$$
$$= \alpha N_0(2t)^\alpha[\sigma^2 + (\sigma^4 + 4Bt\sigma^2)^{1/2}]^{-\alpha-1}$$
$$\times\left[2\sigma + \frac{1}{2}(\sigma^4 + 4Bt\sigma^2)^{-1/2}(4\sigma^3 + 8Bt\sigma)\right] . \quad (5)$$

We have used IPC images with a wide range of exposure times; in addition, since vignetting affects some sources of background but not others, the background characteristics vary across the face of the detector. Thus, equation (5) must be modified to accommodate these circumstances. To deal with exposures of different duration, we compute $n(\sigma)$ for exposure times t spaced at 500 s intervals over their entire range, weight the calculations by a normalized distribution function $f(t)$, and sum the results. The function $f(t)$ is derived from the image exposure times displayed in Figure 1. In addition, vignetting due to the *Einstein* optics substantially reduces the effective exposure time at off-axis field angles θ, so exposure times must be modified by the normalized vignetting function $v(\theta)$ (see Wu et al. 1991).

The adjustment for spatial variations in the background is more complicated. Both source counts and background counts from the X-ray background and solar-scattered X-rays are vignetted, but the particle background is not (Wu et al. 1991). Hence, the background rate B consists of two parts: B_X for the vignetted X-ray background, and B_P for the particle background. B_P was determined in two independent ways by Wu et al. (1991), who derived a mean value of $\sim 1.4 \times 10^{-4}$ counts s^{-1} arcmin^{-2}. The total background rates for source-subtracted IPC images are strongly clustered near 1.6 counts s^{-1} (Fig. 7); thus, the mean photon background rate is $\sim 4.5 \times 10^{-4}$ counts s^{-1} arcmin^{-2}. Assigning B_X the appropriate on-axis value of 7.9×10^{-4} counts s^{-1} arcmin^{-2}, $B_X v(\theta)$ summed over θ and weighted by area gives the above mean background rate for photons.

Finally, we would like to compute $n(\sigma)$ in different radial zones on the IPC. Different normalization constants are

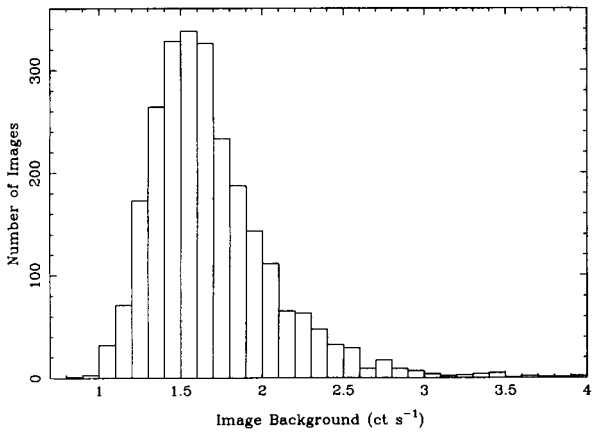

FIG. 7.—Histogram of total source-subtracted background count rates for IPC images used to construct the Two-Sigma Catalog.

therefore necessary for the different zones, and we replace the constant N_0 with $C(\theta)$. Thus, equation (5) transforms to the following:

$$n(\sigma, \theta) = \sum_t (\alpha C(\theta) f(t)[2tv(\theta)]^\alpha$$
$$\times [\sigma^2 + \{\sigma^4 + 4[B_X v(\theta) + B_P]t\sigma^2\}^{1/2}]^{-\alpha-1}$$
$$\times [2\sigma + \tfrac{1}{2}\{\sigma^4 + 4[B_X v(\theta) + B_P]t\sigma^2\}^{-1/2}$$
$$\times \{4\sigma^3 + 8[B_X v(\theta) + B_P]t\sigma\}) . \quad (6)$$

Plots of $n(\sigma, \theta)$ together with the signal-to-noise distribution for sources in the Two-Sigma Catalog are displayed in Figure 8, for 5′ wide annuli centered on the optical axis of the IPC. In Figure 8 we have omitted 3350 sources detected in fields with total background count rates in excess of 2.3 counts s^{-1}, since we have assumed a constant value of 1.6 counts s^{-1} in the calculations. The normalization constants $C(\theta)$ were determined by numerically integrating equation (6) over the limits $[5, \infty]$ for each annulus and setting the result equal to the actual number of cataloged sources above 5 σ in that annulus.

At off-axis angles greater than 5′ the signal-to-noise distributions of sources in Figure 8 are fitted very well by the model, above 4 σ in each radial range. Targets of the IPC observations contaminate the distribution in the first panel of Figure 8, causing the normalization determined by the number of sources with significance above 5 σ to be too high. However, this provides added confidence that the model fits off-axis, where sources were detected serendipitously, are accurate. Between 3.5 and 4 σ an obvious break occurs in the source signal-to-noise distributions. At the lower values of σ, it is clear that the departure of the data from the model, for a given σ, increases as the off-axis angle is increased. Thus, our inference above that the fraction of spurious sources increases with θ is confirmed. The break occurs right near the detection thresholds used in the EMSS and Deep Survey reanalysis, adding support to those investigators' choices for the signal-to-noise threshold σ_{th}.

The results of the modeling indicate that 28%, or $\sim$13,000, of the entries in the Two-Sigma Catalog are celestial X-ray sources, assuming all the sources above 4 σ are real. Below 4 σ, this fraction is 22%. We are not bound by our initial choice of 2 σ for the catalog's signal-to-noise threshold, and our estimates of the reliability of the catalog as a function of both σ and θ permit us to apply σ thresholds which vary with off-axis angle. This is certain to

challenge lies in the determination of which 28% of the entries in the catalog are the real celestial X-ray sources. The catalog itself is not reliable enough to make the direct study of sources at the 2 σ level possible. We could, therefore, limit ourselves to sources detected above 4 σ to avoid spurious sources, as in the EMSS; this would provide us with $\sim$1400 new X-ray sources, after omission of the targets and previously identified EMSS sources. However, all such sources will have fluxes at or above the EMSS sensitivity threshold, and we would have the arduous task of seeking their optical counterparts in the rather large $\sim$1′ radius IPC position error circles. An alternative approach is to apply filters (i.e., astronomical catalogs at other wavelengths) to the Two-Sigma Catalog, in order to isolate the real celestial X-ray sources from the statistical fluctuations. The advantages of this technique are that, depending on the choice of filter, one can explore fainter X-ray sources of types not well represented in other surveys and efficiently locate their optical counterparts. The disadvantage of this procedure is that a certain amount of contamination due to chance coincidences and false X-ray sources is admitted, but the level of contamination is easily determined. Since it took over 10 years to complete 96% of the optical identifications of the 835 EMSS sources, we have opted for the second approach. As will be discussed below, large samples of X-ray sources that are $\sim$90% reliable can be obtained this way, even though the catalog itself contains only 28% real sources. The filters we have used are catalogs from surveys of the radio and infrared sky.

The principal motivation for studying new populations of faint X-ray sources is to search for new components of the cosmic X-ray background (XRB). The XRB is now thought to arise from the integrated emission of faint discrete X-ray sources (Mather et al. 1990). However, known classes of luminous extragalactic X-ray sources, such as quasars, Seyfert galaxies, and galaxy clusters, have failed to demonstrate the spectral and spatial properties required to account for the origin of the XRB (Fabian & Barcons 1992). Two promising candidates at this time are star-forming galaxies (e.g., Griffiths & Padovani 1990) and obscured Seyfert galaxies (e.g., Madau, Ghisellini, & Fabian 1994; Comastri et al. 1995). An excellent means for isolating both of these types of galaxies is by infrared selection. Therefore, we have cross-correlated the IPC Two-Sigma Catalog with the *IRAS* Faint Source Catalog (FSC). In addition, although radio-loud objects are not expected to make a major contribution to the XRB, we have cross-correlated the Two-Sigma Catalog with the Green Bank 6 cm Northern Sky Catalog (Becker, White, & Edwards 1991) and the Texas 80 cm interferometric catalog (J. Douglas 1991, private communication). As we discuss below, fascinating X-ray sources not represented in the EMSS have been found in both the radio and infrared samples.

4.1. *Radio Selection*

Correlations between radio and X-ray emission have been observed spanning several orders of magnitude in luminosity, for a wide variety of objects, including elliptical and S0 galaxies (Fabbiano, Gioia, & Trinchieri 1989), 3CR radio galaxies (Fabbiano et al. 1984), and quasars (Worrall et al. 1987). The correlations are usually strongest for the nuclear (or "core") radio power and the soft X-ray luminosity. Complete radio information exists for the EMSS AGNs, which has been used to compare the properties of radio-loud and radio-quiet AGNs (Della Ceca et al. 1994). Hamilton & Helfand (1993) found a significant correlation between submillijansky radio sources and fluctuations greater than 2 σ in deep *Einstein* IPC images, concluding that star-forming galaxies, which make up the majority of sources at these radio fluxes, could contribute significantly to the soft X-ray background. However, Boyle et al. (1993), in a similar study involving a deep *ROSAT* image, found only a marginal correlation between X-ray and radio sources. This debate, plus the finding by Brinkmann, Siebert, & Boller (1994) that a considerable number of Molonglo radio sources contained in the *ROSAT* All-Sky Survey sources are radio- and X-ray–bright but optically faint, has motivated us to examine the properties of radio-selected sources in the Two-Sigma Catalog. We have utilized high- and low-frequency samples of radio sources. An advantage of using radio selection for X-ray sources is that radio positions can be determined to arcsecond precision, which greatly simplifies the identification of their optical counterparts.

4.1.1. *Cross-Correlation Statistics and Follow-up VLA Observations*

The Green Bank 6 cm catalog derived by Condon, Broderick, & Seielstad (1989) was compiled by Becker et al. (1991). The catalog contains 53,522 sources at declinations in the range $0° \leq \delta \leq 75°$, with a flux limit of 40 mJy at the equator and 20 mJy at the highest declinations. The positions of the 6 cm sources are accurate to 50″ (2 σ). Positions of sources in the unpublished Texas 80 cm catalog (J. Douglas 1991, private communication) can be accurate to $\sim$5″, but are sometimes ambiguous because of the interferometer's sidelobes. The flux limit of the Texas catalog, which contains 67,751 sources, is 250 mJy and the catalog covers the declination range $-25° < \delta < 72°$. Texas sources are assigned quality flags which can be used to select those sources with the most accurately measured positions and fluxes.

The results of the cross-correlations between the *Einstein* Two-Sigma Catalog and the 6 and 80 cm radio catalogs are displayed in Figures 9*a* and 10*a*, respectively. The number of matches as a function of the X-ray/radio position offset, normalized by the solid angle of the annulus represented in each offset bin, are plotted. The reason for plotting the offset distribution in this manner is that two uncorrelated catalogs will have a constant solid angle-normalized number in each offset bin; correlations are revealed by peaks above this constant level at small offsets, and the constant level establishes directly the chance coincidence rate. In both Figures 9*a* and 10*a* strong correlations are observed. To verify that the constant level in each plot accurately represents the chance coincidence rate, we shifted the positions of the radio catalog sources by some arbitrary amount, say 15′, and reperformed the matches. This process simulates the results obtained for two uncorrelated catalogs, and, as indicated by the dashed lines in Figures 9 and 10, confirms the chance coincidence level in each graph.

The chance coincidence fraction is known at every position offset. Therefore, our sample of radio-selected X-ray sources can be defined on the basis of a desired level of reliability by accepting only those matches with offsets smaller than some limit. If we choose our offset limit to be 60″ in both cross-correlations, we find that 598 X-ray sources match 6 cm radio sources with an 87% "real rate" (i.e., 13% are chance coincidences), and that 589 X-ray sources match 80 cm radio sources at a real rate of 85%. To

TABLE 1

RADIO-SELECTED X-RAY SOURCES

Object	z	Classification	S_6	S_{20}	S_{80}	log P_6	N_H	Seq. #	σ	C_X	F_X	log L_X	$\Delta_{R/X}$	Notes
0014+3152	1.100	QSO	110	417	1531	27.14	5.42	2718	3.13	0.0108	4.7	45.77	45.9	1
0035+1211	0.090	E	75	...	...	24.46	4.28	7508	4.14	0.0133	4.9	43.27	28.5	
0049+0019	0.400	QSO	68	...	...	25.83	3.43	8454	4.66	0.0087	3.3	44.52	47.7	
0053−0952	0.101	BL Lac	56	...	341	24.43	3.93	8992	5.86	0.0203	7.3	43.55	59.5	2
0111−0014	0.389	NLRG	175	352	916	26.21	3.41	203	5.43	0.0160	6.1	44.75	32.0	3
0126+0725	0.090	Sey	32	...	...	24.09	4.25	454	4.06	0.0167	6.1	43.37	56.5	4
0137+5036	...	...	30	...	...	...	16.7	3351	2.42	0.0063	1.5	...	43.2	5
0145+3438	0.857	QSO	55	...	...	26.55	4.68	8366	6.10	0.0079	3.3	45.33	1.1	
0202+2332	0.176	E	101	236	639	25.20	7.07	852	2.80	0.0033	1.4	43.34	40.0	
0230+3429	0.458	BL Lac	220	233	...	26.48	5.80	5142	3.89	0.0080	3.6	44.69	34.2	
0458+6530	...	BL Lac	37	...	...	...	14.6	456	17.85	0.2420	127.2	...	15.3	
0655+6940	1.971	QSO	314	215	...	28.32	4.76	3441	2.76	0.0120	5.0	46.52	36.6	
0713+3647	0.070	E	148	334	616	24.52	6.89	3554	3.04	0.0090	3.8	42.93	31.2	2
0724+1555	...	...	62	255	1145	...	7.23	7334	3.30	0.0043	1.0	...	29.5	5
1033+0021	0.097	BLRG	242	563	576	25.03	4.88	8961	2.81	0.0143	5.4	43.38	22.3	3
1126+2342	3.04	QSO	104	149	340	28.42	1.34	331	3.14	0.0078	2.2	46.74	8.3	
1136+2814	0.830	QSO	56	...	354	26.52	1.89	6348	2.71	0.0034	1.1	44.82	25.0	
1200+2812	0.672	QSO	100	130	...	26.54	1.74	4258	4.34	0.0122	3.7	45.11	21.0	
1201+2814	0.141	NLRG	67	...	410	24.82	1.73	4258	3.15	0.0059	1.7	43.22	13.8	6
1330+1721	0.609	QSO	94	131	...	26.41	1.81	4023	2.10	0.0065	2.0	44.74	32.0	
1508+5714	4.30	QSO	279	149	191	29.34	1.55	9143	6.08	0.0216	6.4	47.70	22.2	
1559+0847	0.188	E	47	...	...	24.93	3.68	10438	3.89	0.0072	2.5	43.66	16.5	
1600+0908	0.488	QSO	103	180	501	26.21	3.75	10438	8.03	0.0253	10.0	45.20	31.7	
1606+2836	0.050	Sey	106	189	...	24.08	3.43	5719	3.55	0.0054	1.9	42.33	53.8	7
1613+0913	0.171	E	48	173	...	24.84	4.13	4109	2.27	0.0132	4.8	43.85	25.7	
1619+0614	0.343	E	102	307	1153	25.85	4.70	4103	2.79	0.0101	3.8	44.42	24.6	3,8
1648+5330	0.029	LINER	146	181	222	23.74	2.75	7829	3.14	0.0113	3.6	42.13	55.5	9
1707+2241	0.464	QSO	159	492	2166	26.35	4.83	4933	2.15	0.0046	1.9	44.43	33.2	3
1720+2501	2.25	QSO	372	669	434	27.88	4.70	420	2.40	0.0099	4.1	46.61	32.8	
1745+6228	3.87	QSO	574	764	1852	28.56	3.35	8869	2.59	0.0205	7.7	47.63	34.1	
1755+6237	0.027	Sey1.9	128	...	784	23.62	3.27	8896	3.28	0.0340	12.7	42.61	42.0	
1832+6845	0.205	Cl/BL	64	189	452	25.15	6.06	8651	5.60	0.0538	12.9	44.46	15.0	10
1922+4748	1.52	QSO	317	388	734	27.99	7.47	4617	2.16	0.0027	1.3	45.60	0.7	
2121+2459	1.25	QSO	109	...	...	27.29	8.73	5712	4.98	0.0075	3.7	45.82	49.9	
2130−0527	0.329	QSO	91	171	355	25.76	4.03	4441	2.98	0.0152	6.1	44.59	39.8	
2248+2441	0.056	Sey1.9	...	...	...	...	5.28	7681	3.74	0.0050	1.2	42.23	29.8	11
2318+0814	0.124	E	60	...	347	24.65	4.87	2598	3.18	0.0053	2.0	43.17	39.4	
2324+4222	0.067	E	20	...	124	23.62	9.67	3361	3.71	0.0155	7.1	43.17	52.5	12
2354+4709	0.045	E	566	1646	671	24.71	9.54	4618	3.27	0.0063	2.9	42.42	2.5	3
2357+4650	0.575	QSO	83	...	...	26.29	9.62	4618	3.49	0.0086	4.4	45.02	17.6	

NOTES.—(1) A B2 radio source; not a known X-ray source when we observed it. X-ray detection recently published (Wilkes et al. 1994). (2) Weak [N II] emission line. (3) A 4C radio source. (4) Chance coincidence? Radio source coincident with E galaxy (at same z) 20″ northwest of weak-lined AGN. (5) Optical object observed is a faint star. Probable chance coincidence. (6) In cluster Abell 1451. Weak emission lines. (7) IC 4590. Weak emission lines, E galaxy continuum. (8) Hα region not observed; classification tentative. (9) In group of galaxies (Arp 330); X-ray emission could be extended. (10) Hα measurement needed to firmly establish classification. Very strong [O II]; possible cluster or BL Lac object. (11) Chance coincidence. A VLA image shows that the galaxy is a weak radio source, but a much stronger compact radio source is located 15″ to the northeast. (12) A B3 radio source.

catalog names (relating to their B1950.0 coordinates), the redshifts z, and classifications determined from our spectra are given in the first three columns. To clarify a few of the classifications used, broad- and narrow-line radio galaxies are denoted BLRG and NLRG, Sey and LINER are used for Seyfert and low-ionization nuclear emission-line region galaxies, E denotes an early-type galaxy spectrum devoid of strong emission lines, and Cl/BL is used for the one object which could be a cluster or a BL Lac object. The 6, 20, and 80 cm radio flux densities (in mJy) appear next, followed by the 5 GHz radio power (in W Hz^{-1}) for each object. Radio fluxes at 20 cm are taken from the Green Bank 20 cm Northern Sky Catalog of White & Becker (1992). For objects with 80 cm flux densities only, S_6 was estimated by extrapolating from the 80 cm measurement, assuming a power-law spectrum with index $\alpha = 0.7$. The Galactic H I column (in units of 10^{20} cm^{-2}) in the direction of each object (Stark et al. 1992), the IPC sequence number, the signal-to-noise ratio of the X-ray detection, and the IPC count rate are provided in the next four columns of Table 1. The X-ray fluxes ($\times 10^{-13}$ ergs cm^{-2} s^{-1}) in the 0.16–3.5 keV IPC band, which follow, assume a 1 keV thermal spectrum for normal galaxies or a power law with photon index $\Gamma = 2$ for AGNs, in addition to the tabulated Galactic N_H value. The X-ray luminosity L_X (in ergs s^{-1}) was computed assuming $H_0 = 50$ km s^{-1} Mpc^{-1} and $q_0 = 0$. The radio/X-ray position offsets (in arcsec) are listed last.

The classification of our quasars was straightforward. Classifications of other emission-line spectra were made on the basis of the emission-line flux ratios and velocity widths (Veilleux & Osterbrock 1987), incorporating the radio luminosity information. Seyfert galaxies usually have radio powers at 20 cm below a few times 10^{24} W Hz^{-1} (Ulvestad & Wilson 1989); therefore, we adopt a limit of 10^{24} W Hz^{-1} at 5 GHz to distinguish radio galaxies from the lower radio power Seyferts and LINERs. BL Lac objects were classified using the criterion established by Stocke et al. (1991), that the Ca II break "contrast" be less than 25%. For one BL Lac, the 18 σ X-ray source 0458+6530, we could not determine a redshift. None of the early-type galaxies in our list appear to be members of galaxy clusters on the POSS images, including the one (1201+2814) supposedly situated

been observed with *ROSAT*, we have listed Position Sensitive Proportional Counter (PSPC) count rates. For those quasars with IPC detections only, we have estimated the PSPC count rate by multiplying the IPC count rate by a factor of 2, which is appropriate for most X-ray sources (see Appendix F of the *ROSAT* mission description). Note that 1508+5714 is 50 times brighter than the $z = 4.32$ quasar and thus provides the only feasible opportunity to examine in detail quasar X-ray emission at $z > 4$. We have recently carried out an *ASCA* observation of 1508+5714 to study its X-ray properties in the 2–60 keV (rest) range.

There is a putative dearth of radio-loud quasars at high redshifts, which has prompted the suggestion that radio-loud and radio-quiet quasars have evolved differently (Schmidt et al. 1995). The three high-z quasars in our sample are, by definition, all radio-loud; in fact, 1508+5714 and 1745+6224 are currently the highest redshift radio-loud quasars known. It would appear, based on the frequency of such quasars in our list, that X-ray selection is an efficient means for finding high-z radio-loud quasars.

4.1.2.2. High-L_X Normal Early-Type Galaxies

One of the surprises uncovered during the EMSS optical identification process was several normal elliptical galaxies with X-ray luminosities $L_X \approx 10^{43}$ ergs s^{-1} (Stocke et al. 1991), an order of magnitude more luminous than early-type galaxies surveyed previously with *Einstein* (Fabbiano et al. 1989). Radio- and X-ray–loud, but optically undistinguished, galaxies are also present among Molonglo 408 MHz Survey radio sources detected in the *ROSAT* All-Sky Survey (Brinkmann et al. 1994). We have found several similar "optically passive" X-ray galaxies: eight of the 40 objects listed in Table 1 have normal early-type galaxy classifications and X-ray luminosities which range from 10^{43}–$10^{44.5}$ in the 0.16–3.5 keV band, typical of broad-line AGNs. Our galaxies differ from those contained in the EMSS in that they are all fairly radio-loud ($P_{5\,\mathrm{GHz}} > 10^{24}$ W Hz^{-1}), whereas the EMSS galaxies, with lower average redshifts than ours, are mostly undetected at 6 cm ($S_6 < 1$ mJy). However, this difference may simply be an artifact of our radio selection, and the X-ray emission mechanisms may be the same in the two sets of galaxies.

The most obvious possibilities for the nature of these X-ray–luminous early-type galaxies is that they are either optically weak BL Lac objects, in which starlight dominates the continuum, or radio galaxies situated in X-ray–emitting clusters. As discussed above, we have already examined the Ca II break contrast in the spectra of these objects. The eight galaxies in question here all have break contrasts typical for normal early-type galaxies, but this does not rule out some BL Lac activity. Therefore, we obtained deep VLA and CCD images for five of the galaxies to test further the BL Lac and cluster hypotheses. The CCD images indicate that while none of these galaxies is in a rich cluster, all have nearby galaxian companions at small projected separations. Similarly, the VLA images reveal that none of the galaxies have the extended, distorted radio tails common to radio galaxies in the cluster environment. On the other hand, the radio emission is not dominated by an unresolved, compact core in any of the galaxies, which convincingly rules out BL Lac activity (Kollgaard et al. 1992). Instead, the radio morphologies of these galaxies are amorphous or double-lobed with signs, in two cases, for a weak core component. The radio emission appears to be confined to the optical extent of the galaxy. Figure 12 (Plate 4) displays the optical spectrum, optical R-band image, and VLA 20 cm radio image of 2324+4222, an optically passive X-ray galaxy at a redshift of 0.068. The spectrum of 2324+4222 is clearly devoid of emission lines. The compact-double radio structure has a size of $\sim 15''$ and is contained well within the optical extent of the galaxy. Several galaxies are located within 3′ (~ 350 kpc) of the bright elliptical.

There are two promising alternatives for the origin of the X-rays in these objects. First, some sort of nonstandard AGN may be present. For example, the radio galaxy 3C 264 was observed to have a nuclear pointlike X-ray source in an *Einstein* HRI observation, yet its optical spectrum is remarkably dull: a starlight-dominated early-type galaxy continuum and only the slightest hint of Hα + [N II] emission lines (Elvis et al. 1981). The radio and X-ray luminosities of 3C 264, as well as its amorphous radio structure (Baum et al. 1988), are comparable to those of our objects. 3C 264 might therefore represent an AGN prototype for our optically passive X-ray galaxies. Alternatively, the X-ray emission in these objects could arise in a hot, diffuse medium associated with a small group of galaxies. Such emission has been recently discovered with *ROSAT* and, as noted above, all the galaxies for which we have CCD images have nearby companions. As an example, the X-ray emission from the galaxy group HCG 62 (Ponman & Bertram 1993) extends over at least 360 kpc and has a luminosity of 1×10^{43} ergs s^{-1} in the *ROSAT* band. We have marginal evidence that the closest of our galaxies, 2324+4222 (shown in Fig. 12), is extended in the IPC image: the signal-to-noise ratio of the detection of this source increases steadily as the aperture within which photons are collected is increased from 1 (S/N = 3.71 σ) to 2 (S/N = 4.05 σ) to 3 (S/N = 4.42 σ) times the size of an IPC point source. ROSAT HRI observations, scheduled for three of the brightest sources, will determine whether the X-ray emission is point-like or extended in these objects. These results, along with our radio and optical images, will be published elsewhere (Moran, Helfand, & Becker 1996).

4.2. *Infrared Selection*

Infrared galaxies have also been studied extensively at X-ray wavelengths, frequently in the context of the XRB. As mentioned above, two promising candidates for the origin of the XRB are obscured Seyferts and star-forming galaxies, both of which are expected to turn up in IR-selected samples. In a search for obscured Seyfert galaxies, *IRAS* Point-Source Catalog (PSC) galaxies within *HEAO 1* error boxes were studied by Kirhakos & Steiner (1990), who found a large number of type 2 Seyfert galaxies that they interpreted to be obscured Seyfert 1s, on the basis of their hard X-ray properties. However, the identification of these *IRAS* galaxies as X-ray sources is very uncertain due to the large size (1° × 3°) of the *HEAO 1* error boxes. In the soft X-ray regime, the *Einstein* IPC and *IRAS* PSC databases have been used to establish correlations between soft X-ray and far-infrared luminosities for normal and star-forming galaxies (David, Jones, & Forman 1992), as well as for broad-line AGNs (Green, Anderson, & Ward 1992). Optical spectroscopy of 11 IPC/PSC sources by Fruscione & Griffiths (1991) further established the presence of starburst galaxies in X-ray/IR-selected samples and provided preliminary support to the hypothesis of Griffiths & Padovani

TABLE 3

INFRARED-SELECTED X-RAY SOURCES

Object	z	Classification	S_{60}	S_{100}	log L_{FIR}	N_H	Seq. #	σ	C_X	F_X	log L_X	$\Delta_{IR/X}$	$\Delta_{O/X}$	Notes
00188+2214	0.0195	H II	0.403	<3.399	43.56	4.08	7765	5.90	0.0081	2.02	41.53	37.3	12	1
01105+0201	0.0462	Sey1.9	0.552	1.599	44.56	8.88	8458	3.19	0.0045	2.25	42.34	57.5	63	2,3
01227+3341	0.0280	H II	0.298	<0.616	43.74	5.11	4199	2.56	0.0045	1.73	41.78	53.1	68	
01445+3503	0.0655	Comp	0.232	0.510	44.44	4.72	8366	4.35	0.0064	1.78	42.54	36.2	19	
02585−1515	0.1159	?	0.288	1.851	45.43	4.25	9183	3.48	0.0058	1.45	42.79	37.5	70	4
04061−1307	0.0789	Sey1.9	0.188	<1.038	44.46	3.67	10648	2.91	0.0038	1.48	42.63	59.1	60	2
08012+1008	0.0343	H II	0.229	0.810	43.97	2.70	181	3.68	0.0047	1.13	41.77	16.3	24	5
08045+6301	0.0702	Sey2	0.221	<0.971	44.43	4.37	8357	3.06	0.0026	0.72	42.21	25.0	42	2
08083+6223	...	Star	0.227	1.134	...	...	8357	3.48	0.0034	...	...	33.6	41	
08255+2630	0.0526	Comp	0.773	<2.982	44.72	3.70	5929	3.14	0.0045	1.75	42.34	53.8	70	
09131+7500	0.1266	H II	0.347	<0.888	45.16	2.08	8439	2.44	0.0017	0.51	42.60	38.2	15	
09446+1359	0.0739	Sey1.9	0.466	0.654	44.77	3.04	4944	2.81	0.0172	4.55	43.06	28.1	11	
10200+4839	0.0625	H II	0.293	0.565	44.47	1.13	4614	2.13	0.0058	1.48	42.42	36.4	10	
10518+1801	0.0542	H II	0.516	1.048	44.60	2.58	7757	2.85	0.0042	1.01	42.13	38.2	45	6
11078+3614	0.0711	H II	0.389	0.887	44.75	2.13	3122	2.53	0.0050	1.50	42.54	42.0	40	6
11151+2934	0.0232	Sey1.8	0.317	0.864	43.70	1.53	1844	3.78	0.0205	4.89	42.06	24.5	23	
12013−0326	0.0127	H II	0.244	0.560	43.02	2.53	4289	2.97	0.0064	1.53	41.03	57.5	80	
12134+1257	0.0655	Sey1.9	0.421	0.950	44.70	2.57	4303	4.07	0.0104	2.68	42.72	29.5	14	7
12230+0755	0.0372	Comp	0.441	1.018	44.23	1.60	6993	5.71	0.0195	4.68	42.46	41.5	43	
13006+3556	0.0371	H II	2.743	4.090	44.94	1.04	5392	3.98	0.0016	0.48	41.47	41.7	87	6
13049+3437	0.2224	Sey2	0.438	0.912	45.83	1.04	2608	4.01	0.0105	2.37	43.79	23.1	25	
13342+0332	0.0231	H II	0.259	0.848	43.65	1.97	5547	3.98	0.0047	1.39	41.51	29.0	26	
14060+7207	0.0341	Sey1.9	0.529	1.108	44.21	1.87	10197	3.22	0.0081	1.99	42.01	34.5	34	
14203+3005	0.1144	Sey1.9	0.960	1.387	45.49	1.33	5557	3.03	0.0077	1.80	43.05	22.2	9	
14362−0657	0.0868	IZw1	0.836	0.607	45.03	5.43	5382	2.78	0.0074	3.23	43.06	32.0	37	
14445+1147	0.0317	LINER	0.187	0.864	43.88	1.66	10474	3.02	0.0033	0.80	41.55	41.5	25	8
15033+2617	0.0553	Sey2	0.237	0.716	44.37	3.40	1907	4.08	0.0038	1.02	42.15	37.1	45	2
16008+3339	0.0625	H II	0.200	<1.109	44.28	2.29	3986	3.06	0.0082	2.42	42.64	44.6	65	9
16022+1753	0.0412	LINER	0.661	1.215	44.45	3.39	3713	8.24	0.0269	10.2	42.89	12.8	37	10
16075+2838	0.1690	Sey	0.840	1.006	45.76	3.42	5719	2.69	0.0036	1.36	43.29	53.6	60	
16480+5329	0.0267	H II	0.214	<1.634	43.56	2.75	7829	3.14	0.0113	3.65	41.93	59.9	74	11
17039+6039	0.0968	Sey2	0.398	0.600	44.96	2.29	5688	2.65	0.0010	0.25	42.04	33.2	40	12
17079+7118	0.0400	H II	0.191	0.748	44.05	4.13	29	3.65	0.0013	0.47	41.52	38.6	16	
17549+6520	0.0803	Sey1	0.374	0.845	44.84	3.67	8749	4.82	0.0443	8.54	43.41	49.8	51	
17551+6209	0.0844	Sey1.9	0.388	1.017	44.93	3.37	8897	2.30	0.0146	3.92	43.12	29.6	21	
17583+6934	0.0795	Sey1	0.207	<1.060	44.51	3.41	8848	3.15	0.0178	4.78	43.15	35.5	41	
23489+0827	0.0417	Sey2	0.424	<1.775	44.25	6.12	5744	2.97	0.0053	1.50	42.04	25.0	35	

NOTES.—(1) IC 1546, weak emission lines. In galaxy group; elliptical companion ($z = 0.0208$) ~ 1′ west-northwest. (2) Very reddened spectrum. (3) UGC 768. (4) Faint object and noisy spectrum; classification uncertain. Weak [N II], Hα emission lines; [N II]/Hα ≈ 1. (5) Mrk 1209. (6) Close H II galaxy pair (at same z). (7) Mrk 764; classified as starburst by Balzano (1983). (8) E(?) galaxy with weak emission lines in group of galaxies; [N II]/Hα ≫ 1. (9) Chance coincidence? Nearby M star. (10) NGC 6040 (= Arp 122); S nucleus has LINER spectrum, possible broad Hα. N nucleus is reddened; possible Seyfert 2. (11) In group of galaxies (Arp 330); northern companion has LINER spectrum (see Table 1); X-ray emission could be extended. (12) Close H II companion at $z = 0.0971$.

computed far-infrared luminosity (in ergs s^{-1}) are listed in the next three columns. L_{FIR} ($=4\pi D_L^2 F_{FIR}$ ergs s^{-1}) is computed using the formulae $F_{FIR} = 1.26 \times 10^{-11}$ $(2.58 S_{60\mu m} + S_{100\mu m})$ and $D_L = cz(1 + z/2)/H_0$, where z is the redshift. For objects with flux density upper limits at 100 μm, we estimated S_{100} assuming $\alpha(60, 100) = -1$ in order to compute L_{FIR}. As in § 4.1.2, we assume $H_0 = 50$ km s^{-1} Mpc^{-1} and $q_0 = 0$. The Galactic H I column toward each FSC source ($\times 10^{20}$ cm^{-2}), the IPC image sequence number containing the X-ray source, the significance of the X-ray detection, and the IPC source count rate are given in the next four columns. These data were used to compute the X-ray flux (in units of 10^{-13} ergs cm^{-2} s^{-1}) and luminosity (in ergs s^{-1}) in the 0.16–3.5 keV band assuming a $kT = 1$ keV thermal spectrum for normal and H II galaxies and a power-law spectrum with photon index $\Gamma = 2$ for AGNs. Finally, the IR/X-ray and optical/X-ray position offsets (in arcsec) for each IR/X-ray coincidence are listed in the last two columns.

All of the objects we observed have emission-line optical spectra. Spectral classifications were determined using the emission-line flux-ratio diagnostics described by Veilleux & Osterbrock (1987) and Filippenko & Terlevich (1992) along with the emission-line velocity width information. Table 3 indicates that most of the objects in our sample fall into the categories of Seyfert galaxies (Sey), LINERs, and normal late-type galaxies and starburst galaxies (H II). One object observed, a bright K star, is likely to be both the X-ray and the infrared source. (Our "galaxies" subsample of the *IRAS* FSC is not completely free of stellar sources.) One of the remaining objects is a I Zw 1–type Seyfert galaxy, and three others are "starburst/Seyfert composite" galaxies, which we describe more fully below. Note that several of the objects are interacting galaxies or close galaxy pairs. Any assertions we make based on the representation of various classes in our sample are somewhat preliminary, since we have a relatively small sample that is not complete. However, there should not be any strong selection biases in this sample of serendipitously detected X-ray sources.

We expect there to be six chance coincidences among the 37 objects in our sample. In principle, the optical/X-ray position offsets $\Delta_{O/X}$ (penultimate column of Table 3), which are accurate to ~5″, could help distinguish these chance coincidences. However, the largest value of $\Delta_{O/X}$ is 87″, and only three objects have offsets in excess of 70″. Since several EMSS sources have optical/X-ray offsets this large, $\Delta_{O/X}$ for

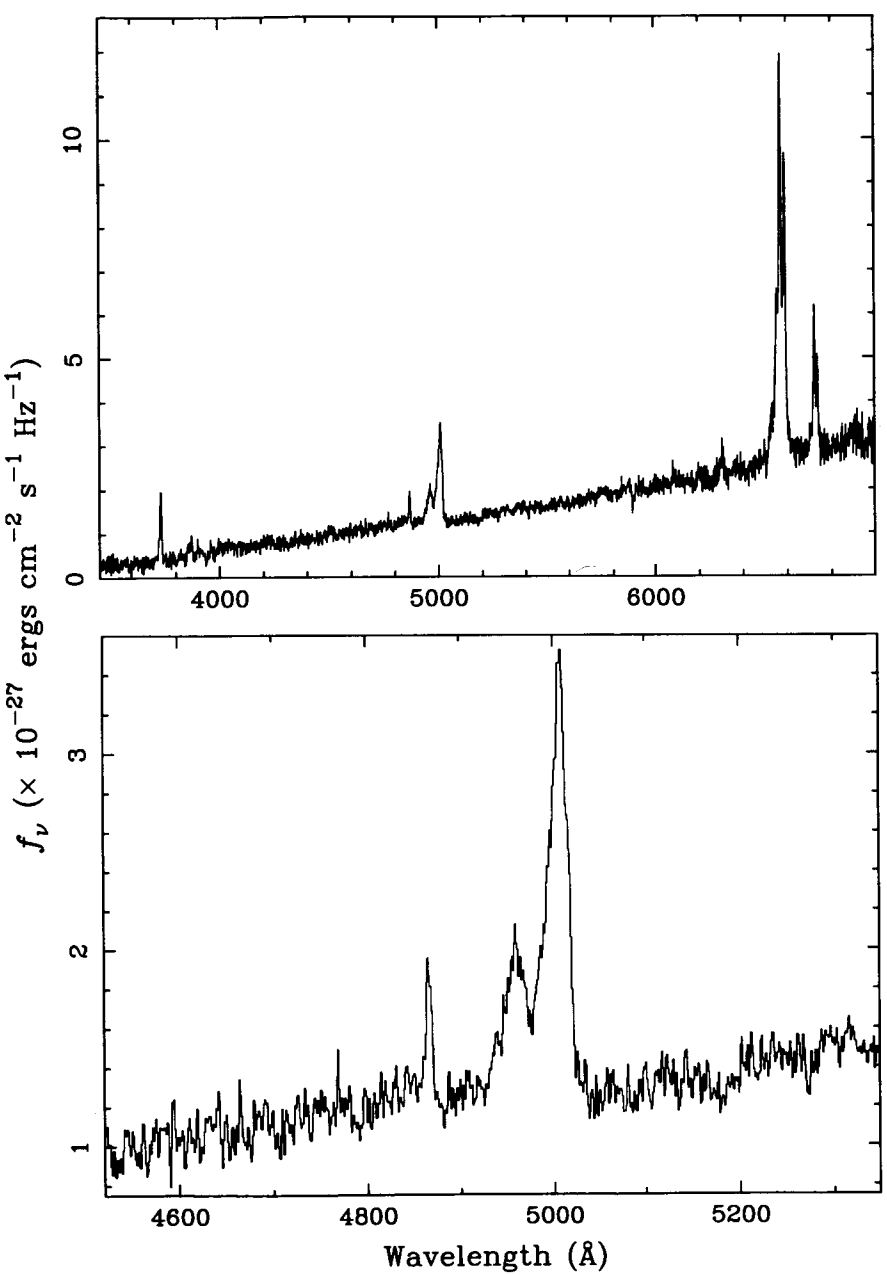

FIG. 14

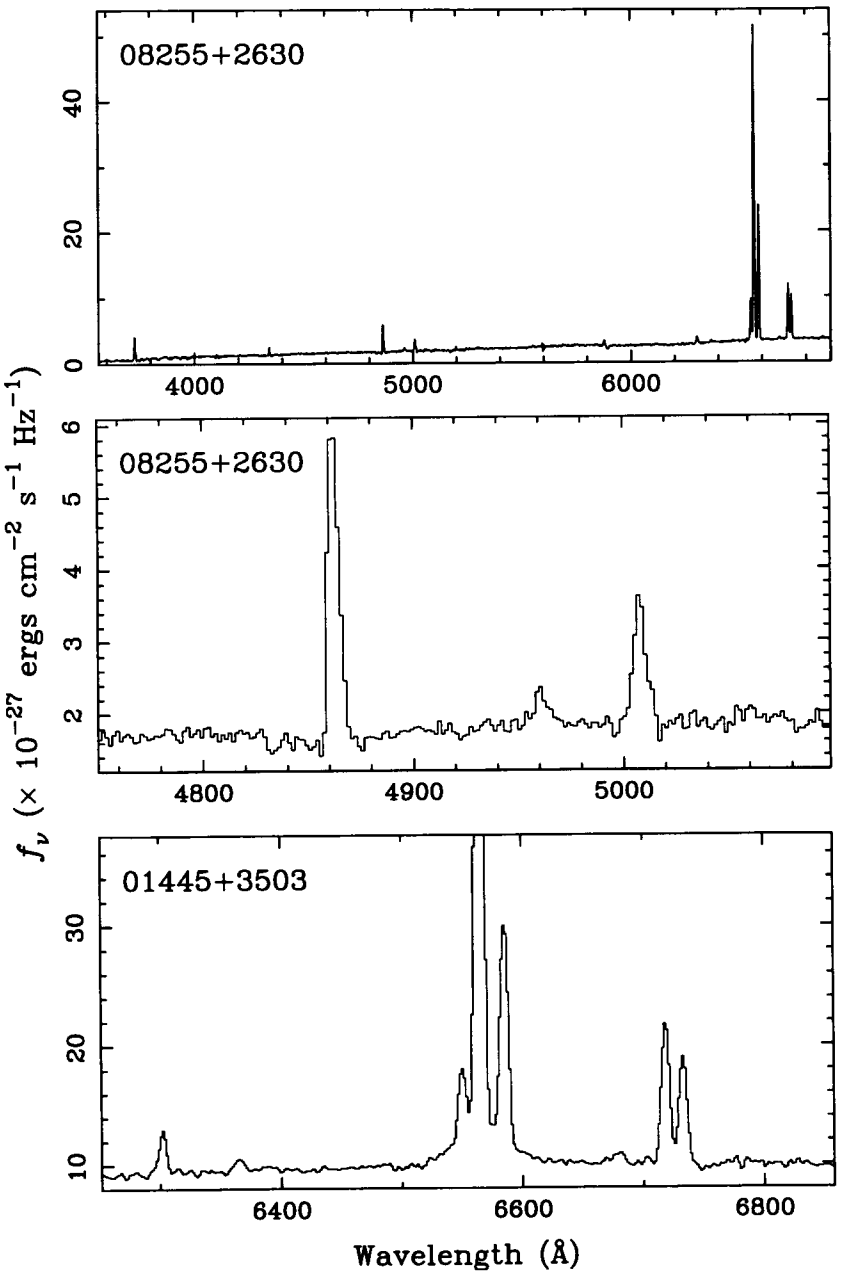

FIG. 15

FIG. 14.—The unusual spectrum of *IRAS* F16075+2838, and detail of the [O III], Hβ region

FIG. 15.—Spectrum of *IRAS* F08255+2630 (*top*), a starburst/Seyfert composite object, has primarily starburst galaxy characteristics. However, a close look at the [O III], Hβ region (*middle*) reveals broad [O III] lines (FWHM = 377 km s^{-1}), which must arise in an AGN. The spectrum of another composite object, F01445+3503 (*bottom*) indicates a weak, broad Hα feature as well, not present in F08255+2630.

PLATE 4

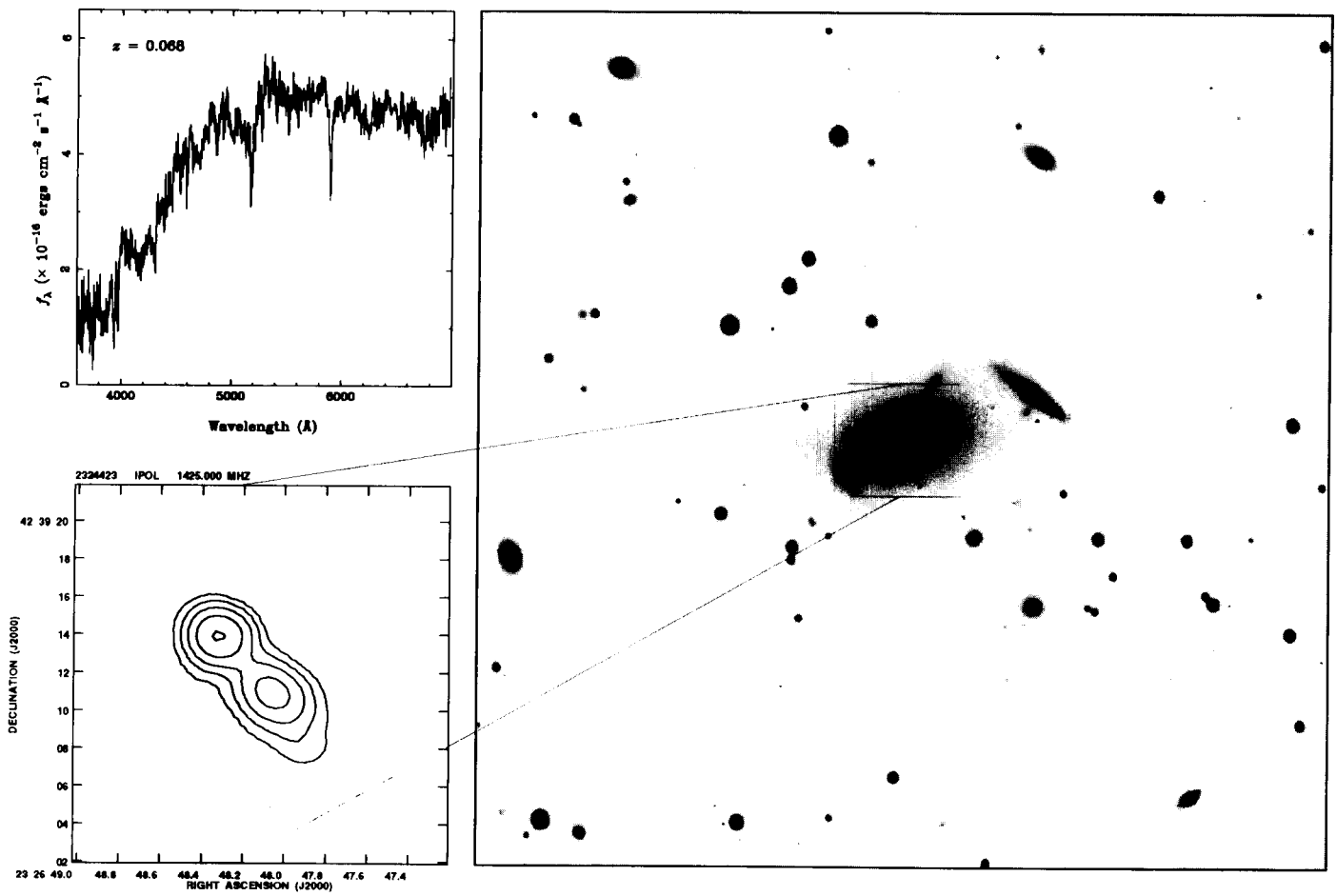

FIG. 12.—Optical spectrum, 20 cm VLA A-array radio image, and 900 s *R* band optical image of the optically passive X-ray galaxy 2324+4222

REFERENCES

Allen, S. W., et al. 1992, MNRAS, 259, 67
Balzano, V. A. 1983, ApJ, 268, 602
Barcons, X., & Fabian, A. C. 1990, MNRAS, 243, 366
Baum, S. A., Heckman, T., Bridle, A., van Breugel, W., & Miley, G. 1988, ApJS, 68, 643
Bechtold, J., et al. 1994a, AJ, 108, 374
———. 1994b, AJ, 108, 759
Becker, R. H., Helfand, D. J., & White, R. L. 1992, AJ, 104, 531
Becker, R. H., White, R. L., & Edwards, A. L. 1991, ApJS, 75, 1
Becker, R. H., White, R. L., & Helfand, D. J. 1995, ApJ, 450, 559
Boller, T., Meurs, E. J. A., Brinkmann, W., Fink, H., Zimmermann, U., & Adorf, H.-M. 1992, A&A, 261, 57
Boyle, B. J., Staveley-Smith, L., Stewart, G. C., Georgantopoulos, I., Shanks, T., & Griffiths, R. E. 1993, MNRAS, 265, 501
Brinkmann, W., Siebert, J., & Boller, T. 1994, A&A, 281, 355
Comastri, A., Setti, G., Zamorani, G., & Hasinger, G. 1995, A&A, 296, 1
Condon, J. J., Broderick, J. J., & Seielstad, G. A. 1989, AJ, 97, 1064
David, L. P., Jones, C., & Forman, W. 1992, ApJ, 388, 82
Della Ceca, R., Zamorani, G., Maccacaro, T., Wolter, A., Griffiths, R., Stocke, J. T., & Setti, G. 1994, ApJ, 430, 533
Elvis, M., Fiore, F., Wilkes, B., McDowell, J., & Bechtold, J. 1994, ApJ, 422, 60
Elvis, M., Schreier, E. J., Tonry, J., Davis, M., & Huchra, J. P. 1981, ApJ, 246, 20
Fabbiano, G. 1989, ARA&A, 27, 87
Fabbiano, G., Gioia, I. M., & Trinchieri, G. 1989, ApJ, 347, 127
Fabbiano, G., Miller, L., Trinchieri, G., Longair, M., & Elvis, M. 1984, ApJ, 277, 115
Fabian, A. C., & Barcons, X. 1992, ARA&A, 30, 429
Filippenko, A. V., & Terlevich, R. 1992, ApJ, 397, L79
Fink, H., & Briel, U. G. 1993, A&A, 274, L45
Fruscione, A., & Griffiths, R. E. 1991, ApJ, 380, L13
Gelderman, R., & Whittle, M. 1994, ApJS, 91, 491
Giacconi, R., et al. 1979, ApJ, 234, L1
Gioia, I. M., Maccacaro, T., Schild, R. E., Stocke, J. T., Liebert, J. W., Danziger, I. J., Kunth, D., & Lub, J. 1984, ApJ, 283, 495
Gioia, I. M., Maccacaro, T., Schild, R. E., Wolter, A., Stocke, J. T., Morris, S. L., & Henry, J. P. 1990, ApJS, 72, 567
Green, P. J., Anderson, S. F., & Ward, M. J. 1992, MNRAS, 254, 30
Griffiths, R. E., et al. 1983, ApJ, 269, 375
Griffiths, R. E., & Padovani, P. 1990, ApJ, 360, 483
Halpern, J. P., Helfand, D. J., & Moran, E. C. 1995, ApJ, 453, 611
Halpern, J. P., & Oke, J. B. 1987, ApJ, 312, 91
Hamilton, T. T., & Helfand, D. J. 1987, ApJ, 318, 93
———. 1993, ApJ, 418, 55
Hamilton, T. T., Helfand, D. J., & Wu, X. 1991, ApJ, 379, 576
Harnden, F. R., Fabricant, D. G., Harris, D. E., & Schwarz, J. 1984, SAO Spec. Rep. No. 393
Harris, D. E., et al. 1990, The *Einstein Observatory* Catalog of IPC X-Ray Sources (Cambridge: SAO)
Hasinger, G., Burg, R., Giacconi, R., Hartner, G., Schmidt, M., Trümper, J., & Zamorani, G. 1993, A&A, 275, 1
Henry, J. P., et al. 1994, AJ, 107, 1270
Hook, I. M., McMahon, R. G., Patnaik, A. R., Browne, I. W. A., Wilkinson, P. N., Irwin, M. J., & Hazard, C. 1995, MNRAS, 273, L63
Kirhakos, S. D., & Steiner, J. E. 1990, AJ, 99, 1722
Kollgaard, R. I., Wardle, J. F. C., Roberts, D. H., & Gabuzda, D. C. 1992, AJ, 104, 1687
Maccacaro, T., Della Ceca, R., Gioia, I. M., Morris, S. L., Stocke, J. T., & Wolter, A. 1991, ApJ, 374, 117
Maccacaro, T., et al. 1982, ApJ, 253, 504
Madau, P., Ghisellini, G., & Fabian, A. C. 1994, MNRAS, 270, L17
Mather, J. C., et al. 1990, ApJ, 354, L37
Moran, E. C., Halpern, J. P., Bothun, G. D., & Becker, R. H. 1992, AJ, 104, 990
Moran, E. C., Halpern, J. P., & Helfand, D. J. 1994, ApJ, 433, L65
———. 1995, ApJS, submitted
Moran, E. C., Helfand, D. J., & Becker, R. H. 1996, in preparation
Morris, S. L., Stocke, J. T., Gioia, I. M., Schild, R. E., Wolter, A., Maccacaro, T., & Della Ceca, R. 1991, ApJ, 380, 49
Moshir, M., et al. 1992, Explanatory Supplement to the *IRAS* Faint Source Survey, Version 2, JPL D-10015 8/92 (Pasadena: JPL)
Oppenheimer, B. R., Gaidos, E. J., & Helfand, D. J. 1996, in preparation
Osterbrock, D. E., & Shaw, R. A. 1988, ApJ, 327, 89
Pickering, T. E., Impey, C. D., & Foltz, C. B. 1994, AJ, 108, 1542
Ponman, T. J., & Bertram, D. 1993, Nature, 363, 51
Primini, F. A., Murray, S. S., Huchra, J., Schild, R., Burg, R., & Giacconi, R. 1991, ApJ, 374, 440
Schmidt, M., van Gorkom, J. H., Schneider, D. P., & Gunn, J. E. 1995, AJ, 109, 473
Stark, A. A., Gammie, C. F., Wilson, R. W., Bally, J., Linke, R. A., Heiles, C., & Hurwitz, M. 1992, ApJS, 79, 77
Stephens, S. A. 1989, AJ, 97, 10
Stocke, J. T., Morris, S. L., Gioia, I. M., Maccacaro, T., Schild, R., Wolter, A., Fleming, T. A., & Henry, J. P. 1991, ApJS, 76, 813
Tananbaum, H., et al. 1979, ApJ, 234, L9
Ulvestad, J. S., & Wilson, A. S. 1989, ApJ, 343, 659
Veilleux, S., & Osterbrock, D. E. 1987, ApJS, 63, 295
Véron, M. P., Véron, P., & Zuiderwijk, E. J. 1981, A&A, 98, 34
Véron, P., Véron, M. P., Bergeron, J., & Zuiderwijk, E. J. 1981, A&A, 97, 71
Wang, Q., Hamilton, T. T., Helfand, D. J., & Wu, X. 1991, ApJ, 374, 475
White, R. L., & Becker, R. H. 1992, ApJS, 79, 331
Whittle, M., Pedlar, A., Meurs, E. J. A., Unger, S. W., Axon, D. J., & Ward, M. J. 1988, ApJ, 326, 125
Wilkes, B. J., Tananbaum, H., Worrall, D. M., Avni, Y., Oey, M. S., & Flanagan, J. 1994, ApJS, 92, 53
Worrall, D. M., Giommi, P., Tananbaum, H., & Zamorani, G. 1987, ApJ, 313, 596
Wu, X., Hamilton, T., Helfand, D. J., & Wang, Q. 1991, ApJ, 379, 564

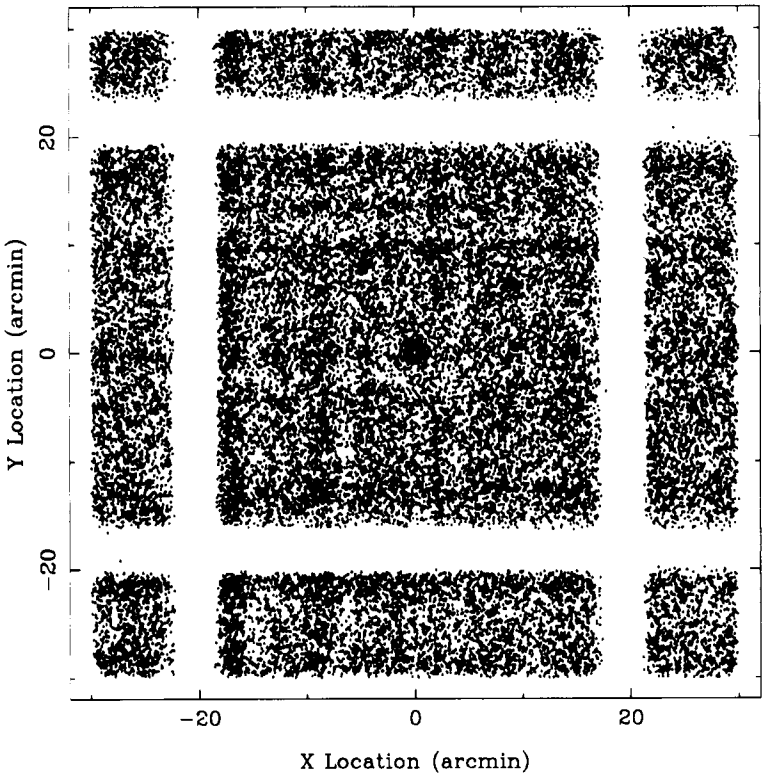

FIG. 4*a*

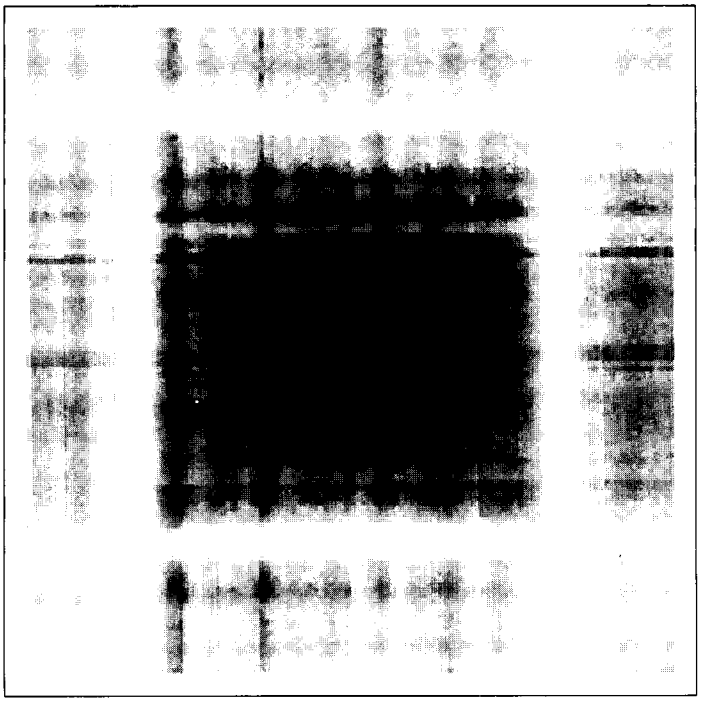

FIG. 4*b*

FIG. 4.—(*a*) Location on the IPC of sources in the Two-Sigma Catalog; (*b*) the IPC flat field. Comparison of (*a*) and (*b*) indicates that more/fewer sources were detected in places where the IPC is more/less sensitive. The white bars correspond to the IPC window support ribs.

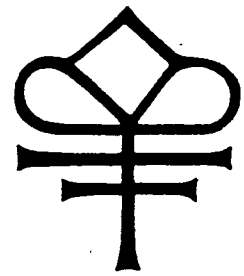

Detailed Analysis of the Cross-Correlation Function between the X-Ray Background and Foreground Galaxies

ALEXANDRE REFREGIER AND DAVID J. HELFAND
Columbia Astrophysics Laboratory, Columbia University
538 West 120th Street, New York, NY 10027

RICHARD G. MCMAHON
Institute of Astronomy
Madingley Road, Cambridge CB3 0HA
United Kingdom

To appear in: *The Astrophysical Journal* (March 1997)

COLUMBIA UNIVERSITY

DEPARTMENTS OF

PHYSICS and ASTRONOMY

NEW YORK, NEW YORK 10027

Columbia Astrophysics Laboratory Contribution Number 602

To appear in ApJ, March 1, 1997, Vol. 477

Detailed Analysis of the Cross-Correlation Function between the X-Ray Background and Foreground Galaxies

Alexandre Refregier[1] and David J. Helfand
Columbia Astrophysics Laboratory, 538 W. 120th Street, New York, NY 10027
email:refreg@odyssey.phys.columbia.edu,djh@carmen.phys.columbia.edu

and

Richard G. McMahon
Institute of Astronomy, Madingley Road, Cambridge CB3 OHA, UK
email:rgm@mail.ast.cam.ac.uk

ABSTRACT

Recent ROSAT surveys suggest that galaxies can constitute the new class of faint sources required to explain the full phenomenology of the cosmic X-Ray Background (XRB). To test this hypothesis without resorting to optical identifications, we compute the two-point cross-correlation function (CCF) estimator $W_{xg}(\theta)$ between 62 *Einstein*-IPC fields (.81-3.5 keV) and the APM Northern galaxy catalog ($13.5 < E < 19.0$). At zero-lag ($\theta = 0$), we detect a 3.5σ correlation signal with an amplitude of $W_{xg}(0) = .045 \pm .013$. This signal passes a series of control tests. At non-zero lag ($\theta > 0$), the angular dependence of W_{xg} has two main features: the main signal for $\theta \lesssim 4'$, and an almost flat plateau with an amplitude of $W_{xg}(\theta \gtrsim 4') \simeq .015$. When fields with galaxy clusters as *Einstein* targets are removed, the plateau virtually disappears, and the zero-lag amplitude becomes $W_{xg}(0) = .029 \pm .013$. We develop a simple, 2-dimensional formalism to interpret the CCF which takes into account the point-spread function of the imaging X-ray detector. Three distinct effects can produce a correlation signal: the X-ray emission from galaxy themselves, the clustering of galaxies with discrete X-ray sources, and the clustering of galaxies with diffuse X-ray emission. It is likely that the plateau at large angles is due to the last effect through the residual diffuse X-ray emission from clusters of galaxies. We do not detect any significant clustering between discrete X-ray sources and galaxies. Using only the fields with non-cluster targets, we find that the mean X-ray intensity of APM galaxies in the .81-3.5 keV band is $(2.2 \pm 1.1) \times 10^{-6}$ cts s^{-1} arcmin^{-2}, corresponding to $1.5 \pm .8\%$ of the XRB intensity. The mean X-ray flux of galaxies with $\langle E \rangle = 17.5 \pm .3$ is then

[1]also at the Department of Physics, Columbia University

$(8.1 \pm 4.7) \times 10^{-16}$ ergs s^{-1} cm^{-2}. This agrees within 1σ with the X-ray flux expected from earlier direct studies of brighter, nearby galaxies, which were shown to result in a total integrated galaxy contribution to the XRB of about 13%. We discuss how this powerful cross-correlation method can be used to measure the flux of X-ray sources well below the detection limit of X-ray instruments, and, perhaps, to probe otherwise undetectable faint diffuse X-ray emission.

Subject headings: Cosmology: Diffuse Radiation - X-Rays: Galaxies - Galaxies: Statistics - X-Rays: General - Methods: Statistical

1. Introduction

In spite of significant recent progress, the nature of the cosmic X-Ray Background (XRB) remains one of the outstanding puzzles in astrophysics (for reviews, see Fabian & Barcons 1992; Zamorani 1995; De Zotti et al. 1995; Hasinger 1996). The observation of the distortion of the Cosmic Microwave Background spectrum with COBE (Mather et al. 1990) precludes the possibility that the hard XRB ($\epsilon \gtrsim 2$ keV) originates from a homogeneous diffuse hot plasma. The alternative explanation, namely a superposition of discrete sources, is supported, at least in the soft band ($\epsilon \lesssim 2$ keV), by deep ROSAT surveys (Hasinger et al. 1993; Vikhlinin et al. 1995a,b,c) in which about 60% of the XRB is resolved into discrete sources, of which, in turn, about 60% are AGN. However, reconciling the full phenomenology of the soft and hard XRB with known properties of AGN has led to several difficulties (Hasinger 1996). First, no single class of known objects has a spectrum consistent with that of the XRB. Also, the surface density of faint ROSAT sources is higher (Hasinger et al. 1993) than expected from the luminosity function of known AGN (Boyle et al. 1993). In addition, fluctuation analyses with GINGA and HEAO1 (Butcher et al. 1994; Mushotzky & Jahoda 1992) imply more sources in the hard band than expected from the ROSAT deep counts by a factor of 2-3.

New detailed unified AGN models stimulated by recent observations could provide a self-consistent solution (for a review, see Setti & Comastri 1996). Another possibility is that a new class of sources becomes important at low fluxes. It has been recently proposed that galaxies, whose fraction is observed to rise at faint fluxes in optical identifications of deep ROSAT surveys, could constitute this new class (Jones et al. 1995; Carballo et al. 1995; Boyle et al. 1995; Romero-Colmenero et al. 1996; see also Hasinger 1996).

One way to study the contribution of galaxies to the XRB in addition to the time-consuming optical-identifications, is to cross-correlate the XRB intensity with galaxy catalogs. A sensitive statistical measure of the correlation at a given angular lag θ is provided by the two-point cross-correlation function (CCF) $W_{xg}(\theta)$. The $\theta = 0$ value of W_{xg}, or "zero-lag" value, is often used, since, in most cases, most of the signal resides at small angles. However, the full correlation signal is provided by the "non-zero lag" ($\theta > 0$) sector of W_{xg}.

This approach was initiated by Jahoda et al. (1991) who computed W_{xg} at zero lag between 2-10 keV HEA0 1 A-2 maps of the XRB and the UGC and ESO galaxy catalogs. They found a significant correlation signal with an amplitude of $W_{xg}(0) = (3 \pm 1) \times 10^{-3}$, and concluded that as much as 50-70% of the XRB could be due to X-ray sources associated with present-epoch galaxies. Lahav et al. (1993) confirmed the correlation signal by applying the technique to 4-12keV GINGA maps of the XRB compared with the UGC and IRAS galaxy catalogs. However, they pointed out that a correct interpretation of the correlation requires taking source clustering into account. Their revised estimate of the fraction of the XRB due to a non-evolving population of X-ray sources spatially associated with local galaxies is $30 \pm 15\%$. From a careful modelling of the correlation found between the HEA0 1 A-2 maps and the IRAS galaxy catalog, Miyaji et al. (1994) derived a local X-ray emissivity which correspond to about 20% of the XRB without evolution and which can be accounted for by AGN alone (see also Barcons et al. 1995). A similar fraction (10-30%) was obtained by Carrera et al. (1995a,b) from a measurement $W_{xg}(\theta)$ at non-zero lag, between GINGA and several galaxy catalogs.

The aforementioned correlation studies were focused on the hard ($E > 2$ keV) XRB. Because only data from non-imaging X-ray instruments were available in this band, this work was restricted to rather large angular scales ($\theta > 1$ deg). In addition, only catalogs of bright, nearby galaxies were employed. More recently, Roche et al. (1995) detected a correlation signal between ROSAT-PSPC fields and faint galaxies ($B < 23$). The high angular resolution of ROSAT allowed them to probe small angular scales ($\sim 15''$). However, their consideration of only three ROSAT fields limited their statistics. By applying a detailed correlation formalism to the ROSAT results, Treyer & Lahav (1995) concluded that about 22% of the .5-2 keV XRB is due to faint galaxies with $18 < B < 23$.

In order to test these results at intermediate angular scales ($\sim 1'$) and with improved statistics, we have cross-correlated 62 *Einstein*-IPC fields with the APM Northern Galaxy catalog ($13.5 < E < 19$). To extract the full correlation information, we have computed both the zero and non-zero lag CCF. The improved statistics allows us to give a better estimate of the statistical uncertainty in the correlation signal. Several control experiments provide added confidence in the significance of our results. The *Einstein* energy band (.1-3.5 keV) is sufficiently broad for testing the energy dependence of the signal. In addition, we develop a simple, 2-dimensional formalism to interpret the angular dependence of W_{xg} which takes into account the Point Spread Function (PSF) of the imaging X-ray instrument.

This paper is organized as follows. We first describe the X-ray and galaxy data (§2). We then outline our procedure for measuring the correlation function estimator W_{xg} (§3). In §4, we present the zero and non-zero lag results, along with the analysis of the various control samples. We then present our interpretation formalism (§5) and discuss the implications of the detected correlation for the contribution of galaxies to the XRB (§6). The details of the calculations involved in the interpretation of W_{xg} are relegated to appendix A. In appendix B, we explicitly evaluate two multi-dimensional integrals which appear in this interpretation. Finally, a treatment of the statistics of W_{xg} is presented in appendix C. The zero-lag results have already been reported in a

brief form in Refregier et al. (1995).

2. Data

2.1. X-Ray

The original X-ray data consisted of northern (Dec.> $-5°$) *Einstein* Imaging Proportional Counter (IPC) fields (Giaconni et al. 1979) at high galactic latitude ($|b| > 25°$). We originally selected 77 random fields with typical exposure times greater than 5000 s. We avoided fields containing bright sources and/or large areas of diffuse emission. The mean exposure time was $\langle t_{exp} \rangle \simeq 1.4 \times 10^4$ s. In order to focus on the unresolved component of the XRB, sources were excised down to 3.5σ. This corresponds to a mean excision flux of $\langle S_{exc}(.81 - 3.5\mathrm{keV}) \rangle = (4.8 \pm .5) \times 10^{-14}$ ergs cm^{-2} s^{-1}. The source excision and flat-fielding procedures are described in Hamilton et al. (1991) and Wu et al. (1991). The type of target was recorded for each field and classified into four broad categories (see Table 1): galactic sources, extragalactic discrete sources (galaxies, QSO, etc), clusters (and superclusters) of galaxies, and deep fields. This allowed us, in particular, to study subsamples of fields with and without clusters of galaxies as targets.

The photons in each one-square-degree field where binned into $64''$ pixels. The Point-Spread Function (PSF) for the IPC is close to a gaussian with standard deviation $\sigma_{psf} \simeq .5'$. A typical X-ray field is shown as the grey-scale map in figure 1. The blank region in the $4'$-wide criss-cross pattern, due to the window support ribs, has been excluded from our analysis. We considered two energy bands: "soft" (.16-.81 keV) and "hard" (.81-3.50 keV). The hard band is to be considered as the data set of interest, whereas the soft band, which is dominated by emission from the Milky Way, is used as a control data set. In general, fields in the *Einstein* archive have different levels of contamination from solar X-rays scattered into the telescope by the residual atmosphere. This is parametrized by the Viewing Geometry (VG) flag with VG=1 (VG=3), corresponding to low (high) contamination. For the real data set, only exposures with relatively low solar contamination (VG=1-2) were considered. Another control data set was constructed by keeping higher solar contaminations (VG=2-3). Even though the low and high contamination data sets both contain VG=2 exposures and thus overlap, they can be compared to test the qualitative dependence of the correlation signal on solar contamination.

For the *Einstein*-IPC, counts result from several effects (Wu et al. 1991). The instrumental background due to cosmic-ray particle contamination and calibration source leakage amounts to $\langle i^{part} + i^{calib} \rangle = (1.1 \pm .1) \times 10^{-4}$ cts s^{-1} arcmin^{-2}. The latter and following intensities correspond to the hard band (.81-3.5 keV) and to the subset of our fields with targets other than galaxy clusters. The solar contamination for $VG = 2 - 3$ exposures is well described by a bremmstrahlung spectrum with $kT = .25$ keV and produces, on average, about $.19 \times 10^{-4}$ cts s^{-1} arcmin^{-2} (Wang et al. 1991). We thus estimate that, for $VG = 1 - 2$ exposures, this contribution produces $\langle i^{sol} \rangle = (.1 \pm .1) \times 10^{-4}$ cts s^{-1} arcmin^{-2}. The XRB, including the contribution from the Milky

Way, produces $\langle i^{XRB} \rangle = (1.4 \pm .1) \times 10^{-4}$ cts s^{-1} arcmin^{-2}. By integrating the number-flux relation measured by Gioia et al. (1990) in the context of the *Einstein* Medium Sensitivity Survey (EMSS), we estimate that the source excision mentioned above amounts to the removal of an average of $\langle i^{exc} \rangle = (.10 \pm .03) \times 10^{-4}$ cts s^{-1} arcmin^{-2}. (We have assumed a mean power law spectrum with index .7 for the sources and $N_H = 3 \times 10^{20}$ cm^{-2} to convert from the EMSS band). The final expected count rate is thus $\langle i \rangle \equiv \langle i^{part} + i^{calib} + i^{XRB} - i^{exc} \rangle = (2.5 \pm .3) \times 10^{-4}$ cts s^{-1} arcmin^{-2}. For our data set, we measure a mean intensity of $\langle i \rangle = (2.73 \pm .01) \times 10^{-4}$ cts s^{-1} arcmin^{-2}, consistent with the expected count rate.

2.2. Galaxies

The APM Northern Catalog (Irwin & McMahon 1992; Irwin et al. 1994) consists of scans of E and O Palomar Observatory Sky Survey (POSS-I) plates by the SERC Automatic Plate Measuring (APM) machine in Cambridge (Kibblewhite et al. 1984). Objects are assigned position coordinates, E and O apparent magnitudes, a morphological class and various morphological parameters. The objects in the raw APM object catalog were classified on the basis of a compactness parameter similar to that used by Maddox et al. (1990b). The morphological classes comprise stars, galaxies, noise and merged objects. The catalog includes objects down to $E \simeq 20$.

In this study, we rejected 10 fields which had abnormal patterns of galaxies due mostly to spurious object detections around bright stars. We only considered the E-plate objects with $13.5 < E < 19$. This choice maximized the performance of the automatic image classifier, and resulted in about 530 galaxies per degree square. In this magnitude range and in our latitude range, the number of stellar objects outnumber galaxies by a factor of about 5. In figure 1, a typical distribution of galaxies in this magnitude range is displayed as filled circles. The positional accuracy of the APM objects is better than one arcsecond. Being much smaller than our pixel size (64″), this uncertainty is negligible in our analysis. In order to avoid potential complications at POSS plate boundaries, we chose the field centers to lie further than 45′ from the plate edges. Catalogued stellar objects found in the same fields were used as a control data set.

It is useful to convert E-magnitudes into other magnitude systems. As was summarized by Koo & Kron (1992), the mean colors of galaxies is independent of magnitude for $b_J \lesssim 22$ and is close to $< b_J - r_f >_{gal} = 1.1 \pm .1$. Using figures 1 and 4 in Butcher & Oemler (1985), we infer that, for galaxies, $< B - R >_{gal} = 1.9 \pm .2$, $< B - V >_{gal} = 1.1 \pm .1$, and thus that $< V - R >_{gal} = .8 \pm .2$. By measuring the magnitudes of stellar standards with the Automated Plate Scanner, Humphreys et al. (1991) have shown that, for the POSS plates, $E - R \simeq -.011 + .148(V - R) + .058(V - R)^4$, for $-.2 < V - R < 1.7$. Assuming that this relation also holds for the APM measurements, the above colors translate to $< E - R >_{gal} = .3 \pm .2$, $< V - E >_{gal} = .5 \pm .3$, and $< B - E >_{gal} = 1.6 \pm .3$. Finally, figure 9 in Butcher & Oemler (1985), yields $< b_J - E >_{gal} = 1.1 \pm .3$.

The mean magnitude of our galaxy sample is given by $\langle E \rangle \equiv \int_{E_{min}}^{E_{max}} dE E \frac{dn}{dE} / \int_{E_{min}}^{E_{max}} dE \frac{dn}{dE}$,

where E_{min} and E_{max} are the magnitude limits of the sample, and $\frac{dn}{dE}$ is the mean number of galaxies per unit solid angle and per unit magnitude. In our sample, $E_{min} = 13.5$ and $E_{max} = 19$, as stated above. A fit to the number-magnitude relation in our sample yields $\log(dn/dE) \simeq -3.44 + .30E$ galaxies deg^{-2} (.5 mag)$^{-1}$, so that $\langle E \rangle \simeq 17.7$. However, our directly measured number-magnitude relation is flatter than the one measured for the southern APM catalog (Maddox et al. 1990), which after using the above $b_J - E$ conversion is well fitted by $\log(dn/dE) \simeq -8.8 + .6E$ galaxies deg^{-2} (.5 mag)$^{-1}$, for $E \lesssim 19$. This discrepancy is probably due to a systematic overcorrection for saturation for galaxy magnitudes. (The slope of the stellar APM counts *is* consistent with the stellar counts of Metcalf et al. 1991). The northern and southern APM counts agree if we use corrected APM magnitudes defined as $E' = 8.52 + .50E$. In this case, our sample limits are $E'_{min} = 15.3$ and $E'_{max} = 18.1$ and the mean magnitude becomes $\langle E' \rangle \simeq 17.4$. Given the uncertainty involved in this correction, we take our mean magnitude to be $\langle E \rangle \simeq 17.5 \pm .3$.

The contamination by misclassified objects in the APM galaxy catalog was estimated at bright magnitudes by direct visualization of 841 objects on five different POSS plates. The stellar contamination was observed to vary from plate to plate and as a function of magnitude, and is dominated by misclassified stars. The mean ratio of the number of true galaxies to the total number of objects classified as galaxies in the APM is $\langle N^g \rangle / \langle N \rangle \simeq .7 \pm .2$ for $15 \lesssim E \lesssim 16.5$ and tends to decrease with magnitude, at least in this magnitude range. Direct visualization for $E \gtrsim 16.5$ is unreliable. Using deeper AAT plates, Maddox et al. (1990b) estimate that, for the southern APM galaxy catalog, $\langle N^g \rangle / \langle N \rangle \simeq .95$, for $17 < b_J < 20$. We thus finally set $\langle N^g \rangle / \langle N \rangle \simeq .8 \pm .2$ as our estimate for magnitudes close to our mean $\langle E \rangle$.

2.3. Final Sample

From the resulting set of 67 fields, we removed overlapping fields giving preference to those with higher exposure times. This was done to avoid correlating the same region of the sky more than once. (Two fields overlapping by less than 15′ were left in the sample). The final field sample contained $N_f = 62$ fields which were labeled by their *Einstein* sequence numbers. Their center positions along with the associated POSS plate numbers, exposure times, *Einstein* target types, mean X-ray intensities, and mean galaxy surface densities are listed in table 1. Figure 1 shows one of the X-ray fields superimposed on the associated distribution of galaxies.

An additional control data set was generated by scrambling the X-ray/galaxy field pairs. To summarize, we considered the following data sets:

1. Hard-Galaxies: Hard-band (.81-3.5 keV) XRB (low solar contamination) crossed with galaxies: the real data set

2. Hard(Solar)-Galaxies: Hard-band XRB with high solar contamination crossed with galaxies

3. Soft-Galaxies: Soft-band (.16-.81 keV) diffuse emission (with a large Galactic component) crossed with galaxies

4. Hard-Stars: Hard-band XRB crossed with stars

5. Hard-Galaxies (Scrambled): As in set 1, but with scrambled field pairs.

The first data set is the principal ("real") data set. We should not detect any correlation for the scrambled set (set 5), since it involves pairs of unrelated regions of the sky. As mentioned above, the soft band XRB is dominated by X-rays from the Milky Way. Thus, for data sets 2 and 3, the fraction of the X-ray counts potentially correlated with galaxies is smaller than that for the real set; we therefore expect the correlation to be smaller for these two sets. Stars contribute a non-negligible fraction of the XRB: the fraction of stars optically identified in the *Einstein* Medium Sensitivity Survey (Stocke et al. 1991) and deep ROSAT XRB surveys (see Hasinger 1996, for a summary) are 26% and 15%, respectively. Given the significant (mostly stellar) contamination of the galaxy catalog, it is important to test whether stars contribute to the CCF. This is achieved by the use of data set 4. After binning galaxies (and stars) into 64″ pixels, the correlation analysis was performed in the same way for the five data sets. This provides a direct and powerful test of the physical and statistical significance of any resulting correlation signal.

3. Procedure

3.1. Correlation Function and Estimator

Our main goal was to estimate the two-point angular cross-correlation function w_{xg} for the two data sets described above. This function is a sensitive measure of correlations between two-dimensional data sets (see eg., Peebles 1980; Jahoda et al. 1991). To define w_{xg}, let us consider two infinitesimal cells C_1 and C_2 with solid angles $\delta\Omega_1$ and $\delta\Omega_2$ with angular separation θ_{12}. Let δN_1 be the number of of galaxies in C_1, and δI_2 be the XRB flux (in ergs cm^{-2} s^{-1}) in C_2. Then, w_{xg} is defined by

$$< \delta N_1 \delta I_2 >= \langle n \rangle \langle i \rangle \, [1 + w_{xg}(\theta_{12})] \, \delta\Omega_1 \delta\Omega_2, \tag{1}$$

where $\langle n \rangle$ is the mean number of galaxies per sr and $\langle i \rangle$ is the mean XRB intensity (in ergs cm^{-2} s^{-1} sr^{-1}), and the brackets denote a sky average. By taking $\delta\Omega_1$ to be sufficiently small, one can show that equation (1) implies that $w_{xg}(\theta)$ is the mean fractional excess in the XRB intensity at an angle θ from a given galaxy.

In practice, measurement cells have a finite size and one can not measure w_{xg} directly. Instead, one computes the finite-cell estimator W_{xg} defined as

$$W_{xg}(\theta) \equiv \frac{\eta(\theta)}{\langle N \rangle \langle I \rangle} - 1, \tag{2}$$

where $\langle N \rangle$ and $\langle I \rangle$ are the number of galaxies and the XRB flux averaged over all available cells. The quantity $\eta(\theta)$ in the numerator is defined by

$$\eta(\theta_{12}) \equiv \langle N_1 I_2 \rangle_{\theta_{12}}, \tag{3}$$

where the bracket denotes the product of N and I averaged over cell C_1 and C_2 with a angular separation θ_{12}. (Our data set, which consists of many disjoint fields, was analyzed with the specific averaging scheme described in §3.2.) In general, W_{xg} depends on the cell size α and can thus be thought of as being a function of two variables: $W_{xg} = W_{xg}(\alpha, \theta)$. If the XRB and the galaxy counts are uncorrelated, $\eta(\theta) = \langle N \rangle \langle I \rangle$ and thus $W_{xg} = 0$. On the other hand if they are correlated (anticorrelated) W_{xg} is positive (negative).

Formally, the correlation function w_{xg} is equal to the estimator W_{xg} for infinitely small cell size, i.e.

$$w_{xg}(\theta) = \lim_{\alpha \to 0} W_{xg}(\alpha, \theta). \tag{4}$$

Conversely, W_{xg} is obtained from w_{xg} as

$$W_{xg}(\alpha, \theta_{12}) = \frac{1}{2\pi\alpha^4} \int d\phi_{12} \int_{C_1} \int_{C_2} d\Omega_1' d\Omega_2' w_{xg}(\theta_{12}'), \tag{5}$$

where the $d\Omega_i'$ integrals are over two cells C_1 and C_2 separated by an angle θ_{12} with polar coordinates (θ_{12}, ϕ_{12}) in a coordinate system whose origin is the center of C_1. The $d\phi_{12}$ integral operates as an average over all possible relative positions of the two cells while keeping their separation θ_{12} constant. We have taken the cells to be be squares with sides α. Equation (5) can be derived by subdividing the two cells into infinitesimal subcells and by using equation (1) in equation (2).

3.2. Implementation

In our experiment, our minimal cells are the X-ray pixels: squares with a side length of $\alpha_p = 64''$. The galaxies (and the stars) were also binned into such pixels. All invalid pixels, i.e. pixels under the support ribs or outside the *Einstein* field were ignored. We varied the cell size α by binning adjacent pixels together. Boundary cells, i.e. cells lying across the field edge or across the ribs, were rejected if less than 33% of their area were valid. The choice for this threshold was rather arbitrary and reflected a tradeoff between wasting pixels and having too many cells with large uncertainties. A moderate variation of this threshold (between 20% and 60%) did not affect our results significantly. We thus obtained values of W_{xg} at zero-lag for cell sizes $\alpha = n\alpha_p$, where n is an integer. We only considered one-pixel cells ($\alpha = \alpha_p$) for our non-zero lag measurements.

For each field, we computed $\eta(\theta)$ (Eq. [3]) as follows

$$\eta(\theta) = \frac{1}{N_c} \sum_{i=1}^{N_c} \frac{1}{N_c(i,\theta)} \sum_{j=1}^{N_c(i,\theta)} I_i N_j, \tag{6}$$

where N_c is the total number of cells in the field, I_i is the X-ray flux in C_i, and N_j is the number of galaxies in C_j. The first sum runs over all cells in the field. The second sum runs over all $N_c(i,\theta)$ cells C_j a distance θ away from C_i.

This estimate is slightly different from the more standard one (see e.g. Carrera et al. 1995a,b) which consists in directly averaging $I_i N_j$ over all pairs of cells (C_i, C_j) separated by an angle θ. These two definitions agree in the limit of an infinite field size. For a field of finite size, our definition provides a consistent treatment of boundary cells. For the scrambled data set, the "standard" definition yielded small but significant correlation at large angle, where the finite field effect is most significant. These spurious correlations were absent when we used the definition of equation (6). We also note that, even though the roles of I_i and N_j are not formally symmetric in equation (6), an inversion of N and I did not noticeably affect our measurements.

Both the X-ray and the galaxy data were subject to field-to-field variations due to differences in particle background contamination, solar X-ray contamination, plate sensitivity, seeing, etc. As a result, the fields could not be treated as a single data set. Since, in fact, we intend to focus on angular separations much smaller than the field size ($\theta \ll 1°$), we have instead computed W_{xg} for each field separately. As we will see in §4.1, the distribution of W_{xg} is not gaussian. However, by the central limit theorem, the distribution of the average of W_{xg} over all fields is close to gaussian. A detailed description of the statistics of W_{xg} is given in appendix C. Our final values and 1σ error estimates were thus be taken be

$$W_{xg} \pm \delta W_{xg} \equiv \frac{1}{N_f} \sum_{f=1}^{N_f} W_{xg,f} \pm \frac{1}{\sqrt{(N_f)}} \sigma_{rms}(W_{xg}), \tag{7}$$

where $W_{xg,f}$ is the value of W_{xg} for the f'th field, and σ_{rms} is the r.m.s. standard deviation computed over all fields. For the scrambled data set, we constructed $N_{scramble} = 400$ and 200 field pairs for the zero and non-zero lag measurements, respectively. This large number reduces the uncertainty in the mean and in the r.m.s. standard deviation. The final error estimate for the scrambled data set was normalized to N_f.

4. Results

4.1. Zero-Lag Results

As we will see below, most of the correlation signal lies at $\theta = 0$. We therefore first consider the zero-lag results in great detail in order to assess the reality and uncertainty of the signal.

Table 1 gives our measured values of $W_{xg}(\alpha_p, 0)$ in each field for the real data set. Figure 2 shows the distribution of $W_{xg}(\alpha_p, 0)$ in histogram form for the real data set. For comparison, a subset of the scrambled data set containing N_f fields is also shown. There is a small but significant positive offset in the real values which yield a correlation of $W_{xg}(\alpha_p, 0) = .045 \pm .013$, with a

significance of 3.5σ. As noted above, the distribution of W_{xg} is clearly non-gaussian for the real data set. This is not surprising since η (Eq. [3]) is the product of two random variables and is thus expected to follow a skewed distribution. The origin of unusually high correlations for several outlyer fields will be discussed in detail in §4.4. Here, we simply note that, after the removal of the six fields with $W_{xg} > .17$, the mean correlation is $W_{xg}(\alpha_p, 0) = .020 \pm .008$, which is now significant at the 2.4σ level. The scrambled set yields a correlation of $W_{xg} = -.001 \pm .008$ which, as expected, is consistent with zero.

Figure 3 shows $W_{xg}(\alpha_{cell}, 0)$ with cell sizes ranging from α_p to $8\alpha_p$ for each of the five data sets. The mean values and their associated errors are listed in table 2. Although the measurements at different cell sizes are not independent, their comparison gives a measure of the robustness of the signal. The real data set yields a positive correlation for all values of α shown. The solar-contaminated and Soft-Galaxies data sets yield lower correlations. As we noted above, this is expected since the large contribution of solar and Galactic X-rays, in each case respectively, results in a smaller relative contribution of the XRB to the observed intensity.

We do not detect any significant correlation between stars and the hard-band XRB. This is somewhat surprising since the contribution of stars to the XRB in ROSAT deep surveys is about 15% (Hasinger 1996), and since stars outnumber galaxies by a factor of about five in our magnitude range. The absence of correlation could be due to the soft nature of characteristic stellar spectra which mitigate their contribution in the hard band. We leave a quantitative discussion of the limits our analysis can place on mean stellar X-ray fluxes and on their contribution to the XRB to future work. The importance of this result in the context of our study of galaxies and the XRB is that it simplifies the interpretation of W_{xg}. We can indeed safely assume that misclassified stars contaminating our galaxy sample do not contribute to the correlation signal.

As expected, the scrambled data set yields correlation values consistent with zero for all α's. It is worth noting that the uncertainty for the scrambled set ($\delta W_{xg}(\alpha_p, 0) \simeq .008$) represents about 38% of the variance (i.e. the square of the standard deviation) for the real set ($\delta W_{xg}(\alpha_p, 0) \simeq .013$). In general, two effects contribute to the variance of W_{xg}: the intrinsic variation in the correlation signal from one region of the sky to another, and the statistical uncertainty involved in measuring W_{xg} in finite fields. If we take the variance for the scrambled set to be representative of the latter effect, we conclude that the intrinsic field-to-field variation represents about 62% of the variance of W_{xg}. One must therefore be cautious when using bootstrap error estimates since these do *not* account for the intrinsic variance.

As a further test of the reality of the signal, we plotted W_{xg} versus various related parameters in figure 4. No obvious correlations exists between W_{xg}, the mean number of galaxies, the mean XRB flux, Galactic latitude, or the X-ray exposure time. This indicates that our signal does not suffer from major systematic biases.

4.2. Non-Zero-Lag Results

Now that we have established the existence of a significant signal at zero-lag, we can obtain the full correlation information by studying W_{xg} at nonzero-lag. Figure 5 shows our measurement of $W_{xg}(\alpha_p, \theta)$ as a function of θ. The results are shown both for the real and the scrambled data sets. The mean values of W_{xg} and their error bars are listed in table 3 for each value of θ.

As noted above, most of the signal in the real data set lies at small angles ($\theta < 3'$). The scrambled set yields correlations consistent with zero, as expected. The striking feature in figure 5 is the presence of a significant plateau for $\theta \gtrsim 4'$ with an amplitude of $W_{xg}(\alpha_p, \theta \gtrsim 4') \simeq .015$. We will discuss its nature in §4.4.

In figure 6, we plotted the values of W_{xg} at $\theta = 10\alpha_p$ against that at $11\alpha_p$ for each field. A correlation (of the correlation function!) is clearly present. This shows that our measurements of W_{xg} at different values of θ are not statistically independent. This is due to the fact that the PSF (and perhaps the clustering scale) extends beyond one pixel. This correlation must be taken into account when estimating errors or when fitting to the angular dependence of W_{xg}. In appendix C we present a treatment of this correlation using multi-variate gaussian statistics. In particular, we show how one can estimate the covariance matrix $V_{i,j}$ of $W_{xg}(\alpha_p, \theta_i)$ from our data. The resulting values for the elements of $V_{i,j}$, shown in figure 13, demonstrate that the correlation effect is most severe for $\theta \lesssim 3\alpha_p$ and for $\theta \gtrsim 8\alpha_p$.

4.3. Comparison of Zero-Lag and Non-Zero Lag Results

We now consider a comparison of the zero and non-zero lag signals. This is not only a check of the consistency of our results but also allows us to verify the reality of the correlation at large angle which should contribute to the zero-lag correlation for large cell sizes.

For this comparison, we choose a phenomenological form for the underlying correlation function w_{xg} which reproduces the nonzero-lag results and check that it is consistent with the zero-lag results. We take $w_{xg}(\theta)$ to be the sum of a gaussian and a constant, i.e.

$$w_{xg}(\theta) = a_0 + a_1 e^{-\frac{1}{2}(\theta/\theta_0)^2}, \tag{8}$$

where a_0, a_1 and θ_0 are constants. The estimator W_{xg} can then be computed by introducing equation (8) in equation (5). We obtain

$$W_{xg}(\alpha, \theta) = a_0 + a_1 \Lambda(\alpha, \theta_0, \theta) \tag{9}$$

where Λ is the integral defined in equation (B1). A semi-analytical expression for Λ is given in appendix B.1 and its angular dependence is plotted in figure 12 for $\alpha = \alpha_p$ and $\theta_0 = 0'.5$.

Our best fit parameters for $W_{xg}(\alpha_p, \theta)$ at nonzero-lag are $a_0 = .013$ and $a_1 = .087$. For convenience, we fixed $\theta_0 \equiv \sigma_{psf} = 0'.5$. The result of the fit is shown in figure 5 as the dot-dashed

curve. The resulting cell size dependence of W_{xg} at zero-lag is shown in figure 3, as a similar curve. The agreement is acceptable even though the measured values of W_{xg} are slightly higher than the one inferred from the non-zero lag results. This is probably due to the ambiguity in the treatment of boundary cells (see discussion in §3.2). (In fact, a variation of the pixel inclusion threshold can slightly improve the agreement). Note also that the zero-lag measurements confirms the presence of a significant correlation all the way up to $\alpha \simeq 8'$, which corresponds to $\theta \simeq 4'$.

4.4. Correlation at Large Angles

The plateau in W_{xg} at large angle is rather surprising. Its reality is confirmed both by the scrambled results and by the fact that it appears consistently both in the zero and non-zero lag measurements (at least for $\theta \simeq 4'$).

In previous studies (Lahav et al. 1993; see also the other cross-correlation studies discussed in §1), the correlation signal was taken to arise from two terms in the correlation function: the "Poisson" term and the "clustering" term. The Poisson term corresponds to the case of the galaxies themselves emitting X-rays, and the clustering term corresponds to the spatial clustering of galaxies with discrete X-ray sources. As we will see in detail in §5, these two terms produce, in our context, correlation signals with specific angular dependence given by the two functions Λ and Ξ displayed in figure 12. For both terms, W_{xg} falls off for $\theta \gtrsim 4'$ and thus can not produce the plateau observed in our measurement. This can be seen more quantitatively in figure 5 where the dotted curve correspond to the best fit to the Poisson + clustering terms (see §5.3). The fit is poor for $\theta \gtrsim 4'$.

One possibility is that the plateau is due to the hot X-ray gas in clusters of galaxies. Diffuse emission from the clusters in our fields is mostly, but not completely, removed by our point source excision algorithm and can thus contribute signal to the very sensitive CCF. An example is provided by the field displayed in figure 7. This field has the highest zero-lag value of W_{xg} in our data set (i.e. it is the right-most field in figure 2). A cluster of galaxies appears as an excess in residual X-rays and in the surface density of galaxies in the upper left-hand corner of the field. Bright nearby clusters have typical X-ray sizes of about $10'$, a scale which is consistent with the scale of the plateau. Note that the field displayed in figure 7 is extreme; most fields in our data set, including those with cluster targets, such as the one in figure 1, do not show any obvious cluster emission. A search of the NED database (Helou et al. 1991), indeed reveals that only three of the cluster-target fields have an X-ray detected cluster within a radius of $20'$ of the field center.

To test this hypothesis we use the fact that 29 out of our 62 fields had clusters of galaxies as their *Einstein* targets. These are flagged with a target type of 3 in table 1. (Fields with superclusters as targets often contain clusters of galaxies and were thus also included). In figure 8, we show the value of W_{xg} at $\theta = 0$ vs. that at $\theta = 7\alpha_p$ with different symbols for fields with cluster and with non-cluster targets. The value of $W_{xg}(\alpha_p, 7\alpha_p)$ is taken to be representative of

the plateau for each field and is listed in table 1. As can be seen in this figure, the zero-lag value has little relation to the presence of a cluster, except for a few outlyers. This is in contrast with the non-zero lag values which are significantly larger for cluster target fields. The values of W_{xg} as a function of θ for each of the cluster and non-cluster data sets are listed in table 3. At zero-lag, the non-cluster fields yield a mean correlation of $W_{xg}(\alpha_p, 0) = .029 \pm .013$, a significance of 2.2σ. In figure 9, the mean W_{xg} is shown separately for cluster and non-cluster fields. The value for all fields combined is redisplayed for comparison. In spite of the somewhat degraded statistics, it is clear that the plateau is virtually absent for non-cluster target fields, whereas it is enhanced for cluster target fields. This suggests that the plateau is indeed caused by the residual diffuse X-ray emission in clusters of galaxies.

5. Interpretation of the Correlation Function

Now that we have established the existence of a positive correlation signal for our data set, we need to interpret its angular dependence and thus infer information about galaxies and the XRB. For this purpose, Treyer & Lahav (1995) have developed a detailed formalism which involves a projection of the 3-dimensional CCF into 2-dimensions. Here, we consider a similar but fully 2-dimensional approach. This has the advantage of being simple and of involving few model parameters. In addition, we include the effect of the PSF of the X-ray imaging detector. The formalism presented in §5.1 is general and can be adapted to any measurement of the CCF between an imaged diffuse background and a population of discrete sources. After applying this formalism to our specific case in §5.2, we compare its prediction with our non-zero lag measurements in §5.3

5.1. Formalism

In general, the total X-ray flux $I_j \equiv I_j^x$ measured in a cell C_j can be decomposed into

$$I_j^x = I_j^i + I_j^p + I_j^d, \tag{10}$$

where the terms, correspond to the instrumental background (i) (due to cosmic ray interactions, calibration source leakage, and solar-scattered X-rays), the emission from point X-ray sources (p), and the diffuse component of the XRB (d), from left to right respectively. A source is considered discrete if its solid angle is negligible compared to the PSF and to the cell size. Thus, in our situation, the diffuse component of the XRB includes the emission from the intracluster gas in nearby clusters of galaxies. We can also decompose the galaxy catalog object counts $N_j \equiv N_j^o$ in C_j as

$$N_j^o = N_j^g + N_j^s \tag{11}$$

where N_j^g is the number of galaxies (g) in C_j and N_j^s is the number of spurious objects (s) misclassified as galaxies.

Introducing equations (10) and (11) in equation (3), we obtain

$$\eta = \eta_{is} + \eta_{ps} + \eta_{ds} + \eta_{ig} + \eta_{pg} + \eta_{dg} \tag{12}$$

where $\eta_{ab}(\theta) \equiv \langle I_i^a N_j^b \rangle_{\theta_{ij}=\theta}$. As before, the brackets refer to an average over cells separated by an angle θ.

Since the galaxy catalog and the X-ray maps were constructed independently, I^i and N^o are not correlated. Thus, $\eta_{is} + \eta_{ig} = \langle I^i \rangle \langle N^s \rangle + \langle I^i \rangle \langle N^g \rangle$.

As we noted in §4.1, stars are not significantly correlated with the XRB intensity, at least in our experimental conditions. Other misclassified objects such as plate flaws are obviously not correlated with the XRB. We thus obtain $\eta_{ps} + \eta_{ds} = \langle I^p \rangle \langle N^s \rangle + \langle I^d \rangle \langle N^s \rangle$.

We have seen in §4.4 that the diffuse component of the XRB is likely to affect the CCF. An analysis of the diffuse term would involve a modelling of clusters of galaxies and of their redshift distribution. This is beyond the scope of the present study. We therefore leave η_{dg} unexpanded. In §5.3, we will show how we can nevertheless proceed using the subset our measurements for non-cluster target fields.

We are left with $\eta_{pg}(\theta)$ to evaluate. For this purpose, we define the PSF, ψ, so that a point source with flux S_p, placed at $\boldsymbol{\theta}_p$, produces an observed X-ray intensity at $\boldsymbol{\theta}_o$ given by

$$i(\boldsymbol{\theta}_o) = S_p \psi(\theta_{op}). \tag{13}$$

We assume that $\psi(\boldsymbol{\theta})$ is azimuthally symmetric so that it only depends on $\theta \equiv |\boldsymbol{\theta}|$. This definition implies that ψ is normalized so that

$$\int_S d\Omega_s \psi(\theta_s) = 1, \tag{14}$$

where the integral is over the whole sky.

The derivation of η_{pg} using this definition of ψ is given in detail in appendix A. The result consists of the two standard terms (see eg. Treyer & Lahav, 1995) modified to include the effect of the PSF: the "Poisson" term (Eq. [A5]) and the "clustering" term (eq. [A10]). Introducing these results into equations (12) and (2), we finally obtain

$$W_{xg} = W_{xg}^{\rm poisson} + W_{xg}^{\rm clustering} + W_{xg}^{\rm diffuse}, \tag{15}$$

where

$$W_{xg}^{\rm poisson}(\theta_{12}) = \frac{\langle I^g \rangle}{\langle I \rangle \langle N \rangle} \frac{1}{2\pi\alpha^2} \int_0^{2\pi} d\phi_{12} \int_{C_1} d\Omega_1' \int_{C_2} d\Omega_2' \psi(\theta_{12}') \tag{16}$$

and

$$W_{xg}^{\rm clustering}(\theta_{12}) = \frac{\langle I^p \rangle \langle N^g \rangle}{\langle I \rangle \langle N \rangle} \frac{1}{2\pi\alpha^4} \int_0^{2\pi} d\phi_{12} \int_{C_1} d\Omega_1' \int_{C_2} d\Omega_2' \int_S d\Omega_s' \overline{w}_{pg}(\theta_{1s}') \psi(\theta_{2s}'). \tag{17}$$

In the two equations above, the $d\Omega_1'$ and $d\Omega_2'$ integrals are over two cells C_1 and C_2 separated by $\boldsymbol{\theta}_{12}$. The $d\Omega_s'$ integral is over the whole sky (S). The brackets denote an average over all available

cells. The function $\overline{w}_{pg}(\theta)$ is the effective CCF between the positions of point X-ray sources and galaxies. It is defined in equation (A9) as the X-ray flux-weighted average of the flux-dependent CCF w_{pg}. That such an averaging is necessary is not surprising since, after all, the X-ray point sources with fluxes just below the excision threshold dominate the anisotropy of the observed XRB and are thus the one most susceptible to producing a correlation with the galaxies. As noted above, the term $W_{xg}^{\rm diffuse} \equiv (\eta_{dg} - \langle I^d \rangle \langle N^g \rangle)/(\langle I \rangle \langle N \rangle)$ is left unexpanded.

As can be inferred from inspecting their functional form, the three terms above correspond to three distinct effects responsible for a correlation between the XRB and galaxies:

1. Poisson: the galaxies emit X-rays.
2. Clustering: the galaxies are spatially clustered with discrete X-ray sources.
3. Diffuse: the galaxies are spatially clustered with diffuse X-ray emission.

5.2. Application

We can now apply the above formalism to our specific case. For the *Einstein*-IPC, the PSF is gaussian so that, after normalization (Eq. [14]),

$$\psi(\theta) \equiv \frac{1}{2\pi\sigma_{psf}^2} e^{-\frac{1}{2}(\theta/\sigma_{psf})^2} \tag{18}$$

To proceed, we need to know the angular dependence of $\overline{w}_{pg}$ which describes the clustering of galaxies with point X-ray sources. Information about the clustering of sources can be deduced from the measurement of their Auto-Correlation Function (ACF). The angular ACF w_{gg} of galaxies in the southern APM catalog is well described by a power law of the form $w_{gg}(\theta) = (\theta/\theta_{gg})^{-\beta_{gg}}$ in the range $.01° < \theta < 1°$ (Maddox et al. 1990a). The slope was measured to be $\beta_{gg} = .668$ and is magnitude-independent. On the other hand, the correlation amplitude θ_{gg} does depend on magnitude and ranges from about $10''$ to $151''$ for $B_J \simeq 20$ and 17.5, respectively. Such a scaling of the ACF with magnitude is expected from the projection the spatial ACF into 2-dimensions (Groth & Peebles, 1997; Phillips et al. 1978). Vikhlinin & Forman (1995) studied the clustering of ROSAT X-ray sources with a .5-2 keV flux lower limit of about 10^{-14} ergs cm^{-2} s^{-1}, close to our flux excision limit S_{exc}. They found that the ACF of ROSAT point X-ray sources, w_{pp}, also follows a a power law with a slope of $\beta_{pp} = .7 \pm .3$ and a normalization of $\theta_{pp} = 4''$ for θ between $30''$ and $1000''$.

The two slopes β_{gg} and β_{pp} are both consistent with the value $\beta \simeq .7$. It is thus reasonable to assume that the magnitude-dependent CCF, w_{pg}, defined in equation (A7) is also described by a power law of the form: $w_{pg}(S^p, S^g; \theta) = (\theta/\theta_{pg}(S^p, S^g))^{-\beta}$, where S^p and S^g are the X-ray and optical fluxes of the point X-ray sources and galaxies, respectively, and $\beta \simeq .7$. Since the flux

dependence of w_{pg} is limited to its normalization $\theta_{pg}(S^p, S^g)$, we can factor the θ dependence of $\overline{w}_{pg}$ out of the integrals in equation (A9) and obtain

$$\overline{w}_{pg}(\theta) = \left(\frac{\theta}{\overline{\theta}_{pg}}\right)^{-\beta}, \tag{19}$$

where $\overline{\theta}_{pg}$ is left as a free parameter to be determined.

With the specific functional forms of equations (18) and (19), equation (16) becomes

$$W_{xg}^{\rm poisson}(\alpha,\theta) = \frac{\langle I^g\rangle}{\langle I\rangle\langle N\rangle}\frac{\alpha^2}{2\pi\sigma_{psf}^2}\Lambda(\alpha,\sigma_{psf},\theta), \tag{20}$$

while equation (17) becomes

$$W_{xg}^{\rm clustering}(\alpha,\theta) = \frac{\langle I^p\rangle\langle N^g\rangle}{\langle I\rangle\langle N\rangle}\left(\frac{\alpha}{\overline{\theta}_{pg}}\right)^{-\beta}\Xi(\alpha,\sigma_{psf},\beta,\theta), \tag{21}$$

where Λ and Ξ are the integrals defined in equations (B1) and (B8), respectively. In Appendix B we describe our semi-analytic evaluation of Λ and our numerical evaluation of Ξ. The functions are both displayed in figure 12. Two useful analytical fits to Λ and Ξ for the parameters relevant to the present study are given in equations (B7) and (B9), and are also displayed on this figure. (The analytical fit for Λ is indistinguishable from Λ itself on the figure.)

5.3. Fit Results

Our remaining task is to compare our theoretical expectations with our measurement of the CCF. The three terms contributing to W_{xg} have different angular dependences and can thus, at least in principle, be isolated by a fitting to measurements of W_{xg} at different values of θ.

As we noted in §4.4, the Poisson and clustering terms can not produce the plateau observed for the combined cluster plus non-cluster data set. The best fit parameters to a combination of the poisson term and the clustering term (see Eq. [22] below) are $a_{\rm poisson} = 0$ and $a_{\rm clustering} \simeq .05$. (The two parameters are constrained to be positive). The best fit is shown in figure 5 as the dotted curve. As we already noted, the fit is poor for $\theta \gtrsim 4'$.

Given the disappearance of the plateau when only non-cluster target fields are considered (see §4.4), it is likely that the plateau is due to residual diffuse X-ray emission from clusters of galaxies which contribute to W_{xg} through the diffuse term. Although we do not pursue this here, it would be worthwhile to model such diffuse emission and to derive the expected angular dependence of $W_{xg}^{\rm diffuse}$.

Let us now focus on the non-cluster target fields for which the plateau is virtually absent. If we *assume that the diffuse term is negligible for the non-cluster data set*, we are left to fit

$W_{xg}(\alpha,\theta)$ to the following function

$$W_{xg}(\alpha,\theta) = a_{\rm poisson}\Lambda(\alpha,\sigma_{psf},\theta) + a_{\rm clustering}\Xi(\alpha,\sigma_{psf},\beta,\theta), \tag{22}$$

where $a_{\rm poisson}$, and $a_{\rm clustering}$ are free parameters. So as to reduce the number of free parameters, we fix $\beta = .7$ in accordance with the discussion in §5.2.

We have noticed in §4.2, that the measurements of W_{xg} at different values of θ are not statistically independent. In appendix C, we describe our procedure for the fit (Eq. [C5]) assuming that the set of values of W_{xg} follow a multi-variate gaussian distribution (Eq. [C1]). The covariance matrix (Eq. [C2]) is estimated from the data (Eq. [C4]) and is displayed in figure 13.

The result of the fit to our measurement of $W_{xg}(\alpha_p,\theta)$ for $0 \leq \theta \leq 8\alpha_p$ are displayed in figure 10. This figure shows the constant probability contours of χ^2 (Eq. [C7]) with $9 - 2 = 7$ degrees of freedom. We have used the analytical fits for Λ and Ξ given in equations (B7) and (B9), respectively. The best fit (Eq. [C8]) occurs for $a_{\rm poisson} = .04 \pm .02$ and $a_{\rm clustering} = .005 \pm .004$. The errors correspond to the 1σ estimates for each parameter taken separately (Eq. [C10]) and are also displayed on figure 10. The resulting best fit is displayed as the solid line in figure 9.

The value of χ^2 for the best-fit parameters is 5.1. The fit is thus acceptable. It worth noting that a fit which does *not* takes the covariance of W_{xg} into account (i.e. one for which the covariance matrix $\mathbf{V}$, in Eq. [C2], is diagonal) yields $\chi^2 \simeq 2.1$ which correspond to a fit which is "too good". The covariance of W_{xg} must therefore be taken into account in order not to underestimate the measurement errors.

By comparing equations (20) and (21) with equation (22), we can deduce the following physical quantities

$$\langle I^g \rangle = \frac{2\pi\sigma_{psf}^2}{\alpha^2}\langle N\rangle\langle I\rangle a_{\rm poisson} \tag{23}$$

and

$$\overline{\theta}_{pg} = \alpha\left(\frac{\langle I\rangle\langle N\rangle}{\langle I^p\rangle\langle N^g\rangle}\right)^{\frac{1}{\beta}} a_{\rm clustering}^{\frac{1}{\beta}}. \tag{24}$$

Our measurements for the non-cluster data set yield $\langle N\rangle = .149 \pm .002$ objects per cell and $\langle I\rangle = (3.11 \pm .01) \times 10^{-4}$ cts s^{-1} per cell. From our estimates in section 2, we have $\langle N^g\rangle/\langle N\rangle = .8 \pm .2$ and $\langle I^{XRB}\rangle/\langle I\rangle = .6 \pm .1$. If we assume that the diffuse component of the XRB is negligible, we can set $\langle I^p\rangle \simeq \langle I^{XRB}\rangle$. (Alternatively, any difference between $\langle I^p\rangle$ and $\langle I^{XRB}\rangle$ can be absorbed in the definition of $\overline{\theta}_{pg}$). With these numerical values and setting $\alpha = \alpha_p$, we obtain $\langle i^g\rangle = (2.2 \pm 1.1) \times 10^{-6}$ cts s^{-1} arcmin^{-2} and $\overline{\theta}_{pg} = .10 \pm .16$ arcsec. The errors correspond to 1σ. The implication of these final values are discussed in the next section.

6. Galaxies and the X-Ray Background

6.1. Clustering

Let us first consider our measurement for the galaxy/X-ray-sources clustering amplitude $\overline{\theta}_{pg}$. Our value for $\overline{\theta}_{pg}$ is consistent with 0 at the 1σ level. Note that negative values of $\overline{\theta}_{pg}$ are of course unphysical and are thus excluded. Therefore, we do not detect any significant clustering between discrete X-ray sources and galaxies. Our value for $\overline{\theta}_{pg}$ can thus be interpreted as an upper limit.

As we noted in section 5.2, the amplitudes for the auto-correlation of galaxies (Maddox et al. 1990a) and of ROSAT X-ray sources (Vikhlinin & Forman 1995) are $10'' < \theta_{gg} < 151''$ (for $20.5 > b_J > 17.5$), and $\theta_{pp} \simeq 4''$, respectively. Our value $\overline{\theta}_{pg} = .10 \pm .16$ arcsec is thus considerably smaller than these two amplitudes. In our analysis, we are in effect cross-correlating two population of sources with different mean X-ray flux: the X-ray sources dominated by the sources just below the excision flux limit S_{exc} (i.e. mostly AGN at $z > .2$), and the galaxies (at $z \lesssim .2$), which, as will will see below, have a much smaller mean X-ray flux. Thus, it is not surprising that our cross-correlation clustering amplitude be smaller than the two associated auto-correlation clustering amplitudes.

6.2. X-ray Emission from Galaxies

The statistical significance of our detection for the Poisson term is also low: our measurement of $\langle i^g \rangle$ is only 2σ away from 0. This can easily be improved by performing the analysis with a larger number of fields. We can nevertheless draw several useful conclusions from our measurement.

Using our estimation of $\langle I^{XRB} \rangle$ (see section 2), we deduce that the fraction of the XRB contributed by APM galaxies with $13.5 < E < 19$ is $\langle I^g \rangle / \langle I^{XRB} \rangle = .015 \pm .008$ in the hard (.81-3.5 keV) band. This fraction should not be mistaken for the total contribution of APM-like galaxies distributed over all space.

The mean X-ray flux of the catalogued galaxies is easily computed to be $\langle S^g \rangle \equiv \langle i^g \rangle / \langle n^g \rangle = (2.1 \pm 1.1) \times 10^{-5}$ cts s^{-1} in the hard band. The X-ray spectra of galaxies can described by a thermal bremsstrahlung model with $kT \sim 1 - 2$ keV and $kT \gtrsim 5$ keV, for ellipticals and spirals, respectively (Kim et al. 1992). If we adopt such a model with $kT = 3 \pm 2$ keV and $N_H \simeq 3 \times 10^{20}$ cm^{-2}, the above flux corresponds to $\langle S^g(.81 - 3.5\text{keV}) \rangle = (8.1 \pm 4.7) \times 10^{-16}$ ergs cm^{-2} s^{-1}. In the more conventional *Einstein* and ROSAT bands, this corresponds to $\langle S^g(.2 - 4.0\text{keV}) \rangle = (9.1 \pm 5.0) \times 10^{-16}$ and $\langle S^g(.5 - 2.0\text{keV}) \rangle = (5.4 \pm 3.0) \times 10^{-16}$ ergs cm^{-2} s^{-1}, respectively. We note that this flux is three orders of magnitude below the flux limit of the *Einstein* Medium Sensitivity survey ($\sim 10^{-13}$ ergs s^{-1} cm^{-2} in the .2-4 keV band; see Gioia et al. 1990) and more than one order of magnitude below those for deep ROSAT surveys with mostly complete optical identifications ($\sim 10^{-14}$ ergs s^{-1} cm^{-2} in the .5-2 keV band; see Hasinger 1996). This is of course a consequence of the statistical nature of our measurement.

It is noteworthy that $\langle S^g \rangle$ is about two orders of magnitude below the discrete source detection threshold in our fields ($\langle S_{exc}(.81 - 3.5\mathrm{keV}) \rangle \simeq 4.8 \times 10^{-14}$ ergs cm^{-2} s^{-1}). Even though this seems surprising at first, we will see below that $\langle S^g \rangle$ is consistent with the mean X-ray flux expected for galaxies in our sample, i.e. for galaxies with $\langle E \rangle \simeq 17.5$. On the other hand, galaxies with X-ray fluxes close to S_{exc} are expected to have a mean magnitude of $\langle E \rangle \simeq 13.5$. They are thus, on average, much brighter in the optical than the galaxies we considered. Another way to understand the low value of $\langle S^g \rangle$, is to consider the surface density of X-ray sources. According to the X-ray logN–logS relation measured with ROSAT (Hasinger et al. 1993), the number density of X-ray sources with fluxes above $\langle S_{exc} \rangle$ is $n(> \langle S_{exc} \rangle) \simeq 7$ deg^{-2}, much lower than our galaxy surface density ($\langle n^g \rangle \simeq 530$ deg^{-2}). On the other hand, an extrapolation of this logN-logS relation yields $n(> \langle S^g \rangle) \sim 10^3$ deg^{-2}, close to $\langle n^g \rangle$.

The X-ray emission of "normal" galaxies has been extensively studied in the past (see Fabbiano 1989 for a review). For spiral (S) and irregular (Irr) galaxies, the X-ray emission is dominated by binary X-ray sources and SNR. For elliptical (E) and S0 galaxies, it is likely to be composed of a baseline component of X-ray binaries and a hot gaseous component. Fabbiano et al. (1992) have constructed a catalog of *Einstein* X-ray measurements for more than 450 galaxies. The catalog is mostly optically selected and is thus appropriate for a comparison with our results. We selected the 222 and 132 galaxies with *Einstein*-IPC fluxes classified as "normal" S+Irr and E+S0 galaxies. In figure 11, we show the resulting S(.2-4.0 keV) X-ray fluxes vs. the optical B-magnitudes for S+Irr and for E+S0 galaxies separately. Flux upper limits are indicated by stars. Early-type galaxies tend to have higher X-ray fluxes than late-type galaxies. This is likely due to the contribution of the hot gaseous component which is absent in most late-type galaxies.

For S+Irr galaxies, a correlation between $log(S)$ and B is significant at the 99.99% confidence level (ignoring upper limits). The correlation for E+S0 galaxies is only significant at the 91% level. These confidence levels were computed using the linear correlation coefficient for detected galaxies. If, as is customary, we assume a constant X-ray-to-optical flux ratio we obtain the relation $\log S = -\frac{2}{5}B - c$, where c is a constant. Ignoring galaxies with upper limits for S, we find $c = -7.9 \pm .6$ and $c = -7.3 \pm .6$, for the late and early type galaxies, respectively. The errors correspond to 1σ. (The above late-type relation is only slightly different from the one proposed by Fabbiano et al. which corresponds to $c = -8 \pm 1$). These relations are shown as the dashed lines in figure 11. Note that the early-type relation must be taken with caution since no strong correlation is found for this sample. In general, the fraction of late-type to early-type galaxies must be known to predict the mean flux of our mixed APM sample. In the absence of a more significant correlation between X-ray and optical flux for the early-type sample, a comparison with each sample separately is sufficient.

Our measurement is shown as the cross in figure 11. The conversion of §2.2 was used to transform $\langle E \rangle$ into $\langle B \rangle = 19.1 \pm .4$. As is apparent on the figure, our results agree within 1σ with the X-ray-to-optical flux relations inferred from the catalog of Fabbiano et al., simultaneously for both the early and late type samples. We conclude that our correlation results are consistent with

an extrapolation of the known X-ray-to-optical flux ratio of normal galaxies. Our result therefore confirm earlier estimates of the contribution of galaxies to the XRB obtained by integrating the optical number-magnitude relation of galaxies combined with the assumed constant X-ray to optical flux ratio. By applying this method to earlier but similar *Einstein* measurements of the X-ray-to-optical flux ratios (Fabbiano & Trinchieri, 1985; Trinchieri & Fabbiano, 1985), Giacconi & Zamorani (1987) concluded that galaxies contribute about 13% of the 2 keV XRB. Our results do not exclude the possibility that a change in the X-ray-to-optical flux ratio for galaxies with $E \gtrsim 19$ results in a larger contribution to the XRB.

7. Conclusions

Our measurement of the cross-correlation function estimator W_{xg} between 62 *Einstein*-IPC fields (.81-3.5 keV) and $13.5 < E < 19$ Northern APM galaxies therefore leads to the following conclusions:

At zero-lag, we detect a 3.5σ correlation signal with an amplitude of $W_{xg}(\alpha_p, 0) = .045 \pm .013$. This signal passes our series of control tests. Intrinsic field-to-field variations contribute about 62% of the variance of W_{xg}. We therefore warn against the sole use of bootstrapping error estimates which do not include this source of uncertainty.

At non-zero lag, the angular dependence of $W_{xg}(\alpha_p, \theta)$ has two main features: the main signal for $\theta \lesssim 4'$ and, for $\theta \gtrsim 4'$, an almost flat plateau with an amplitude of about $W_{xg}(\alpha_p, \theta \gtrsim 5') \simeq .015$. When fields whose *Einstein* targets are cluster of galaxies are removed from our sample, the plateau virtually disappears, and the zero-lag amplitude becomes $W_{xg}(\alpha_p, 0) = .029 \pm .013$. The agreement between zero-lag and non-zero-lag results were shown to be acceptable.

We developed, from first principles, a formalism to interpret the angular dependence of W_{xg} taking into account the PSF of the X-ray imaging detector. We find that the correlation signal can be produced by three distinct effects: 1. the X-ray emission from the galaxies themselves, 2. the clustering of galaxies with discrete X-ray sources, and 3. the clustering of galaxies with diffuse X-ray emission. These three contributions correspond to the Poisson, clustering and diffuse terms in the expansion of W_{xg}. These terms have different angular dependences, and can thus, in principle be isolated with our formalism.

Even though the diffuse component probably contributes little to the total intensity of the XRB, it can have a significant effect on W_{xg} through the diffuse term. It is likely that the diffuse X-ray emission from clusters of galaxies only partially excised by our point-source finding algorithm produces the oberved plateau in W_{xg}.

After assuming that the diffuse term is negligible for our non-cluster target subsample and that the CCF between galaxies and X-ray point sources has the form $\overline{w}_{pg}(\theta) = (\theta/\overline{\theta}_{pg})^{-.7}$, we could fit $W_{xg}(\theta)$ with the Poisson+clustering term. For the fit, we took proper care of the statistical

correlation of measurements of W_{xg} at different values of θ which were shown not to be statistically independent. We find that the galaxy X-ray sources correlation amplitude $\overline{\theta}_{pg}$ is $.10 \pm .16$ arcsec. As expected, this is smaller that the amplitude for the autocorrelation of galaxies and X-ray sources separately. Our value for $\overline{\theta}_{pg}$ is consistent with zero at the 1σ level and can thus be taken as an upper limit; we therefore do not detect a significant clustering between galaxies and point X-ray sources.

From the consideration of the fields with non-cluster targets, the mean X-ray intensity produced by galaxies in the .81-3.5 keV band is $\langle i^g \rangle = (2.2 \pm 1.1) \times 10^{-6}$ cts arcmin^{-2} s^{-1} which corresponds to $1.5 \pm .8\%$ of the XRB in this band. The mean X-ray flux of galaxies with $\langle E \rangle = 17.5 \pm .3$ is then $\langle S^g(.81 - 3.5keV) \rangle = (8.1 \pm 4.7) \times 10^{-16}$ ergs s^{-1} cm^{-2}. This is well below the flux limits of both *Einstein* and ROSAT surveys with mostly complete optical identifications. A comparison with the X-ray catalog of galaxies of Fabbiano et al. (1992) shows that this flux agrees within 1σ with that expected for both early and late-type galaxies assuming a constant X-ray-to-optical flux ratio. With such an assumption, Giacconi & Zamorani (1987) concluded that normal galaxies contribute about 13% of the 2 keV XRB. Our results, however, do not rule out the possibility of a larger contribution from galaxies with $E \gtrsim 19$.

From an observational standpoint, it would be worthwhile to improve the statistics by increasing the number of fields. It would also be useful to apply the technique with high statistics to deeper galaxy samples and to other X-ray bands. From a theoretical point of view, the diffuse term and, in particular, the effect of diffuse emission from galaxy clusters deserve more attention. Investigations of the non-gaussian distribution of W_{xg} would allow a better treatment of errors and would perhaps allow the extraction of more information from the correlation signal.

It is important to note that our formalism does not require any input parameters. (With better statistics, the exponent for w_{pg}, which was fixed to $\beta = .7$ in this study, can be left as a free parameter). Results for $\langle S^g \rangle$ and $\overline{\theta}_{pg}$ can therefore be considered as measurements rather than as a fit to a model. This cross-correlation technique is thus a powerful way to measure the mean flux and clustering amplitude of sources too faint to be resolved. In addition, if our conclusions regarding the origin of the plateau are confirmed, this technique can perhaps be used to probe faint diffuse X-ray emission which would otherwise be undetectable.

We thank E. Moran for customizing the *Einstein* archive software and S. Maddox and M. Irwin for their help with the APM catalog. We thank O. Lahav, M. Treyer, A. Blanchard, R. Pilla, C. Cress, A. Chen and J. Halpern for useful discussions. We are also grateful to K. Jahoda, the referee, for his detailed comments and suggestions. This research has made use of the NASA/IPAC Extragalactic Database (NED) which is operated by the Jet Propulsion Laboratory, Caltech, under contract with the National Aeronautics and Space Administration. This work was supported by the National Aeronautics and Space Administration under the Long Term Space Astrophysics Research Program grant NAGW2507, and NASA contract number NAS5-32063. This paper is Contribution Number 602 of the Columbia Astrophysics Laboratory.

A. Computation of η_{pg}

In this section we compute η_{pg}, the main ingredient in the interpretation of W_{xg}, taking into account the effect of the PSF of the X-ray instrument. This quantity was defined in Section 5.1 as

$$\eta_{pg}(\theta) \equiv \langle I_i^p N_j^g \rangle_{\theta_{ij}=\theta}, \tag{A1}$$

where I_i^p is the flux in C_i from point X-ray sources, N_j^g is the number of galaxies in C_j, and the average is over cells with separation θ.

Using the definition of the PSF (eq. [13]), we can write

$$I_i^p = \int_{C_i} d\Omega_i \int_S d\Omega_s \hat{i}^p(\boldsymbol{\theta}_s)\psi(\theta_{si}), \tag{A2}$$

where $\hat{i}^p(\boldsymbol{\theta}_s)$ is the intrinsic intensity of the XRB due to point sources at $\boldsymbol{\theta}_s$ (i.e. the intensity which would be measured with a delta-function PSF). The second integral is over the whole sky.

We proceed in the usual way (Treyer & Lahav 1995), by partitioning the sky S and the cell C_j into infinitesimal subcells labeled by k and l, respectively. Then, η_{pg} becomes

$$\eta_{pg} = \left\langle \left(\int_{C_i} d\Omega_i \sum_{k \in S} \delta\hat{I}_k^p \psi(\theta_{ik}) \right) \left(\sum_{l \in C_j} \delta N_l^g \right) \right\rangle \tag{A3}$$

where $\delta\hat{I}_k^p$ is the intrinsic X-ray flux from point sources in subcell k, anf δN_l^g is the number of galaxies in the subcell l.

Upon isolating the instances where the k and l subcells coincide, we can separate the above equation into two terms, namely

$$\eta_{pg} = \left\langle \int_{C_i} d\Omega_i \left(\sum_{k \in C_j} \delta\hat{I}_k^p \delta N_k^g + \sum_{k \neq l} \delta\hat{I}_k^p \delta N_l^g \right) \psi(\theta_{ki}) \right\rangle \tag{A4}$$

Following common usage (see eg. Treyer & Lahav, 1995), we denote these two terms by $\eta_{\rm poisson}$ and $\eta_{\rm clustering}$, respectively.

A.1. Poisson Term

If the k-subcells are sufficiently small, they will contain either 0 or 1 galaxies. As a result, the quantity inside the bracket in $\eta_{\rm poisson}$ is equal either to 0 or to the X-ray flux of the galaxy, respectively. Upon replacing the k-summation by an integral, we thus obtain

$$\eta_{\rm poisson}(\theta_{ij}) = \langle I^g \rangle \frac{1}{2\pi\alpha^2} \int_0^{2\pi} d\phi_{ij} \int_{C_i} d\Omega_i' \int_{C_j} d\Omega_j' \psi(\theta_{ij}'), \tag{A5}$$

where $\langle I^g \rangle$ is the mean X-ray flux emitted by the catalogued galaxies into a cell of side length α. As usual, the $d\phi_{ij}$ integral operates as an azimuthal average over the relative positions of the two cells.

A.2. Clustering Term

The treatment of the clustering term is more complicated. This is due to the fact that this term involves, as its name indicates, the clustering between X-ray sources and galaxies, which, in general, is flux-dependent. Let us thus decompose the product $\delta\hat{I}_k^p \delta N_l^g$ in $\eta_{\rm clustering}$ (eq. [A4]) as,

$$\left\langle \delta\hat{I}_k^p \delta N_l^g \right\rangle = \int dS^p \int dS^g S^p \left\langle \frac{d(\delta N_k^p)}{dS^p} \frac{d(\delta N_l^g)}{dS^g} \right\rangle, \tag{A6}$$

where S^p is the X-ray flux of the X-ray point sources, and S^g is the X-ray (or optical) flux of the galaxies. The quantities $d(\delta N_k^p)/dS^p$ and $d(\delta N_l^g)/dS^p$ are, respectively, the number of X-ray sources and galaxies in the k and l-subcell per unit flux. To simplify the notation, the integration limits relevant for both data sets, although present, have not been displayed explicitly.

For sufficiently small subcells, the product in the bracket is equal to the joint probability $\delta P_{kl}^{pg}(S^p, S^g)$ of finding an X-ray source in the k-subcell with flux S^p and a galaxy in the l-subcell with flux S^g. This probability can be parametrized in terms of the CCF w_{pg} between X-ray sources and galaxies in the usual fashion (see eg. Eq. [1]) as

$$\delta P_{kl}^{pg}(S^p, S^g) = \left\langle \frac{dn^p}{dS^p} \right\rangle \left\langle \frac{dn^g}{dS^g} \right\rangle [1 + w_{pg}(S^p, S^g; \theta_{kl})] \delta\Omega_k \delta\Omega_l \tag{A7}$$

where $\delta\Omega_m$ is the solid angle of subcell m, and n refers to the appropriate number of sources per unit solid angle. The flux dependence of w_{pg} is explicitly displayed.

Equation (A6) can thus be conveniently written as

$$\left\langle \delta\hat{I}_k^p \delta N_l^g \right\rangle = \langle i^p \rangle \langle n^g \rangle [1 + \overline{w}_{pg}(\theta_{kl})] \delta\Omega_k \delta\Omega_l, \tag{A8}$$

where $\langle i^p \rangle = \int dS^p S^p \langle dn^p/dS^p \rangle$ is the mean X-ray intensity due to point sources, and the effective CCF $\overline{w}_{pg}$ is defined by

$$\overline{w}_{pg}(\theta) \equiv \frac{1}{\langle i^p \rangle \langle n^g \rangle} \int dS^p \int dS^g \left\langle \frac{dn^p}{dS^p} \right\rangle \left\langle \frac{dn^g}{dS^g} \right\rangle S^p w_{gp}(S^p, S^g; \theta). \tag{A9}$$

With this in hand, and by turning summations into integrals in the second term of equation (A4), we finally obtain

$$\eta_{\rm clustering}(\theta_{12}) = \langle I^p \rangle \langle N^g \rangle \left[1 + \frac{1}{2\pi\alpha^4} \int_0^{2\pi} d\phi_{12} \int_{C_1} d\Omega_1' \int_{C_2} d\Omega_2' \int_S d\Omega_s' \overline{w}_{pg}(\theta_{1s}') \psi(\theta_{2s}') \right]. \tag{A10}$$

B. Useful Functions

B.1. Semi-analytic Calculation of Λ

In this appendix, we evaluate the integral $\Lambda(\alpha, \sigma, \theta_{12})$. This expression is handy for our phenomenological fit of W_{xg} (§4.3) and appears in the Poisson term of W_{xg} when the effect of

the PSF is taken into account (§5.2). Let us consider two 2-dimensional square cells, C_1 and C_2, with mutually parallel sides of length α. Denote their separation by the vector $\boldsymbol{\theta}_{12}$ whose polar coordinates are (θ_{12}, ϕ_{12}) in a coordinate system with origin at the center of C_1. Then, Λ is defined by

$$\Lambda(\alpha, \sigma, \theta_{12}) \equiv \frac{1}{2\pi} \int_0^{2\pi} d\phi_{12} \hat{\Lambda}(\alpha, \sigma, \theta_{12}, \phi_{12}) \tag{B1}$$

where the $d\phi_{12}$ integral operates an azimuthal average of $\hat{\Lambda}$ itself defined by

$$\hat{\Lambda}(\alpha, \sigma, \theta_{12}, \phi_{12}) \equiv \frac{1}{\alpha^4} \int_{C_1} d^2\theta'_1 \int_{C_2} d^2\theta'_2 e^{-\frac{1}{2}(\theta'_{12}/\sigma)^2}, \tag{B2}$$

where the $d^2\theta$ integrals run over the two cells, and $\theta'_{12} = |\boldsymbol{\theta}'_1 - \boldsymbol{\theta}'_2|$. The α^{-4} factor was included to make Λ dimensionless.

In general, the three length scales involved in $\hat{\Lambda}$ (namely α, θ_{12} and σ) are comparable and, thus, one can not apply any simplifying approximations. The integral can nevertheless be performed analytically. For this purpose, let us choose the axes of the above coordinate system to be parallel to the cell sides. One can then conveniently separate $\hat{\Lambda}$ as follows

$$\hat{\Lambda} = \frac{1}{\alpha^4} \tilde{\Lambda}_{12}(\alpha, \sigma, \bar{x}_2) \tilde{\Lambda}_{12}(\alpha, \sigma, \bar{y}_2), \tag{B3}$$

where $(\bar{x}_2, \bar{y}_2)$ are the coordinates of the center of C_2 and,

$$\tilde{\Lambda}(\alpha, \sigma, \bar{t}_2) \equiv \int_{-\alpha/2}^{\alpha/2} dt_1 \int_{\bar{t}_2 - \alpha/2}^{\bar{t}_2 + \alpha/2} dt_2 e^{-\frac{1}{2}(t_2 - t_1)^2/\sigma^2}. \tag{B4}$$

Note that, in this notation, $\bar{x}_2 = \theta_{12}\cos(\phi_{12})$, and $\bar{y}_2 = \theta_{12}\sin(\phi_{12})$. We operate a change of coordinate defined by: $\tau_1 = t_2 - t_1$, $\tau_2 = t_1 + t_2$. The integration region in Eq. B4 turns from a square to a diamond which can be subdivided into four regions. The symmetry about the $\tau_2 = \bar{t}_2$ axis allows integration inside the upper two regions only. Thus, $\tilde{\Lambda}$ becomes

$$\frac{1}{2} \times 2 \left(\int_{\bar{t}_2 - \alpha}^{\bar{t}_2} d\tau_1 \int_{\bar{t}_2}^{\tau_1 + \alpha} d\tau_2 + \int_{\bar{t}_2}^{\bar{t}_2 + \alpha} d\tau_1 \int_{\bar{t}_2}^{-\tau_1 + 2\bar{t}_2 + \alpha} d\tau_2 \right) e^{-\frac{1}{2}(\tau_1/\sigma)^2}. \tag{B5}$$

The $\frac{1}{2}$ factor comes from the Jacobian of the coordinate transformation.

After performing the two integrals in Eq. B5 and after some algebra, we finally get

$$\begin{aligned} \tilde{\Lambda}(\alpha, \sigma, t) \;=\; & \sigma^2 \left[e^{-\frac{1}{2}(t+\alpha)^2/\sigma^2} + e^{-\frac{1}{2}(t-\alpha)^2/\sigma^2} - 2e^{-\frac{1}{2}t^2/\sigma^2} \right] \\ & + \sqrt{\frac{\pi}{2}} \sigma [-2t \,\mathrm{erf}\left(\frac{t}{2\sigma}\right) + (t-\alpha)\,\mathrm{erf}\left(\frac{t-\alpha}{2\sigma}\right) \\ & + (t+\alpha)\,\mathrm{erf}\left(\frac{t+\alpha}{2\sigma}\right)] \end{aligned} \tag{B6}$$

where erf is the error function.

To evaluate Λ we need to average the above result over ϕ_{12}. We do so by numerically averaging $\hat{\Lambda}$ over 20 values of ϕ_{12} between 0 and $\pi/4$. Figure 12 shows the resulting values for $\Lambda(\theta)$ as a function of θ for the parameters relevant to our study, i.e. for $\alpha = \alpha_p = 64''$ and $\sigma = \sigma_{psf} = .5'$. For comparison with other relevant functions, $\Lambda(0)$ was normalized to 1. The actual normalization is $\Lambda(0) \simeq .551$.

It is convenient to fit the following analytical form to $\Lambda(\theta)$

$$\Lambda(\theta) \simeq \lambda_1 e^{-\frac{1}{2}(\theta/\lambda_2)^2}, \tag{B7}$$

where λ_1 and λ_2 are coefficients whose best-fit values are .552 and .677 arcmin, respectively. The fit results in a mean residual RMS of .0052 and is indistinguishable from the solid line in figure 12.

B.2. Numerical Evaluation of Ξ

The other useful function, Ξ, appears in the clustering term of W_{xg} when the effect of the PSF is included (§5.2). Let us consider again the two cells, C_1 and C_2, described in appendix B.1. The desired function Ξ is defined as

$$\Xi(\alpha, \sigma, \beta, \theta_{12}) \equiv \frac{1}{4\pi^2\alpha^4\sigma^2} \int_0^{2\pi} d\phi_{12} \int_{C_1} d\Omega_1' \int_{C_2} d\Omega_2' \int_S d\Omega_s \left(\frac{\theta_{1s}'}{\alpha}\right)^{-\beta} e^{-\frac{1}{2}(\theta_{2s}'/\sigma)^2} \tag{B8}$$

where $\boldsymbol{\theta}_{is}' = |\boldsymbol{\theta}_i' - \boldsymbol{\theta}_s'|$, $i = 1, 2$. As usual, the $d\phi_{12}$ integral performs an azimuthal average. The $d\Omega_1'\ d\Omega_2'$ integrals are over C_1 and C_2, respectively. The $d\Omega_s$ integral is over the whole sky. The constant in front of the integral was included to make Ξ dimensionless.

Given the cumbersome nature of equation (B8), we approximated Ξ by Monte-Carlo (MC) integration for the parameter values relevant to our analysis, i.e. for $\alpha = \alpha_p = 64''$, $\sigma = \sigma_{psf} = .5'$, and $\beta = .7$. The desired accuracy was set to .04, and the all-sky integral was approximated by a square cell of side $25\alpha_p$ centered on the midpoint between C_1 and C_2.

The result of the MC integration is shown in figure 12 for values of θ ranging from 0 to $8'$. As before, Ξ has been normalized to 1 at $\theta = 0$. Its actual normalization is $\Xi(0) \simeq 1.480$.

It is here also convenient to fit $\Xi(\theta)$ with an analytical function to facilitate modelling of the observed correlation function. We choose the form

$$\Xi(\theta) \simeq \left(\frac{\sqrt{\theta^2 + \xi_0^2}}{\alpha}\right)^{-\beta} \tag{B9}$$

where ξ_0 is the only free parameter. The best fit occurs for $\xi_0 \simeq .573 \pm .008$ arcmin and yields a reduced χ^2 of .32 for 28 degrees of freedom. The result of the fit is also shown in figure 12. The power law $(\theta/\alpha)^{-\beta}$ (after being renormalized) is also plotted and can be seen to agree well with Ξ for $\theta \gtrsim 3.'$. This is to be expected since this power law is the asymptotic form of equation (B8) for $\theta \gg \alpha, \sigma$.

C. Statistics of W_{xg}

In this appendix, we describe our treatment of the statistics of W_{xg} taking into account their non-gaussian nature and the correlation between measurements at different angular lags. We first show how we can approximate the distribution of our data with the multi-variate gaussian distribution (§C.1). We then estimate the covariance of W_{xg} from the data (§C.2). Finally, in §C.3, we apply these results to the fit of our measurement to the Poisson+Clustering model of equation (22). While most of the following treatment is standard, we have used the formalism and notation given in Lupton (1993).

C.1. Multi-Variate Gaussian Approximation

Let us consider the distribution of W_{xg} at a given angular lag θ_i. For simplicity, let $W_{f,i} \equiv W_{xg,f}(\alpha_p, \theta_i)$, where f refers to one of the N_f fields in our data set and $i = 1, \ldots, N_\theta$. Let us denote the intrinsic mean and rms standard deviation of the distribution of $W_{f,i}$ as $\overline{W_i}$ and σ_{W_i}, respectively.

One complication comes from the fact that $W_{f,i}$ is, in general, not normally distributed (see figure 2). Nevertheless, by the central limit theorem, the distribution of the average $W_i \equiv \sum_{i=1}^{N_f} W_{f,i}/N_f$ is close to a normal distribution with mean $\overline{W_i}$ and standard deviation $\sigma_{W_i}/\sqrt{N_f}$, if N_f is sufficiently large. In the case of our non-cluster-target data set, N_f is equal to 33 and should be large enough to satisfy this condition.

Another complication comes from the fact that the distribution of the W_i's at different i's are, in general, not independent. This can be seen in figure 6. This is due to the fact that the same fields are used for the measurements at each θ_i and that the PSF (and the galaxy/X-ray-sources CCF w_{gp}, if present) extend beyond one pixel. As a result, the joint distribution of the W_i's can not be assumed to be simply the product of normal distributions.

We choose the simplest approximation to the joint distribution of correlated normal variables, namely the multi-variate normal distribution. Under this approximation, the joint Probability Distribution Function (PDF) for the averages $\mathbf{W} \equiv (W_1, \ldots, W_{N_\theta})^T$ is

$$p(\mathbf{W}) = \frac{1}{\sqrt{(2\pi)^{N_\theta}|V|}} \exp\left(-(\mathbf{W} - \overline{\mathbf{W}})^T \mathbf{V}^{-1} (\mathbf{W} - \overline{\mathbf{W}})/2\right) \qquad \text{(C1)}$$

where $\overline{\mathbf{W}} = (\overline{W_1}, \ldots, \overline{W_{N_\theta}})^T$, and $\mathbf{V}$ is the $N_\theta \times N_\theta$ covariance matrix which is given by

$$\mathbf{V} = \langle (\mathbf{W} - \overline{\mathbf{W}})(\mathbf{W} - \overline{\mathbf{W}})^T \rangle. \qquad \text{(C2)}$$

The quantity $|V|$ is the determinant of $\mathbf{V}$, and the superscript ^{T} stands for transpose. An estimate for $\mathbf{V}$ from the data is derived in the next section.

C.2. Estimate for the Covariance

Let us consider a large number N_r of realizations of our experiment. This would involve the measurement of $W_{xg}(\theta_i)$ for $N_r \times N_f$ fields. Our actual measurement is, say, the $r = 1$ realization. Let us denote the resulting measurements as $W_{r,f,i}$, and their average within realization r as $W_{r,i} \equiv \langle W_{r,f,i} \rangle_f$. In the previous expression and hereafter, a bracket of the form $\langle \cdots \rangle_l$ denotes an average over the index l.

We can then express equation (C2) as

$$\begin{aligned} V_{i,j} &\simeq \left\langle (W_{r,i} - \overline{W_i})(W_{r,j} - \overline{W_j}) \right\rangle_r \\ &= \frac{1}{N_f^2} \sum_{f=1}^{N_f} \sum_{f'=1}^{N_f} \langle W_{r,f,i} W_{r,f',j} \rangle_r - \overline{W}_i \overline{W}_j . \end{aligned} \tag{C3}$$

When $f \neq f'$, $W_{r,f,i}$ and $W_{r,f',j}$ correspond to measurements in different fields and are thus independent. Hence, $\sum_{f \neq f'} \langle W_{r,f,i} W_{r,f',j} \rangle_r = N_f(N_f - 1)\overline{W}_i \overline{W}_j$. On the other hand, when $f = f'$, $W_{r,f,i}$ and $W_{r,f,j}$ involve measurements in the same field and are thus *not* independent. To estimate this term from the available data, we approximate $\langle W_{r,f,i} W_{r,f,j} \rangle_r \simeq \langle W_{1,f,i} W_{1,f,j} \rangle_f$, where, as noted above, the $r = 1$ realization corresponds to our actual experiment. Then, $\sum_{f=f'} \langle W_{r,f,i} W_{r,f,j} \rangle_r \simeq \sum_f W_{1,f,i} W_{1,f,j}$.

By combining the $f \neq f'$ and $f = f'$ terms into equation (C3) and after using the approximation $\overline{W}_k \simeq \langle W_{f,k} \rangle_f \equiv W_k$, we finally obtain

$$V_{ij} \simeq \frac{1}{N_f} \langle (W_{f,i} - W_i)(W_{f,j} - W_j) \rangle_f , \tag{C4}$$

where the $r = 1$ subscript has been dropped. Note that the diagonal elements, V_{ii} are simply equal to $\langle (W_{f,i} - W_i)^2 \rangle_f / N_f \simeq \sigma_i^2 / N_f$, as they should be.

Our measurement of the covariance matrix $\mathbf{V}$ for the non-cluster data set is displayed in figure 13. Correlations at low ($\theta \lesssim 3\alpha_p$) and at high ($\theta \gtrsim 8\alpha_p$) angular lags are clearly visible.

C.3. Fit to Linear Model

In §5.3, we need to fit our measurements of $\mathbf{W}$ to the function $\mathbf{f}(\boldsymbol{\theta}; \mathbf{a}) \equiv a_{poisson} \boldsymbol{\Lambda}(\boldsymbol{\theta}) + a_{clustering} \boldsymbol{\Xi}(\boldsymbol{\theta})$, where $\mathbf{a} \equiv (a_{poisson}, a_{clustering})^T$ (Eq. [22]). This corresponds to a fit to the $N_a = 2$ parameter linear model (see eg. Lupton 1993, p.81)

$$\mathbf{W} = \mathbf{f}(\boldsymbol{\theta}; \mathbf{a}) + \boldsymbol{\epsilon} \equiv \mathbf{M}\mathbf{a} + \boldsymbol{\epsilon}, \tag{C5}$$

where $\mathbf{M}$ is a $N_\theta \times N_a$ matrix with rows equal to $(\Lambda(\theta_i), \Xi(\theta_i))$, $i = 1, \ldots, N_\theta$, and $\boldsymbol{\epsilon}$ is the N_θ-dimensional vector of errors with $\langle \boldsymbol{\epsilon} \rangle = \mathbf{0}$ and covariance matrix $\langle \boldsymbol{\epsilon} \boldsymbol{\epsilon}^T \rangle \equiv \mathbf{V}$.

Within the multi-variate approximation of equation (C1), the probability density for our data set $\mathbf{W}$ to result from a model with parameters $\mathbf{a}$ is

$$p(\mathbf{W};\mathbf{a}) = \frac{1}{\sqrt{(2\pi)^{N_\theta}|V|}} e^{-X^2(\mathbf{W};\mathbf{a})/2}, \tag{C6}$$

where,

$$X^2(\mathbf{W};\mathbf{a}) \equiv (\mathbf{W} - \mathbf{f}(\boldsymbol{\theta};\mathbf{a}))^T \mathbf{V}^{-1} (\mathbf{W} - \mathbf{f}(\boldsymbol{\theta};\mathbf{a})). \tag{C7}$$

The best fit to our model correponds to the value $\hat{\mathbf{a}}$ of $\mathbf{a}$ for which $p(\mathbf{W};\mathbf{a})$ is maximum. Setting the derivative of X^2 to 0 yields

$$\hat{\mathbf{a}} = (\mathbf{M}^T \mathbf{V}^{-1} \mathbf{M})^{-1} \mathbf{M}^T \mathbf{V}^{-1} \mathbf{W}. \tag{C8}$$

Note that $\hat{\mathbf{a}}$ is a bilinear combination of multi-variate normal variables and thus itself follows a multivariate normal distribution (with two variables). Thus, the PDF of $\hat{\mathbf{a}}$ is

$$p(\hat{\mathbf{a}}) = \frac{1}{\sqrt{2\pi|U|}} \exp\left(-(\hat{\mathbf{a}} - \overline{\mathbf{a}})^T \mathbf{U}^{-1} (\hat{\mathbf{a}} - \overline{\mathbf{a}})/2\right), \tag{C9}$$

where $\mathbf{U} \equiv \langle (\hat{\mathbf{a}} - \overline{\mathbf{a}})(\hat{\mathbf{a}} - \overline{\mathbf{a}})^T \rangle$ is the covariance matrix of $\hat{\mathbf{a}}$, and $\overline{\mathbf{a}}$ corresponds to the true distribution of $\mathbf{W}$, i.e. $\overline{\mathbf{W}} = \mathbf{f}(\boldsymbol{\theta};\overline{\mathbf{a}})$. By combining equations (C8) and (C2), it is easy to show that $\mathbf{U} = (\mathbf{M}^T \mathbf{V}^{-1} \mathbf{M})^{-1}$. Taken individually, each of the a_i's are normally distributed with standard deviations simply given by

$$\sigma_{\hat{a}_i} = U_{ii}. \tag{C10}$$

These standard deviations are the estimates for the 1σ errors of the best-fit parameters taken separately.

A measure of the goodness of fit is provided by $X^2(\mathbf{W};\hat{\mathbf{a}})$. This quantity follows a χ^2-distribution with $N_\theta - N_a$ degrees of freedom. Its value must be close to $N_\theta - N_a$ for the fit to be acceptable.

Figure 10 shows the probability contours for X^2 in the $\mathbf{a}$-plane for our fit to the non-cluster data set. The best fit parameters (Eq. [C8]) and their associated uncorrelated 1σ errors (Eq. [C10]) are also shown.

REFERENCES

Barcons, X., Franceschini, A., De Zotti, G., Danese, L., & Miyaji, T., 1995, ApJ, 455, 480

Boyle, B. J., Griffiths, R. E., Shanks, T., Stewart, G. C., & Georgantopoulos, I., 1993, MNRAS, 260, 49

Boyle, B. J., McMahon, R. G., Wilkes, B. J., & Elvis, M., 1995, MNRAS, 272, 462

Butcher, H. R., & Oemler, A. Jr., 1985, ApJS, 57, 665

Butcher, J. A., et al., 1994, MNRAS, in press

Carballo, R., et al., 1995, MNRAS, 277, 1312

Carrera, F. J., Barcons, X., Butcher, J. A., Fabian, A. C., Lahav, O., Stewart, G. C., & Warwick, R. S. 1995a, AdSpR, 16, 111

——, 1995b, submitted to MNRAS

De Zotti, G., Toffolatti, L., Franceschini, A., Barcons, X., Danese, L., & Burigana, C. 1995. in Proc. of the International School of Space Science 1994 course: X-Ray Astronomy. ed G. Bignami et al. in preparation.

Fabbiano, G., & Trinchieri, G., 1985, ApJ, 296, 430

Fabbiano, G., 1989, ARA&A, 27, 87

Fabbiano, G., Kim, D.-W., & Trinchieri, G., 1992, ApJS, 80, 531

Fabian, A. C., & Barcons, X. A. 1992, ARA&A, 30, 429

Giaconni, R., et al. 1979, ApJ, 230, 540

Giaconni, R., & Zamorani, G., 1987, ApJ, 313, 20

Gioia, I. M., Maccacaro, R. E., Schild, R. E., Wolter, A., Stocke J. T., Morris, S. L., & Henry, J. P., 1990, ApJS, 72, 567

Groth, E. J., & Peebles, P. J. E., 1977, ApJ, 217, 385

Hamilton, T., Helfand, D. J., & Wu, X., 1991, ApJ, 379, 576

Hasinger, G., 1996, in Examining the Big Bang and Diffuse Background Radiations, eds Kafatos, M., & Kondo, Y. (Netherlands: IAU), 245

Hasinger, G., Burg, R., Giacconi, R., Hartner, G., Schmidt, M., Trumper, J., & Zamorani, G., 1993, A&A, 275, 1. Erratum in A&A, 291, 348

Helou, G., Madore, B. F., Schmitz, M., Bicay, M. D., Wu, X., & Bennett, J., 1991, in Databases and On-Line Data in Astronomy, eds Egret, D., & Albrecht, M. (Dordrecht: Kluwer)

Humphreys, R. M., Landau, R., Ghigo, F. D., & Zumach, W., 1991, ApJ, 102, 395

Irwin, M., & McMahon R. G., 1992, Gemini, 37,1

Irwin, M., Maddox, S., & McMahon, R. G., 1994, Spectrum, 2, 14

Jahoda, K., Lahav, O., Mushotzky, R. F., & Boldt, E., 1991, ApJ, 378, L37. Erratum in 1992, ApJ, 399, L107

Jones, L. R., et al., 1995, in Proc. of the 35^{th} Herstmoncieux Conference: Wide-Field Spectroscopy and the Distant Universe, eds Maddox, S., & Aragon-Salamanca, A. (Singapore: World Scientific Publishing)

Kibblewhite et al. 1984. Astronomical Microdensitometry Conference, NASA Conf. Pub., 2317, 277

Kim, D.-W., Fabbiano, G., & Trinchieri, G., 1992, ApJS, 80, 645

Koo, D. C, & Kron, R. G., 1992, ARA&A, 30,613

Lahav, O., et al., 1993, Nature, 364, 693

Lupton, R., 1993, Statistics in Theory and Practice (Princeton: Princeton Univ. Press)

Maddox, S. J., Efstathiou, G., Sutherland, W. J., & Loveday, J. 1990a. MNRAS, 242, 43p

Maddox, S. J., Sutherland, W. J., Efstathiou, G., & Loveday, J., 1990b, MNRAS, 243, 692

Maddox, S. J., Sutherland, W. J., Efstathiou, G., Loveday, J., & Peterson, B. A., 1990c, MNRAS, 247, 1p

Mather, J. C., et al., 1990, ApJ, 354, L37

Metcalf, N., Shanks, T., Fong, R., & Jones, L. R., 1991, MNRAS, 249, 498

Miyaji T., Lahav O., Jahoda K., & Boldt E. 1994, ApJ, 434,424

Mushotzky, R. & Jahoda, K., 1992, in The X-Ray Background, eds. Barcons, X. & Fabian, A. C. (Cambridge: Cambridge University Press), 80

Phillips, S., Fong, R., Ellis, R. S., Fall, S. M., & MacGillivray, H. T., 1978, MNRAS, 182, 673

Peebles, P. J. E., 1980, The Large-Scale Structure of the Universe. (Princeton: Princeton Univ. Press)

Refregier A., Helfand D. J., & McMahon R. G, 1995, in proceedings of the conference Röntgenstrahlung from the Universe, held in Würzburg, Germany in Sept 95. in press.

Roche N., Shanks T., Georgantopoulos I., Stewart G. C., Boyle B. J., & Griffiths R. E. 1995, MNRAS, 273, L15

Romero-Colmenero, E., Branduardi-Raymont, G., Carrera, F. J., Jones, L. R., Mason, K. O., McHardy, I. M., & Mittaz, J. P. D., 1996, preprint, astro-ph/9604134

Setti, G., & Comastri, A., 1996, in Examining the Big Bang and Diffuse Background Radiations, eds Kafatos, M., & Kondo, Y. (Netherlands: IAU), 263

Stocke, J. T., et al., 1991, ApJS, 76, 813

Treyer M. A., & Lahav O. 1995, submitted to MNRAS

Trinchieri, G., & Fabbiano, G., 1985, ApJ, 296, 447

Vikhlinin, A., & Forman, W. 1995, ApJ, 455, L109

Vikhlinin, A., Forman, W., Jones, C., & Murray, S., 1995a, ApJ, 451, 542

——, 1995b, ApJ, 451, 553

——, 1995c, ApJ, 451, 564

Wang, Q., Hamilton, T., Helfand, D. J., & Wu, X., 1991, ApJ, 374, 475

Wu, X., Hamilton, T., Helfand, D. J., & Wang Q. 1991, ApJ, 379, 564

Zamorani, G. 1995. in Background Radiation Meeting (1993). ed Calzetti, D., et al. (Cambridge: Cambridge Univ. Press)

Table 1. Field characteristics and cross-correlation results

Seq. No.[a]	POSS[b]	R.A.[c]	Dec.[c]	b [d]	t_{exp} [e]	Target[f]	$\langle I \rangle$[g]	$\langle N \rangle$[h]	$W_{xg}(0)$	$W_{xg}(7\alpha_p)$
29	756	17h 09m 59s	71d 09m 59s	33.7	20053	4	2.44	0.194	-0.048	-0.015
270	1201	01h 16m 29s	08d 13m 59s	-53.7	15572	3	2.49	0.072	0.074	-0.001
280	1563	12h 24m 59s	09d 29m 59s	71.2	41941	3	3.67	0.101	0.081	0.019
294	779	23h 48m 23s	26d 52m 59s	-33.8	10722	3	3.15	0.146	-0.004	-0.008
322	1093	16h 15m 47s	35d 04m 59s	45.6	8377	3	3.36	0.146	0.023	0.090
330	1069	17h 00m 59s	33d 50m 59s	36.2	6058	3	3.74	0.268	0.181	0.143
351	887	04h 30m 29s	05d 14m 59s	-27.4	26346	2	2.99	0.101	-0.077	-0.002
352	1367	12h 07m 59s	39d 39m 59s	75.1	6151	2	3.25	0.121	0.154	-0.014
486	456	08h 38m 01s	13d 23m 04s	30.1	11777	2	2.89	0.172	-0.007	0.002
499	1336	07h 40m 56s	38d 00m 30s	26.1	11357	2	2.75	0.188	-0.039	-0.036
543	1130	21h 34m 03s	00d 18m 11s	-35.7	8145	2	3.06	0.238	0.020	0.033
554	661	09h 23m 55s	39d 15m 22s	46.2	7807	2	3.04	0.149	-0.003	-0.051
1759	601	01h 02m 23s	32d 29m 59s	-30.0	9856	3	3.47	0.173	-0.028	0.014
2003	769	17h 26m 59s	50d 11m 59s	33.5	19069	2	3.03	0.118	-0.078	-0.025
2113	1353	11h 10m 59s	22d 23m 59s	67.3	4402	2	2.71	0.108	-0.049	0.047
2598	316	23h 17m 43s	07d 45m 46s	-48.5	8724	3	3.82	0.132	0.078	0.023
3438	743	16h 27m 57s	40d 58m 11s	43.5	6001	3	3.81	0.300	0.111	-0.033
3954	11	03h 12m 30s	14d 17m 55s	-35.7	11405	3	2.45	0.102	-0.089	0.003
4303	1385	12h 13m 11s	13d 22m 59s	73.7	7731	3	3.05	0.106	0.045	0.003
4374	601	00h 55m 05s	30d 04m 58s	-32.5	14281	2	2.62	0.157	0.044	0.051
4496	932	03h 34m 13s	00d 25m 28s	-41.6	1507	1	3.54	0.065	-0.089	0.032
5391	110	12h 57m 44s	35d 53m 59s	81.3	38271	4	2.66	0.137	0.117	-0.038
5392	110	13h 01m 11s	35d 53m 59s	81.1	37802	4	2.80	0.108	-0.028	-0.031
5394	1259	01h 12m 44s	-01d 42m 53s	-63.7	12830	2	2.61	0.083	0.138	0.004
5425	1372	16h 35m 26s	11d 55m 40s	35.0	6379	2	4.06	0.233	0.018	0.052
5504	924	08h 49m 36s	28d 30m 59s	37.7	16489	1	2.85	0.135	-0.028	-0.029
5688	1414	17h 03m 59s	60d 47m 59s	36.4	18837	2	2.96	0.180	0.121	0.011
5721	1560	12h 28m 43s	07d 41m 52s	69.7	25140	4	3.30	0.053	0.213	-0.008
6083	1259	01h 12m 35s	-00d 01m 59s	-62.1	10458	3	3.32	0.125	0.252	0.199
6084	1259	01h 22m 59s	-01d 45m 59s	-63.1	8273	3	3.29	0.126	0.067	0.092
6104	1429	15h 10m 17s	07d 36m 59s	51.2	7729	3	4.25	0.175	0.081	0.195
6366	136	15h 47m 29s	12d 32m 59s	45.8	11061	2	3.62	0.205	0.045	-0.008
6828	1244	00h 38m 13s	32d 53m 41s	-29.7	10833	3	2.72	0.096	-0.005	-0.019
6830	425	03h 03m 30s	17d 07m 06s	-34.8	11762	3	2.40	0.163	-0.019	-0.019
6832	1369	16h 00m 22s	41d 09m 42s	48.7	9377	3	2.86	0.153	0.080	-0.000
6986	1560	12h 19m 21s	04d 45m 05s	66.3	10273	3	3.14	0.071	-0.005	0.004
6994	1576	12h 22m 52s	18d 27m 59s	79.2	10053	3	2.79	0.036	0.407	0.001
7036	1398	12h 15m 35s	28d 27m 10s	82.5	10073	2	2.92	0.153	0.034	0.050
7039	1578	12h 49m 48s	-00d 55m 39s	61.7	12049	2	3.07	0.045	0.200	-0.014
7397	1069	16h 56m 01s	35d 25m 04s	37.5	10257	1	2.96	0.178	-0.008	0.008
7480	83	16h 04m 49s	15d 59m 37s	43.4	5814	2	3.52	0.273	0.070	0.012
7605	799	21h 42m 06s	14d 32m 35s	-28.3	9138	2	2.80	0.141	0.049	0.002
7769	1051	14h 00m 35s	09d 22m 59s	65.3	6646	3	3.32	0.174	0.020	0.032
7858	83	16h 04m 21s	17d 55m 44s	44.2	10538	3	3.82	0.190	0.036	0.063
8366	1225	01h 46m 42s	34d 56m 12s	-26.2	12328	3	2.97	0.352	-0.060	0.025
8468	65	14h 27m 43s	10d 56m 43s	61.6	9014	2	3.03	0.184	-0.032	-0.042
8672	745	17h 12m 59s	64d 39m 59s	34.8	7878	3	3.25	0.290	0.135	0.069
8926	745	17h 10m 59s	63d 39m 59s	35.2	7818	3	3.52	0.280	0.443	0.200
8982	1051	14h 13m 33s	13d 34m 17s	65.9	9832	2	3.60	0.097	0.060	-0.032
9084	11	03h 08m 30s	14d 28m 53s	-36.2	11920	3	3.09	0.113	0.016	0.024
10087	1174	22h 34m 01s	28d 13m 20s	-25.6	6490	2	2.73	0.286	0.087	0.041
10379	1202	02h 13m 46s	17d 52m 40s	-40.3	8817	3	3.25	0.110	-0.026	0.035

Table 1—Continued

Seq. No.[a]	POSS[b]	R.A.[c]	Dec.[c]	b [d]	t_{exp} [e]	Target[f]	$\langle I \rangle$[g]	$\langle N \rangle$[h]	$W_{xg}(0)$	$W_{xg}(7\alpha_p)$
10384	1421	14h 44m 03s	07d 41m 21s	56.4	6548	3	3.24	0.133	0.011	-0.015
10393	1440	14h 26m 33s	01d 30m 36s	55.1	2238	2	3.06	0.110	0.088	-0.099
10437	1051	14h 14m 13s	09d 06m 38s	62.8	9294	2	3.78	0.142	0.011	-0.032
10452	1283	02h 35m 06s	01d 45m 29s	-51.2	16227	3	3.28	0.074	-0.043	0.051
10464	1119	15h 32m 46s	23d 40m 05s	53.0	16905	2	3.11	0.131	0.008	-0.017
10474	1087	14h 44m 35s	11d 47m 59s	58.8	9729	3	3.93	0.145	0.053	-0.019
10533	1056	16h 48m 41s	05d 04m 59s	28.9	33324	2	4.39	0.208	-0.005	0.018
10632	363	03h 23m 37s	02d 14m 46s	-42.4	9269	1	4.00	0.121	-0.046	0.033
10671	860	21h 44m 01s	04d 20m 30s	-35.3	10532	3	3.36	0.114	-0.066	0.005
10682	1195	00h 14m 19s	16d 19m 59s	-45.5	16733	0	2.56	0.104	0.018	-0.030

[a] ***Einstein*** Observatory sequence number

[b] POSS E-plate number

[c] Right Ascension and Declination (1950)

[d] galactic latitude (°)

[e] ***Einstein***-IPC Exposure time for VG=1-2 (s)

[f] ***Einstein*** target type: 1 = galactic sources, 2 = discrete extragalactic sources (galaxies, QSO,etc), 3 = clusters of galaxies and superclusters, 4 = deep surveys; one field, labeled 0, has no target type specified in the *Einstein* database

[g] Mean X-ray intensity (10^{-4} cts s^{-1} $arcmin^{-2}$)

[h] Mean galaxy counts ($arcmin^{-2}$)

Table 2. Zero-lag results. The values for $W_{xg}(\alpha, 0)$ are given for the real (hard-galaxies) and control data sets. The cell size α is shown in units of the pixel size $\alpha_p = 64''$, and the errors correspond to 1σ.

α/α_p	hard-gals	hard-gals(sol)	soft-gal	hard-stars	scrambled
1	0.045±0.012	0.029±0.012	0.013±0.011	0.002±0.004	0.004±0.006
2	0.037±0.011	0.030±0.010	0.013±0.010	0.001±0.003	0.003±0.006
3	0.035±0.011	0.026±0.009	0.013±0.009	0.004±0.003	-0.005±0.005
4	0.019±0.008	0.020±0.009	0.015±0.006	0.000±0.002	0.002±0.004
5	0.023±0.009	0.020±0.007	0.020±0.007	0.001±0.002	0.003±0.004
6	0.022±0.008	0.019±0.006	0.004±0.005	0.001±0.002	0.001±0.003
7	0.021±0.007	0.017±0.006	0.008±0.004	-0.001±0.001	0.002±0.003
8	0.020±0.007	0.016±0.007	0.010±0.004	0.001±0.001	0.000±0.002

Table 3. Non-zero lag results. The value for $W_{xg}(\alpha_p, \theta)$ at different values of θ is given for the whole data set (all) and for the subsamples containing only fields with cluster and non-cluster targets. The results for the scrambled set are given in the last column. The angular lag θ is shown in units of the pixel size $\alpha_p = 64''$.

θ/α_p	all	cluster	non-cluster	scrambled
0	0.045±0.013	0.064±0.023	0.029±0.013	-0.002±0.010
1	0.028±0.008	0.041±0.016	0.018±0.007	-0.000±0.005
2	0.018±0.009	0.037±0.016	0.002±0.007	-0.000±0.004
3	0.013±0.007	0.022±0.012	0.005±0.005	0.001±0.003
4	0.021±0.007	0.042±0.013	0.002±0.004	-0.001±0.003
5	0.014±0.007	0.030±0.013	0.000±0.003	0.002±0.003
6	0.014±0.007	0.031±0.013	-0.000±0.005	0.002±0.003
7	0.015±0.006	0.034±0.011	-0.001±0.004	-0.001±0.003
8	0.016±0.005	0.028±0.011	0.005±0.004	0.000±0.003
9	0.014±0.005	0.027±0.010	0.003±0.005	0.001±0.003
10	0.019±0.005	0.030±0.009	0.010±0.006	0.003±0.003
11	0.012±0.006	0.025±0.010	0.000±0.005	0.003±0.004
12	0.014±0.005	0.023±0.008	0.006±0.006	0.004±0.004

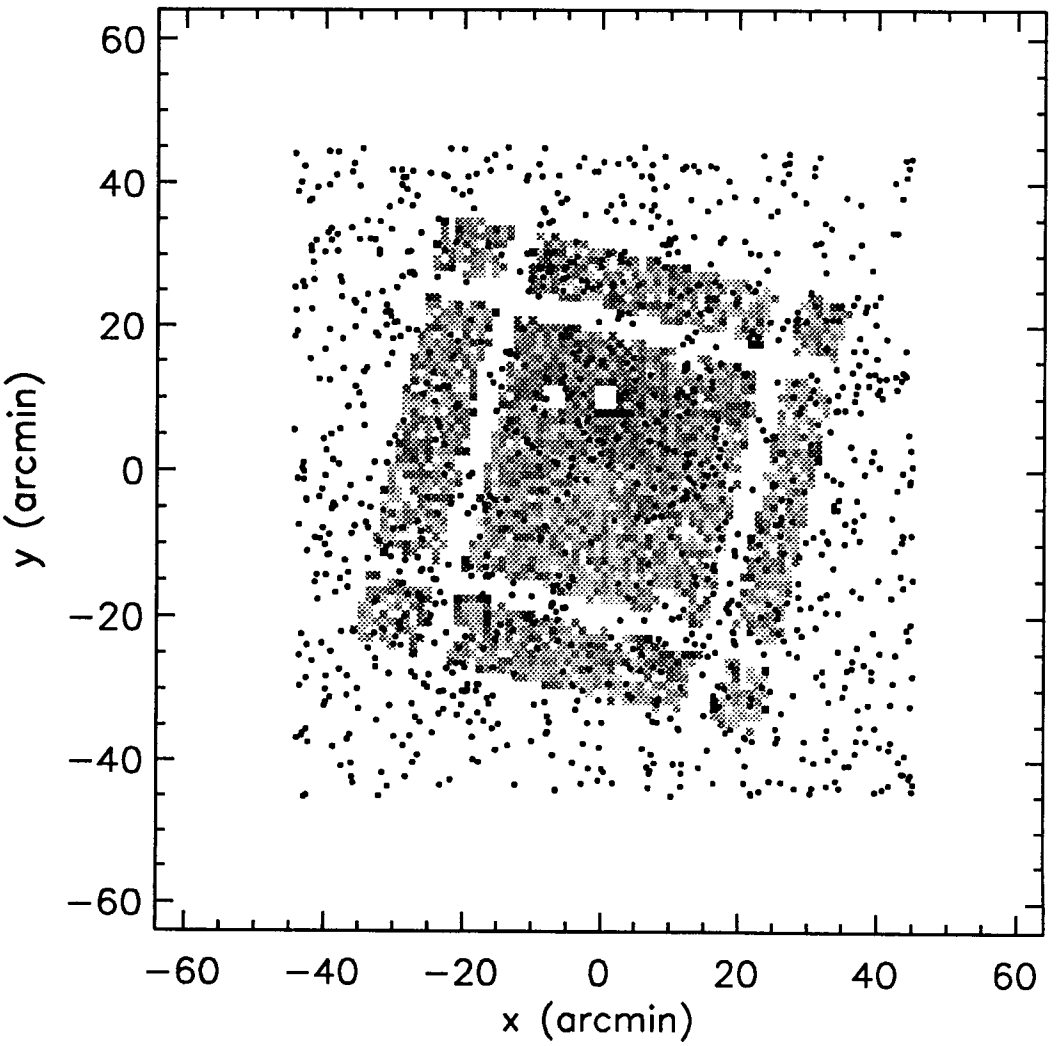

Fig. 1.— Example for a XRB galaxy field pair. This field corresponds to *Einstein*-IPC sequence number 2598. The axes give offsets from the center positions with R.A. and Dec. increasing in the negative-x and positive-y directions, respectively. The .81-3.5 keV XRB intensity is shown as the grey-scale map. Positions of APM galaxies with $13.5 < E < 19.0$ are shown as filled circles.

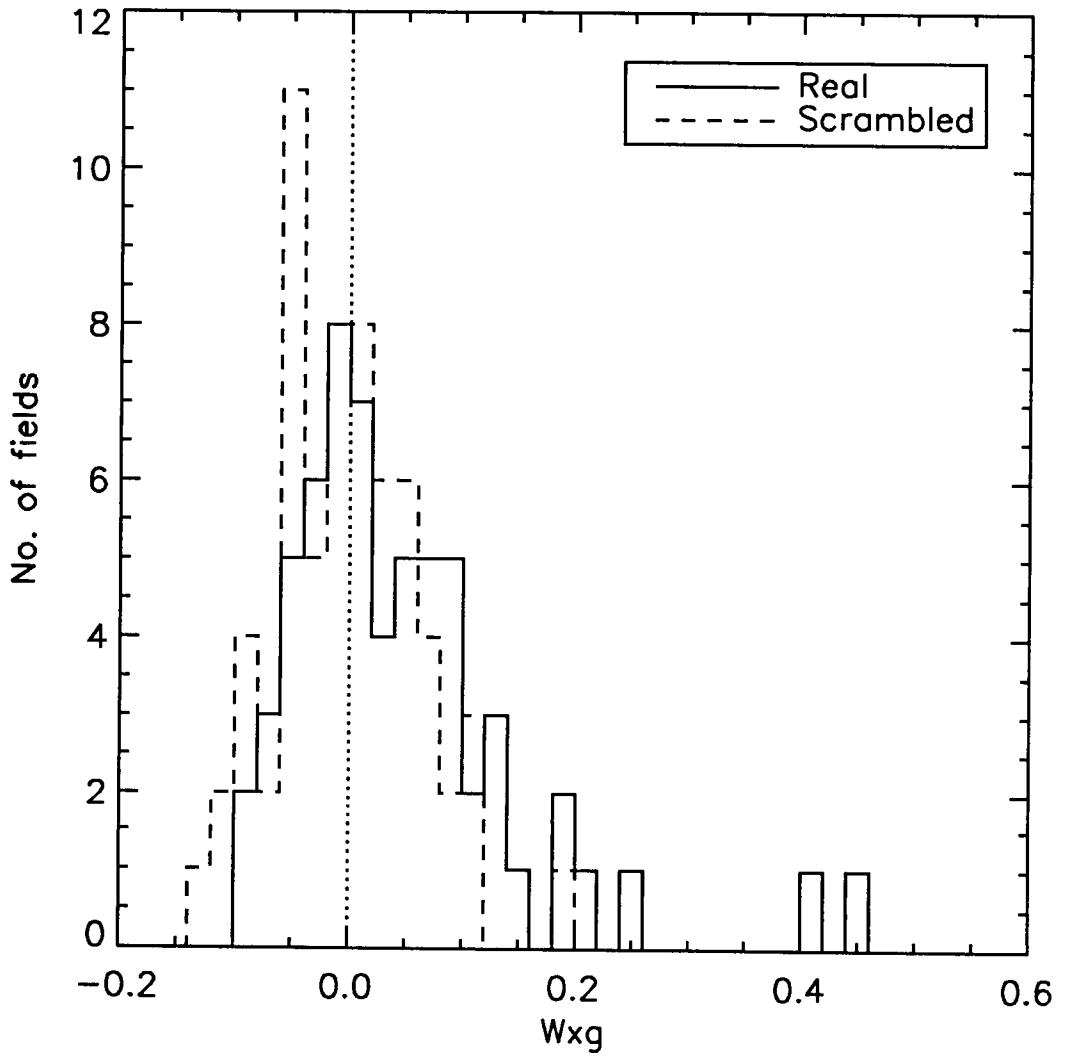

Fig. 2.— Distribution of $W_{xg}(\alpha_p, 0)$ for the real and scrambled data sets. The mean values are $.04 \pm .01$ and $-.001 \pm .008$ for the real and scrambled sets, respectively.

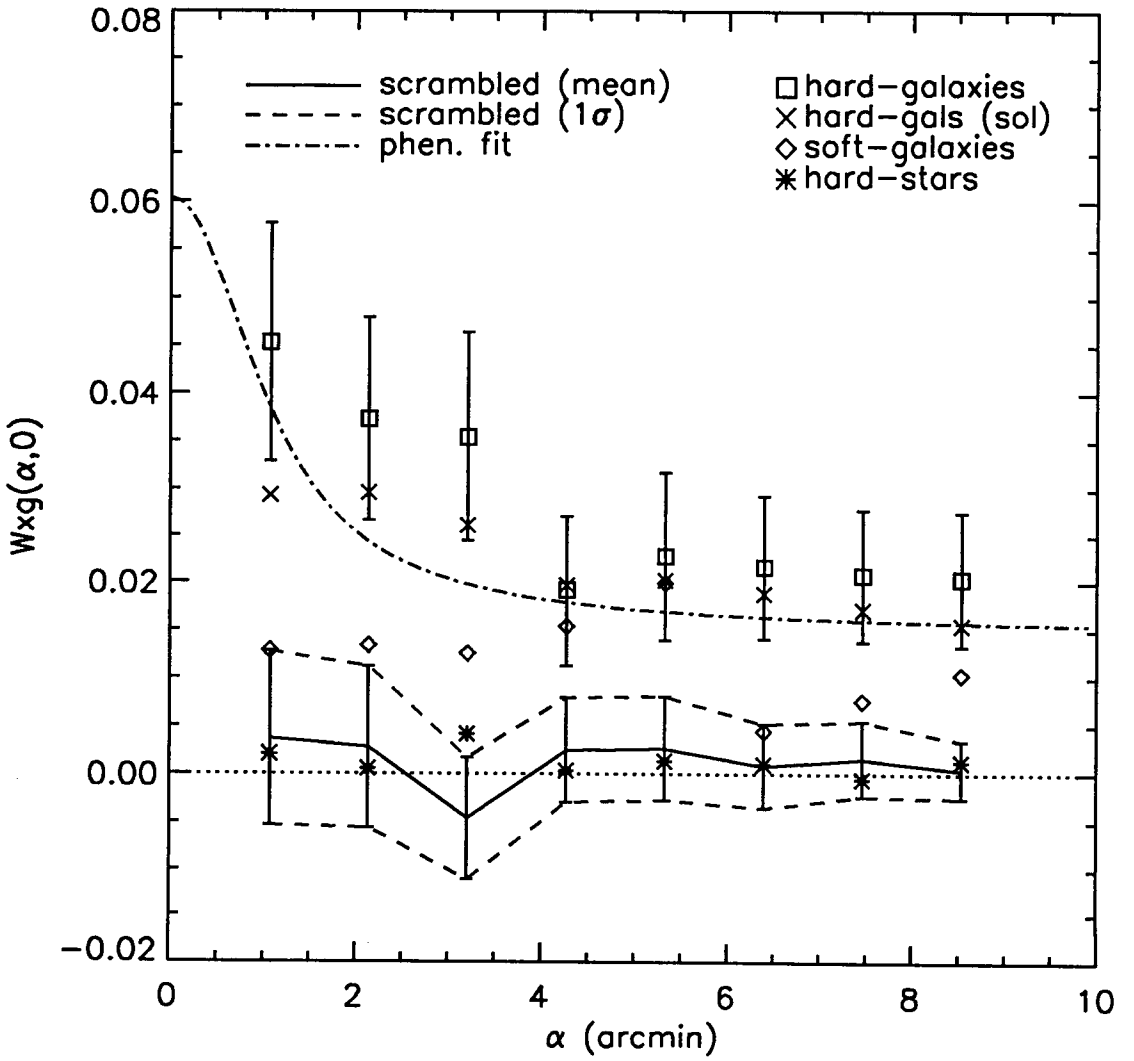

Fig. 3.— Zero-lag results. The values for $W_{xg}(\alpha, 0)$ is shown as a function of cell size α for the real (hard-galaxies) data set and for the control data sets (hard XRB with high solar contamination and galaxies, soft XRB and galaxies, hard XRB and stars, hard XRB with galaxies for scrambled field pairs for which the dashed lines delimit the $\pm 1\sigma$ uncertainties). The dotted-dashed line correspond to the zero-lag values expected from our phenomenological fit to the non-zero-lag results (see text).

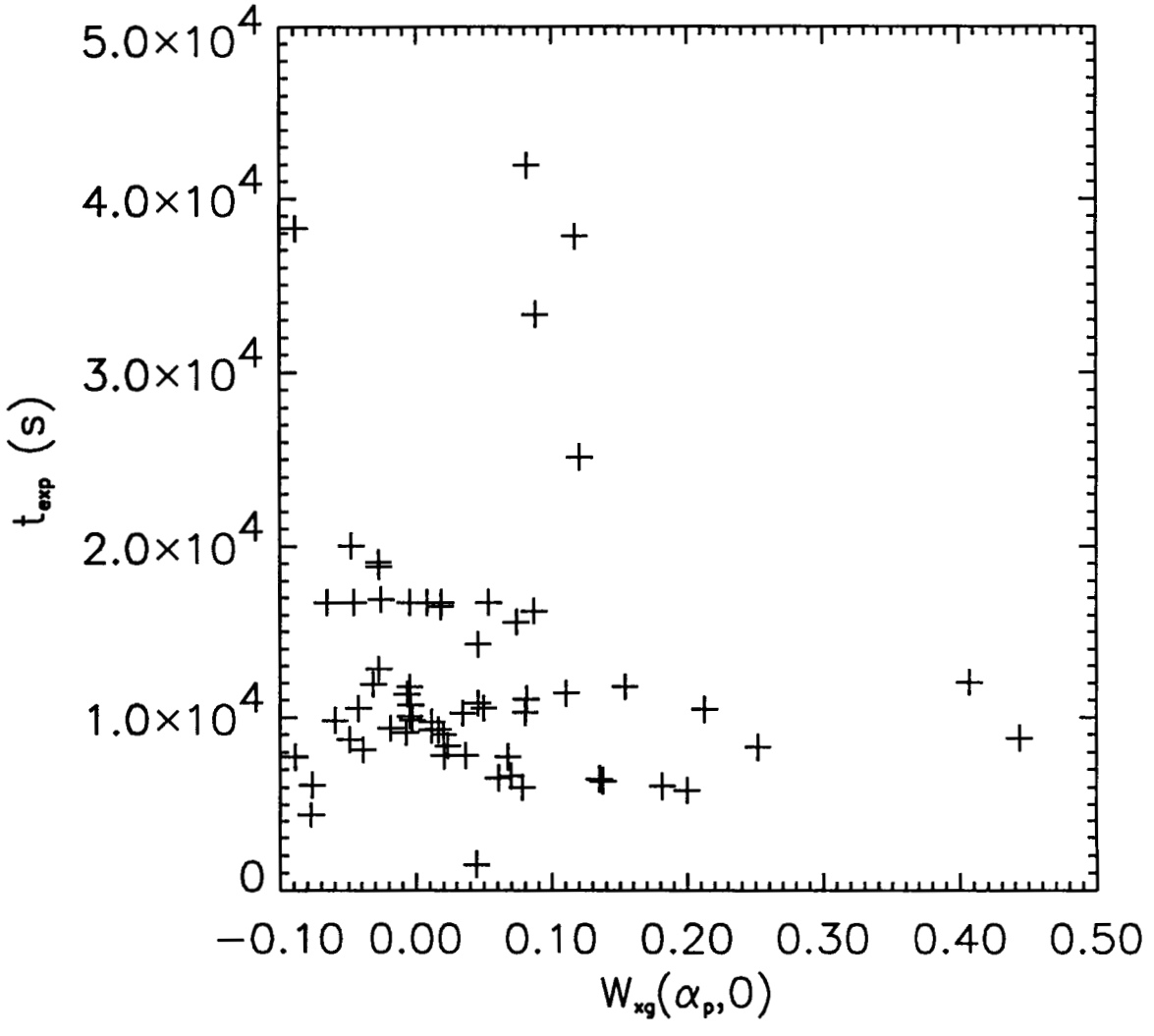

Fig. 4.— $W_{xg}(\alpha_p, 0)$ for the real data set vs. various quantities: (a) *Einstein*-IPC exposure time; (b) absolute Galactic latitude; (c) mean XRB flux in the .81-3.5 keV band (VG=1-2); and (d) mean number of APM galaxies with $13.5 < E < 19$.

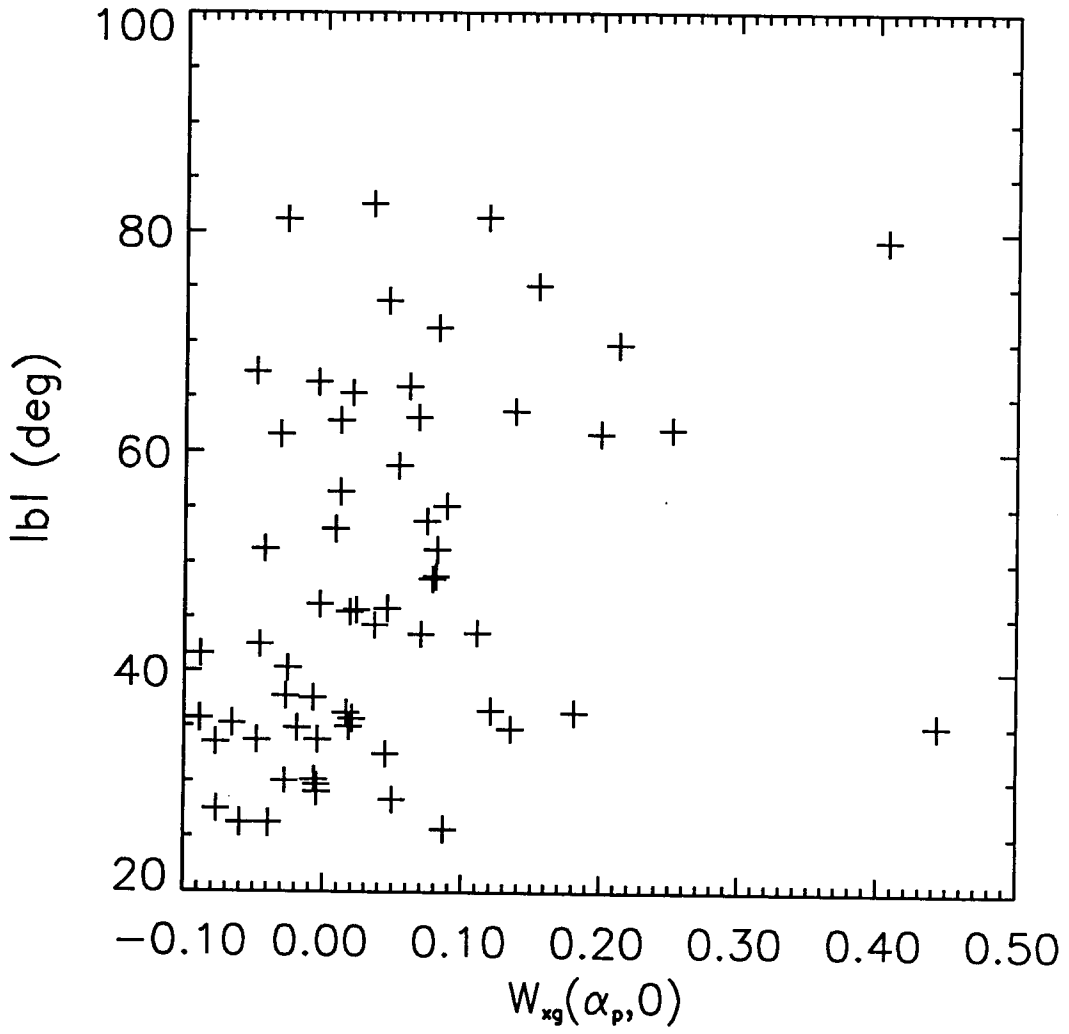

Fig. 4b.—

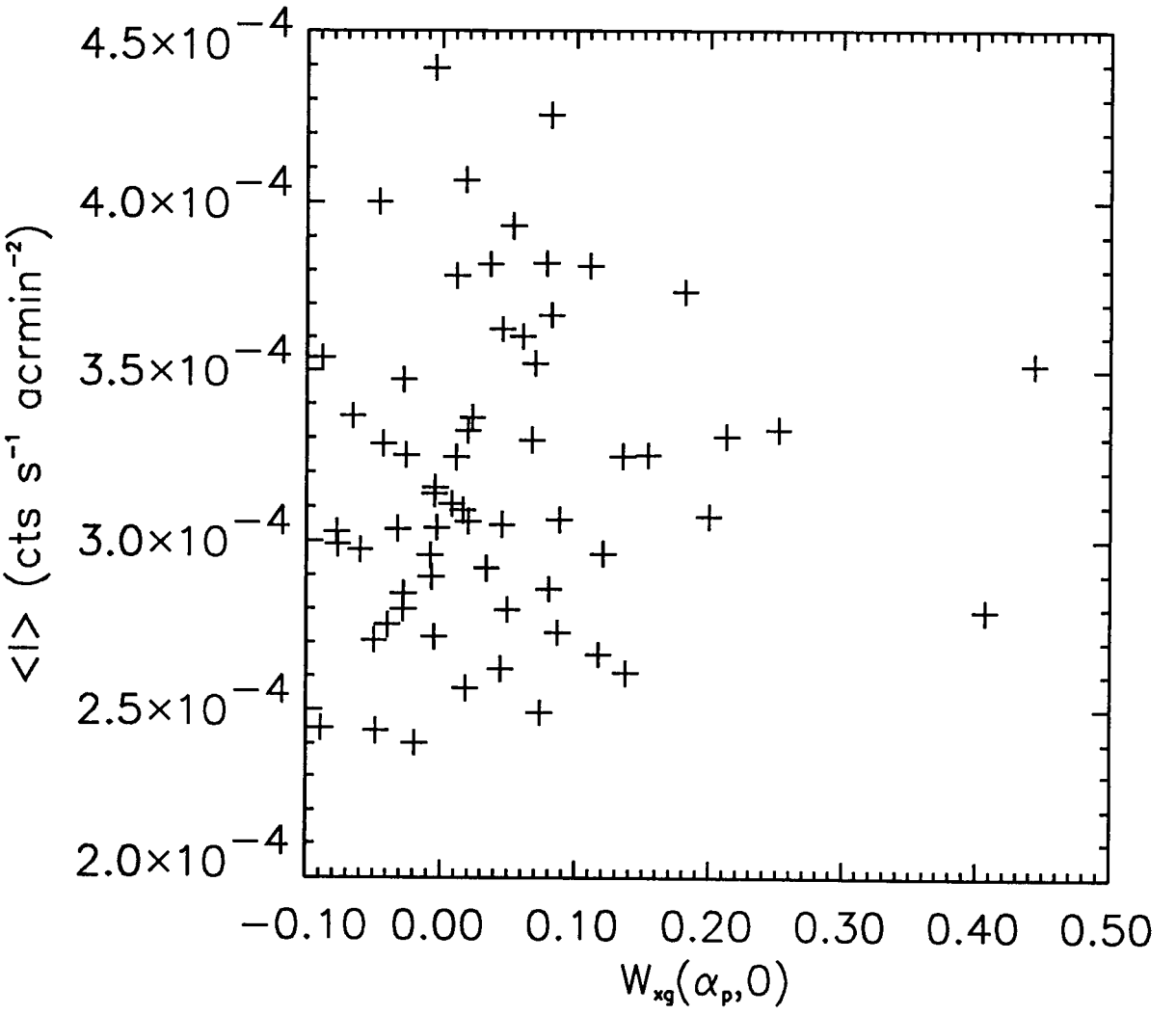
4.5×10⁻⁴
4.0×10⁻⁴
3.5×10⁻⁴
3.0×10⁻⁴
2.5×10⁻⁴
2.0×10⁻⁴
<I> (cts s⁻¹ acrmin⁻²)
−0.10
0.00
0.10
0.20
0.30
0.40
0.50
W_xg(α_p,0)

Fig. 4c.—

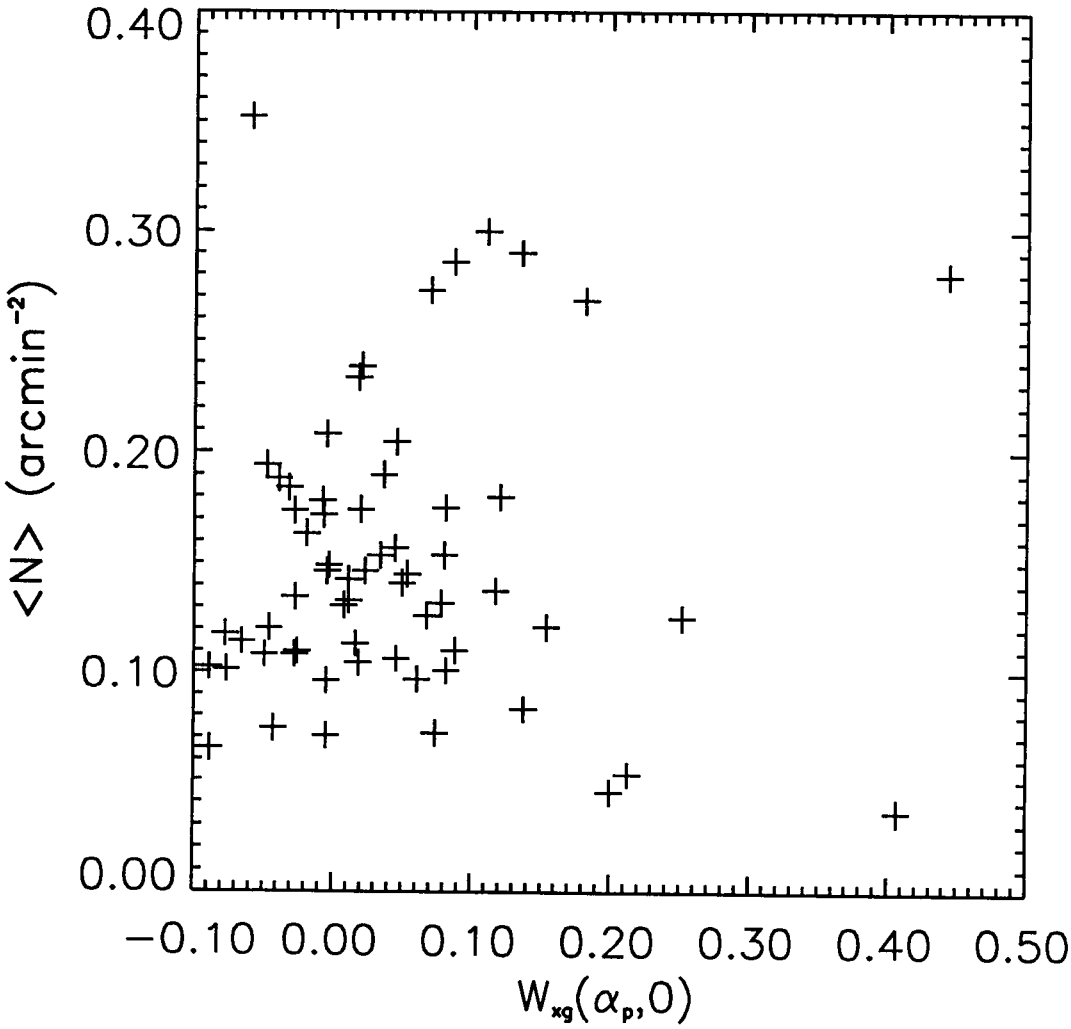
0.40
0.30
0.20
0.10
0.00
<N> (arcmin^{-2})
−0.10
0.00
0.10
0.20
0.30
0.40
0.50
$W_{xg}(\alpha_p, 0)$

Fig. 4d.—

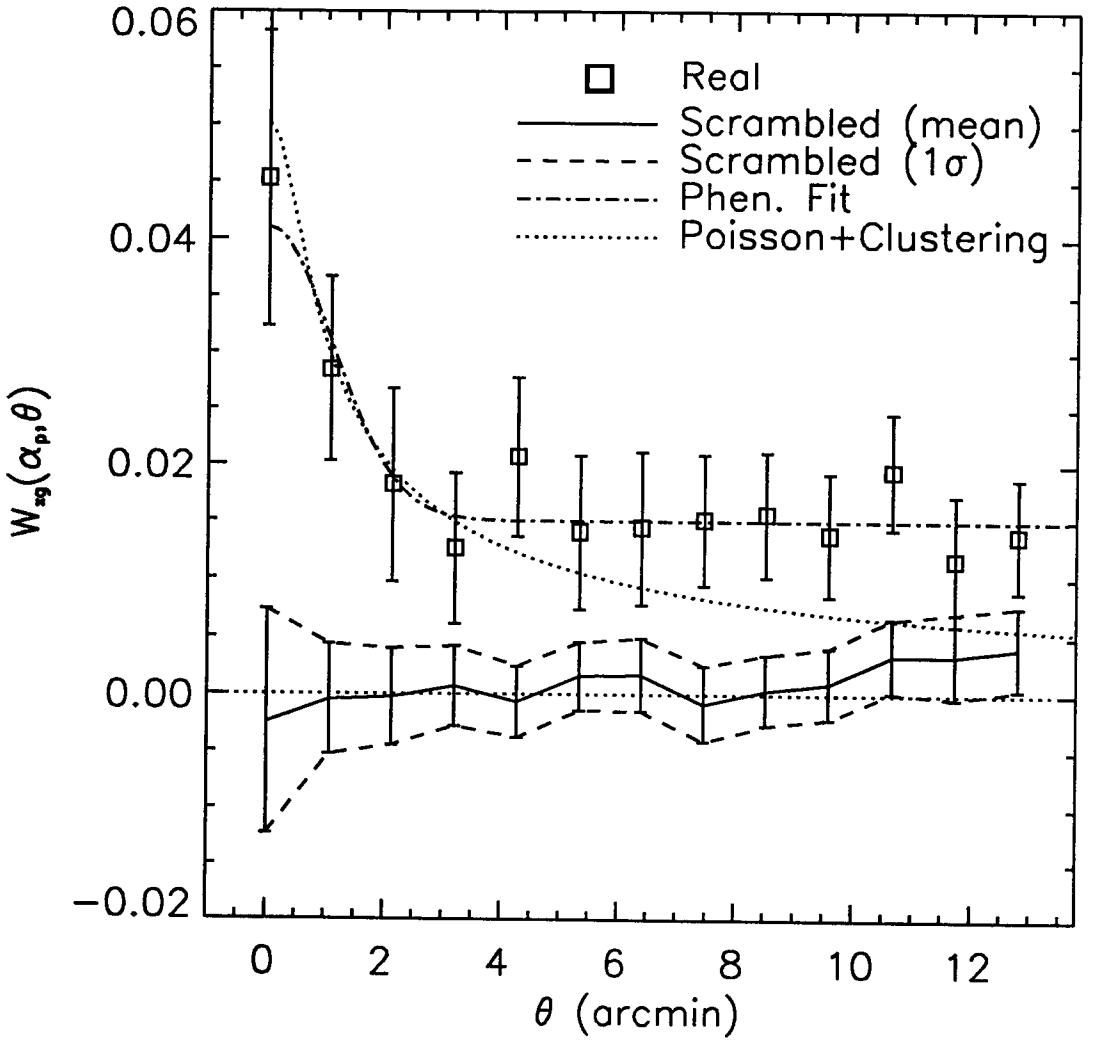

Fig. 5.— Non-zero lag results. $W_{xg}(\alpha_p, \theta)$ vs. θ for the real and the scrambled data set. The dot-dashed curve shows the result of a phenomenological fit used for a comparison with the zero-lag results. The dotted curve corresponds to the best fit to the Poisson + clustering terms, while constraining the fit parameters to be positive.

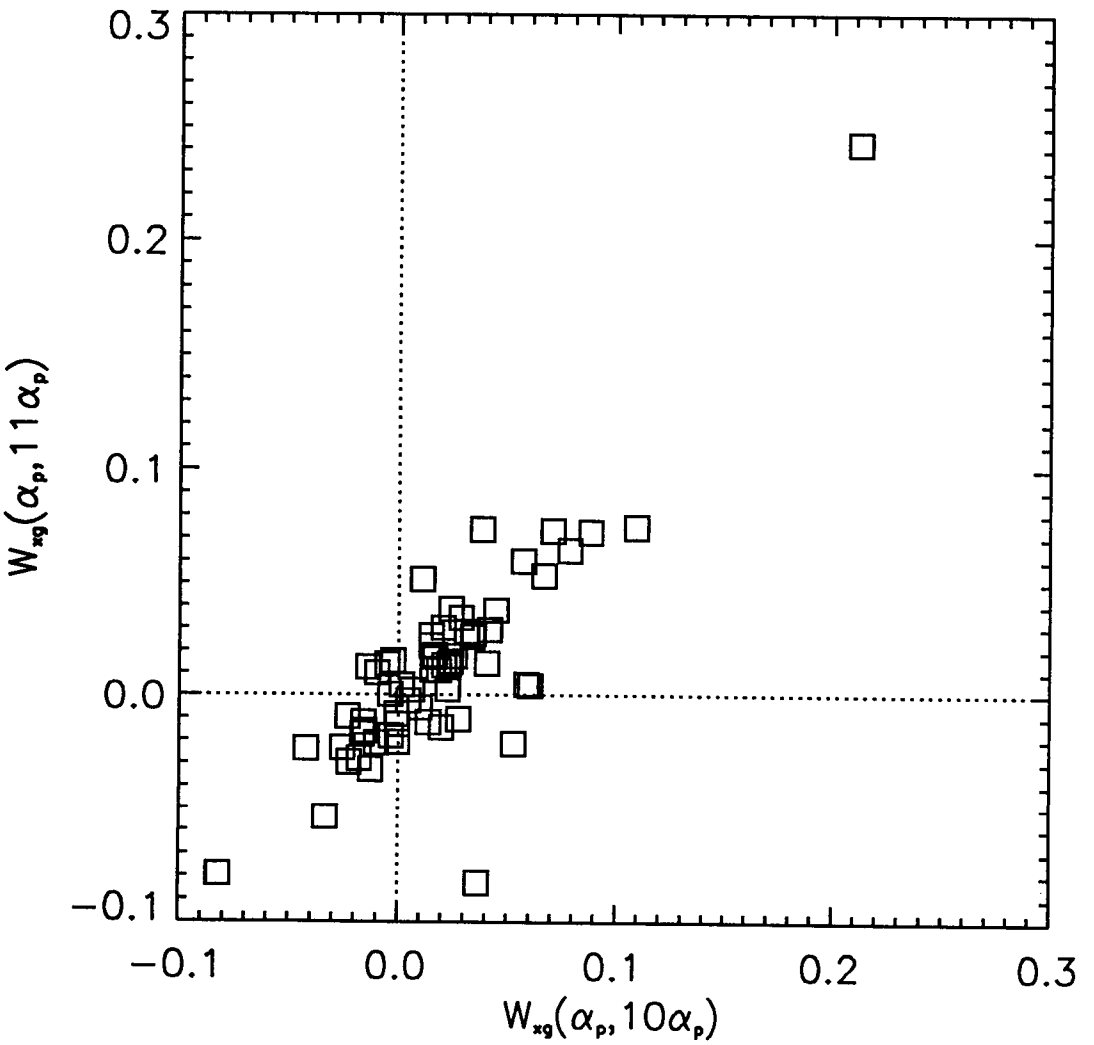

Fig. 6.— Illustration of the correlation between measurements of $W_{xg}(\alpha_p, \theta)$ at different values of θ. For each of the 62 fields, W_{xg} at $\theta = 10\alpha_p$ is plotted against that at $\theta = 11\alpha_p$.

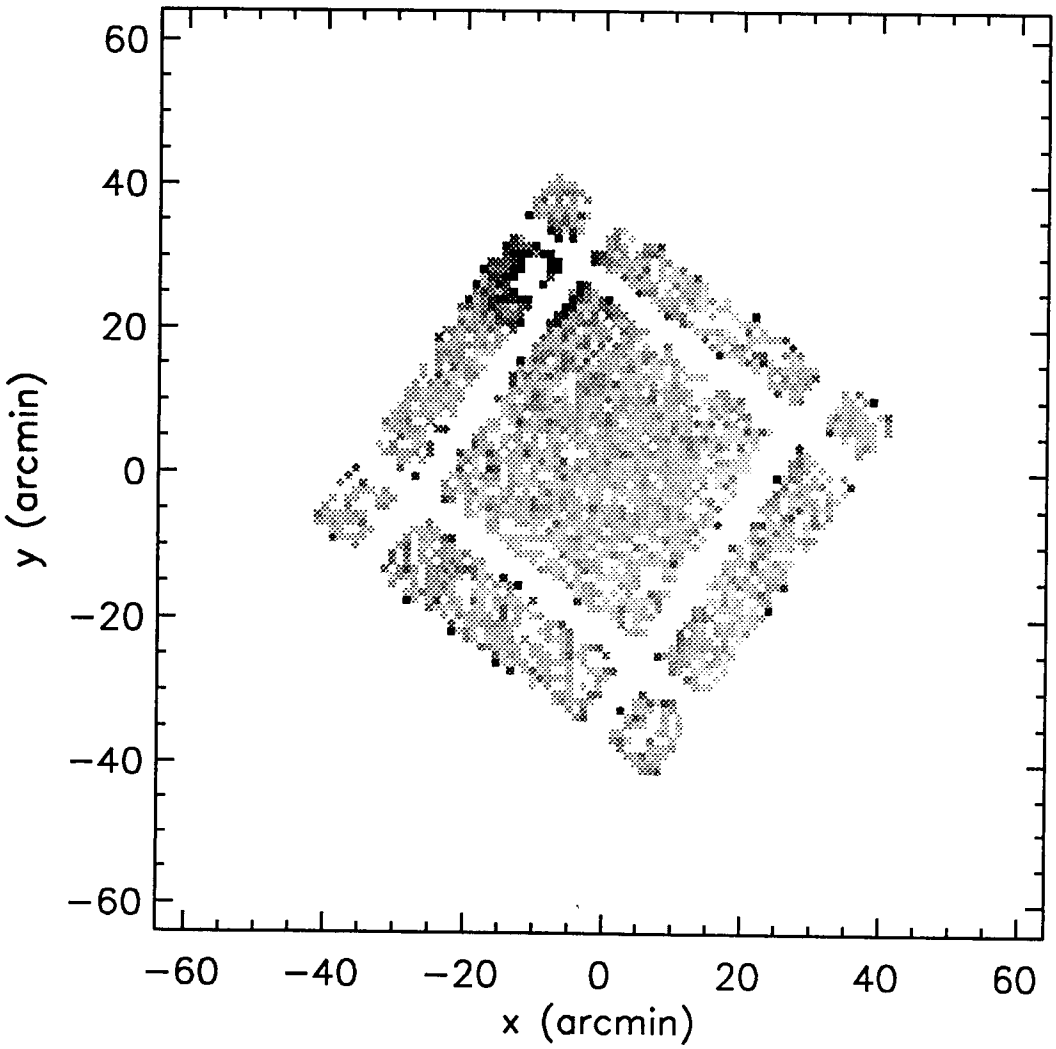

Fig. 7.— Field with sequence number 8926. For clarity, the .81-3.5 keV XRB intensity (a) and the distribution of galaxies with $13.5 < E < 19.0$ (b) are shown separately. This field has the highest non-zero lag correlation in our data set. A cluster of galaxies is visible in the upper left-hand corner.

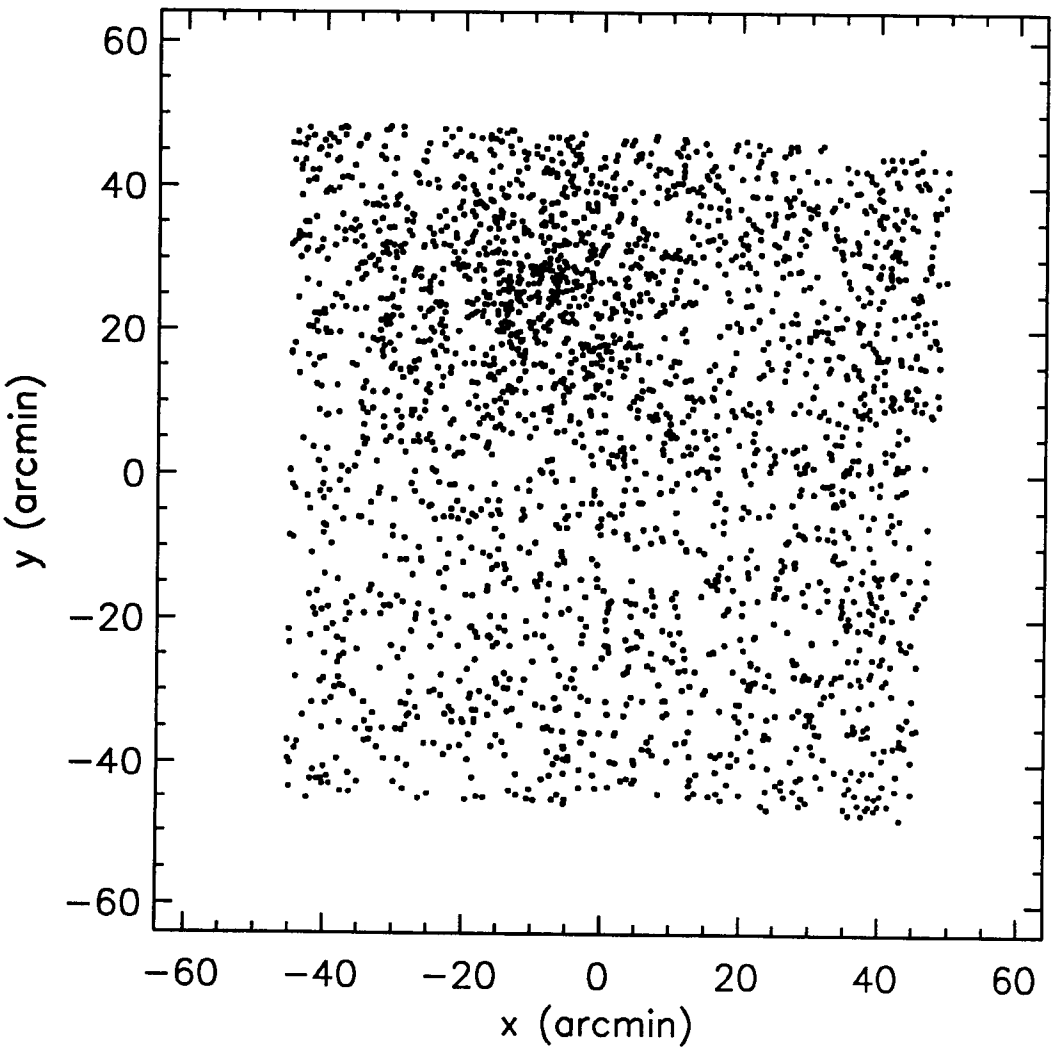

Fig. 7b.—

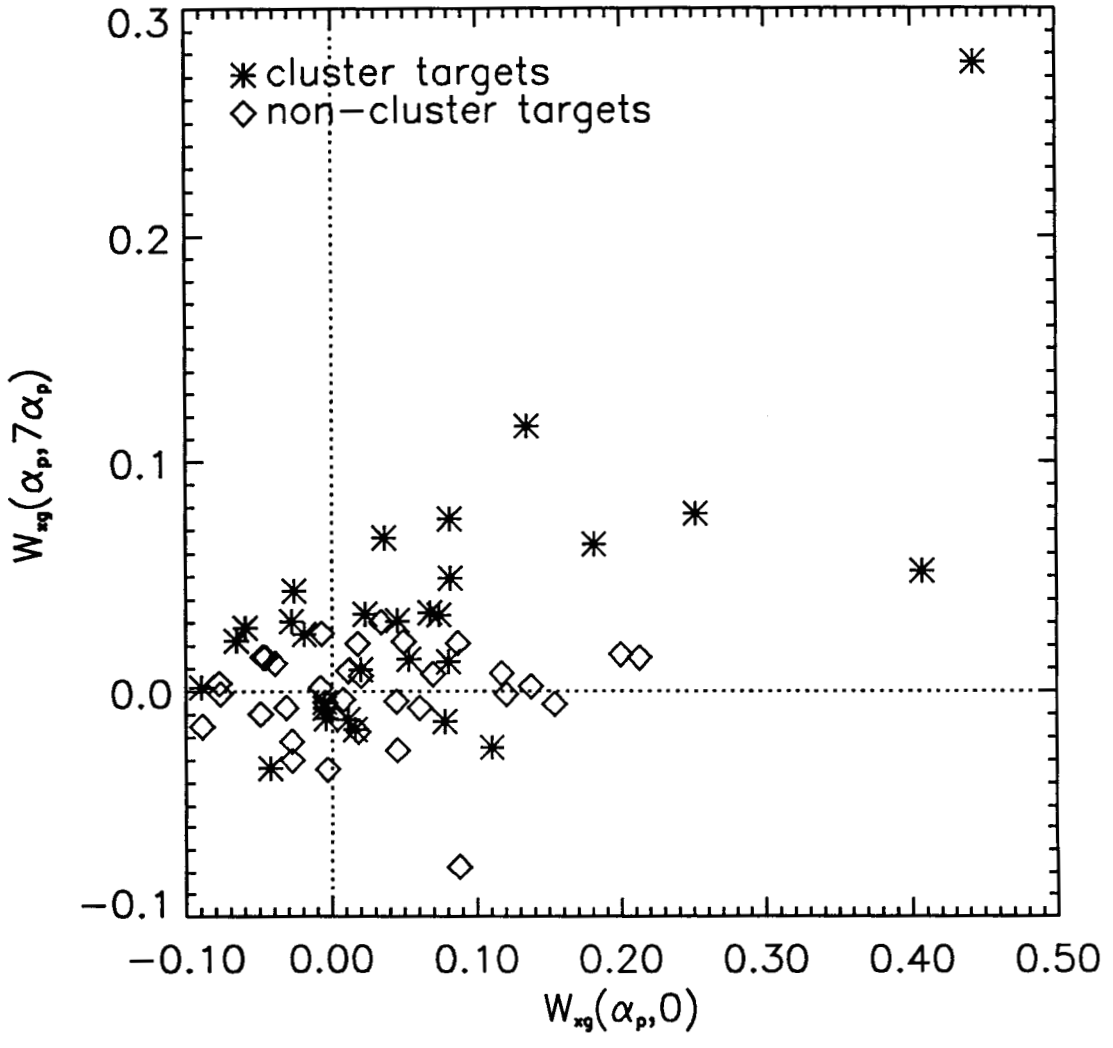

Fig. 8.— Zero-lag vs. Non-zero lag values of W_{xg} for each field. $W_{xg}(\alpha_p, 7\alpha_p)$ is taken as representative of the non-zero lag value. Fields with clusters and non-cluster *Einstein* targets are displayed as stars and diamonds, respectively.

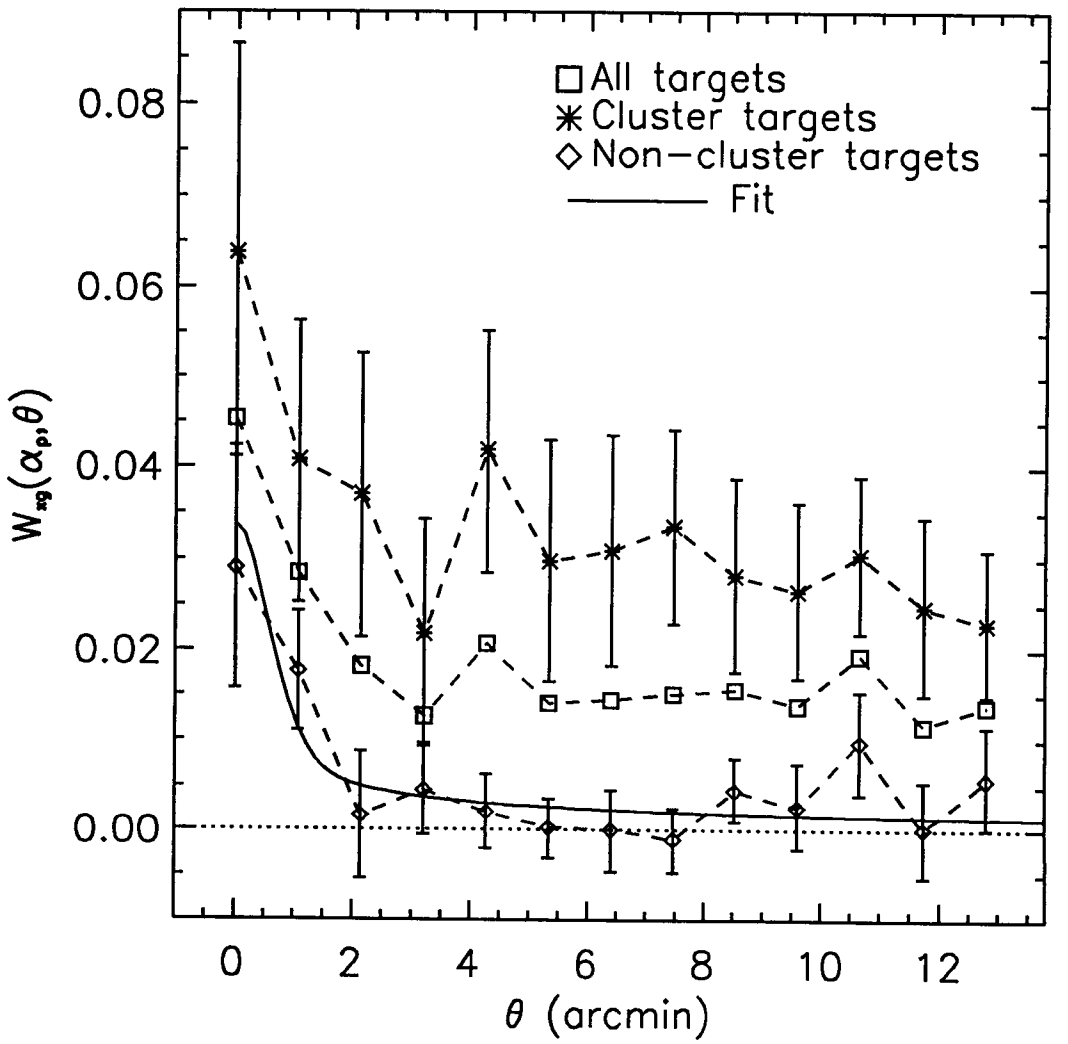

Fig. 9.— Non-zero lag results for cluster and non-cluster targets separately. The value of W_{xg} for all fields combined is redisplayed for comparison. The solid line is the best fit of the Poisson + clustering terms to the non-cluster target field values.

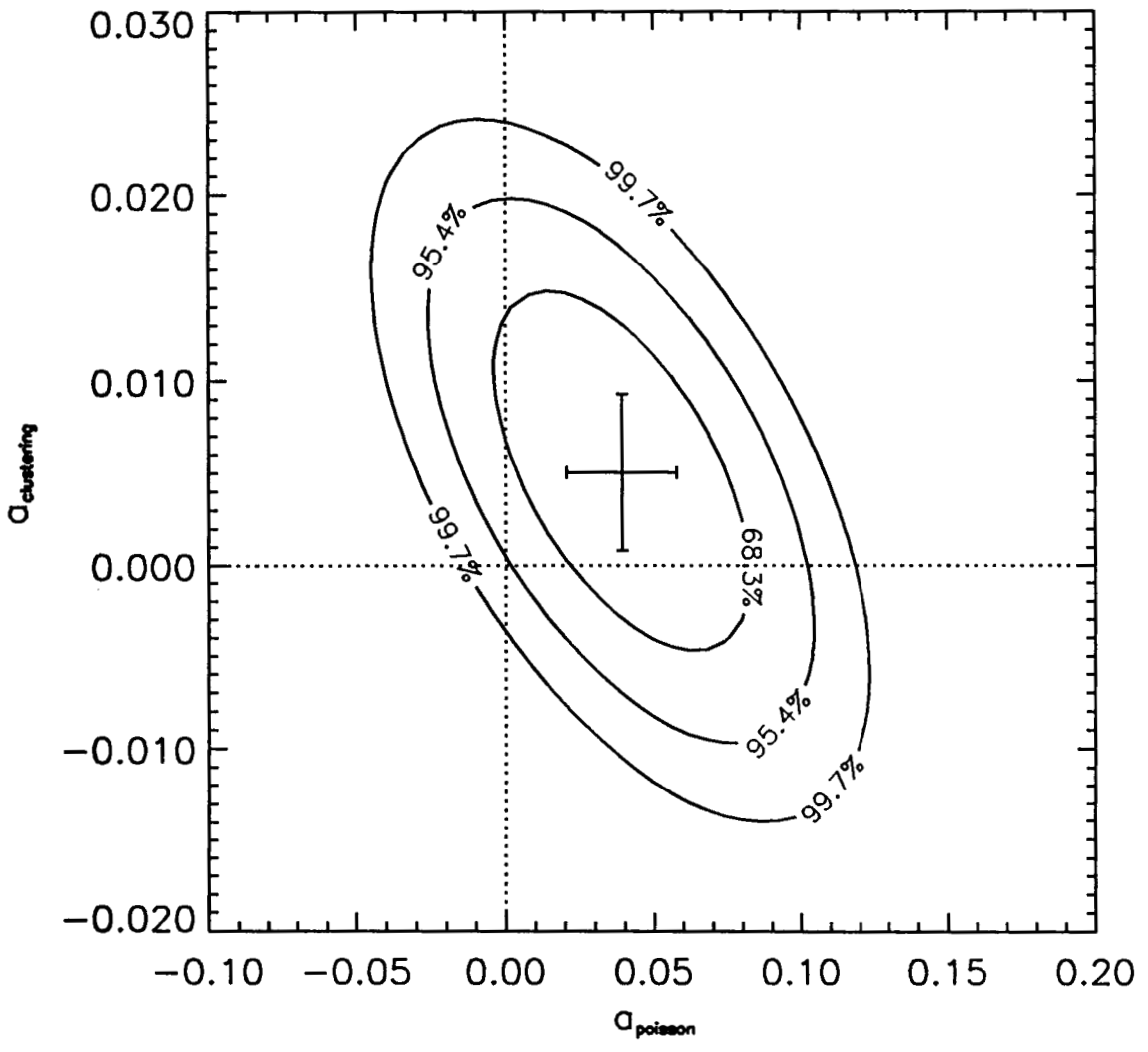

Fig. 10.— Confidence contours for the fit of the Poisson + clustering terms to the non-cluster fields values of $W_{xg}(\alpha_p, \theta)$. The best fit parameters and their associated error bars are displayed as the cross.

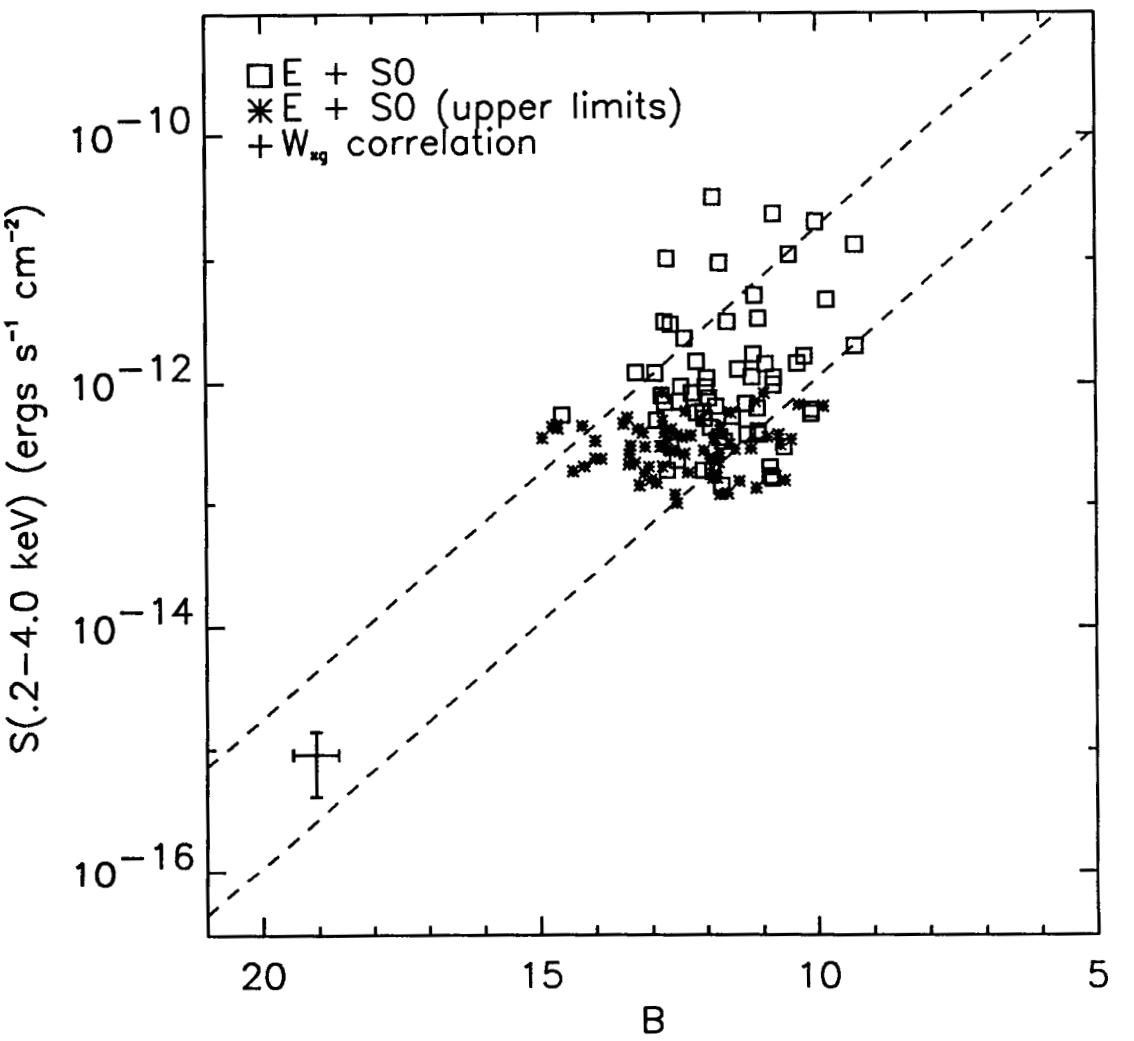

Fig. 11.— Apparent B-magnitudes and X-ray fluxes for the galaxies in the catalog of Fabbiano et al. (1992). The values are shown separately for: (a) Spirals and Irregulars, and (b) Ellipticals and S0s. The dashed lines correspond to the 1σ limits for each of these types of galaxies, assuming a constant X-ray-to-optical flux ratio. The value of the mean galaxy flux derived from our cross-correlation analysis is indicated as the cross.

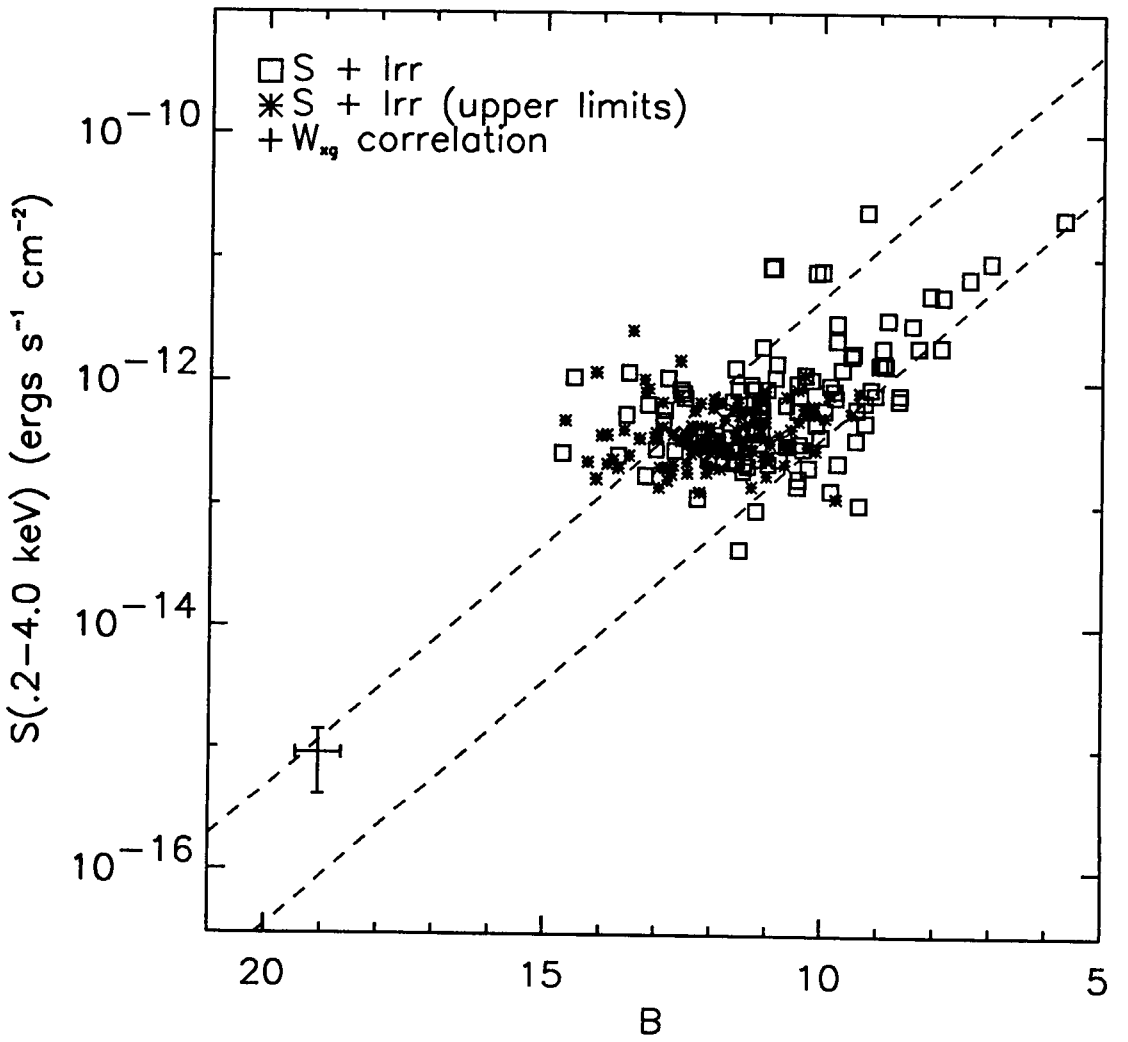
□S + Irr
✱S + Irr (upper limits)
+ W_{xg} correlation
10^{-10}
10^{-12}
10^{-14}
10^{-16}
S(.2–4.0 keV) (ergs s^{-1} cm^{-2})
20
15
10
5
B

Fig. 11b.—

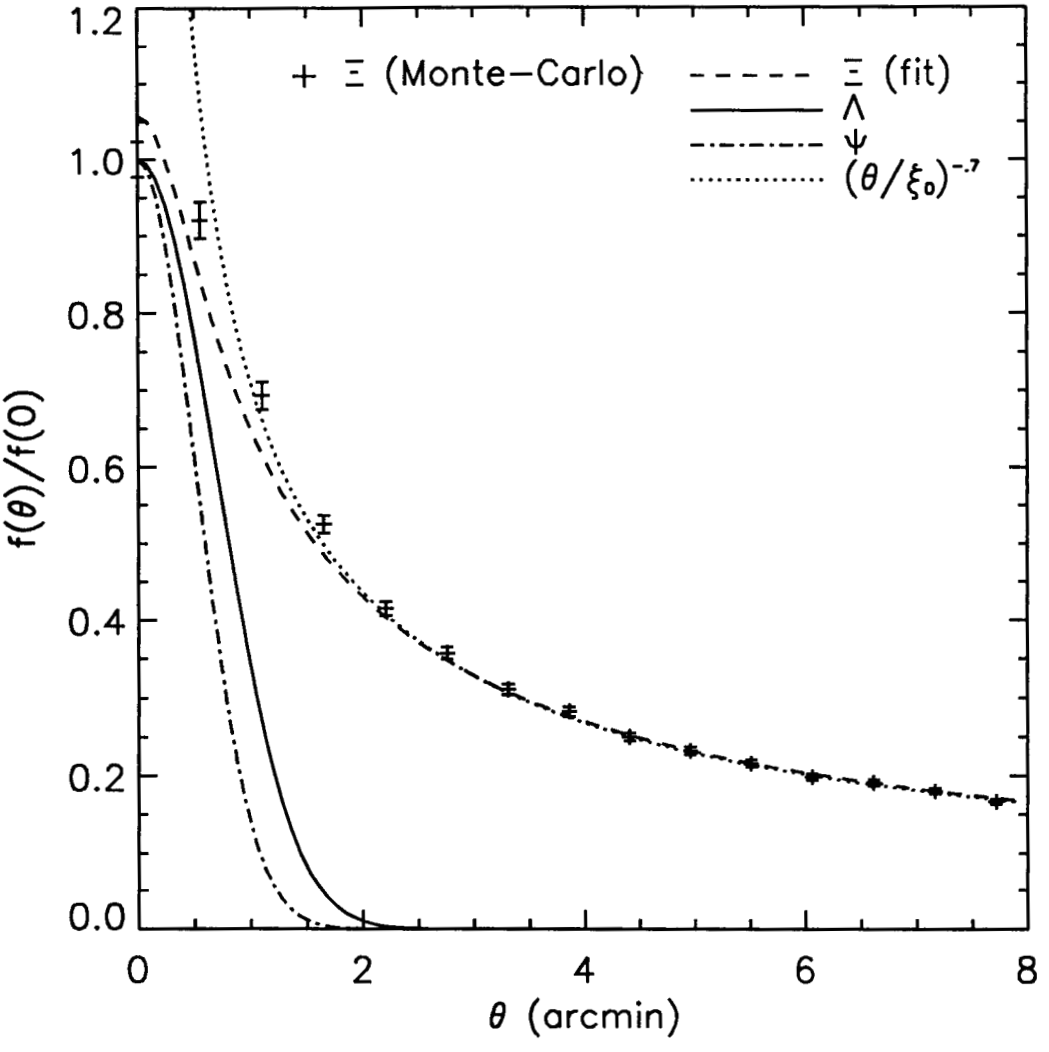

Fig. 12.— Functions used in the interpretation of W_{xg} for parameters relevant to our study, i.e. for $\alpha = \alpha_p = 64''$, $\sigma = \sigma_{psf} = .5'$, and $\beta = .7$. The dot-dashed curve is the PSF. The solid curve is $\Lambda(\alpha, \sigma, \theta)$. The crosses are the result of the Monte-Carlo evaluation of $\Xi(\alpha, \sigma, \beta, \theta)$ with error bars corresponding to 2σ limits. The dashed curve is the analytic function used to model Ξ. For comparison, the asymptotic form $(\theta/\xi_0)^{-\beta}$ is displayed as the dotted line. All functions have been normalized to one at $\theta = 0$. The actual normalizations are $\Lambda(0) \simeq .551$ and $\Xi(0) \simeq 1.480$.

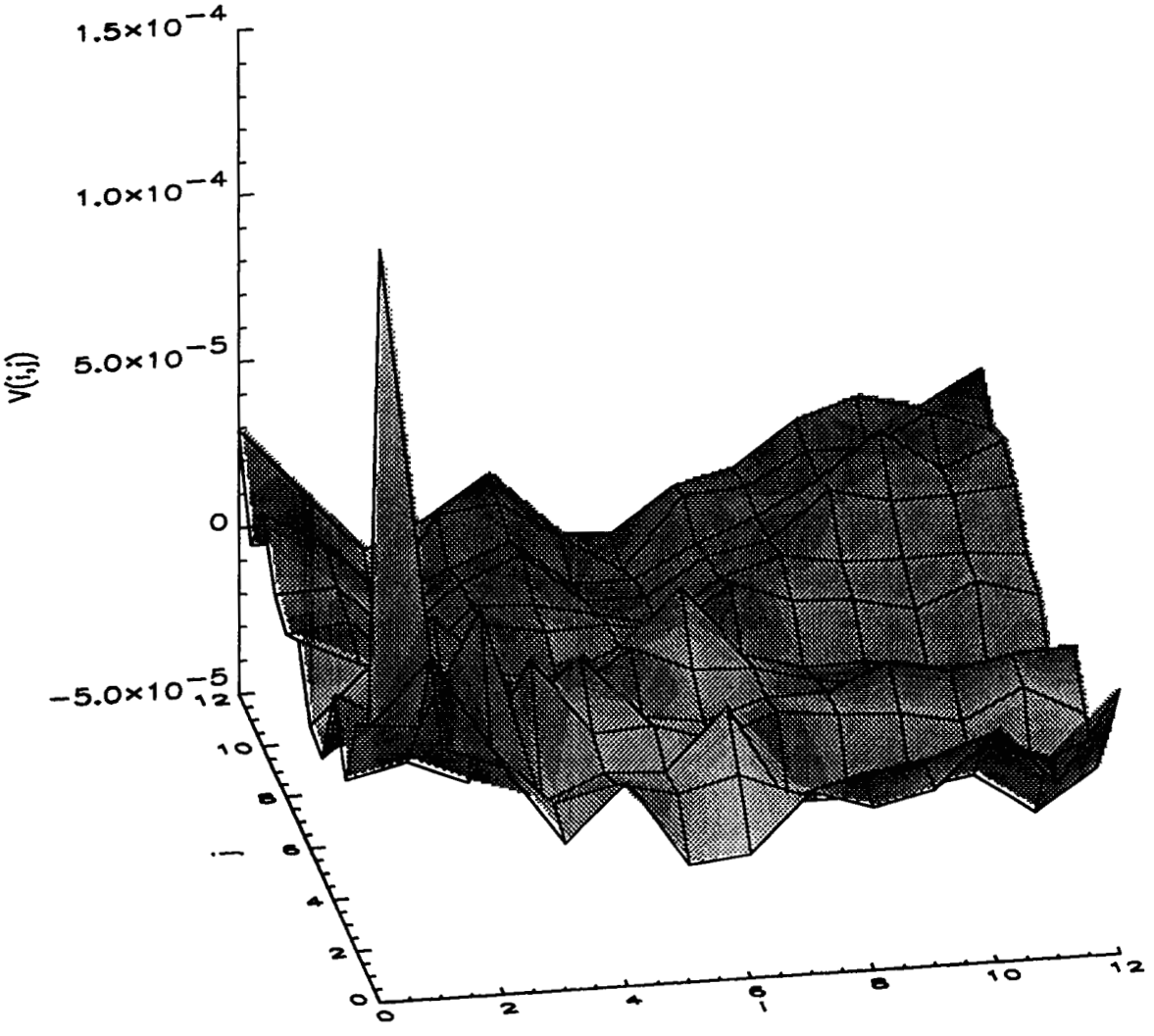

Fig. 13.— Covariance $V(i,j)$ of $W_i \equiv W_{xg}(\alpha_p, \theta_i)$. The indices i and j correspond to θ/α_p.

A Survey of the Einstein IPC Database for Extended X-ray Sources

B. R. Oppenheimer[1], D. J. Helfand

Department of Astronomy, Columbia University,

538 West 120th Street, New York, NY 10027

and

E. J. Gaidos

Department of Physics & Center for Space Research,

Massachusetts Institute of Technology, 77 Massachusetts Ave.,

Cambridge, MA 02139

Received _____; accepted _____

[1]current address: Department of Astronomy, California Institute of Technology, 105-24, Pasadena, CA 91125

ABSTRACT

We present the results of a new analysis of the entire set of data collected by the Imaging Proportional Counter (IPC) on board the Einstein Observatory. Our survey is distinct from previous work such as the Einstein Extended Medium Sensitivity Survey (EMSS) in that it is designed to find extended sources and diffuse emission rather than point sources. In addition, the source detection algorithm is substantially improved over that used for the EMSS. We have searched for sources using circular apertures with radii of 1.25′, 2.35′, 4.20′ and 6.10′. We have constructed criteria to ascertain which of the detections are truly diffuse and which of the sizes best approximates each detection. Using these criteria we have produced a catalog of 1326 extended source candidates at high Galactic latitude ($|b| > 20\,\mathrm{deg}$). Cross-correlating this list with existing source catalogs yields a reasonably comprehensive identification of the known sources in our list. We find that 354 sources coincide with Abell clusters of galaxies, and 48 more with Zwicky Clusters that are not also Abell Clusters. Other objects are identified with galaxies, supernova remnants, AGN, and stars; the first two categories are often truly extended objects, while the latter two sets of objects can appear extended as a consequence of their soft X-ray spectra and the broad point spread function of the IPC at low energies. A total of 321 extended sources remain unidentified. Many of these may be heretofore uncataloged clusters and groups of galaxies at moderate redshifts.

1. Introduction

Fifteen years ago, The Einstein Observatory completed a three-year program of pointed observations that provided the first arcminute-resolution images of the X-ray sky (Giacconi et al 1979; Elvis 1990). To date, however, no comprehensive survey of the Einstein Imaging Proportional Counter (IPC) database has been undertaken to search specifically for patches of diffuse emission or discrete extended X-ray sources. Previous analyses of these data employed search algorithms which were designed to find point sources. Of great importance in this regard are the Extended Medium Sensitivity Survey (EMSS) which provides a catalog of point sources for a subset (one-third) of the IPC data (Gioia et al. 1990; Stocke et al. 1991), and the Two-Sigma Catalog of Moran et al. (1996) which extends this discrete source survey to a larger number of fields and to fainter flux levels. Clearly, however, the algorithm most sensitive to finding point sources will not be optimal for finding extended sources, and may even miss some altogether. For this reason we have designed a new source detection algorithm which can find sources of any size with good sensitivity and have applied it to the complete set of 4100 IPC observations. Moran et al. (1996) provide a complete description of this algorithm and a detailed comparison of it with the EMSS algorithm in the point source domain. Herein, we describe a survey of the IPC data which uses this algorithm to find extended sources at high Galactic latitude, and then determines their identity using catalogs of objects observed at other wavelengths.

Besides the obvious motivation for this work—to complement the various existing point-source catalogs—we believe that this catalog of diffuse and extended sources will be particularly useful in studies of the X-ray evolution of galaxy groups and clusters. It is likely that many of the unidentified, extended sources that we find will reveal themselves to be clusters of galaxies in optical follow-up work. These clusters of galaxies are, necessarily, not present in the Abell and Zwicky catalogs. As a result, they ought to be optically fainter,

and perhaps younger, clusters of galaxies with substantial X-ray luminosities. Therefore, our catalog of X-ray sources may probe the properties of galaxy clusters with higher redshift and less-evolved populations than previously possible. The certainty of this statement can be affirmed with optical observations. Indeed, Tucker et al. 1995 conducted a similar, but much more restricted study of this nature. They found that optical followup observations of 10 of their candidate extended X-ray sources were in fact due to clusters of galaxies. Thus, it would seem that a much larger, more comprehensive search through the Einstein IPC data is waranted. Furthermore, because our survey places fewer *a priori* constraints on the morphology and sizes of the sources it finds, the possibility of finding new types of diffuse X-ray sources exists.

In order to identify the extended X-ray sources we find, we have cross-correlated our catalog with a number of other catalogs of Galactic and extragalactic objects. The final product of this research, then, is a list of extended X-ray sources detected with the IPC along with any identifications provided by the various catalogs. Observation of the unidentified X-ray sources at other wavelengths, particularly in the optical, could lead to interesting discoveries, including, perhaps, an improved understanding of the X-ray evolution of galaxy clusters.

In Section 2 of this paper, we describe the survey methodology, including the source detection algorithm, the procedures for removing duplicate and spurious sources, and the mechanism for selecting out extended sources. Section 3 briefly summarizes the statistics of the identified component of the catalog, while section 4 discusses comparisons with the Einstein Extended Medium Sensitivity Survey (Gioia et al. 1991) and the ROSAT All-Sky Survey (Voges et al. 1996), and offers a few comments on the utility of our new catalog. We conclude with a summary of this work and access information for those interested in using the catalog.

2. The Survey Methodology

2.1. Source Detection Algorithm

A survey of this nature requires the construction of a detection algorithm sensitive to faint, diffuse sources. The algorithm we use is a slightly modified form of the one implemented by Moran et al. (1996) to generate their Einstein Two-Sigma Catalog. Briefly, the distinctions between our procedures and the standard Einstein processing system include the application of a flat field to compensate for IPC detector nonuniformities, improved data editing, a circular (rather than square) source aperture, a local background determination for each search cell, and an iterative source search algorithm. The modifications to this new procedure required for the current application simply entail provisions that allow one to search for sources of any size.

We surveyed the IPC data four times, each time for a different source size, or detection aperture. For each aperture, we kept a record of every source detected with a significance of greater than 2.5σ. This is necessary so that the behavior of signal-to-noise ratio as a function of aperture size can be used later in establishing actual source size. For construction of the final catalog, however, a substantially higher, aperture-dependent σ threshold was adopted (see below).

The smallest aperture we used has a radius of $1.25'$, the optimal size for a point-source, as determined by the point spread function of the telescope (see Hamilton et al. (1991) for a justification of this choice); the background annulus extends from $3'$ to $6'$ as in Moran et al. (1996). The other three apertures have radii of $2.35'$, $4.20'$ and $6.10'$. The four aperture radii represent a rough linear progression in their square roots, with some rounding due to the image pixel size. The background annuli for these large apertures are correspondingly larger such that the area in the annulus (and, thus, the statistical uncertainty in the background

determination) is roughly the same for all four apertures. An extended source detected with the four radii indicated above ought to show an increase in significance out to the limiting radius of the object. Beyond this radius, the significance should drop rapidly as more background flux is included in the source aperture. Thus, by examining the progression of the signal-to-noise ratios for a given source as it is detected in each of the four apertures, we can ascertain whether the source's X-ray emission is point-like or extended.

There are several reasons this method was chosen over one which, for example, might conduct a two dimensional (2D) gaussian fit to every source detected. Foremost among the reasons is that a 2D gaussian fit makes rather strong constraints on the source morphology. Many extended X-ray sources are known which would clearly not be well modelled by such constraints. For example, many supernova remnants limb-brightened, irregular shapes. Further, because of the size of the IPC database (more than five gigabytes), a 2D gaussian fitting algorithm would be considerably more time-consuming.

2.2. Removal of Spurious and Duplicate Sources

After generating four large lists (one for each aperture) of source candidates greater than 2.5σ above background, we proceeded to limit the number of spurious sources and, for a source that appears in more than one of the four lists, to decide what sky position to use to represent the source in the final catalog. We did this in several steps.

First, we have adopted the same requirements as Moran et al. (1996) on the minimum number of usable pixels (i.e., those unblocked by the counter window support ribs or compromised by the presence of a nearby source) in both the source aperture and the background annulus required to admit a candidate to the final source list (60% and 30% of the full areas, respectively). As described in that paper, these requirements result in a significant reduction in spurious detections. For the survey using the $1.25'$ aperture, our search employed

images with 32″ pixels. For the larger apertures, however, we rebinned the data into 64″ pixels because it greatly expedited the search while exacting a relatively insignificant cost compared to the use of smaller pixels.

To reduce further the number of spurious dections, we only used data within the central 38′ x 38′ square of the detector bounded by the window support ribs. In the outer regions of the IPC, the ratio of X-rays to non-X-ray background falls significantly, and large numbers of spurious, low-significance sources swamp the few real detections.

A third and obvious method to remove spurious sources is to increase the signal-to-noise ratio threshold. To this end, a plot of detected source positions as a function of IPC instrumental coordinates is useful. For real celestial sources, such a plot should exhibit an excess of detections at the field center, along with a random distribution of sources scattered over the rest of the field. The central enhancement is a result of the fact that most pointings were targeted at known or suspected X-ray sources. The random component of the distribution, due to serendipitously detected sources, should show an enhanced source density in regions where the instrument is more sensitive; i.e., where the flat-field correction is larger.

Figure 1 shows such plots for all sources detected in each of the four catalogs. Apertures 1 and 2 (with 1.25′ and 2.35′ radii) exhibit some of the more prominent features of the flat-field such as the enhanced sensitivity along the vertical band near the left edge and just to the right of the center. (Figure 4 in Moran et al. (1996) displays a grey-scale plot of the flat-field.) These features are, as expected, harder to see in the plots of source detections for the two larger apertures, because the source size tends to wash out the arcminute-scale detail. Of note in these plots is a distinct clumping of sources in the corners of the detector. These are primarily spurious detections, an artifact of the local background subtraction technique which begins to fail at field edges where the numbers of usable pixels in both the aperture

and the background annulus are near the limits set by the algorithm. Figure 2 demonstrates the effect of increasing the minimum significance requirement on these sources. The first plot shows the aperture 3 (4.20′ radius) detections greater than 4.5σ. The second plot shows aperture 4 (6.10′ radius) detections greater than 5σ. The excess source density in the field corners is essentially gone in these plots, indicating that many spurious sources have been removed.

By examining many plots, such as those in Figure 2, with varying signal-to-noise ratio thresholds, we decided to retain any source such that the aperture 1 (1.25′) detection is greater than 3σ, the aperture 2 (2.35′) detection is greater than 4σ, the aperture 3 (4.20′) detection is greater than 4.5σ *or* the aperture 4 detection (6.10′) is greater than 5σ. As long as the source passed at least one of these three criteria, it would pass this step designed to limit the number of spurious detections in the final catalog. The final catalog, however, includes only sources which appear in at least two of the three larger apertures. This intermediate step, in which we also include the sources that appear in aperture 1, allows us to characterize the differences between point-like and extended sources. (See §2.3)

At this point we removed overlapping sources and combined the four separate catalogs into one master database. Within each of the four catalogs individually, we ascertained which sources overlapped each other based on the aperture radius. We then retained only the one source with the highest signal-to-noise ratio in each set of overlapping sources. After doing this for all four catalogs, we determined which sources from each catalog fell inside sources in the other catalogs. Using this information, we generated a single, large catalog. For each source, a position is listed, along with the signal-to-noise ratio and the flux calculated in each of the four apertures (with a null value listed when a given source was not detected in a particular aperture). In cases where several smaller sources sat within a larger source, we would use list the highest signal-to-noise ratio among the smaller sources. The positions are the averages of the positions of up to four detections (one in each aperture), weighted

according to the position variances which we define as r_i^2 / σ_i^2, where r_i is the radius of aperture i, and σ_i is the signal-to-noise ratio measured for aperture i.

Since we are looking for unidentified, extended sources, we excised from the list sources with galactic latitude within 20 degrees of the galatic equator or whose average photon-counting rates exceed 3 ct/s. Such fields either (1) include bright, well-studied diffuse X-ray sources, (2) contain very bright point sources with significant non-Gaussian point-spread-function wings which arise from scattering of the incident X-rays off mirror imperfections and which are not effectively removed by the source excision algortihm in the search program, resulting in spurious detections of diffuse sources, or (3) have high non-X-ray background rates which also enhance the false source detection rate. The final product is a 7418 entry master catalog. (The full version of this catalog is available in electronic form at http://astro.caltech.edu/$\tilde{}$bro.)

2.3. Selecting Extended Sources

In order to produce a scheme by which we might distinguish a truly diffuse source from a point source, we take advantage of the great effort expended over the last fifteen years in identifying IPC X-ray sources (e.g., Stocke et al. 1991 and references therein). Specifically, we matched our list of 7419 sources with the 2E Catalog available from the Harvard-Smithsonian Center for Astrophysics via EINLINE. All matches were recorded, along with the difference in position between our detection and the EINLINE catalog entry. A total of 241 stars and 193 quasars were identified within 1.5′ of our positions. Furthermore, 484 sources in our master catalog were identified with galaxy clusters within 6.2′(370 within 4.1′; although there are only 268 galaxy clusters identified as such in EINLINE, several of them were detected multiple times because of their large size). Virtually all of the identifications in the 2E catalog are a result of either the detection of the pointing target or individual

spectroscopic followup of serendipitous sources (rather than simply matching catalogs of objects from other wavelength regimes). Therefore, the false identification rate is very low. As a consequence, by comparing how the σ_i values for a known point source (*i.e.* a star or quasar) behave as i increases with the behavior of the σ_i values for known extended sources (*i.e.* galaxy clusters), we can develop criteria for discerning unidentified point sources from unidentified extended sources. To this end, we define the quantity $\sigma_{ij} = \sigma_i \ / \ \sigma_j$, the ratio of a source's σ values in two different apertures. These six ratios provide a simple means to determine the behavior of signal-to-noise ratio as a function of aperture size.

In figure 3, we compare the normalized σ_{ij} distributions for stars and quasars. The two are strikingly similar, as expected for two sets of objects that are both unresolved in the IPC. There is a small, statistically insignificant difference in the mean values for several of the distribution (see Table 1). These differences are, however, in the sense expected and reflect the spectral difference between the two source classes: stars, with softer spectra on average, produce broader point-spread-function distributions due to the poorer electron cloud localization in the IPC for low-energy photons. Given the small differences these spectral distinctions make, as well as the fact that the extended sources for which we are searching can be expected to have a wide variety of spectral temperatures, we sum the σ_{ij} distributions of these two source types to produce our point-source template distributions.

Figure 4 displays these point-source distributions plotted together with our measurements of the σ_{ij} distributions for the galaxy clusters found in the 2E catalog. The dramatic difference is immediately apparent. The cluster distributions are much broader, reflecting the range of intrinsic cluster X-ray emission profiles, and the means are at much lower values (Table 1), demonstrating the increase in signal-to-noise as more source flux is included with increasing aperture size (and less source flux is included in the background annulus).

In order to isolate the truly extended sources in the catalog, we derive criteria for

separating point-like and extended sources using the σ_{ij} distributions. The intention is to produce a final catalog of truly extended sources with little contamination by point sources. We thus assign "cutoff ratios" for the σ_{13}, σ_{14} and σ_{24} distributions, in which the point source distributions are quite well separated from the cluster distributions. The "cutoff ratios" used are 0.75, 0.70, and 0.85, respectively. The meaning of the "cutoff ratios" is the following: If an object is detected in all four apertures, or any subset of the apertures for which any of these three σ_{ij} exists, and its existing σ_{13}, σ_{14} and σ_{24} fall below the corresponding "cutoff ratios," it is far more likely to be an extended source than a point source.

The "cutoff ratios" were selected by chosing the point in the plots in Figure 4 where the point source distribution crosses the cluster distribution. This effectively treats the distributions as probability distributions. Thus, in the region below the "cutoff ratio" a given source is more likely to be extended than point-like. In §4 we estimate the degree of contamination by point sources in the final catalog.

The result of applying these cutoff ratios to our master catalog is the Einstein Extended Source Survey (which we dub the EXSS). To produce the EXSS, we took sources from the master catalog only if they obeyed the following set of rules: (1) it appears in all four apertures and has σ_{13}, σ_{14} and σ_{24} which are less than the corresponding "cutoff ratios"; or (2) it appears in only two of the three largest apertures and still obeys the applicable "cutoff ratios." No sources detected in aperure 1 only were retained. We also removed any sources in the vicinity of the Large Magellanic Cloud, the Small Magellanic Cloud, the Hyades and the Virgo cluster. Any source appearing in only one of apertures 2, 3, or 4 was saved in a separate list. There are 333 such sources. The EXSS catalog contains 1326 sources. These catalogs can be obtained in electronic form at http://astro.caltech.edu/~bro.

3. Previously known EXSS sources

To optimize the efficiency of our optical followup program designed to find heretofore unknown, X-ray-selected galaxy clusters and groups, we identified as many of the extended source candidates as possible.

Obtaining the Abell and Zwicky catalogs of galaxy clusters from HEASARC, we identified every EXSS source within 12′ of the central position of an Abell cluster or closer to a Zwicky cluster than the quadrature sum of 6′ and the size of each Zwicky cluster. 273 sources were coincident with Abell Clusters and 120 with Zwicky Clusters. 47 sources were identified through cross-correlation with the EMSS catalog and 183 with the EINLINE catalog.

Cross-correlation with the Positions and Proper Motions catalog (Röser & Bastian 1991) found 115 sources coincident to within 3.0′ of stars. In an attempt to identify the remaining 835 unidentified, extended X-ray sources, we queried the NASA/IPAC Extragalactic Database (NED) We searched with a 12′ radius at each position in our catalog. The result was that of the 835 sources, some 150 contained galaxies that belong to known galaxy clusters, groups or sets of interacting galaxies, including Southern Clusters, clusters in the Catalog of Galaxies and Clusters of Galaxies, Arp's Peculiar Galaxies and the outlying galaxies of some Abell and Zwicky clusters that were not within the radii used above to match Zwicky and Abell Clusters with EXSS sources. Another 323 sources contain one or more galaxies (as found by NED), 37 contain quasars, and 4 are associated with H II regions.

After this elaborate exercise in cross-correlation, the catalog retains 321 unidentified sources. These we put forth as the unidentified subset of the EXSS. The EXSS sources which contain objects in other catalogs we consider identified. Although it is entirely possible that the origin of the X-rays does not lie in the objects found through cross-correlation, in most instances this would be rather difficult to show. Furthermore, since our incentive is to identify previously unknown clusters of galaxies, our optical follow-up program would be

severly hampered if we had to search in areas around large galaxies and bright stars, which very well may be the source of the X-rays detected in the EXSS. We remind the reader once again that these enitre EXSS catalog is available in electronic form for any other conceivable purposes.

Of the 321 unidentified EXSS sources, 124 contain known radio sources and 47 contain known infrared sources (with some overlap between the two sets). 163 contain no cataloged objects in any other wavelength band. We consider the sources which contain infrared sources and radio sources to be unidentified in the sense that their astrophysical nature is unknown. Many of these cases can be explained by chance coincidence: for these 321 sources we searched in NED about 40 square degrees on the sky. Assuming 2.86 Greenbank sources per square degree (Gregory & Condon 1990) and 2 IRAS sources per square degree outside the galactic plane (Beichman et al. 1988), we would expect to find about 80 IRAS sources and about 115 Greenbank sources within the bounds of our X-ray sources. The fact that we find fewer leads us to conclude that it is possible to explain all of these associations as chance coincidences. The small number statistics cannot say whether there are too few of our X-ray sources thus associated.

Table 2 presents a full listing of all 321 unidentified EXSS sources. The table lists for each source the weighted-average position (as described above), the largest signal-to-noise ratio we detected it at, the radius of the aperture with which that detection was made, and the flux measured through this aperture. This radius should be considered our best attempt at measuring the size of the source. In addition, the last field in the table indicates what, if any, type of source (radio or infrared) exists within the unidentified EXSS source. One wishing to know which particular radio or infrared source is responsible for a given association can conduct a simple search in NED using the position listed in Table 2.

4. Brief Analysis

Cross-correlating our EXSS catalog with the the recently published Rosat All Sky Survey Bright Source Catalog (hereafter called RASS; Voges et al. 1996) yields interesting results. Of the 146 EXSS sources coincident with RASS sources, 99 or 68% show source extent beyond that of the ROSAT point spread function. Those that do not have a source extent measurement listed are not necessarily point sources. The extent parameter might not be listed for some other reason specific to each source.

Figure 7 shows that the EXSS aperture number is roughly consistent with the RASS source extent parameter.

A more quantitative analysis of this work can be provided by a direct comparison of the results with the EMSS. First we cross-correlated the master catalog with the EMSS. Some 607 of the 835 EMSS sources are identified with sources in our master catalog. (The other 228 sources were not found because they lie outside the rib structure of the IPC, areas excluded from our search. In Figure 5 we have plotted our best signal-to-noise ratio versus the EMSS signal-to-noise ratio for each of these 607 sources. Symbols denote which aperture yielded the best signal-to-noise ratio in our search. Virtually every point in the plot lies above the line of equality. At the low σ end, a few points fall below the line, but these are relative low-significance sources, whose signal-to-noise ratios are very sensitive to the detection algorithm used. Above 10 σ on the σ_{EMSS} axis, only three points fall below the line of equality. The two at about $\sigma_{EMSS} = 18$ are sources that are half-obscured by the rib at the edge of the field we searched. These objects have slightly reduced signals because they are partially cut out by the EXSS search scheme, since it does not use data under the ribs. These two sources correspond to EMSS sources MS0134.4+2027 and MS1332.6-2935. The aperture 4 size source below the line at $\sigma_{EMSS} = 13$ corresponds to the EMSS source MS1701.5+6102. This object appears in several sequence numbers of IPC data. The exposure with the longest

integration time has the object outside the rib structure. This exposure is the one which EMSS used to make its measurements. Since we were restricted to sources within the ribs, we had to use an exposure with a shorter integration time. Therefore, the source has a lower signal-to-noise ratio in our catalog. The same circumstances might explain some of the other, lower-significance points that sit below the line along which σ equals σ_{EMSS}.

What Figure 5 demonstrates without doubt is that our algorithm always achieves higher signal to noise ratios. Furthermore, the use of multiple apertures is shown to be beneficial: Most of the aperture 1 sources are near the line of equality, while the larger aperture sources are farther above the line, in general. The fact that virtually all of the points lie above the line shows that EXSS is far more sensitive to fainter sources. As another example of the value of this new algorithm, we find an average increase of 44.3% in the signal-to-noise ratio for 79 galaxy clusters first detected in the EMSS. Some of these clusters were detected at significance levels 2.5 times higher than their EMSS detections. These successes bode well for our search for X-ray selected clusters amongst the unidentified component of the EXSS.

Indeed, Figure 6 shows a plot similar to that of Figure 5, but in this case, only sources that pass the requirements for being extended are included. In this plot only two points lie below the line. These are both a result of partial obscuration by the ribs because they are so close to the edge of our fields. In this plot, circles surround the points that correspond to galaxy clusters. These are consistently detected with far greater signal-to-noise ratios in our survey. The two aperture-three objects that also sit far above the line are stars. This is expected because stars are typically soft sources. Therefore, bright stars will appear to be extended as a result of the Einstein Observatory optics.

This comparison with the EMSS permits an estimation of the contamination by point sources in the EXSS. In the master catalog of 7418 sources prior to selection of extended sources, 152 sources coincide with EMSS stars, 313 with AGN and 28 with BL Lac objects. In

addition, 79 sources in the master catalog coincide with EMSS galaxy clusters. In contrast, the EXSS (the master catalog after applying our filter for extended sources) has only 6 sources coincident with EMSS stars, 15 with AGN and 1 with a BL Lac object. That is, only about 4% of the point-like objects make it through the "cutoff ratio" filters. In contrast, we retained 27% of the clusters after the application of the filters.

5. Conclusions

The sources we present in Table 2 have a high probability of being real, celestial, extended X-ray sources. They are all extended and as yet unidentified with known astrophysical objects. In some cases they are coincident with unidentified infrared or radio sources. These associations may be the result of chance coincidence. These 321 sources, though, have been selected in an elaborate manner designed to find previously unidentified galaxy clusters. An survey of these sources in optical light should reveal their identity. If they are in fact galaxy clusters, they ought to be of relatively high redshift, in comparsion to Abell Clusters, for example. Identifying such high redshift clusters is important in understanding the much debated issues surrounding galaxy and galaxy cluster evolution.

This research has made use of the High Energy Astrophysics Science Archive Research Center, provided by the NASA-Goddard Space Flight Center. This research has also made use of the NASA/IPAC Extragalactic Database (NED) which is operated by the Jet Propulsion Laboratory, Caltech, under contract with the National Aeronautics and Space Administration. BRO is supported by a National Science Foundation Graduate Research Fellowship. This work was supported by the National Aeronautics and Space Administration under contract NAS5-32063 at Columbia University, and is Contribution Number 6xx of the Columbia Astrophysics Laboratory.

REFERENCES

Gioia, I. M., Maccacaro, T., Schild, R. E., Wolter, A., Stocke, J. T., Morris, S. L., & Henry, J. P. 1990, ApJS, 72, 567

Gregory, P. C. & Condon, J. J. 1990, The 87GB Catalog of Radio Sources (Greenbank, W Va.: National Radio Astronomy Observatory)

Hamilton, T. T., Helfand, D. J., & Wu, X. 1991, ApJ, 379, 576

Beichman, C.A., Neugebauer, G., Habring, H. J., Clegg, P. E. & Chester, T. J., ed. 1988, IRAS Catalogs and Atlases (Washington, D. C.: National Aeronautics and Space Administration)

Moran, E. C., Helfand, D. J., Becker, R. H., & White, R. L. 1996, ApJ, 461, 127

Röser, S. & Bastian, U. 1991, The PPM Star Catalogue (Heidelberg: Spektrum Academishe Verlag)

Stocke, J. T., Morris, S. L., Gioia, I. M., Maccacaro, T., Schild, R., Wolter, A., Fleming, T. A., & Henry, J. P. 1991, ApJS, 76, 813

Tucker, W. H., Tananbaum, H. & Remillard, R. A. 1995 ApJ. 444, 532

Voges, W., Aschenbach, B., Boller, Th., Bräuninger, H., Briel, U., Burkert, W., Dennerl, K., Englhauser, J., Gruber, R., Haberl, F., Hartner, G., Hasinger, G., Kürster, M., Pfeffermann, E., Pietsch, W., Predehl, P., Rosso, C., Schmitt, J. H. M. M., Trümper, J. and Zimmermann, H.-U. 1996, A & A, in press

Elvis, M. 1990 "Imaging X-ray Astronomy" (Cambridge:Cambridge University Press)

Giacconi, R. et al. 1978

This manuscript was prepared with the AAS LaTeX macros v4.0.

Fig. 1.— Locations of source detections greater than 2.5σ on the face of the IPC instrument. (a) 15456 detections with aperture 1, (b) 15265 detections with aperture 2, (c) 16567 detections with aperture 3 and (d) 14048 detections with aperture 4.

Fig. 2.— Locations of source detections on the face of the instrument. (a) 4505 sources greater than 4.5σ detected with aperture 3 and (b) 3740 sources greater than 5σ detected with aperture 4.

Fig. 3.— Normalized distributions of σ_{ij} for sources identified as stars and quasars by EINLINE. The shaded histogram indicates the distribution for quasars. The unshaded histogram corresponds to the stars.

Fig. 4.— Distributions of σ_{ij} for sources identified as galaxy clusters (shaded histogram) and as point-sources (the sum of the two histograms in Fig. 3) by EINLINE.

Fig. 5.— Plot of σ vs. σ_{EMSS}. Solid sqares represent aperture 4 sized sources. Solid triangles represent aperture 3 sized sources, while crosses and open stars represent aperture 2 and aperture 1 sized sources respectively. The diagonal line indicates where σ equals σ_{EMSS}. See §6 for further discussion.

Fig. 6.— Plot of σ_{EXSS} vs. σ_{EMSS}. Symbols have the same meaning as in Fig. 5. This plot only shows extended sources (sources in the EXSS). See §6 for further discussion.

Fig. 7.— EXSS aperture number vs. RASS source size. Aperture number 2 corresponds to 2.35′, aperture 3 to 4.2′, and aperture 4 to 6.1′.

TABLE 1. Mean Values of σ_{ij} Distributions

Object Type	$< \sigma_{12} >$	$< \sigma_{13} >$	$< \sigma_{14} >$	$< \sigma_{23} >$	$< \sigma_{24} >$	$< \sigma_{34} >$
Stars	0.95±0.06	0.89±0.05	0.92±0.06	0.96±0.06	1.00±0.07	1.08±0.07
Quasars	1.00±0.07	0.92±0.06	0.93±0.07	0.94±0.07	0.96±0.07	1.03±0.07
Clusters	0.88±0.06	0.70±0.08	0.62±0.08	0.82±0.08	0.76±0.08	0.93±0.08

TABLE 2. Unidentified Sources in the Einstein Extended Source Survey

R.A. (1950): ^{h}	^{m}	^{s}	Dec. (1950): $^\circ$	$'$	$''$	Ap.	Flux	σ	ID
0	4	34.34	15	49	8.0	4	0.026	4.72	Radio
0	14	10.95	16	13	38.2	3	0.010	5.02	IR
0	18	50.31	1	16	5.8	4	0.031	5.29	Radio
0	19	50.10	-12	45	5.0	4	0.023	5.34	Radio
0	20	0.16	-12	19	34.1	3	0.017	4.56	none
0	26	40.14	88	36	48.9	4	0.024	5.71	none
0	26	45.45	6	9	23.4	4	0.054	5.16	none
0	32	42.85	-7	43	39.3	4	0.049	5.15	IR
0	35	29.21	29	33	48.3	4	0.039	6.73	none
0	37	59.62	40	12	53.7	4	0.016	5.70	Radio
0	39	3.75	40	28	40.2	3	0.008	5.49	Radio
0	42	38.18	0	50	13.6	3	0.050	5.07	Radio
0	45	1.61	24	14	20.3	3	0.032	4.95	Radio
0	45	47.53	-12	13	53.9	3	0.034	4.56	IR
0	49	6.46	88	50	48.7	4	0.020	5.32	IR
0	56	39.04	29	59	18.5	3	0.011	4.86	none
1	4	37.66	-21	39	41.0	4	0.026	4.68	none
1	7	8.16	14	55	13.2	4	0.053	5.29	none [a]
1	14	55.00	-1	3	4.2	4	0.020	5.42	none
1	16	40.61	0	-57	2.3	4	0.028	5.91	none
1	17	17.99	8	14	54.7	4	0.014	6.15	Radio
1	20	32.45	-3	36	21.1	4	0.026	5.80	Radio
1	21	44.20	7	0	4.4	3	0.029	4.31	Radio
1	22	10.80	23	22	2.6	4	0.055	5.50	Radio
1	22	47.94	19	5	47.7	3	0.026	5.98	Radio
1	33	5.48	15	27	15.3	3	0.016	4.65	none
1	34	48.17	-5	4	35.9	4	0.063	6.53	IR
1	34	51.85	15	21	31.4	4	0.022	5.09	none
1	35	1.84	20	32	24.9	3	0.014	4.53	none
1	37	24.49	-18	22	12.3	3	0.023	4.90	Radio
1	38	50.29	4	27	34.9	4	0.044	6.38	Radio
1	39	14.88	-30	25	7.4	3	0.018	6.10	none
1	58	9.75	12	48	26.7	3	0.020	4.50	none
1	59	22.57	-8	51	32.7	3	0.017	4.52	none
2	3	48.39	23	16	32.0	4	0.021	6.25	none
2	4	26.69	-37	50	10.8	4	0.038	5.72	Radio
2	15	1.48	-51	32	13.6	4	0.055	5.63	none
2	24	55.31	-10	41	38.3	4	0.029	6.83	none
2	27	40.80	-12	54	26.1	4	0.052	5.11	none
2	36	46.03	16	33	10.3	4	0.047	5.11	none
2	40	6.10	6	47	10.2	3	0.027	5.68	none
2	55	43.32	20	41	55.6	4	0.033	5.51	none
2	58	3.03	7	29	28.7	3	0.019	5.22	none
2	59	42.27	-14	48	3.3	4	0.026	5.46	IR
3	4	12.56	15	23	7.7	3	0.014	4.82	none
3	5	19.02	-12	26	16.1	3	0.027	4.76	none
3	5	32.87	10	26	10.5	4	0.050	5.49	Radio
3	9	19.88	14	41	46.4	3	0.011	4.81	none

TABLE 2. (continued)

R.A. (1950): h	m	s	Dec. (1950): °	′	″	Ap.	Flux	σ	ID
3	24	37.76	28	23	37.3	3	0.029	4.82	Radio
3	30	26.22	-9	20	38.8	3	0.059	4.71	none
3	32	6.44	-26	2	9.7	4	0.073	5.24	Radio.
3	44	13.75	-25	8	23.1	4	0.060	5.39	IR
3	46	33.64	23	17	28.7	3	0.033	6.73	none
3	46	35.40	17	17	28.4	4	0.061	6.34	Radio
3	52	20.65	2	50	26.4	4	0.071	5.80	none
3	58	46.53	10	25	36.2	3	0.028	4.55	none
4	1	20.22	-36	32	8.8	3	0.034	4.80	none
4	6	26.04	-12	20	50.5	3	0.046	4.71	none
4	10	6.17	7	37	54.6	4	0.038	5.97	none
4	15	26.29	-6	11	53.7	4	0.031	5.15	none
4	15	30.03	-5	49	13.1	3	0.029	4.58	none
4	21	23.31	0	27	31.7	4	0.051	5.36	Radio
4	31	12.13	5	30	30.4	3	0.010	5.05	IR
4	31	33.13	5	8	15.0	3	0.010	5.75	none
4	33	14.13	10	19	39.0	4	0.047	5.17	none
4	33	18.14	-10	21	2.5	4	0.079	5.11	none
4	38	41.93	-15	39	36.0	4	0.023	5.25	none
4	39	22.40	-16	10	17.3	3	0.009	5.64	Radio
4	40	47.34	8	28	50.3	4	0.034	5.30	none
4	45	1.94	-59	37	9.0	4	0.033	6.25	none
4	46	52.27	-59	9	8.3	3	0.025	4.98	Radio
5	2	10.88	-11	54	2.6	4	0.020	6.18	none
5	2	13.55	-12	1	18.3	3	0.017	6.02	none
5	3	35.44	-11	44	9.4	4	0.021	5.58	none
5	9	34.71	-44	57	38.5	3	0.036	4.57	none
5	13	2.88	-8	13	22.3	4	0.043	5.49	IR
5	38	51.76	-44	0	47.3	4	0.033	4.70	none
6	1	9.05	-31	58	52.4	4	0.063	5.50	none
6	14	10.12	-59	8	15.1	4	0.028	5.56	IR
6	14	39.71	-59	23	41.5	4	0.028	5.54	IR
6	15	42.30	-59	32	14.8	3	0.019	4.52	Radio
6	26	35.32	-55	11	11.4	4	0.021	5.26	none
6	35	54.74	-75	32	41.0	4	0.055	4.64	none
6	43	41.43	53	17	36.4	4	0.043	5.07	IR
7	33	44.40	65	30	56.5	3	0.018	4.91	Radio
7	39	42.54	37	46	51.3	3	0.011	4.83	Radio
7	52	53.26	39	23	28.5	3	0.031	5.08	Radio
7	59	40.37	14	22	36.4	4	0.024	5.70	Radio
8	3	15.11	21	21	27.0	3	0.023	4.85	Radio
8	6	23.03	20	57	23.0	4	0.021	5.66	Radio
8	8	48.79	62	59	56.8	3	0.015	4.43	IR
8	8	49.40	66	51	53.0	4	0.029	4.75	none
8	16	49.41	52	53	31.5	4	0.029	5.23	none
8	20	36.58	2	18	13.4	4	0.026	5.16	none
8	23	9.43	26	53	4.3	4	0.026	5.93	Radio
8	23	15.64	29	15	36.2	3	0.015	5.25	Radio.

TABLE 2. (continued)

R.A. (1950): h	m	s	Dec. (1950): °	′	″	Ap.	Flux	σ	ID
8	24	22.27	26	47	11.0	4	0.028	5.78	Radio
8	37	24.85	13	12	58.1	4	0.020	6.68	none
8	41	50.45	19	7	1.9	4	0.028	6.35	none
8	42	1.67	19	16	0.0	4	0.018	5.15	none
8	47	20.79	51	35	20.6	3	0.037	4.94	none
8	48	44.58	33	26	47.4	4	0.085	5.65	Radio
8	52	28.67	6	17	4.2	4	0.039	5.15	Radio
8	59	0.82	-13	59	43.2	4	0.056	5.70	none
8	59	18.33	18	12	47.7	4	0.066	5.10	none
8	59	25.73	-13	47	9.8	3	0.067	5.48	IR
9	7	21.58	2	56	32.8	3	0.025	4.70	none
9	20	21.91	34	33	24.2	4	0.028	5.34	Radio
9	23	47.37	38	57	46.4	3	0.019	5.47	Radio
9	24	42.54	-5	31	40.1	3	0.019	5.22	Radio
9	26	27.61	-5	45	49.6	3	0.019	5.11	none
9	26	55.04	6	17	35.3	4	0.023	5.23	none
9	46	5.96	7	42	48.0	4	0.039	5.21	Radio
9	48	46.43	11	53	22.6	4	0.046	5.85	none
9	51	11.40	44	18	2.1	4	0.043	5.28	Radio
9	54	12.36	32	23	43.2	4	0.047	5.20	Radio
9	54	52.96	22	54	54.2	4	0.041	5.68	none
10	1	1.97	5	14	48.8	4	0.061	4.63	none
10	3	21.13	-29	45	42.3	4	0.049	5.10	Radio
10	4	14.22	1	7	27.6	3	0.035	4.66	none
10	9	47.67	35	16	57.3	4	0.050	5.08	Radio
10	15	36.57	1	18	50.8	4	0.039	5.27	none
10	20	56.40	-10	17	10.2	3	0.034	4.72	Radio
10	28	31.04	31	28	57.5	3	0.018	4.92	Radio
10	29	12.97	31	20	5.6	3	0.018	5.30	IR
10	30	28.42	9	18	34.9	4	0.036	5.95	Radio
10	40	42.63	56	14	45.3	3	0.034	4.92	none
10	43	4.99	9	22	40.3	4	0.022	5.28	none
10	45	52.61	6	59	18.9	4	0.048	5.76	Radio
10	47	12.77	7	0	47.5	3	0.046	5.41	Radio
10	49	22.60	-18	22	30.3	4	0.051	4.94	none
11	6	2.13	37	52	5.4	4	0.026	5.13	Radio
11	9	53.56	-26	17	41.9	4	0.021	5.83	none
11	9	58.96	35	55	37.3	3	0.023	5.11	Radio
11	27	12.44	30	28	17.6	4	0.057	5.24	Radio
11	28	31.62	30	20	16.9	4	0.048	5.13	Radio
11	35	11.09	-8	48	28.6	4	0.033	5.09	none
11	37	51.74	28	59	59.9	3	0.015	4.45	Radio
11	39	2.69	34	25	35.6	3	0.026	4.65	Radio
11	39	24.37	66	11	36.6	3	0.016	4.43	none
11	43	45.37	-28	27	13.6	4	0.060	5.14	none
11	45	13.32	-10	12	55.8	3	0.045	4.75	none
11	45	50.07	0	59	42.0	3	0.017	4.63	Radio
11	56	8.83	-27	14	25.8	4	0.040	6.31	none

TABLE 2. (continued)

R.A. (1950): ^{h}	^{m}	^{s}	Dec. (1950): $^\circ$	$'$	$''$	Ap.	Flux	σ	ID
11	58	0.12	1	30	59.2	3	0.032	5.61	IR
11	58	40.38	-18	20	4.4	4	0.062	5.89	none
12	7	0.15	39	40	33.9	3	0.017	4.77	Radio
12	9	54.98	-1	15	42.3	3	0.019	4.50	IR
12	16	21.40	38	11	59.5	3	0.013	5.08	Radio
12	33	29.16	66	23	38.2	4	0.054	6.02	IR
12	38	39.03	-28	42	32.3	4	0.048	5.37	none
12	45	43.47	60	52	23.0	3	0.020	4.56	none
12	46	37.02	59	10	11.0	3	0.032	5.03	IR
12	48	37.52	0	-56	12.6	4	0.022	6.97	none
12	50	59.89	56	35	16.4	4	0.028	5.10	none
12	52	30.54	56	56	25.3	4	0.029	5.22	none
12	54	31.18	-5	28	18.4	3	0.008	4.56	none
12	57	13.92	30	53	17.6	4	0.040	4.52	Radio
12	58	32.65	35	51	39.0	3	0.009	6.59	Radio
12	59	6.63	31	12	48.4	4	0.054	4.73	Radio
13	0	4.87	-2	3	7.7	4	0.030	5.33	Radio
13	1	31.06	63	41	50.5	3	0.028	5.01	IR
13	3	42.55	-1	53	43.2	4	0.059	5.77	IR
13	12	12.22	29	10	31.4	4	0.023	5.10	Radio
13	14	26.05	28	58	3.5	4	0.031	5.68	Radio
13	14	56.39	-22	54	8.5	4	0.024	5.11	none
13	15	58.68	29	25	54.4	4	0.040	5.87	Radio
13	16	1.56	-22	40	14.2	3	0.026	4.86	none
13	18	19.67	70	36	17.2	4	0.038	5.24	Radio
13	22	44.32	-4	53	12.5	3	0.026	4.80	none
13	26	34.83	-8	26	59.5	4	0.084	5.17	none
13	27	30.44	59	1	8.2	3	0.019	4.52	Radio
13	32	8.82	41	22	41.5	3	0.020	4.96	Radio
13	35	58.45	52	16	52.8	4	0.044	5.13	Radio
13	37	44.48	67	50	38.0	3	0.025	4.77	Radio
13	45	55.13	40	9	23.1	4	0.033	4.76	Radio
13	52	11.12	40	18	37.2	4	0.042	5.13	Radio
13	52	48.09	0	50	51.9	4	0.051	5.62	Radio
14	0	29.57	62	11	49.5	4	0.059	5.00	none
14	1	15.92	64	33	40.9	4	0.031	4.89	IR
14	1	51.64	64	25	22.2	4	0.040	6.08	IR
14	4	28.96	72	33	24.2	4	0.051	6.62	IR
14	4	49.80	22	30	18.5	4	0.047	4.97	none
14	9	44.02	52	8	55.8	4	0.025	6.85	none
14	13	19.45	19	19	55.1	3	0.035	4.51	Radio
14	18	26.16	72	20	37.5	4	0.044	5.12	Radio
14	21	11.06	-18	21	27.0	4	0.033	5.46	none
14	22	13.70	1	38	4.3	4	0.061	6.05	none
14	22	18.85	52	13	9.3	3	0.015	4.34	IR
14	25	47.29	1	48	6.6	4	0.026	5.40	none
14	28	23.15	62	12	57.0	3	0.030	4.83	none
14	28	32.21	62	31	3.8	4	0.033	5.17	Radio

TABLE 2. (continued)

R.A. (1950): ^{h}	^{m}	^{s}	Dec. (1950): $^\circ$	$'$	$''$	Ap.	Flux	σ	ID
14	32	26.51	-17	31	23.1	4	0.058	5.46	none
14	32	53.75	-18	51	20.1	3	0.052	4.77	none
14	33	35.50	19	37	4.2	4	0.054	5.94	none
14	42	1.86	27	5	7.8	4	0.031	5.85	none
14	42	53.91	52	7	33.0	3	0.018	4.83	IR
14	43	48.75	12	3	7.1	3	0.019	4.64	none
14	50	43.11	21	16	12.6	4	0.023	5.73	Radio
14	52	20.84	16	3	19.6	4	0.078	5.58	none
14	53	16.00	21	23	44.1	4	0.032	6.45	Radio
14	57	7.18	4	29	46.7	4	0.045	5.28	Radio
14	58	52.12	71	35	58.7	4	0.039	5.91	Radio
14	59	55.27	2	39	14.1	4	0.063	5.82	none
15	1	47.88	-32	55	25.1	4	0.040	5.20	none
15	2	10.38	26	27	32.5	4	0.022	5.21	none
15	2	43.57	22	10	13.3	3	0.018	4.51	none
15	4	40.10	11	2	52.3	4	0.029	6.11	Radio
15	8	43.10	57	28	7.1	4	0.057	5.54	Radio
15	12	55.21	33	27	32.3	4	0.023	5.07	none
15	15	28.58	22	55	20.4	4	0.042	5.28	Radio
15	17	11.63	20	17	3.6	4	0.014	5.42	none
15	20	31.67	71	43	23.8	4	0.060	5.10	Radio
15	23	7.30	30	1	50.4	3	0.027	5.41	Radio
15	24	47.65	22	57	55.0	4	0.025	5.33	none
15	25	26.51	11	19	23.3	4	0.038	5.18	none
15	25	41.61	10	22	39.6	4	0.046	5.35	none[b]
15	28	22.56	10	51	59.5	4	0.049	5.11	none
15	28	34.36	69	51	48.0	4	0.022	5.33	IR
15	29	48.69	-8	31	14.3	3	0.023	4.70	none
15	31	1.85	1	34	31.9	4	0.025	4.83	none
15	31	39.46	31	37	41.3	3	0.012	4.69	Radio
15	31	46.93	1	55	27.1	3	0.029	4.53	none
15	32	16.15	13	42	51.2	4	0.065	5.26	none
15	32	20.00	31	40	7.1	3	0.027	5.96	Radio
15	32	31.36	13	23	49.6	4	0.067	5.09	none
15	33	51.79	23	28	27.1	3	0.015	6.40	none
15	39	4.35	66	8	33.3	2	0.013	4.39	Radio
15	44	36.56	-17	2	39.4	4	0.061	5.15	none
15	47	19.04	5	52	30.5	4	0.074	6.27	Radio
15	48	15.32	5	21	18.0	4	0.062	5.41	Radio
15	50	19.31	-4	43	41.4	4	0.029	5.13	none
15	59	33.46	41	13	3.8	4	0.014	5.25	Radio
16	3	12.51	66	54	59.9	3	0.020	5.50	none
16	5	32.26	30	8	25.3	4	0.048	5.31	Radio
16	6	8.28	17	24	50.9	4	0.030	6.07	IR
16	6	22.79	17	24	31.6	3	0.015	4.66	IR
16	7	3.15	10	48	46.4	4	0.097	5.73	none
16	7	31.38	66	11	51.1	4	0.029	5.36	none
16	7	48.37	-18	25	27.1	3	0.014	5.21	none

TABLE 2. (continued)

R.A. (1950): ^{h}	^{m}	^{s}	Dec. (1950): $^\circ$	$'$	$''$	Ap.	Flux	σ	ID
16	14	4.12	6	21	59.0	3	0.064	4.84	IR
16	15	14.68	32	17	20.7	4	0.025	5.12	Radio
16	18	20.56	5	42	51.9	3	0.042	4.55	none
16	22	25.42	23	37	51.8	3	0.018	4.50	IR
16	23	1.40	26	40	33.1	3	0.006	4.84	IR
16	23	34.47	61	21	55.5	3	0.037	5.17	none
16	25	33.18	41	11	0.4	4	0.036	4.62	Radio
16	26	20.36	15	16	24.7	3	0.033	4.68	none
16	31	24.18	5	39	44.9	4	0.062	5.22	none
16	35	47.60	12	9	43.2	3	0.016	5.06	none
16	36	6.70	11	45	13.0	4	0.033	5.10	Radio
16	43	18.10	-3	21	48.1	4	0.025	5.47	none
16	44	38.65	32	33	7.0	4	0.021	5.04	Radio
16	46	46.78	71	5	4.8	4	0.065	5.26	Radio
16	48	33.10	5	21	26.6	3	0.007	4.73	Radio
16	54	40.05	9	44	6.7	4	0.036	6.01	Radio
16	54	41.27	9	18	34.8	4	0.025	5.13	IR
16	55	43.98	35	9	23.8	3	0.014	5.95	Radio
17	2	2.92	33	59	29.5	3	0.025	6.29	IR
17	3	38.88	0	43	36.6	3	0.025	4.53	none
17	3	43.35	23	46	56.4	3	0.019	4.50	none
17	6	44.97	49	8	19.9	4	0.059	6.41	none
17	7	10.54	54	47	34.9	4	0.053	5.55	none
17	8	0.37	39	41	57.5	4	0.058	6.07	Radio
17	11	18.87	48	41	57.6	3	0.031	4.96	Radio
17	17	57.25	32	37	32.1	4	0.038	5.85	Radio
17	18	55.76	32	49	43.1	4	0.029	5.06	Radio
17	20	44.53	34	15	34.1	3	0.035	4.33	Radio
17	22	25.09	66	57	32.2	4	0.066	4.67	Radio
17	28	28.45	52	33	1.0	4	0.066	5.28	Radio.
17	29	36.53	52	34	51.6	3	0.050	4.51	Radio
17	39	57.78	52	29	36.7	4	0.053	5.16	Radio
17	45	11.74	27	33	51.4	4	0.019	5.34	none
17	45	57.58	69	20	29.1	4	0.071	5.36	Radio
17	49	58.60	70	46	1.0	4	0.147	5.82	Radio
17	56	51.43	63	53	10.2	4	0.089	6.00	Radio
17	58	26.93	64	9	33.9	4	0.052	5.12	Radio
18	9	57.25	78	22	45.1	3	0.028	4.59	none
18	10	44.47	64	31	54.5	4	0.190	5.17	IR
18	20	47.03	64	1	23.5	4	0.072	5.42	Radio
18	28	8.09	64	2	18.0	3	0.058	5.51	Radio
18	32	35.04	64	47	32.4	4	0.161	6.40	Radio [c]
19	13	38.60	67	54	56.8	4	0.032	6.14	none
19	52	14.64	-69	12	30.0	3	0.018	4.52	Radio
19	54	1.24	-69	25	26.5	3	0.024	4.81	none
20	6	42.77	-36	8	23.2	4	0.048	5.24	none
20	11	8.07	-60	8	40.8	4	0.057	5.10	none
20	15	3.37	-3	37	41.2	4	0.042	5.03	none

TABLE 2. (continued)

R.A. (1950): ^{h}	^{m}	^{s}	Dec. (1950): $^\circ$	$'$	$''$	Ap.	Flux	σ	ID
20	55	5.42	-5	7	33.9	4	0.031	5.57	none
21	13	58.27	5	14	11.9	3	0.024	5.12	IR
21	18	12.17	-11	14	50.2	4	0.018	5.06	none
21	20	27.80	16	33	37.6	4	0.029	6.64	Radio
21	22	11.46	5	19	51.6	3	0.037	4.69	none
21	22	42.46	10	5	23.9	3	0.027	5.06	Radio
21	27	24.85	4	35	37.0	4	0.062	5.47	none
21	42	47.71	9	30	8.1	4	0.044	5.33	none
21	42	58.05	3	42	20.6	3	0.009	4.59	none
21	42	59.85	22	25	58.1	3	0.030	5.35	none
21	48	15.66	14	47	12.6	4	0.030	5.10	none
21	52	48.78	-61	2	44.1	4	0.069	5.11	IR
21	55	59.96	3	42	3.1	4	0.025	7.37	none
22	1	4.33	16	56	59.0	4	0.027	5.18	none
22	1	49.32	17	5	16.7	4	0.031	5.60	none
22	6	50.74	-4	24	46.0	3	0.019	4.85	none
22	35	11.48	-15	41	36.7	4	0.050	5.63	none
22	48	58.93	31	22	3.6	2	0.012	4.13	none
22	52	23.37	15	48	38.6	4	0.034	4.55	IR
22	55	27.03	20	18	47.8	3	0.020	4.87	none
23	3	28.01	14	50	39.6	4	0.043	5.42	none
23	3	37.52	-23	30	44.1	4	0.039	6.56	none
23	4	30.93	24	56	11.7	4	0.035	5.56	none
23	9	43.75	-49	51	4.3	3	0.017	4.35	none
23	10	52.80	-50	11	15.0	4	0.025	5.01	none
23	11	51.53	-50	3	51.6	4	0.030	5.21	none
23	12	32.66	-42	39	13.9	4	0.059	5.43	none
23	15	30.72	15	31	47.7	4	0.049	5.52	Radio
23	17	38.78	-42	40	36.0	4	0.051	5.31	none
23	48	14.24	19	36	52.4	4	0.040	6.44	none
23	50	36.90	28	46	42.4	4	0.046	5.14	none
23	57	38.75	29	49	46.1	4	0.041	5.88	IR
23	58	23.84	29	27	14.5	4	0.035	4.75	Radio

[a]This source is coincident with RASS Bright Source J010954.5-151018
[b]This source is coincident with RASS Bright Source J152807.3-101035
[c]This source is coincident with RASS Bright Source J183231.5+644949

Notes to Table 2.

The Ap. column indicates the best aperture used to approximate the source extent. A value of 2 corresponds to 2.35′, 3 to 4.2′ and 4 to 6.1′. Flux is in units of counts per second, and the ID column indicates whether NED found a radio source, an infrared source or neither within 12′ of the EXSS source.

fig1b

field

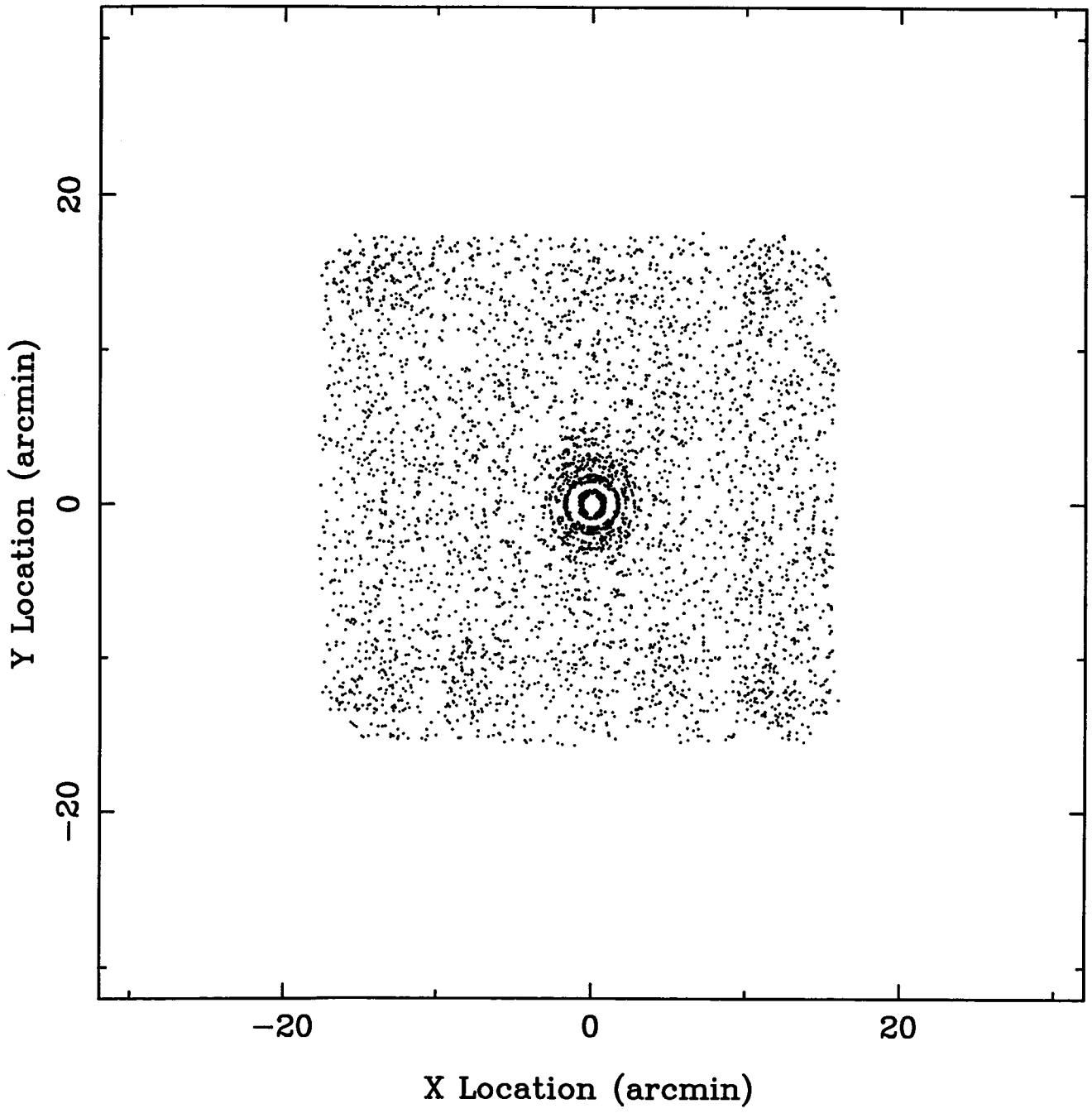

fig 2a

fig2b

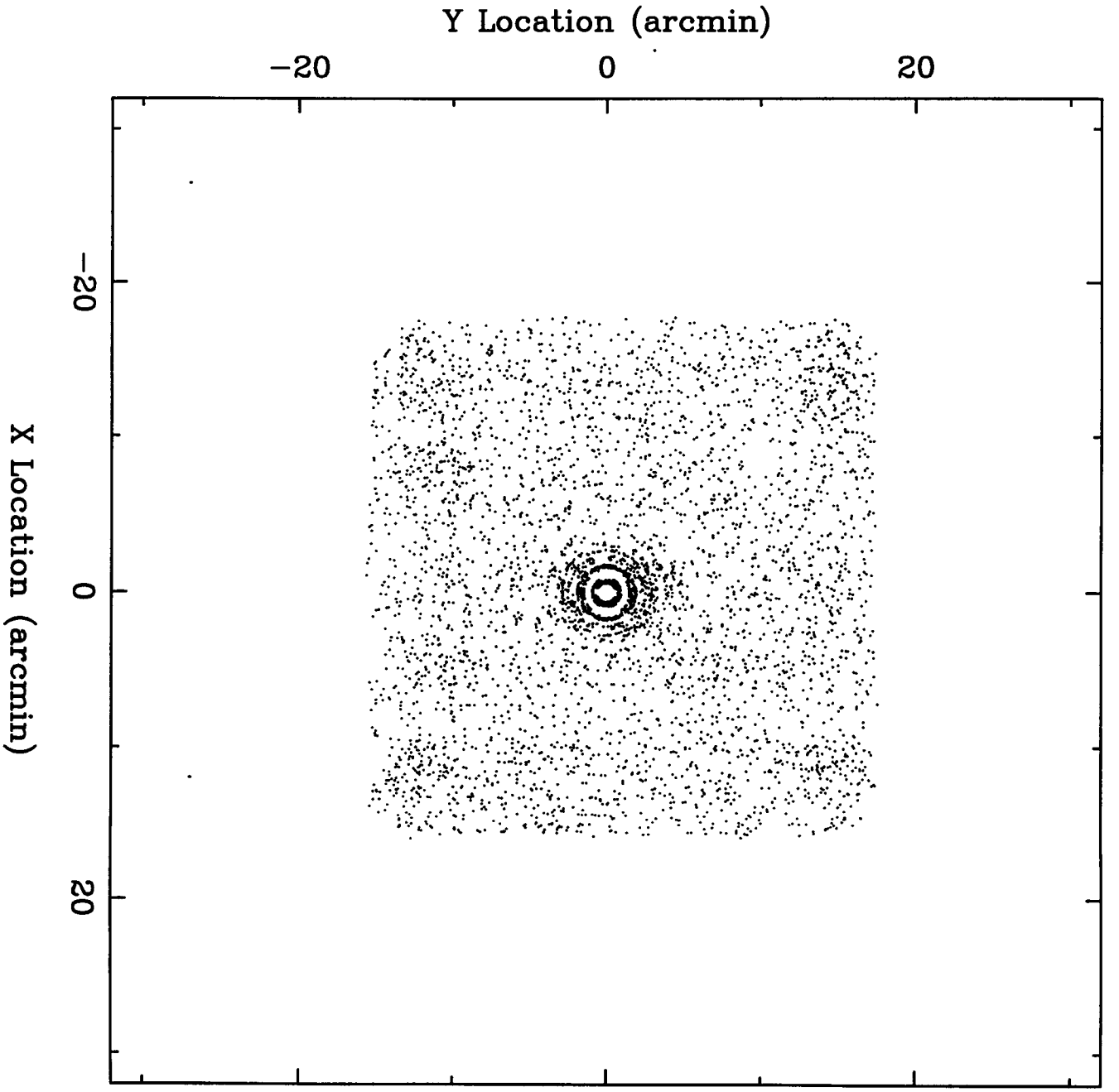
Y Location (arcmin)
−20
0
20
X Location (arcmin)
−20
0
20

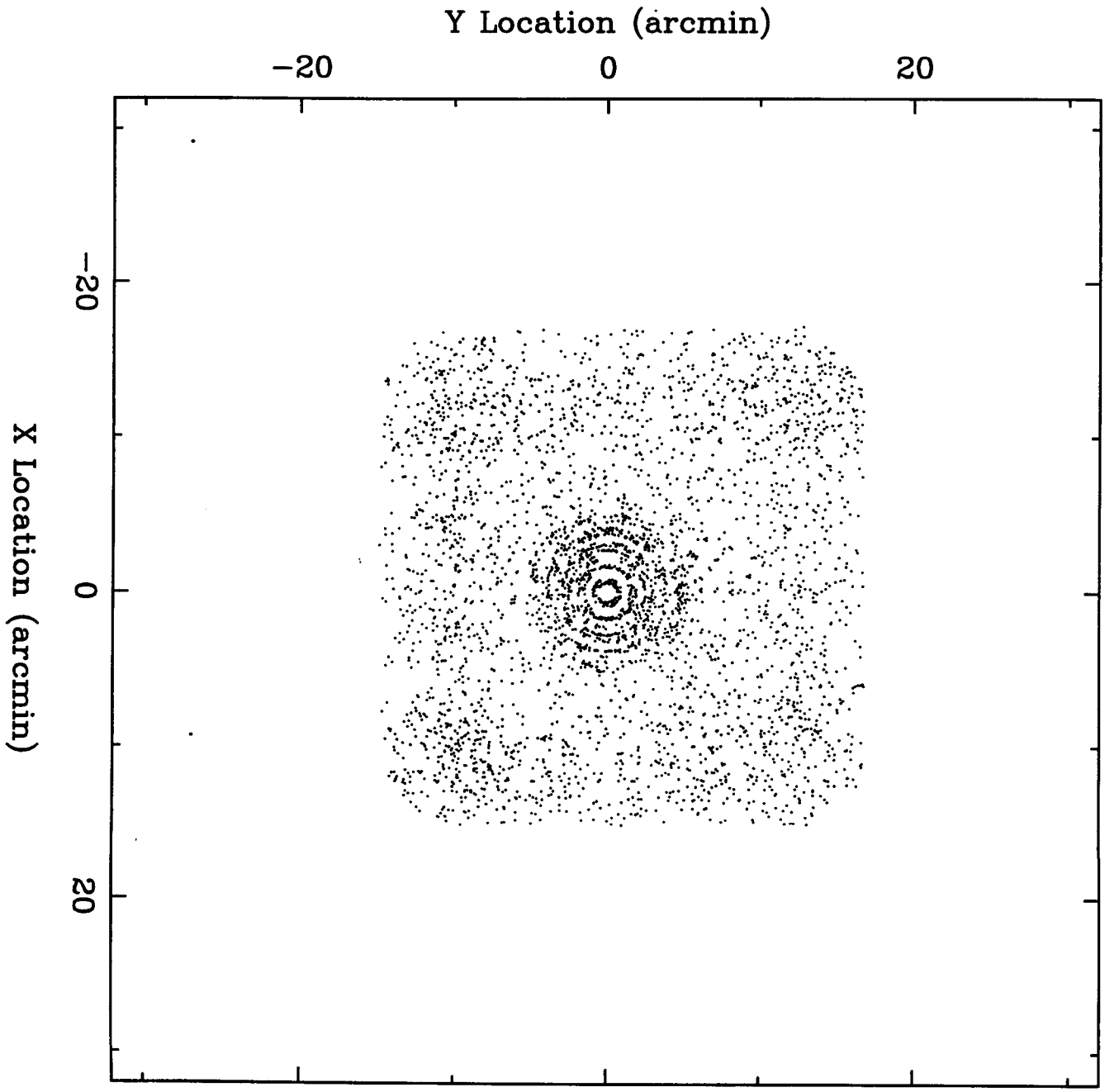
Y Location (arcmin)
−20
0
20
X Location (arcmin)
−20
0
20

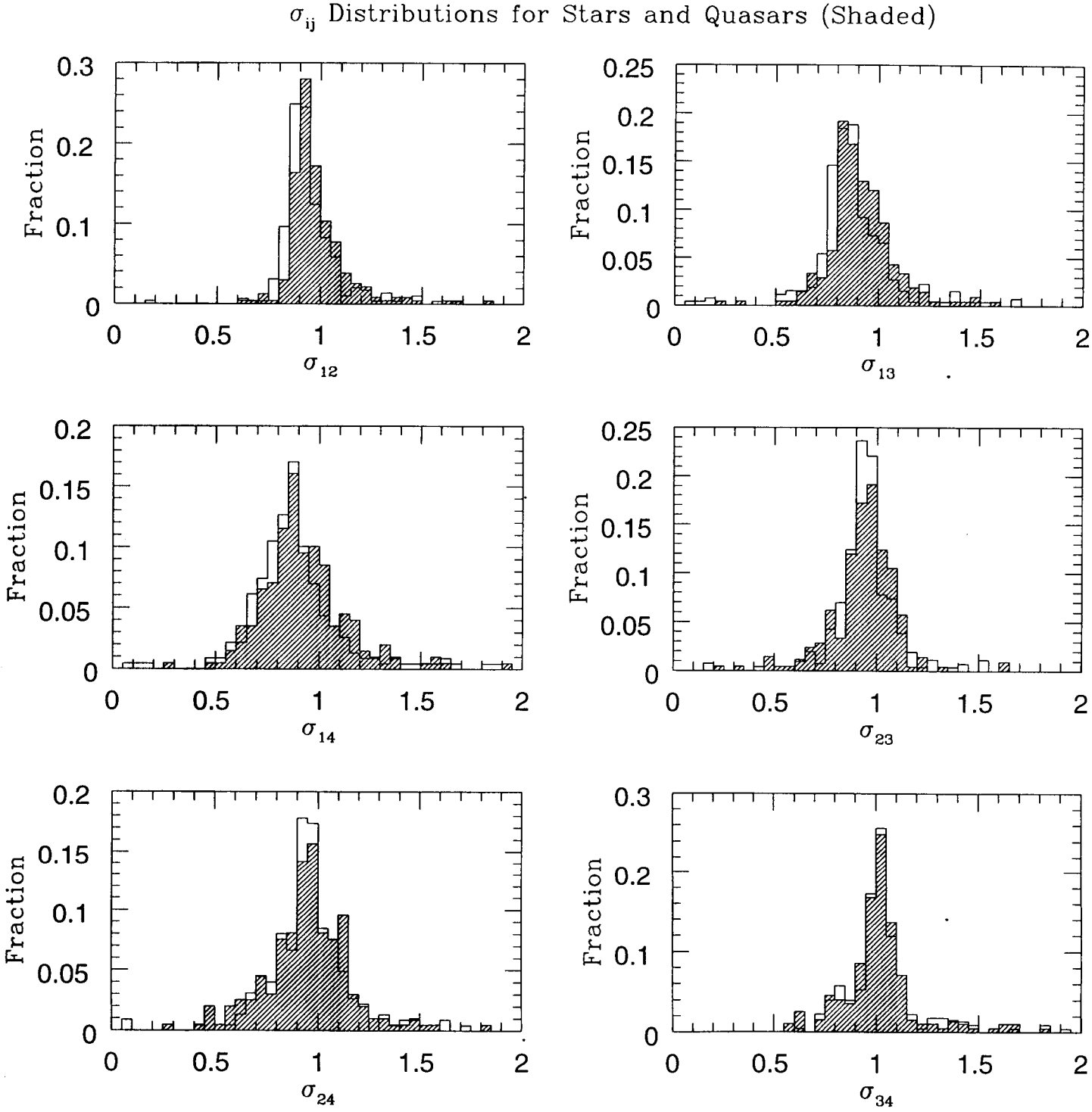
σ_{ij} Distributions for Stars and Quasars (Shaded)
Fraction
σ_{12}
σ_{13}
σ_{14}
σ_{23}
σ_{24}
σ_{34}

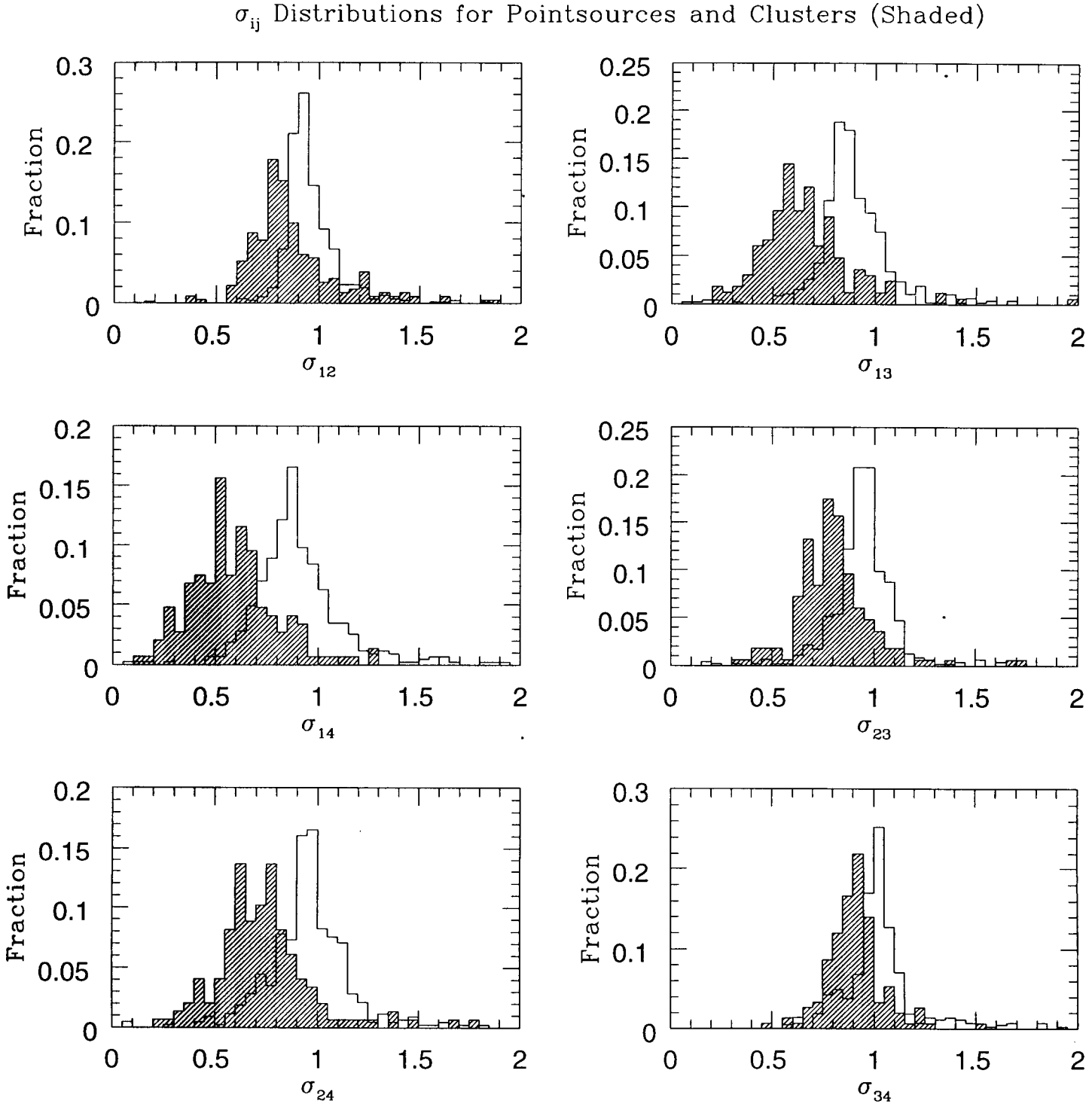
σ_{ij} Distributions for Pointsources and Clusters (Shaded)
Fraction
σ_{12}
σ_{13}
σ_{14}
σ_{23}
σ_{24}
σ_{34}

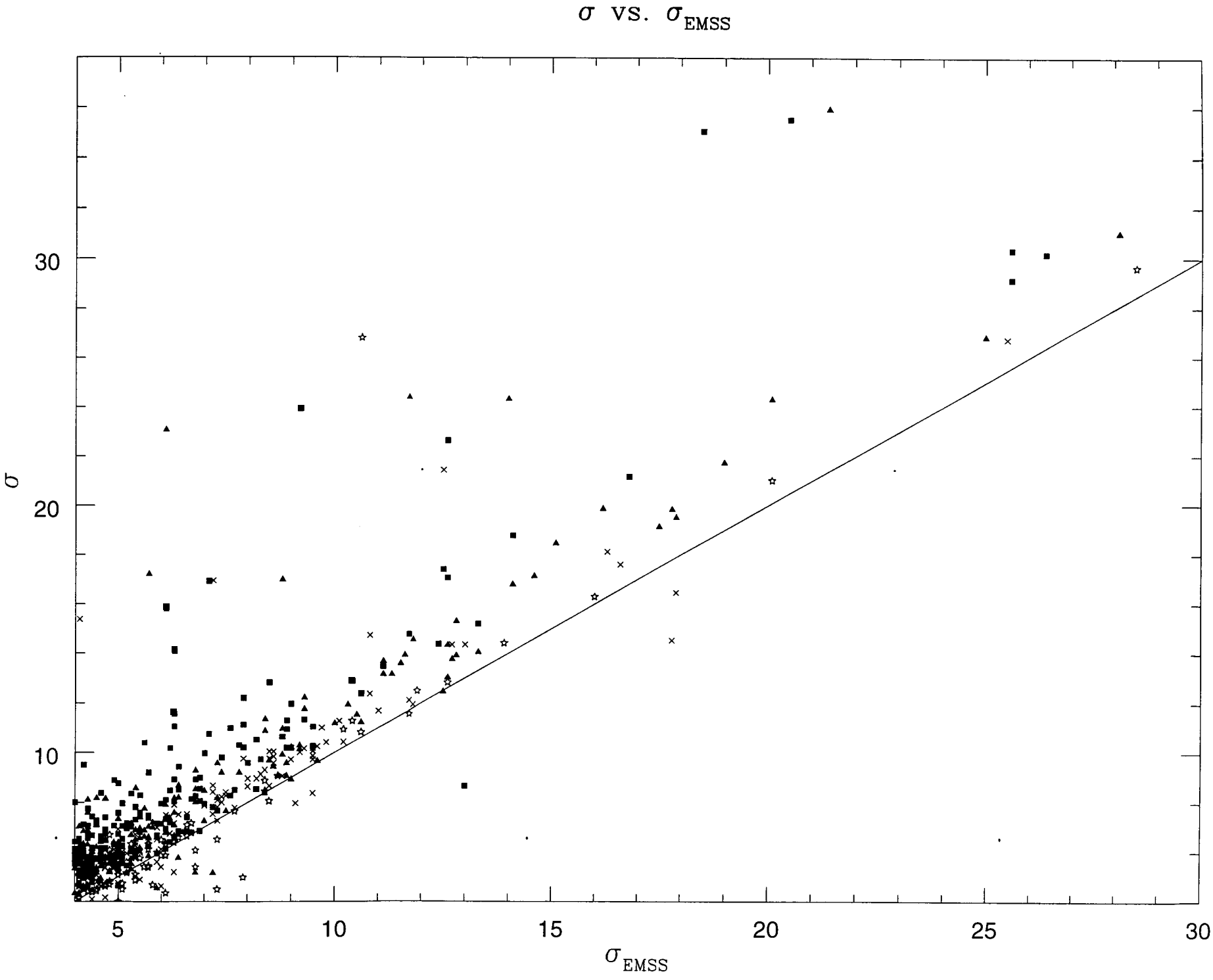
σ vs. σEMSS
30
20
10
σ
5
10
15
20
25
30
σEMSS

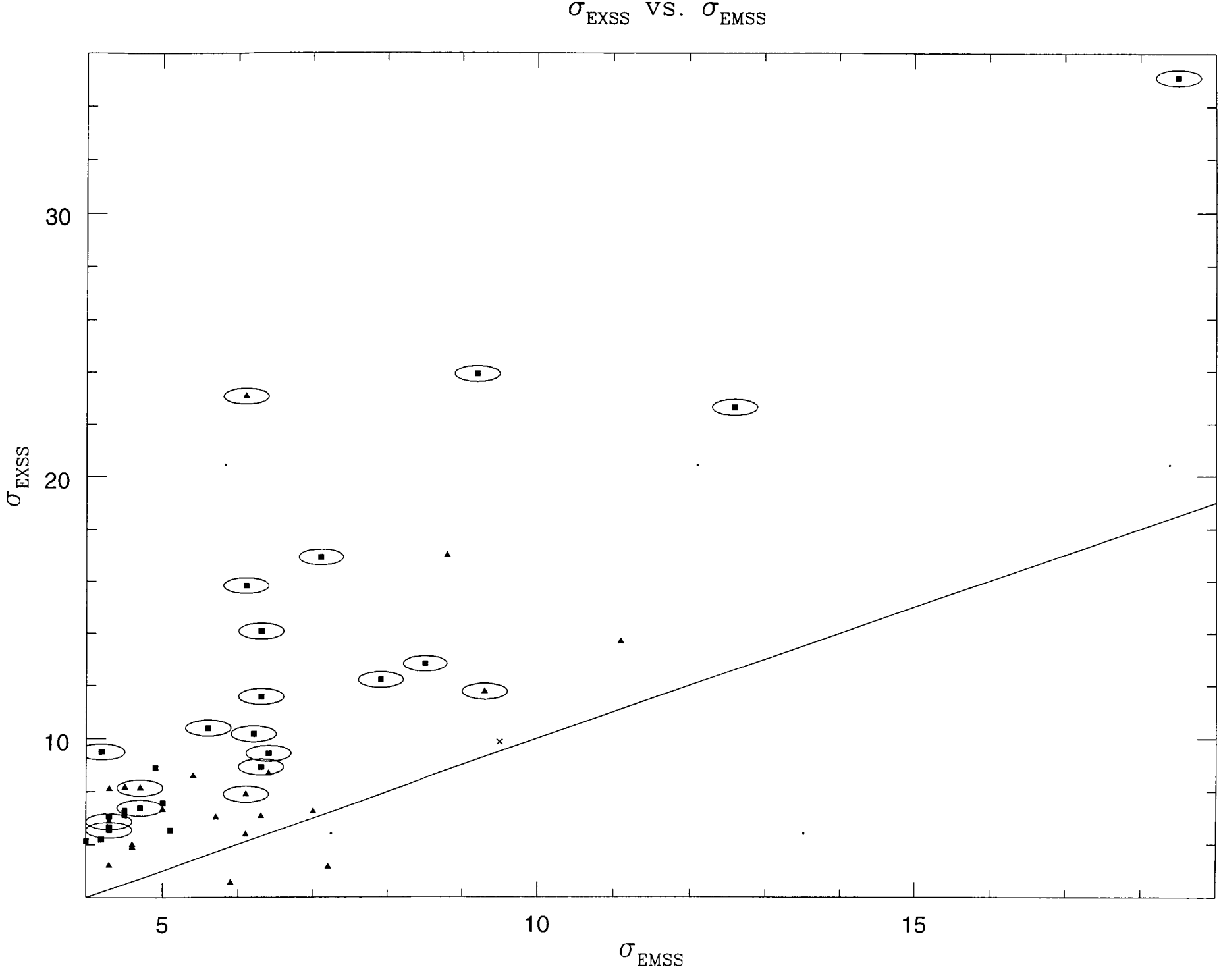
σ_{EXSS} vs. σ_{EMSS}
30
20
10
σ_{EXSS}
5
10
15
σ_{EMSS}

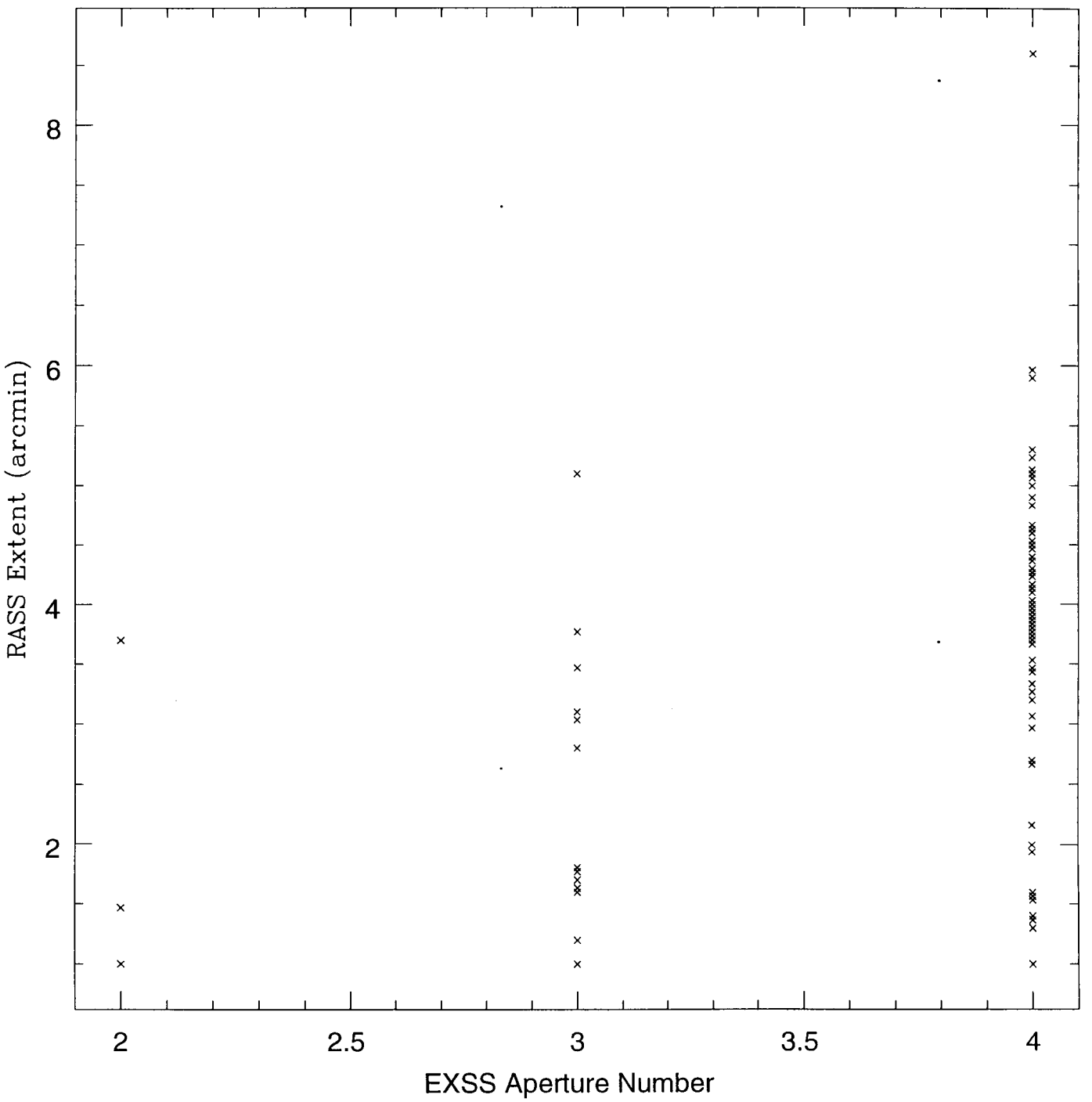
RASS Extent (arcmin)
8
6
4
2
2
2.5
3
3.5
4
EXSS Aperture Number

SILVER NEEDLES IN THE 2-σ HAYSTACK: GALAXIES, CLUSTERS, AND THE XRB

DAVID J. HELFAND[1] & EDWARD C. MORAN
Columbia University, 538 West 120th Street, New York, NY 10027

ROBERT H. BECKER
University of California at Davis, Davis, CA 95616

RICHARD L. WHITE
Space Telescope Science Institute, 3700 San Martin Drive, Baltimore, MD 21218

ABSTRACT We present results from an ongoing program designed to detect the new class(es) of contributors required to explain the spectrum and isotropy of the XRB. Our techniques allow us to find extended emission from clusters missed in the EMSS; in addition, we have discovered a large number of starburst and radio galaxies with $10^{41} < L_x < 10^{43}$ which, as a class, could contribute significantly to the background radiation.

There are three fundamental classes of observations relevant to understanding the cosmic background radiation in any spectral regime: the spectral intensity and shape of the background, its isotropy, and the properites of the resolvable sources which contribute to it. In the case of the X-ray background, recognized contributors include normal galaxies and galaxy clusters (both at the few percent level) and classical AGN (quasars and Seyfert galaxies) which may make up 50% at 1 keV, but whose contribution is substantially less at higher energies where the bulk of the energy density of the background resides. As a consequence, it is now abundantly clear (Fabian and Barcons 1992) that we require a new class (or classes) of sources to explain the origin of the diffuse X-ray background. In particlular, these new populations could help resolve the discrepancy between the number counts obtained in the EMSS (0.3-3.5 keV) and those inferred from the 4-12 keV *Ginga* data (Warwick and Stewart 1989). We report here new techniques we have developed for exploiting the *Einstein* imaging proportional counter (IPC) database in order to identify new types of background contributors.

In order to quantify the number of clusters missed in the EMSS which was optimized to find point-like ($< 2'$) sources, we have searched the 3500 IPC fields without bright sources or very extended diffuse emission (e.g., supernova remnants) for enhancements above the local background (after flat-fielding) on

[1] and Institute of Astronomy, Madingley Road, Cambridge, U.K.

scales of 2.5, 4.5, 8.5, and 12 arcminutes. The resulting catalogs provide a starting point for establishing the number of galaxy clusters and groups missed in a point-source search. For example, there are 1824 "point" sources in these fields with a significance of $> 6\sigma$, whereas there are an additional 502 sources at this significance level seen only with an 8.5′ aperture and over 2000 additional features seen on a 12′ scale. While we have just begun designing filters to select the real sources from the artifacts in these lists, it is clear that the procedure finds missed clusters. The 12′ source with the highest significance (14.5σ) is a known southern cluster which appears as only a 3.6σ excess in a point source search; in our first optical identification of a new cluster, a 2.2σ point "source" appears as a 4.7σ entry in the 12′ catalog and is coincident with a redshift 0.14 cluster. Optical images extracted from the GASP system are being used to construct a list of new cluster candidates for spectroscopic followup observations.

The EMSS (Gioia et al. 1991) characterizes well the point source population in the 0.3-3.5 kev band, but its limited size (800 sources over < 1% of the sky) and single broad energy band mean that it may have missed rare sources and sources with extreme spectra, just the sorts of objects required to explain the source count discrepancy. In order to extend the *Einstein* source catalog and search for the representatives of the required new populations, we have constructed three catalogs containing all IPC fluctuations exceeding a locally determined background by $> 2.0\sigma$ in each of three energy bands: 0.16-3.5 keV, 0.16-1.08 keV, and 1.08-3.50 keV; 1.45×10^5 "sources" are included in these lists. To select the real sources from statistical fluctuations, we apply various filters to these lists by matching them with catalogs from other spectral regimes. For example, matching the broad band list with the Greenbank 6cm (Becker et al. 1991) and Texas 80cm (J. Douglas, p.c.) catalogs, we select 894 and 844 X-ray sources, respectively; the false match rate determined by rematching with randomly offset X-ray positions is under 30%. Subtracting previously catalogued objects, the number of unique radio-selected entries is 872 of which over 500 represent new, radio bright X-ray emitters. We have obtained arcsecond positons for most of the 872 radio sources with the VLA and have produced optical finding charts for each one with the STScI GASP system.

A total of 66 optical counterparts have been observed spectroscopically to date, with 33 of the spectra fully reduced as of this writing. The mix of objects found is quite different from that of the EMSS. Two of the objects are quasars with $z > 3$ (none of which were found in the EMSS), including one at $z = 3.9$, making it the highest redshift X-ray source known (Becker et al. 1992). Only 25% of the total are AGN, however, compared to 51% for the EMSS. Three objects are moderate redshift starburst galaxies (see Fig. 1) while a surprising 13 sources, or 33% of the total are "normal" galaxies (as compared to < 5% in the EMSS). Although their X-ray luminosities range from $10^{41.5}$ to $> 10^{43}$ erg s^{-1}, above the range for nearby normal galaxies (Fabbiano 1989), their optical spectra show no evidence of an active nucleus. Deep optical images for six of these sources reveal that some have nearby companions, while others are isolated. High resolution, multi-frequency radio observations are scheduled in order to determine their morphology and spectra and to help distinguish amongst several possible explanations for their X-ray emission: starlight dominated BL Lacs, group or cluster sources, cooling flow galaxies, buried active nuclei, or some other unexpected new population of X-ray sources.

While our search for extended X-ray sources may help resolve the discrepancy between the low- and high-energy source counts, it is unlikely to reveal a significant new contributor to the hard background. The 2-σ point source catalogs, however, when matched to radio surveys and the IRAS FSC, clearly do reveal X-ray source populations not found in the EMSS. Both the high luminosity starburst galaxies (cf. Griffiths and Padovani 1990) and the new "passive", X-ray luminous galaxies we have found (cf. Boller et al. 1992) are potential contributors to both the soft and hard XRB. X-ray spectral and spatial studies of these objects with ROSAT and ASTRO-D as well as continuing optical and radio followup studies are planned in order to assess their potential for solving the problem of the origin of the X-ray background.

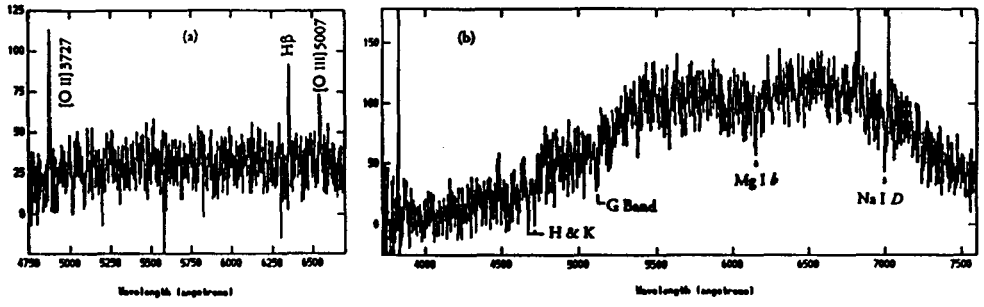

Fig. 1: Optical spectra of radio-selected sources from the 2-σ catalog; a) a $z = 0.31$ starburst galaxy, and b) a $z = 0.19$ "normal" galaxy with a 6 cm flux density of 47 mJy and an implied X-ray luminosity of 10^{43} erg s^{-1}.

ACKNOWLEDGEMENTS

This work was supported in part by NASA under grant NAGW-2507 and contract NAS 5-32063.

REFERENCES

Becker, R.H. et al. 1991, *Ap.J. (Suppl.)*, **75**, 1.
Becker, R.H. et al. 1992, *A.J.*, **104**, 531.
Boller, Th. et al. 1992, *Proc. X-Ray Emission from Active Galactic Nuclei and the Cosmic X-ray Background*, eds. W. Brinkmann and J. Trümper, MPE Report 235, Garching, p. 231.
Fabian, A.C. and Barcons, X. 1992, *Ann. Rev. Astron. Astrophys.*, **30**, 429.
Fabbiano, G. 1989, *Ann. Rev. Astr. Ap.*, **27**, 87.
Gioia, I. et al. 1990, *Ap.J. (Suppl.)*, **72**, 567.
Griffiths, R.E. and Padovani, P. 1990, *Ap.J.*, **360**, 483.
Warwick, R.S. and Stewart, G.C., 1989 in *X-Ray Astronomy: Proc. 23rd ESLAB Symposium*, eds. J. Hunt and B. Battrick (ESA SP-296), p. 1081.

Isolating the Foreground of the X-Ray Background

A. Refregier[1], D.J. Helfand[1], and R.G. McMahon[2]

[1] Columbia Astrophysics Laboratory, 538 W. 120th Street, New York, NY 10027, USA.
[2] Institute of Astronomy, Madingley Road, Cambridge CB3 0HA, UK.

Abstract. The foreground component of the X-ray Background (XRB) can be studied by cross-correlating its intensity with galaxy catalogs. We computed the two-point cross-correlation function W_{xg} between 67 *Einstein* X-ray fields and the APM galaxy catalog. We detected a signal with an amplitude of $W_{xg} = .04 \pm .01$, significant at the 3.5σ level. The reality of this signal was tested with a series of control data sets. We discuss how this signal can be used to constrain models of the XRB.

1. Introduction

One approach to study the cosmic X-ray Background (XRB) is to probe its foreground component by cross-correlation with galaxy catalogs. This method provides information not only on the contribution of the catalogued galaxies themselves to the XRB but also on the relation of the XRB to local large scale structure and clustering.

A recent series of studies has focused on the two-point cross-correlation function W_{xg} between the hard XRB ($\sim 2-10$ keV) and various optical and infra-red galaxy catalogs (Jahoda et al. 1991; Lahav et al. 1993; Miyaji et al. 1994; Carrera et al. 1995). A positive correlation signal was detected. When extrapolated to $z \sim 5$, this signal would indicate that 10-30% of the XRB is due to sources associated with galaxies. More recently, Roche et al. (1995) have found a positive cross-correlation signal between three soft ROSAT-PSPC fields (.5-2.0 keV) and galaxies down to $B \sim 23$. Their use of an imaging X-ray telescope allowed them to probe much smaller angular scales ($\sim 15''$) than the aforementioned studies in the hard band ($> 1\text{deg}^2$). However, their statistics were limited by the small number of fields considered. Treyer & Lahav (1995) have concluded from the soft results that the faint galaxies could contribute about 22% of the XRB in this band.

In order to test these results at intermediate angular scales ($\sim 1'$) and with improved statistics, we computed W_{xg} for 67 *Einstein*-IPC fields with the APM northern galaxy catalog ($E < 19$). The *Einstein* energy-band (.1-2.7 keV) allows flexibility for testing the energy dependence of the correlation. In addition, a large enough signal would allow us to consider several magnitude slices for the galaxies, thereby testing, at least crudely, the redshift dependence of the correlation. In this paper, we focus on the zero-lag results and on the controls we have performed to test their significance. The current analysis along with non-zero lag measurements will be presented in greater detail elsewhere (Refregier et al. 1995).

2. Data

The X-ray data consisted of 67 *Einstein*-IPC fields in which sources were excised down to 3.5σ. Source excision and flat fielding procedures are discussed in Wu et al. (1991) and Hamilton et al. (1991). We chose the fields to be at high Galactic latitude ($|b| > 30^0$ and to have exposure times greater than 6000 sec. We considered two energy bands: "soft" (.1-.56 keV) and "hard" (.56-2.70 keV). The "hard" band should be viewed as the real data whereas the "soft" band, which is dominated by emission from the Milky Way, should be considered as a control data set. Another control data set was constructed by including exposures with high solar contamination (VG=2,3); the "real" data set contained only low solar contamination (VG=1,2) exposures. Each one-square-degree field was subdivided in $64''$ pixels which contain most of the IPC point spread function ($\sim 1'$ at 2σ)

The APM northern catalog was derived from scans of Palomar Observatory Sky Survey plates (Irwin & McMahon 1992; Irwin et al. 1994.) In order to maximize the performance of the automatic image classifier, we restricted our analysis to the red plate objects with E-magnitudes between 13.5 and 19. This sample contained about 530 galaxies per square degree. To avoid complications at plate boundaries, we chose the field centers to lie further than $45'$ from the plate edges. The stars found in the same region of the sky were used as an additional control data set. The galaxies (and the stars) were also binned into $64''$ pixels.

3. Procedure

Our main task was to compute the zero-lag two-point cross-correlation function W_{xg} between the X-ray fields and the galaxies. This function gives a measure of the probability above random to find an excess in the XRB

intensity at the location of a catalogued galaxy. A finite-cell estimator of W_{xg} is given by

$$W_{xg} = \frac{n_{cell} \sum_i N_i I_i}{(\sum_i N_i)(\sum_i I_i)} - 1, \quad (1)$$

where I_i and N_i are the X-ray intensity and the number of galaxies in the i^{th} cell, and n_{cell} is the total number of cells (Jahoda et al. 1991). The cell size was varied by binning adjacent pixels.

Since both the X-ray and the galaxy data were subject to field-to-field variations (due differences in particle background contamination, plate sensitivity, etc), the 67 fields could not be treated as a single data set. Instead, we computed W_{xg} for each field separately, and computed the mean and 1σ uncertainty estimate ($\delta W_{xg} \simeq \sigma_{W_{xg}}/\sqrt{67}$, where $\sigma_{W_{xg}}$ is the rms standard deviation.) The calculation was performed for the real data set and for the aforementioned control data sets. In addition, we tested the statistical significance of our results by producing 400 scrambled realizations of the real X-ray-galaxy field pairs.

4. Results

Figure 1 shows W_{xg} with cell sizes ranging from 1 to 4 pixels for the different data sets. The real data set (hard-galaxies) produces a positive correlation of $W_{xg} = .04 \pm .01$, with a significance of 3.5σ (for a cell size of 64″). Although the measurements at different cell sizes are not independent, their comparison gives a measure of the robustness of the signal. As expected, the soft and solar-contaminated control sets yield lower correlation signals. The hard-stars values for W_{xg} are very close to zero. It is important to note that although the scrambled values are close to zero on average, their uncertainties ($\delta W_{xg} \simeq .01$) are not negligible. This gives a measure of the statistical uncertainty in the correlation signal.

5. Conclusions

We have detected a significant correlation signal between *Einstein* XRB intensity and APM galaxies. The signal passes our control tests. We emphasize the importance of good statistics and of the scrambled data set in obtaining an estimate for the statistical uncertainty involved.

A detailed interpretation of the signal is beyond the scope of this paper. We simply note that, in general, a correlation could result from three effects: (1) X-ray emission from the catalogued galaxies themselves, (2) a spatial correlation between the galaxies and the X-ray sources which form the XRB, or (3) X-ray emission from the hot gas in clusters and groups of galaxies. The first two effects have been referred to as "Poisson" and "clustering" terms in the literature (eg. Lahav et al. 1993). The last effect has been ignored before, but it can be significant. These three contributions have different intrinsic angular scales

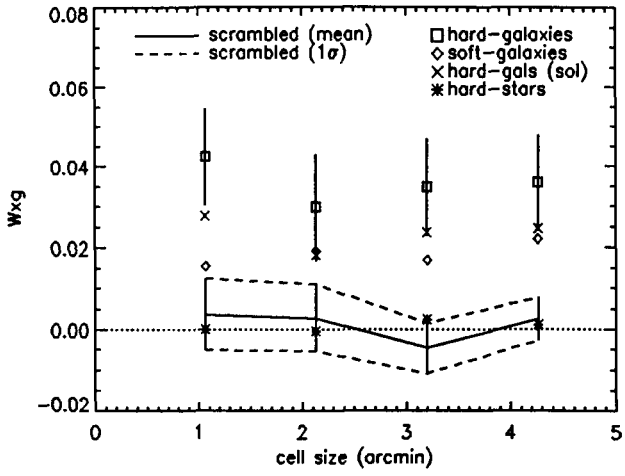

Fig. 1. W_{xg} as a function of the cell size for the real (hard-galaxies) and control data sets (the soft, predominantly Galactic emission with the galaxies, the hard emission with high solar contamination with the galaxies, the hard-band emission with the stars and the hard-galaxies scrambled field pairs.) For clarity, the 1σ uncertainties are only shown for the real and scrambled sets.

and can perhaps be decoupled by a non-zero-lag analysis. We also note that the point-spread function must be taken into account while dealing with imaging X-ray instruments. A discussion of these issues will be presented in Refregier et al. (1995).

Acknowledgements. We thank E. Moran for customizing the *Einstein* archive software and S. Maddox and M. Irwin for their help with the APM catalog. We also thank O. Lahav, M. Treyer, A. Blanchard, and R. Pilla for useful discussions. This work was supported by grant NAGW2507 from NASA, and contract number NAS5-32063. This paper is Contribution Number 585 of the Columbia Astrophysics Laboratory.

References

Carrera F.J., Barcons X., Butcher J.A., et al., 1995, Preprint, Submitted to MNRAS
Hamilton T., Helfand D.J., Wu X., 1991, ApJ 379,576
Irwin M., McMahon R.G., 1992, Gemini, 37,1
Irwin M., Maddox S., McMahon R.G., 1994, Spectrum 2,14
Jahoda K., Lahav O., Mushotzky R.F., Boldt E., 1991, ApJ 378,L37. Erratum in 1992, ApJ 399, L107
Lahav O., Fabian A.C., Barcons X., et al., 1993, Nature 364, 693
Miyaji T., Lahav O., Jahoda K., Boldt E., 1994, ApJ 434,424
Refregier A., Helfand D.J., McMahon R.G., 1995, in preparation
Roche N., Shanks T., Georgantopoulos I., et al., 1995, MNRAS 273, L15
Treyer M. A., Lahav O., 1995, Preprint
Wu X., Hamilton T., Helfand D.J., Wang Q., 1991, ApJ 379,564